



Darwin College Research Report

DCRR-008

Passive Wavelength Athermalisation of Semiconductor Laser Diodes

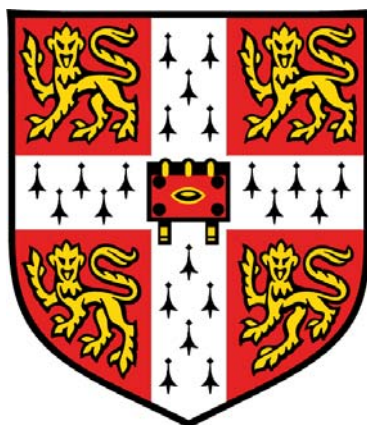
Amyas Phillips

**November 2005
(electronic edition 24 April 2008)**

**Darwin College
Cambridge University
United Kingdom CB3 9EU
www.dar.cam.ac.uk/dcrr**

ISSN 1749-9194

Passive Wavelength Athermalisation of Semiconductor Laser Diodes



Amyas Phillips

Darwin College

Department of Engineering

University of Cambridge

This dissertation is submitted for the degree of

Doctor of Philosophy

April 2005

For my parents

*Transit umbra
Lux permanet*

- inscription on sundial at
Nunwell House (1552), on
the Isle of Wight

Preface and Declarations

Attention is drawn to the fact that copyright of this thesis rests with the author. This copy of this thesis has been supplied on condition that anyone who consults it recognise that the copyright rests with the author and that no quotation from the thesis and no information derived from it may be published without prior written consent of the author. This thesis may be made available for consultation within the University libraries and may be photocopied or lent to other libraries for the purposes of consultation.

The work described was financially supported by the Engineering and Physical Sciences Research Council, with additional funding via a CASE award from Agilent Technologies UK.

This dissertation is the result of my own work and includes nothing which is the outcome of work done in collaboration except where specifically indicated in the text and Acknowledgements.

SIGNED: Amyas Phillips

DATE: April 2005

Acknowledgements

In the course of my research I have been grateful for the support of many people, whose contributions will not be forgotten. First of all, I must thank my supervisor Professor Richard V. Penty; for taking me on as a Ph.D. candidate in the first place and for his apparent confidence in me. Also I would like to thank the head of the Photonic Communications Systems group, Professor Ian H. White. He has fingers in a great many pies but his keen interest, when directed at my work, has been a great source of motivation.

I would also like to extend my appreciation to the senior members of the group, all of whom have assisted me at some time. Dr. Kevin Williams is owed a debt of gratitude and cookies for his work conducting etching sessions and also for assisting me with his deep knowledge of device parameters and modelling. Adrian Wonfor has been a sure guide with theoretical, practical and musical matters of every kind. Dr. Peter Bennett worked for some time in parallel with me, investigating 2D photonic bandgap etches, and apart from lending his hand with experimental work was the instigator of many useful discussions. Gefan Huang, whose work was the taking-off point of this project, has always been generous in sharing his insights on athermal gratings.

The work in this thesis would not have been possible without the financial support of Agilent Technologies UK, in particular Dr. Chris Park, head of university liaison, now of Blaze Photonics, who agreed to sponsor me as soon as I asked but only because he thought I meant I was doing something for charity.

Deep in thought unknitting tangled skeins of problems in front of my computer I have often been roused by the good humour of my fellow students, amongst whom I would especially like to pay my respects to Dr. Kay Ti Tan, Dr. Yew Jun Chai, Laura James and Jeremy Sosabowski, long may they prosper.

Away from research, my parents, my sister, my brother and the dog have always been a constant reassurance. My brother has been of inestimable help by advocating impenetrable titles. Fosbury has always believed wholeheartedly in me and her faith is something I have tried to live up to. I would also like to thank my friends around the world for reminding me that there are lots of other things to be getting on with, creating a sufficiently convincing illusion of greener fields to focus my mind on writing up. I tip my cap to the entire rowing fraternity of Cambridge for ensuring that I have regularly done more work by breakfast than I would otherwise have done by lunchtime. I reserve my final thanks for Eshani Ruwanpura, chief agent of writing and bearer of golden thambilis.

Passive Wavelength Athermalisation of Semiconductor Laser Diodes

Amyas Phillips

Summary

A new method is described of stabilising the emission wavelength of semiconductor light sources against changes in temperature. Beginning with a consideration of the spectral drift of semiconductor Bragg reflectors, theoretical arguments are developed and brought together with state of the art low-cost optical communications technologies to arrive at a design method for athermal vertical cavity surface-emitting laser (VCSEL) devices.

The work is aimed at coarse wavelength-division multiplexing (CWDM), a low-cost, flexible data-communications technology designed for in-building, campus and metropolitan deployments. Temperature-insensitive VCSEL sources are capable of increasing the number of CWDM channels without increasing price per channel.

Drift-engineering of distributed Bragg reflector (DBR) gratings using combinations of materials with different rates of change of refractive index with temperature is introduced. Numerical models are developed to investigate prior experimental results in this field and to explore new possibilities.

Athermal DBRs with symmetrically-offset reflection spectra are examined as a means of obtaining good selectivity with high-contrast reflectors. They are found highly effective but suffer from unavoidable mode hopping. Athermalisation without mode hopping requires stabilisation of the length of the laser cavity, which determines which wavelengths are resonant.

Measured in phase, the length of the cavity generally includes a contribution from the reflection phase of the DBR gratings, which are complex reflectors. It is proposed to use this small contribution to stabilise the 'effective' resonant length of short cavities over temperature. Short cavities in edge-emitting configurations are found theoretically possible, but practically difficult.

VCSELs are DBR devices with high-contrast Bragg reflectors and very short cavities. Developments in long-wavelength (InP-based) VCSEL technology and in customised application-specific optical polymers are combined to introduce drift-engineered VCSEL DBRs. A survey of the reflector design space thus opened up forms the basis of a straightforward athermal design approach.

This approach being wholly dependent upon optical polymer technology, the work concludes with a review of the most flexible polymeric material systems and identifies candidates suitable for this athermalisation application.

List of Publications

- [1] Phillips, A., Huang, H., Penty, R. and White, I.: ‘Proposal for Wavelength Stabilisation over Temperature of Distributed Bragg Reflector Diode Lasers’, 2003, *Semiconductor and Integrated Opto-Electronics Conference 2003*, University of Wales, Cardiff

- [2] Bennett, P.J., Williams, K.A., White, I.H., Kang, D.J., Webster, M., Wood, S.A., Haywood, M.E., Phillips, A.E.W., Penty, R.V. and Blamire, M.G.: ‘Semiconductor laser incorporating a short two-dimensional grating’, 2002, *15th Annual Meeting of the Lasers and Electro-Optics Society*, LEOS 2002, **2**, pp.795-796

- [3] Phillips, A.E.W., Penty, R.V. and White, I.H.: ‘Integrated passive wavelength athermalisation for vertical-cavity semiconductor laser diodes’, *IEE Proceedings – Optoelectronics*, 2005, **152**, (3), pp.174-180

List of Figures

Figure 1-1 Division of telecoms and datacoms ‘worlds’	2
Figure 1-2 Mapping of the ITU-T G.694.2 CWDM wavelength grid.....	6
Figure 1-3 ITU G694.1 200GHz DWDM wavelength spacing compared with part of the ITU G694.2 20nm CWDM grid in the 1530-1565nm C-band.	6
Figure 1-4 Schematic of typical source drift within a single ITU G.694.2 CWDM channel	8
Figure 1-5 Schematic of mode selection and drift factors in single-mode semiconductor lasers.	9
Figure 2-1 Infra-red absorption in semiconductor	21
Figure 2-2 Refractive index for Al _x Ga _{1-x} As.	22
Figure 2-3 Band gap renormalisation theory and experiment.....	23
Figure 3-1 Illustrative variation of l_1 and l_2 with desired Bragg-drift rate for a given Bragg wavelength	29
Figure 3-2 Schematic of mode energy distribution in an edge-emitting laser diode waveguide with a) a normal Bragg grating b) a deep grating	30
Figure 3-3 Drift rate vs. composition of one 16th-order 1310nm grating period constructed from BCB and InP (as in Table 3-2).....	31
Figure 3-4 Athermal powerreflectivity spectrum for 1310nm 16th-order grating specified in Table 3-2, for five temperatures.....	31
Figure 3-5 Cambridge Department of Materials Science Device Materials Group focussed Ion Beam (FIB) machine.....	32
Figure 3-6 Sub-threshold spectrum – 20mA, 20°C (device 1)	35
Figure 3-7 Measured weavelength of lasing mode of test device (1) vs. temperature after etching, before and after inclusion of BCB polymer.....	36
Figure 4-1 Normal reflection from a plane boundary	38
Figure 4-2 Key to wave designations in two-port network scattering parameters	40
Figure 4-3 Top: wave designations in two-port network transmission parameters, Bottom: T- parameterised two-port networks in series	42
Figure 4-4 Normally-incident plane waves at a dielectric interface.....	44
Figure 4-5 Transmission line with no discontinuities	45
Figure 4-6 Schematic of data flow and operating structure of TMM model code	50
Figure 4-7 Example grating structure	55
Figure 4-8 TMM model output for mirror structure described by Jambunathan et al	59
Figure 4-9 Reflectance r spectra produced by the TMM model using the DFB configurations in Table 1-4	61
Figure 4-10 Schematic energy distribution of the TE_0 mode propagating inside a laser cavity of thickness d	62

Figure 4-11	<i>Standard Gaussian (normal) distribution with mean 0, variance 1, and the cumulative integral beneath it.</i>	63
Figure 4-12	<i>Power reflectivity R at 980nm for deep air-gap gratings.</i>	65
Figure 4-13	<i>Reflectivity vs. wavelength, for 980nm Bragg condition grating with 380nm mirrors separated by deeply etched $\lambda/4$ air gaps, with one, two and three mirrors, from left to right.</i>	65
Figure 4-14	<i>Reflectivity vs. wavelength, for 980nm Bragg condition grating with three 380nm mirrors separated by deeply etched $C\lambda/4$ air gaps, where $C=1, 3, 5$ from left to right.</i>	66
Figure 4-15	<i>Reflectivity vs. infill material refractive index, for 980nm wavelength, with three 380nm thick mirrors separated by deeply etched $9\lambda/4$ air gaps.</i>	66
Figure 4-16	<i>Reflection spectra and temperature-dependence data for air-gap grating of 16th order and 1310nm reflection peak designed to be athermalised by infilling with BCB polymer</i>	67
Figure 5-1	<i>Band diagram of a double heterostructure under forward bias.</i>	70
Figure 5-2	<i>FP cavity with the first four possible resonances</i>	73
Figure 5-3	<i>Cavity refractive index vs. T and λ (left) and vs. λ only, for several T (right).</i>	75
Figure 5-4	<i>DBR cavity with complex reflectors.</i>	79
Figure 5-5	<i>Illustrative phase line plot for a 250μm $n=3.2$ FP cavity.</i>	79
Figure 5-6	<i>Schematic threshold current & current density vs. cavity length.</i>	81
Figure 5-7	<i>Drift with temperature of DFB lasing & gain peak wavelengths in a GaInAsP alloy system laser (Oe et al [2]).</i>	82
Figure 5-8	<i>Schematic of data flow and operating structure of cavity model code.</i>	86
Figure 5-9	<i>Reflectivity (top) and reflection-phase (bottom) spectra for combined gratings from Table 4-2</i>	92
Figure 5-10	<i>DBR cavity phase-length in half-wavelengths vs. wavelength, at T_{plot}.</i>	93
Figure 5-11	<i>Wavelengths of all resonant modes over temperature.</i>	93
Figure 5-12	<i>Wavelength of least-loss mode over temperature.</i>	94
Figure 5-13	<i>Temperature-to-temperature least-loss mode-drift rates</i>	94
Figure 5-14	<i>Phase-line (top) and least-loss mode (bottom) plots for example cavity from Table 5-2, modelled as an FP device with cleaved facets</i>	95
Figure 5-15	<i>Wavelength of least-loss mode over temperature for athermal-mirror test device after etching, before (top) and after (bottom) infilling with BCB.</i>	96
Figure 6-1	<i>Repeated mode hopping under modulation (from Sato et al)</i>	98
Figure 6-2	<i>Schematic device configuration for offset-grating wavelength-confinement approach</i>	100
Figure 6-3	<i>Equivalence of grating order m and λ_{Bragg}.</i>	101
Figure 6-4	<i>Individual and combined reflectivity spectra of offset grating pair</i>	102
Figure 6-5	<i>Emission wavelength vs. temperature of DBR with 200μm cavity and offset gratings as described in Figure 6-4. A typical DFB drift is shown for comparison.</i>	103
Figure 6-6	<i>Contribution of DBR mirrors to total cavity phase length</i>	105
Figure 6-7	<i>Overlapped reflectivity peak designed for proof-of-concept single-mode FIBE modification of FP device</i>	106
Figure 6-8	<i>Output spectrum of device before and after FIB etching (20 °C, $\sim I_{\text{th}}+10\text{mA}$).</i>	107

Figure 6-9	<i>Experimental set-up for pulsed-mode LIV and spectral measurements</i>	108
Figure 6-10	<i>Calculated change of the gain spectrum vs. photon energy from Illatzen et al</i>	109
Figure 6-11	<i>Schematic diagram of (a) lasing mode preservation and (b) mode-hop mechanism (from Sato et al [1])</i>	110
Figure 7-1	<i>Schematic of cavity athermalisation mechanism exploiting mirror phase</i>	113
Figure 7-5	<i>Mode-drift rate vs. cavity length survey</i>	115
Figure 7-6	<i>Example drift vs. cavity-length plot with key parameters indicated</i>	118
Figure 7-7	<i>Mode drift vs. cavity length for all twelve mirror designs</i>	119
Figure 7-8	<i>Key drift parameters from each reflector design's drift vs. cavity-length survey</i>	120
Figure 7-9	<i>Key cavity-length parameters from each reflector design's drift vs. cavity-length survey</i>	120
Figure 7-10	<i>Power reflectivity spectrum for N-period grating, N = 1 to 20</i>	122
Figure 7-11	<i>Associated Bragg-peak phase slopes across Bragg peak of N-period grating, N = 1 to 20</i>	123
Figure 7-12	<i>Reflectivity of 3-period InP:BCB grating at 1326nm, vs. gating order and ratio of optical lengths of InP and BCB</i>	124
Figure 7-13	<i>Combinations of layer-thicknesses satisfying the Bragg condition</i>	125
Figure 7-14	<i>Reflection phase across Bragg peak for three alternative configurations of 3rd-order InP:BCB grating</i>	125
Figure 7-15	<i>Power reflectivity spectra for mth-order grating, m = 1 to 20 (left) and associated Bragg-peak phase slopes (odd orders only) (right)</i>	126
Figure 7-16	<i>I_{th}+15mA spectra for device 20-2</i>	128
Figure 7-17	<i>Group effective refractive index vs. wavelength at 10, 30 and 50 °C</i>	128
Figure 7-18	<i>Device 20-1 cavity and grating (left) and angled facet (right)</i>	130
Figure 7-19	<i>Post-etch ASE spectra from 20-1 from the front facet</i>	130
Figure 7-20	<i>DFFT-filtered Device 20-1 ASE spectra (Figure 7-19) (signal power in dBm vs. wavelength in nm)</i>	132
Figure 7-21	<i>Device 20-2 ASE ripple positions normalised about their mean positions over temperature</i>	132
Figure 7-22	<i>RMS difference between modelled and measured mode positions for a range of effective phase indices for a 5.15µm FP cavity (device 20-1)</i>	133
Figure 7-23	<i>Modelled cavity phase slope and mode positions derived from it for n=3.487, with (right) and without (left) grating</i>	134
Figure 7-24	<i>FIB close-up of device 35-4 grating and cavity</i>	135
Figure 7-25	<i>Device 55</i>	136
Figure 7-26	<i>9µW emission spectra for device 55</i>	136
Figure 7-27	<i>Relative drifts of four modes in device 55 emission spectrum, positioned at indicated wavelengths at 20 °C</i>	137
Figure 7-28	<i>External reflectivity at 1315nm & 20C of device 55 grating for a range of air-gaps and phase indices</i>	137
Figure 7-29	<i>Modelled grating reflectivity spectrum at 20 °C for device 55 using n=3.487</i>	138
Figure 7-30	<i>Required cavity length for DBR lasers, vs. mirror reflectivity, for material gain of 50/cm, 100/cm and 200/cm</i>	140
Figure 7-31	<i>Device 69 offset grating, reflectivity (top) and phase (bottom)</i>	141
Figure 7-32	<i>Modelled least-loss cavity mode position vs. temperature, device 69</i>	141

Figure 7-33	<i>FIB image of part of device 69 cascaded short athermal cavity design, total length 51 μm.</i>	141
Figure 7-34	<i>Post-etch post-anneal ASE spectra for device 69, at 140mA, 20 $^{\circ}\text{C}$ and 50 $^{\circ}\text{C}$.</i>	142
Figure 7-35	<i>Drift rates available for 1300nm InP:air ‘deep DFB’.</i>	143
Figure 7-36	<i>Modelled lasing modes of 1:1 air:semiconductor ‘deep DFB’ vs. cavity length L (half-period).</i>	144
Figure 7-37	<i>Device 90, with half-period of 1225nm, 20 periods.</i>	145
Figure 7-38	<i>Device 88 post-etch ASE spectra various drive currents.</i>	145
Figure 7-39	<i>Current density J vs. voltage plots for device 90.</i>	146
Figure 7-40	<i>Laser diode equivalent circuit (left) and related effect on I-V characteristic (right).</i>	147
Figure 7-41	<i>Parallel resistance vs. length of etched sidewall, measured from a selection of devices.</i>	148
Figure 8-1	<i>Schematic of long-wavelength VCSEL with intracavity contacts and dielectric reflector stacks.</i>	153
Figure 8-2	<i>Reflectivity spectra (top) and corresponding reflection phases (bottom) of the nine air-gap mirror designs.</i>	155
Figure 8-3	<i>Reflectivity spectrum (left) and corresponding reflection phase (right) of 70-period quarter-wave InP-InGaAsP bottom DBR.</i>	155
Figure 8-4	<i>Mode drift rate vs. cavity length for a quarter-wave InP-InGaAsP bottom DBR with nine different air-gap top reflectors (see Figure 8-2).</i>	156
Figure 8-5	<i>Total phase-length in half-wavelengths m vs. wavelength for 1652nm cavity with InP-InGaAsP quarter-wave bottom DBR and design 2 top DBR.</i>	157
Figure 8-6	<i>Wavelength of least mirror-loss mode of 1652nm cavity with InP-InGaAsP quarter-wave bottom DBR and design 2 top DBR vs. temperature.</i>	157
Figure 8-7	<i>Drift-rate yields from 3000 simulations of the design used in Figure 8-6 with 2% standard error on cavity and stack thicknesses.</i>	158
Figure 8-8	<i>Modal drift rate vs. cavity length plots, for cavities with the nine grating designs of Figure 8-2 used above and below.</i>	158
Figure 8-9	<i>Enlargement of part of the 5th-order high-drift-mirror cavity-length survey of Figure 8-8 (circled there).</i>	159
Figure 8-10	<i>Total phase-length in half-wavelengths m vs. wavelength for 444nm cavity between design 9 air-gap reflectors.</i>	159
Figure 8-11	<i>Wavelength vs. temperature plot for least mirror-loss mode of 444nm cavity between design 9 reflectors.</i>	160
Figure 8-12	<i>Thermal drift rate of lasing modes of InP-airgap VCSEL (left) and corresponding required material gain (right).</i>	161
Figure 8-13	<i>Thermal drift rate of lasing mode of InP-BCB VCSEL (left) and corresponding required material gain (right).</i>	162
Figure 8-14	<i>Effects of range of polymer infills on characteristics of Agilent double-air-gap VCSEL design.</i>	163
Figure 8-15	<i>Modelled non-hop modal drift Agilent design double air-gap VCSEL infilled with hypothetical polymer of $n=1.52$ and variable dn/dT.</i>	164
Figure 8-16	<i>Non-hop mode drift vs. cavity length cavities bounded by 3-period air-gap reflectors of the Agilent design but infilled with notional polymer of $n=1.52$ and a range of dn/dTs corresponding to those circled in Figure 8-15.</i>	164
Figure 8-17	<i>Main features of mode-drift vs. cavity-length plots.</i>	165

Figure 8-18	<i>Resonant length of athermal design vs. wavelength for temperatures 10-80 °C (left) and corresponding plot of emission wavelength ($m=14$ resonance) vs. temperature.....</i>	166
Figure 8-19	<i>Drift (left) and wavelength (right) distributions of athermal device of Figure 8-18, modelled 3000 times with 2% standard error on each layer</i>	166
Figure 8-20	<i>Modelled mode drift of $\frac{1}{2}\lambda$ InP cavity with 3-period $\frac{3}{4}\lambda$ InP-polymer top DBR and 70-period $\frac{1}{4}\lambda$ InP-nGaAsP bottom DBR.....</i>	167
Figure 8-21	<i>Total resonant phase-length of $\frac{1}{2}\lambda$ InP cavity with hybrid reflectors.....</i>	167
Figure 8-22	<i>Explanation of impact of mirror drift on mode drift in the long-cavity double air-gap (left) and short-cavity hybrid (right) cases.</i>	168
Figure 8-23	<i>Distribution of dm_{mirror}/dT in 30 bins across range found in modeling 8820 polymer-infilled air-gap DBR designs across all design parameters.....</i>	172
Figure 8-24	<i>Matching surveyed reflector designs with available copolymer formulations (schematic).....</i>	173
Figure 8-25	<i>Phase length in half-wavelengths m of 412nm resonant cavity with refractive index $nS = 3.196, 3.204, \text{ and } 3.212$ at $0\text{ }^\circ\text{C}, 40\text{ }^\circ\text{C}$ and $80\text{ }^\circ\text{C}$</i>	174
Figure 8-26	<i>Complex reflection spectrum of 4-period 3rd-order polymer-infilled InP reflector stack with $lS = 515\text{nm}, lP = 194\text{nm}, nS = 3.2$ and $nP = 1.7$ at $20\text{ }^\circ\text{C}$, $TOCS = 2.02 \times 10^{-4}/^\circ\text{C}$ and $TOCP = -1.50 \times 10^{-4}/^\circ\text{C}$</i>	175
Figure 8-27	<i>Temperature drift of wavelength of reflection peak λ_{peak} and zero reflection phase $\lambda\Phi=0$</i>	175
Figure 8-28	<i>Total phase length of cavity (Fig. 4) plus athermalising Bragg reflectors on either side (Fig. 5b) for $0, 40$ and $80\text{ }^\circ\text{C}$</i>	176
Figure 8-29	<i>Wavelength of athermalised cavity resonance $0-80\text{ }^\circ\text{C}$</i>	176
Figure 8-30	<i>Drift rate of reflection peak of range of air-gap gratings.....</i>	177
Figure 8-31	<i>dm_{mirror}/dT for range of air-gap Bragg gratings</i>	177

List of Tables

<i>Table 2-1</i>	<i>Example refractive indices and TOCs</i>	25
<i>Table 3-1</i>	<i>Selection of material properties</i>	29
<i>Table 3-2</i>	<i>Gefan Huang's 1310nm athermal grating parameters</i>	31
<i>Table 3-3</i>	<i>Available etch resolutions and magnifications</i>	34
<i>Table 4-1</i>	<i>Comparison of S and T parameter approaches (from Coldren and Corzine)</i>	43
<i>Table 4-2</i>	<i>Input data structures to TMM model</i>	53
<i>Table 4-3</i>	<i>Output data structures from TMM model</i>	54
<i>Table 5-1</i>	<i>Experimental values for the energy gap, its temperature coefficient, the refractive index temperature dependence, and linear thermal expansion coefficient for some semiconductors. From Oe et al.</i>	72
<i>Table 5-2</i>	<i>Input data structures to cavity model</i>	88
<i>Table 5-3</i>	<i>Output data structures from TMM model</i>	89
<i>Table 7-1</i>	<i>Material and grating parameters at 20 °C</i>	117
<i>Table 7-2</i>	<i>Dimensions and reflection-peak data for twelve reflector designs (3 drifts by 4 grating orders)</i>	118
<i>Table 7-3</i>	<i>Parameters measured from cavity-length survey plots</i>	119
<i>Table 8-1</i>	<i>1320nm Reflector design parameters</i>	154
<i>Table 8-2</i>	<i>Mirror survey parameters</i>	171

Contents

Preface and Declarations	ii
Acknowledgements	iii
Summary	iv
List of Publications	v
List of Figures	vi
List of Tables	xi
Contents	xii
Chapter 1 Introduction	1
1.1 Motivation	1
1.2 Overview	4
1.3 Background	5
1.3.1 CWDM	5
1.3.2 Drift Sources and Strategies	8
1.3.3 Deep Gratings	10
Chapter 2 Refractive Index	13
2.1 Electromagnetic Parameters	13
2.1.1 Electric Permittivity	13
2.1.2 Magnetic Permeability	15
2.1.3 Speed of Light	15
2.2 Origins and Definitions	16
2.2.1 Origins	16
2.2.2 Definitions	16
2.2.3 Dispersion and Absorption	17
2.2.4 Polarisability and Density	18
2.2.5 Plasma Index Contribution	19
2.3 Absorption and Refraction	19
2.3.1 IR Absorption in Semiconductors	19
2.3.2 Kramers-Kronig Relations	21
2.3.3 Refractive Index near the Band-Gap Energy	21
2.4 Thermal Effects	22
2.4.1 Band-Gap Renormalization	22
2.4.2 Thermal Index changes	23
2.4.3 Thermo-Optic Effect	24
Chapter 3 Grating Drift Control	26
3.1 Introduction	26
3.2 Bragg Condition and Drift	26
3.3 Bragg Drift Tuning	27
3.3.1 Zero-Drift Condition	27
3.3.2 Design for Specific Reflector Drift	28
3.3.3 Design Tool	28
3.4 Test Device	30
3.4.1 Grating Parameters	30

3.4.2	Base Device	32
3.4.3	Focussed Ion Beam Etching	32
3.4.3.1	Overview	32
3.4.3.2	Etch Specification	33
3.4.3.3	Etch Considerations	34
3.4.4	Polymer Infill	35
3.4.5	Observations	35
Chapter 4 Reflector Model Development		37
4.1	<i>Bragg Reflector Model Requirements</i>	37
4.2	<i>Reflectivity and Transmissivity</i>	37
4.3	<i>Multiple Reflections in Dielectric Stacks</i>	39
4.3.1	Network Analysis	39
4.3.1.1	Scattering Parameters	39
4.3.1.2	Transmission Parameters	41
4.3.2	Scattering Matrix by Multiplication of Transmission Elements	43
4.3.2.1	Dielectric Interface	43
4.3.2.2	Transmission Line	45
4.3.2.3	Constructing reflection gratings using TMM	46
4.4	<i>Model Code Structure</i>	47
4.4.1	Introduction to Matlab	47
4.4.2	Overview	48
4.4.3	Assumptions	51
4.4.4	Input and Output Data Structures	51
4.4.5	Construction of Grating T-matrix	55
4.4.6	Data Analysis Routines	56
4.4.6.1	Location of Reflection Peak	56
4.4.6.2	Location of Limits of Reflection Peak	57
4.4.6.3	Location of Zero Reflection-Phase	57
4.4.6.4	Measurement of Phase Slopes	58
4.4.6.5	Calculation of Drift Rates	58
4.5	<i>Test and Verification</i>	58
4.5.1	Characteristics of Reflection Spectra	58
4.5.2	Published Deep Gratings	59
4.5.3	Typical DFB Parameters	59
4.5.4	Loss in Deep Bragg Gratings	61
4.5.5	Application to Athermal Mirror Test Device	67
Chapter 5 Cavity Mode Location Model		69
5.1	<i>Motivation</i>	69
5.2	<i>Semiconductor Laser Active Structures</i>	69
5.3	<i>Wavelength Drift in Laser Diode Cavities</i>	71
5.4	<i>Resonance in Fabry-Perot Cavities</i>	72
5.4.1	Resonance Condition	72
5.4.2	Mode Spacing	73
5.4.3	Cavity Phase Length	74
5.4.4	Temperature Sensitivity	77
5.5	<i>Resonance in DBR Structures</i>	78
5.5.1	Contribution of Reflector Phase	78
5.5.2	The Phase Line	79
5.5.3	Temperature Sensitivity	79
5.6	<i>Mode Selection</i>	80
5.6.1	The Gain Condition	80
5.6.2	Threshold Current	81
5.6.3	Mode Selection	82

5.6.4	Least-Loss Mode	83
5.7	<i>Mode-Locating Code</i>	83
5.7.1	Overview	84
5.7.2	Considerations	85
5.7.3	Input and Output Data Structures	86
5.7.4	Bisection Algorithm	90
5.7.5	Mode-Hop Detection	91
5.7.6	Test and Verification	91
5.7.7	Application to Athermal Mirror Test Device	95
Chapter 6 Offset Grating Concept		97
6.1	<i>Improving Wavelength Selectivity</i>	97
6.2	<i>Design Issues</i>	97
6.2.1	Mode Hops	97
6.2.2	Athermal Reflection Peak	99
6.3	<i>Offset Grating Devices</i>	99
6.3.1	Design Procedure	99
6.3.2	Use of Grating Order m	100
6.3.3	Character of Overlap-Peaks	101
6.3.4	Wavelength Confinement	103
6.3.5	Single-Mode Device Modification	105
6.3.6	Pulsed-Drive Investigation	107
6.4	<i>Conclusions</i>	109
Chapter 7 Design and Experimental Assessment of Deeply-Etched Edge-Emitting DBRs		111
7.1	<i>Thermal Compensation using Mirror Phase</i>	111
7.1.1	Cavity Stabilisation Requirement	111
7.1.2	Reflection Phase as Effective Length	112
7.1.3	Cavity Expansion Compensation	112
7.2	<i>Cavity Length vs. Mode Drift Study</i>	114
7.2.1	Cavity Length Survey with Athermal Grating	114
7.2.2	Cavity Length Phenomenology Survey	116
7.3	<i>Designing Reflection and Phase Spectra</i>	121
7.3.1	Effect of Number of Periods	121
7.3.2	Material Proportions	123
7.3.3	Effect of Grating Order	126
7.3.4	Conclusions	126
7.4	<i>Determination of Refractive Index</i>	127
7.5	<i>Single and Double-Grating Devices</i>	129
7.5.1	Devices 20-1 and 20-2	129
7.5.1.1	Design and Observations	129
7.5.1.2	20-1 Data Analysis Using DFT	131
7.5.1.3	Determination of Refractive Index from 20-1	133
7.5.2	Devices 36-3 and 35-4	134
7.5.3	Device 55	135
7.5.4	Conclusions	139
7.6	<i>Serial Microcavities and Active Elements</i>	140
7.6.1	Device 69	140
7.6.2	Active Grating Survey	142
7.6.2.1	Changing material ratio within constant grating period	142
7.6.2.2	Changing period of grating with constant material ratio	143
7.6.3	Devices 88, 89 and 90	144
7.6.4	Electrical Characteristics of Etched Facets	147
7.7	<i>Conclusions</i>	149

Chapter 8 Reflector Survey and Athermal VCSEL Design Methodology	151
8.1 <i>VCSEL Design Notes</i>	151
8.1.1 Advantages of VCSEL Technology	151
8.1.2 Material Systems	152
8.2 <i>Hybrid VCSEL Designs</i>	153
8.2.1 Why Hybrid?	153
8.2.2 Influence of Reflector Drift	153
8.2.2.1 Reduced-drift VCSEL mirror designs	153
8.2.2.2 Hybrid (air-gap and InP-InGaAsP reflectors) results	156
8.2.2.3 Symmetric (double air-gap reflectors) results	158
8.2.2.4 Conclusions	160
8.3 <i>Agilent Air-Gap VCSEL</i>	160
8.3.1 The Agilent Design	161
8.3.2 Mirror Modification Options	161
8.3.3 Polymer Infill Options	162
8.3.4 Conclusions	163
8.4 <i>Infilling with Optical Polymers</i>	163
8.4.1 Air-Gap VCSEL with Tailored-Polymer Infill	163
8.4.2 Hybrid VCSEL Tailored-Polymer Infill	167
8.5 <i>Reflector Survey & Athermal Design Method</i>	169
8.5.1 Athermalisation by Phase-Length Stabilisation	169
8.5.2 Developing an Athermal Design Procedure	169
8.5.3 Mirror Design Survey	170
8.5.3.1 Survey design	170
8.5.3.2 Survey results	171
8.5.3.3 Example Design Procedure	174
8.5.4 Air-Gaps Survey	176
8.5.5 Conclusions	178
Chapter 9 Polymers	180
9.1 <i>Introduction</i>	180
9.2 <i>Structure and Chemistry</i>	180
9.3 <i>Refractive Index</i>	181
9.4 <i>Modern Optical Polymers</i>	182
9.4.1 Halogenated Polyacrylates	182
9.4.2 Fluorinated poly(arylene ethers)	183
9.4.3 Polysiloxanes (Silicone Resins)	183
9.4.4 Benzocyclobutene (BCB)	184
9.4.5 Sol-Gels	184
9.5 <i>Technical Considerations</i>	185
9.5.1 Reliability & Environmental Stability	185
9.5.2 Processing & Fabrication	185
9.6 <i>Conclusion</i>	186
Chapter 10 Conclusion	189
10.1 <i>Review</i>	189
10.2 <i>Conclusions</i>	190
10.3 <i>Evaluation</i>	192
10.4 <i>Future Work</i>	192
Appendix Device List	195

Chapter 1

Introduction

The role of coarse wavelength-division multiplexing (CWDM) in current optical communication is introduced, especially in data communications within buildings, campuses and metropolises. The low-cost, flexible solutions demanded by this market segment are discussed in terms of device engineering and contrasted with competing dense wavelength-division multiplexing (DWDM) technology. Temperature-insensitive sources are shown capable of increasing the channel count of CWDM without adversely impacting price. Mechanisms of the temperature-dependence are introduced and athermalisation strategies considered.

1.1 Motivation

Telecommunications was the application for which optical fibre and semiconductor lasers were developed. High aggregate data rates over long, capital-intensive, point-to-point links characterised this epoch, until the rise of the Internet created huge new demand for data services. The phenomenal increase in data communications over the last two decades has been enabled at its core by the deployment of optical links with enormous data-carrying capacity.

Two key technological advances lie behind these systems: low-loss silica optical fibre and tiny, bright semiconductor light sources capable of rapid modulation. Initially, these were light-emitting diodes (LEDs), producing photons from recombining charge carriers across a simple semiconductor junction. The addition of light-guiding and reflector structures to these devices produced semiconductor lasers. Brighter, faster and just as small, these made possible increased transmission distances and modulation rates. The advent of erbium-doped fibre amplifiers (EDFAs) extended operating ranges even further. The most recent big technological step has been the importation from the radio communications sector of wavelength division multiplexing (WDM). In WDM the non-interference between data channels using different wavelengths of light is exploited to route many channels down a single fibre, transmitting different data streams simultaneously on different wavelengths.

The rise of the internet also shifted the demography of data traffic overwhelmingly towards data rather than voice. Trunk technology has gradually incorporated networking concepts such as rings and packetisation as a result, while conversely the new demand at the periphery of the network has made it economic to bring optical systems much closer to the end-users: as far as data backbones within offices and around campuses (**Figure 1-1**). The requirements of this datacoms market are fundamentally different from those of telecoms, centering on low costs,

small form factors, ease of use and flexibility, with less emphasis on quality of service reliability.

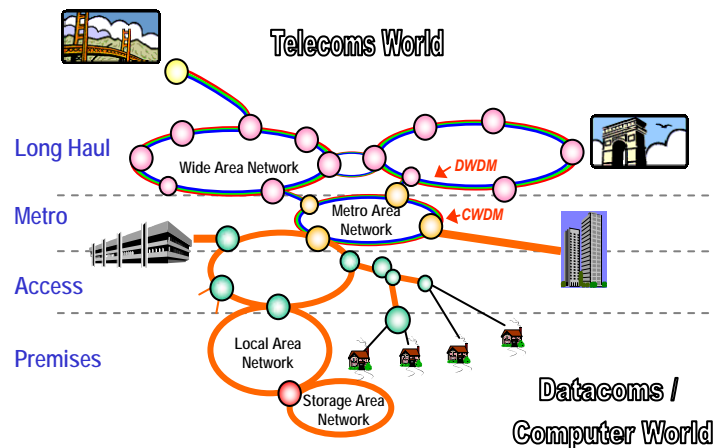


Figure 1-1 Division of telecoms and datacoms 'worlds'

Datacoms and telecoms continue to borrow from and even overlap one another. It is now commonplace, for instance, for a collection of local network segments around a city to be linked to form what is loosely termed a metro area network (MAN), traditionally a preserve of the telecoms industry. WDM technology is another example. Initially confined to trunk routes by its economics, it has in recent years been deployed progressively further from the network core, not far behind optical technology itself. The simultaneous expansion of the datacoms segment in from the network edge has led to widespread deployment of WDM systems in the metropolitan and campus datacoms arena.

Tightly specified telecoms equipment has for some time been able to multiplex as many as 160 wavelengths [1], increasing the data capacity of a single fibre by 160 times. Naturally, 160 sets of transmission and reception equipment are then required, plus multiplexing equipment, but network operators have found it highly economic to increase the capacity of installed base this way. In fact, extensive deployment of such DWDM systems prior to the year 2001 multiplied data capacity much faster than demand, causing a slump in the telecoms industry.

Fitting so many channels within the operating windows of optical fibre requires that they be very closely spaced. The high power densities can put the system into a non-linear regime in which stimulated Raman and Brillouin scattering processes skew the energy distribution across wavelengths and where refractive index depends on signal level, leading to self-phase modulation, cross-phase modulation, self-focussing and four-wave mixing. Quite apart from these problems, fine wavelength control is essential. The engineering problems associated with this apparently simple requirement are considerable.

Semiconductor lasers essentially consist of a long thin waveguide with optical gain and partial reflectors at either end. The reflectors may be simple facets of the semiconductor crystal,

in which case the output spectrum will be made up of a number of sharply-defined wavelengths consistent with the longitudinal resonances or *modes* of the laser cavity, within an envelope peaking at the band-gap energy. This gain spectrum depends on the material used but is typically wide compared to the wavelength-spacing in WDM systems. For this reason, and also because single-mode systems achieve longer transmission distances, designers incorporate wavelength-selective reflector structures made up of periodic variations in the waveguide. These are known as Bragg gratings and may either run the whole length of the cavity, in which case the device is known as a distributed feedback (DFB) laser, or replace the facets as reflectors at either end, an arrangement known as a distributed Bragg grating (DBR). In DFBs the grating is entirely responsible for selecting the laser wavelength; in DBRs the gratings select one of the cavity modes. Both configurations are susceptible by various mechanisms to drift of emission wavelength with operating temperature.

Many optical network components are provided with environmental control or compensatory feedback systems to prevent wavelength drift, over time or temperature. In telecoms, temperature control by Peltier cooling of laser diodes is used, but in datacoms the extra bulk, cost, power requirement and thermal load of this method is unacceptable. Users prefer racks of closely packed low-cost modules, running with low infrastructure requirements in the proverbial broom cupboard.

Re-engineering WDM to emphasise low cost and small form factors has led to the development of coarse WDM systems using only a few wavelengths. Unlike DWDM, which carries a large number of wavelengths closely spaced to fit within fibre-amplifier operating windows, CWDM has been developed specifically for smaller, metropolitan-scale deployments. With link lengths less than 60km there is no amplification requirement and the entire fibre transparency window becomes available. By using a coarse wavelength grid, source wavelengths can be allowed to drift freely. Increased wavelength tolerance cuts component cost dramatically throughout the link, impacting filters and multiplexers as well as sources. The thermoelectric coolers usually needed to control laser temperature are obviated, reducing terminal costs. CWDM cost per channel is less than that of DWDM despite the fact that DWDM component prices have fallen considerably as they undergo commoditisation.

In metro networks the chief attraction of WDM technology is often not so much its high maximum throughput as its ability to allow for future expansion with minimal up-front investment. Installed links can initially be used at well below capacity, without tying up capital in superfluous equipment. As demand increases extra channels can be added, seamlessly and with only incremental cost. CWDM offers a datacoms-orientated alternative to DWDM, sacrificing maximum possible throughput in return for robust, low-cost systems, while retaining

the attraction of easy expandability. Its cost advantages would nevertheless be enhanced were an increased number of channels to be available.

1.2 Overview

CWDM channel spacing is limited by the allowances which must be made for variation of source wavelength. This dissertation develops a low-cost, passive, intergrated method of reducing this variation, based on engineering DBR reflectivity drift through appropriate choice of grating materials and structures.

Drift-engineered Bragg mirrors are a new concept, there being no literature published concerning them to date, although work on them has been carried out previously within this group. The key innovation is the use of two materials possessing significantly different rates of change of refractive index with temperature.

Such materials tend to also have high refractive index contrast. Previous work in this group has found through numerical electromagnetic modelling that where a large refractive index contrast is used the usual approach of modifying the index in regions ‘seen’ only by the evanescent tail of the guided mode in the laser cavity is ineffective. In such cases the mode shape alters to avoid the high-contrast regions. It is necessary to force the propagating mode to ‘see’ the index change by etching the change right through the waveguide. Such integrated *deep gratings* have been reported, and are discussed in section 1.3.3 below.

This investigation takes as its starting point large-spot lasers modified using focussed ion-beam etching (FIBE) to have deep gratings. The trenches of these gratings are filled with benzocyclobutene (BCB), a widely-experimented-upon polymer dielectric which is frequently used as a representative organic optical material. The organic-inorganic hybrid grating which results is designed to be zero-drift, that is, *athermal*. The design of such gratings is discussed in Chapter 3.

The investigation of unexpected results from these devices motivates the coding of numerical models. One calculates grating reflectivity spectra using the transfer matrix method (TMM) (Chapter 4) and the other locates and track cavity resonances over temperature to measure drift rates (Chapter 5).

Pairs of athermal gratings with reflection spectra offset so as to give better wavelength selectivity are investigated in Chapter 6 as a means of stabilising emission wavelength. The approach is shown to work well subject to certain caveats, in particular the tolerability of mode hopping.

Interpreting the varying reflection phase across the grating reflection peak as a contribution to the total optical length of the resonant cavity, Chapter 7 introduces the possibility of using this contribution to cancel out the increase in cavity optical length with temperature. Modelling finds the technique feasible only for very short cavities. Combined with deeply-etched air-gap reflectors, working designs take on the character of ‘horizontal VCSELs’, of which a number are fabricated as experimental devices.

Excessive losses - etch-induced electrical losses and optical losses due to lack of guiding in the grating air gaps – are found to render these devices unviable. Chapter 8 applies these same ideas to VCSELs instead. Grating designs are more limited in this configuration, but a coincidence of developments in long-wavelength (1300-1550nm) VCSEL technology (air-gap Bragg gratings) and recent advances in optical polymer materials is found to open up new opportunities to engineer grating drift. A standard design procedure for devices with athermal emission wavelength is developed, based on a survey of the entire grating design space. An example design is derived from a trial survey.

Customisable optical polymers are pivotal in this scheme and Chapter 9 is devoted to a review of the state of the art in optical polymer technology, identifying candidate systems for this application.

Chapter 10 concludes the work with a consideration of the practicability the method and its place in the current market environment. Remaining problems are outlined and proposals made for future work.

1.3 Background

1.3.1 CWDM

Based on existing uncooled components operating over expected ranges of environmental conditions, International Telecommunication Union (ITU) standard G.694.2 defines eighteen CWDM channels spaced on a 20nm grid from 1270 to 1610nm, utilising most of the silica-fibre transparency window (**Figure 1-2**).

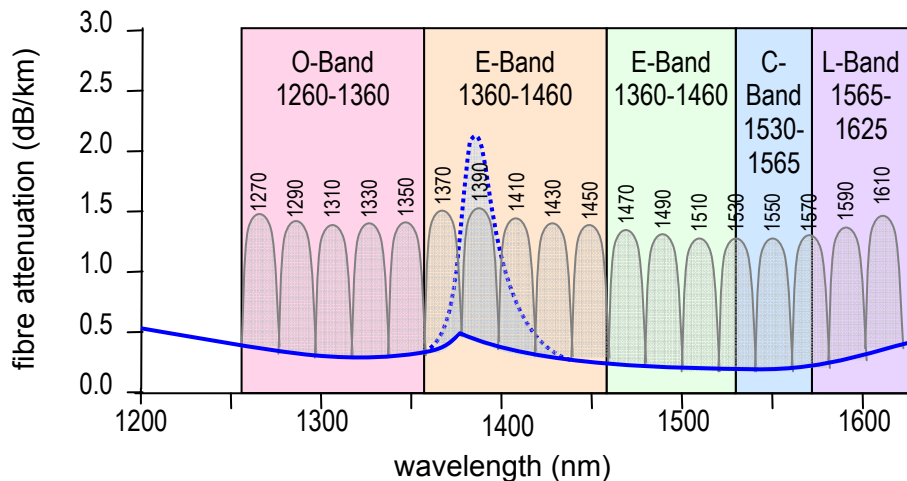


Figure 1-2 Mapping of the ITU-T G.694.2 CWDM wavelength grid (after [2]).

A typical attenuation curve for the installed base of silica fibre is shown (dotted line). Also shown is a curve for low water-peak fibre (solid line). EDFAs cover the C and L bands only, but some manufacturers are beginning to market semiconductor optical amplifiers (SOAs) to extend CWDM link lengths.

The specification purposely includes channels in the water attenuation peak, where absorption due to OH bonds in water trapped in silica fibre is high. This makes provision for exploitation of recently introduced low-water-peak fibre, which offers opportunities for revenue enhancements and cost reductions by opening the 1400nm band.

With such fibre the whole optical fibre transmission spectrum from 1300 to 1600nm is available and all 18 CWDM channels can be utilised. A number of vendors are marketing the option of a greater increase in channel count by populating one or more CWDM pass bands with a group of DWDM channels (**Figure 1-3**). A single 20nm CWDM channel can hold many such channels: 12 at 200GHz spacing, 25 at 100GHz or 50 at 50GHz.

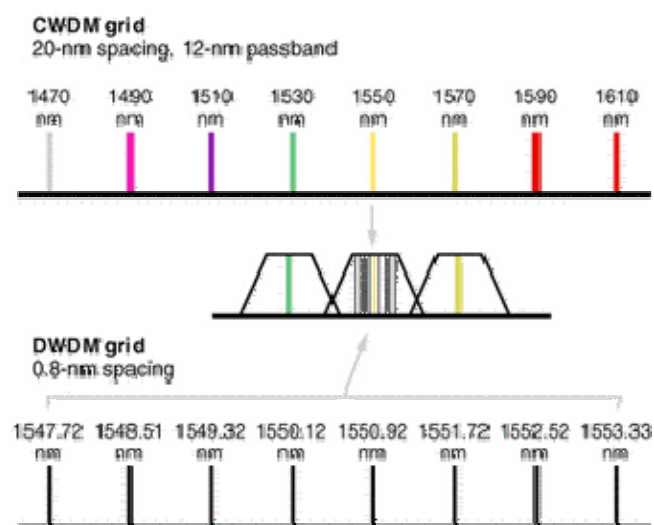


Figure 1-3 ITU G694.1 200GHz DWDM wavelength spacing compared with part of the ITU G694.2 20nm CWDM grid in the 1530-1565nm C-band.

To some extent this also insures against the possible outcome that DWDM commoditisation outstrips CWDM's inherent cost advantages. These advantages are significant, however.

Firstly, the volume occupied by a DWDM laser transmitter is about eight times the volume of a coaxial CWDM laser transmitter. Secondly, the power it consumes is about 20 times greater. For a 16-channel WDM system, CWDM transmitters consume approximately 4W, while the same functionality in a DWDM system can consume over 80W due to the additional load of environmental maintenance.

DWDM laser transmitters are therefore more expensive to package – four to five times so - than uncooled CWDM transmitters, even if otherwise-similar DFB laser sources are used. In fact, further cost advantages accrue through use of directly-modulated CWDM lasers optimised for low cost. These have bit rates up to 2.5Gb/s and are manufactured to more relaxed tolerances.

Further down the link, CWDM filters benefit from lower fabrication costs than DWDM filters due to the reduction in the necessary number of layers. More than 100 layers are typically required for a 200GHz metro DWDM filter, compared to only 50 layers in a 20nm metro CWDM filter. Shorter manufacturing time, smaller bills of materials and higher manufacturing yields mean CWDM filter costs are generally less than half those of comparable DWDM filters.

DWDM sub-channels are therefore only attractive in cases of unanticipated levels of demand.

Another means of increasing CWDM channel count, by as much as a factor of two, without encroaching on the technology's cost advantages, is to address the limitations on channel spacing. The minimum channel spacing, and consequently the number of channels, is limited chiefly by the expected wavelength drift of current uncooled semiconductor laser sources over temperature [3,4] (**Figure 1-4**). Any reduction in this would increase the attractiveness of CWDM, since it would offer users substantial reductions in cabling and racking for a given data capacity, or, alternatively, greater room for future expansion. To date, this problem has not received much attention, although a number of different approaches have been described in the literature.

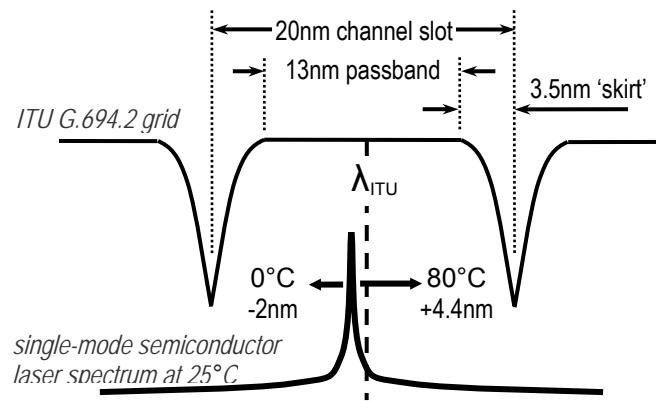


Figure 1-4 Schematic of typical source drift within a single ITU G.694.2 CWDM channel

3.5nm guard bands add to an allowance of $\pm 2.3\text{nm}$ made for manufacturing spread of DFB wavelengths, and an additional $\pm 4.2\text{nm}$ allowed for wavelength drift. Single-mode semiconductor lasers typically show emission wavelength drifts of $\sim 0.08\text{nm}/^\circ\text{C}$, so the allowed range is sufficient for $\sim 100^\circ\text{C}$ operating temperature range.

It is worth noting that, without temperature control, the emission wavelength of a DFB laser would drift from the centre of a 0.4nm (50GHz) DWDM channel to the edge in only 2°C . The much broader 13nm channel slot of CWDM allows laser temperature to drift over a much larger range while remaining in the channel. The 8.4nm allocated for wavelength drift is sufficient to allow the transmitter to operate over a 100°C range, sufficient for outside plant equipment and more than enough for indoor equipment.

1.3.2 Drift Sources and Strategies

All lasers depend on light being reflected back and forth inside a waveguide in which more electrons have been energetically excited to a high energy state (above the band gap, in semiconductors) than remain immediately below it. Photons emitted in electron-hole recombination can stimulate further recombination and hence emission of in-phase light of the same wavelength, leading to light amplification. Wavelengths which can form standing waves within the laser cavity develop the greatest amplitudes and appear as strong emission peaks in the output, the longitudinal resonant modes.

Broadly, the band gap determines the range of wavelengths of emitted photons, the end mirrors determine which wavelengths are reflected for amplification, and the length of the laser cavity determines the resonant wavelengths. Any one of these may dominate the temperature dependence of the laser wavelength, depending on the laser design (**Figure 1-5**).

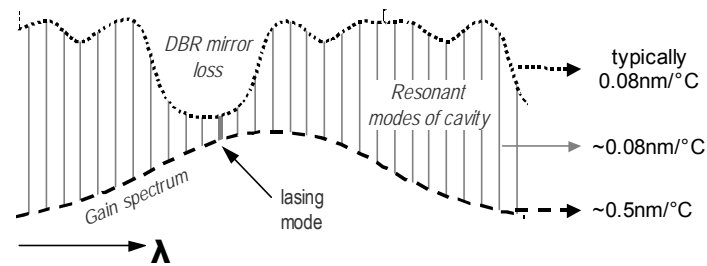


Figure 1-5 Schematic of mode selection and drift factors in single-mode semiconductor lasers.

Drift of the band gap is due to the temperature dependence of the population of free carriers and is known as *bandgap renormalisation* and depends on the material system. Two material systems between them account for the bulk of semiconductor laser diodes; gallium arsenide (GaAs, GaInAs active region) and indium phosphide (InP, AlGaInAs or GaInAsP active region), both showing typical gain-peak drifts of $0.5 \text{ nm}/^\circ\text{C}$. Efforts to develop new systems have been directed mainly at increasing carrier mobility for higher-speed modulation and at obtaining reduced dependence of carrier density on temperature [5,6,7,8], rather than at reducing variation of bandgap with temperature [9,10,11]. Microscale structuring of dopant density such as the creation of quantum wells and dots can be used to engineer some bandgap properties [12,13,14,15], but has thus far not produced any technique of stabilising the gain spectrum with respect to temperature. Organic materials may eventually offer alternatives [16] but reducing bandgap renormalisation does not in any case address mode or grating drift. The work presented in this report has been performed exclusively in the InP material system.

Mirrors at the ends of the laser cavity are necessary to reduce the round-trip loss of the lasing filament below the round-trip gain. Simple cleaved facets provide sufficient refractive index change for 30% power reflectivity. Wavelength-selective mirrors are also possible using Bragg gratings, which use constructive interference of reflections from a series of boundaries to favour reflection at certain wavelengths. Such gratings may be weak and long, such as in DFB lasers or fibre Bragg gratings (FBGs), or short and strong such as in DBR devices, which have a grating at either end of the resonant cavity. DFBs typically show emission wavelength drifts of $0.08 \text{ nm}/^\circ\text{C}$, determined solely by the drift of the grating reflectivity peak.

The reflectivity at each structural or material boundary depends on the change in refractive index experienced by a propagating guided light mode, and wavelength selection depends on constructive interference of reflected light from several such boundaries. Changes in refractive index caused by thermal changes at different temperatures therefore lead to changes in both magnitude and wavelength of the reflectivity spectrum. To avoid this many groups have investigated the use of FBGs in an external-cavity arrangement [17,18]. FBGs used in an this way are relatively temperature insensitive, and are also isolated from the heat dissipated by the

active device. Drift rates as low as 12pm/°C have been reported [19]. The chief problems with this approach have been the cost and size of FBGs, mode hopping [20,21] and developing thermally stable packaging arrangements [22].

Refractive index changes combine with thermal expansion to also change the optical length of the resonant cavity. This causes drift in the wavelengths of the resonant modes. Stabilising the cavity length against this is an obvious and apparently straightforward strategy. Many proposals have been put forward, including use of chirped gratings [23], feedback to tunable lasers [24,25,26], application of hydrostatic pressure and thermal strain [27,28] and suspension of the top mirror from microstructured bimetallic armatures in VCSELs [29,30]. Hybrid cavities incorporating different materials to achieve constant total cavity length have been reported [31,32], but this is hard to do without simply forming a compound cavity and does not necessarily solve the problem of athermalising the reflection gratings.

Thermoelectric coolers can stabilise the temperature with the required precision, but, as already mentioned, they can quadruple the cost of the laser module, as well as increasing the electrical power drawn. Avoiding the need for a costly thermoelectric cooler saves money and also avoids a potential failure mechanism.

1.3.3 Deep Gratings

Deeply-etched gratings such as those mentioned in the overview have been investigated for other reasons, arising from the increasing speed of electronic devices. While copper cable is for the moment sufficient for the final physical link at the network's periphery, optical links are beginning to make an appearance at the other side of the copper divide, transporting extremely high data rates between chips inside computers, or even around chips themselves. One of the technological barriers impeding further adoption is the necessity for very compact, short lasers to enable intrachip links. Short lasers should also allow higher rates of direct modulation, having less parasitic capacitance.

Some work has been published on this problem, describing the use of air-gap DBRs [33,34], polymer-infilled deep gratings [35,36] and multiple microcavities [37,38] to reduce lasing threshold current and laser length by increasing mirror reflectivity. Because of the near-total theoretical reflectivity of such gratings they are sometimes known as 1D photonic bandgap (PBG) structures, analogous to the electronic bandgap of semiconductors.

Although optical interconnects are for the moment limited to such applications as backplanes in mobile telephony base stations, the high rates available and the low interference with nearby channels make them ever more attractive to high-speed circuit designers. As technology progresses more such applications can be expected.

-
- [1] Ito, T., Fukuchi, K., and Kasamatsu, T.: ‘Enabling Technologies for 10 Tb/s transmission capacity and beyond’, *ECOC 2001 CD*, 2001
- [2] Kincade, K.: ‘CWDM breathes life into metro, access, and enterprise applications’, 2003, *Laser Focus World*, March Issue
- [3] Sato, T., Yamamoto, F., Tsuji, K., Takesue, H. and Horiguchi, T.: ‘An Uncooled External Cavity Diode Laser for Coarse-WDM Access Network Systems’, *IEEE Photonics Technology Letters*, 2002, **14**, (7), pp.1001-1003
- [4] Buckman, L.A., Lemoff, B.E. and Dolfi, D.W.: ‘A low-cost compact multimode/singlemode WWDM transceiver module for 10 Gb/s applications’, *OFC 2000 Technical Digest - Trends in Optics and Photonics*, 2000, **37**, (2), pp.67-9
- [5] Chalker, P.R.: ‘Wide bandgap semiconductor materials for high temperature electronics’, 1999, *Thin Solid Films*, **343-344**, pp.616-22
- [6] Yoder, M.N.: ‘Wide bandgap semiconductor materials and devices’, *IEEE Transactions on Electronic Devices*, 1996, **43**, (10), pp.1633-6
- [7] Ledentsov, N.N.: ‘Excitonic waveguiding and lasing in wide bandgap semiconductor’, *Physics of the Solid State*, 1998, **40**, (5), pp.843-5
- [8] Gauggel, H.-P., Geng, C., Scholz, F. and Schweizer, H.: ‘Temperature dependence of short wavelength GaInP/AlGaInP DFB lasers’, *IEEE Lasers and Electro-Optics Society 1995 Annual Meeting - Conference Proceedings*, 1995, **2**, pp.153-4
- [9] Oe, K., and Asai, H.: ‘Proposal on a temperature insensitive wavelength semiconductor laser’, *IEICE Transactions on Electronics*, 1996, **E79-C**, (12), pp.1751-1759
- [10] Kondow, M., Kitatani, T., Nakahara, K., and Tanaka, T.: ‘Temperature dependence of lasing wavelength in a GaInNAs laser diode’, *IEEE Photonics Technology Letters*, 2000, **12**, (7), pp.777-779
- [11] Polimeni, A., Bissiri, M., Augieri, A., von Hogersthal, G.B.H., Capizzi, M., Gollub, D., Fischer, M., Reinhardt, M. and Forchel, A.: ‘Reduced temperature dependence of the band gap in GaAs_{1-y}Ny investigated with photoluminescence’, *Physical Review - Series B*, 2002, **65**, (23), pp.235-325
- [12] Capasso, F. and Cho, A.Y.: ‘Bandgap engineering of semiconductor heterostructures by molecular beam epitaxy: physics and applications’, *Surface Science*, 1994, **299-300**, pp.878-91
- [13] Higashi, T., Yamamoto, T., Ogita, S. and Kobayashi, M.: ‘Experimental analysis of temperature dependence of oscillation wavelength in quantum-well FP semiconductor lasers’, 1998, *IEEE Journal of Quantum Electronics*, **34**, 9, pp.1680-9
- [14] Evans, J.D., Simmons, J.G., Thompson, D.A., Puetz, N., Makino, T. and Chik, G.: ‘An investigation into the temperature sensitivity of strained and unstrained multiple quantum-well, long wavelength lasers: new insight and methods of characterization’ *IEEE Journal of Selected Topics in Quantum Electronics*, **1**, (2), pp.275-84
- [15] Thomson, J.D., Summers, H.D., Smowton, P.M., Herrmann, E., Blood, P., and Hopkinson, M.: ‘Temperature dependence of the lasing wavelength of InGaAs quantum dot lasers’, *Journal of Applied Physics*, 2001, **90**, (9), pp.4859-4861
- [16] Kozlov, V.G., Bulovic, V., and Forrest, S.R.: ‘Temperature independent performance of organic semiconductor lasers’, *Applied Physics Letters*, 1997, **71**, (18), pp.2575-2577
- [17] Adomat, M., Ahlfeldt, H., Broberg, B., Stubbe, R. and Fonjallaz, P.-Y.: ‘Wavelength stabilization of DBR laser using a fiber with multiple gratings’, 1998, *Proceedings of ECOC 1998*, pp.161-2
- [18] Butov, O.V., Golant, K.M. and Nikolin, I.V.: ‘Ultra-thermo-resistant Bragg gratings written in nitrogen-doped silica fibres’, 2002, *Electronics Letters*, **38**, (11), pp.523-524
- [19] Hashimoto, J.-I., Kato, T., Nakanishi, H., Yoshida, K., Sasaki, G., Yamaguchi, A., Katsuyama, T., and Yamabayashi, N.: ‘Eight-Channel Wavelength Multiplexing With 200-GHz Spacing Using Uncooled Coaxial Fiber Bragg Grating External-Cavity Semiconductor Laser Module’, *IEEE Photonics Technology Letters*, 2002, **14**, (11), pp.1617-1619
- [20] Hashizume, N., and Nasu, H.: ‘Mode Hopping Control and Lasing Wavelength Stabilization of Fiber Grating Lasers’, *Furukawa Review*, 2001, **20**, pp.7-10
-

-
- [21] Sato, T.: 'Suppression of Mode-Hop-Induced Optical Signal Deterioration in an External-Cavity-Diode Laser with a Fiber-Bragg Grating for Uncooled Wavelength-Division-Multiplexing Applications', *Applied Optics-LP*, 2003, **42**, (18), pp.3500-3504
- [22] Hashimoto, J. I.: 'Coaxial fiber-Bragg-grating external-cavity semiconductor laser module without temperature control', Proc. 27th European Conf. on Opt. Components, Amsterdam, Netherlands, 2001, **2**, pp.130-131
- [23] Morton, P.A., Mizrahi, V., Tanbun-Ek, T., Logan, R.A., Lemaire, P.J., Presby, H.M., Erdogan, T., Woodward, S.L., Sipe, J.E., Phillips, M.R., Sergent, A.M. and Wecht, K.W.: 'Stable single mode hybrid laser with high power and narrow linewidth', 1994, *Applied Physics Letters*, **64**, (20), pp.2634-2636
- [24] Davies, A.R., Fan, S., Williams, K.A., Penty, R.V. and White I.H.: 'Low Wavelength Drift Uncooled Laser using Tuned Distributed Bragg Reflectors', 2003, *LEOS 2002 Conference Proceedings*, pp861-862
- [25] Davies, A., Fan, S., Penty, R. and White, I.: 'Active Wavelength Control of Tunable Lasers for use in Uncooled WDM systems', 2003, *CLEO 2003 Conference Proceedings*, paper CthW6
- [26] Liu, Y., Davies, A.R., Ingham, J.D., Penty, R.V. and White, I.H.: 'Nanometer Scale Thermal Drift of 4Gbit/s Uncooled Laser for Tight-Channel-Spacing Low-Cost WDM', 2005, *CLEO 2005 Conference Proceedings*
- [27] Cohen, D.A., Heimbuch, M.E., and Coldren, L.A.: 'Reduced temperature sensitivity of the wavelength of a diode laser in a stress-engineered hydrostatic package', *Applied Physics Letters*, 1996, **69**, (4), pp.455-457
- [28] Cohen, D.A., and Coldren, L.A.: 'Passive temperature compensation of uncooled GaInAsP-InP diode lasers using thermal stress', *IEEE Journal of Selected Topics in Quantum Electronics*, 1997, **3**, (2), pp.649-658
- [29] Koyama, F., Amano, T., Furukawa, N., Nishiyama, N., Arai M., and Iga, K.: 'Micromachined semiconductor vertical cavity for temperature insensitive surface emitting lasers and optical filters', *Japanese Journal of Applied Physics Part 1*, 2000, **39**, (3B), pp.1542-1545
- [30] Amano, T., Koyama, F., Nishiyama, N., Matsutani, A., and Iga, K.: 'Temperature Insensitive Micromachined GaAlAs/GaAs Vertical Cavity Wavelength Filter', *IEICE Transactions on Communications*, 2001, **E84-B**, (5), pp.1304-1310
- [31] Chambliss, D.D., and Johnson, M.: 'Wavelength-stabilized semiconductor laser (GaAs-(GaAl)As structure)', *IBM Technical Disclosure Bulletin*, 1983, **26**, (4), pp.2177-2178
- [32] Pezeshki, B., Agahi, F., and Kash, J.A.: 'A gratingsless wavelength stabilized semiconductor laser', *Applied Physics Letters*, 1996, **69**, (19), pp.2807-2809
- [33] Baba, T., Hamasaki, M., Watanabe, N., Kaewplung, P., Matsutani, A., Mukaihara, T., Koyama, F. and Iga, K.: 'A novel short-cavity laser with deep-grating distributed Bragg reflectors', *Japanese Journal of Applied Physics Part 1 - Regular Papers Short Notes & Review Papers*, 1996, **35**, 2B, pp.1390-4
- [34] Raffaele, L., De La Rue, R.M. and Krauss, T.F.: 'Ultrashort in-plane semiconductor microlasers with high-reflectivity microstructured mirrors', 2002, *Optical and Quantum Electronics*, **34**, (1/3), pp.101-111
- [35] Raj, M.M., Wiedmann, J., Toyoshima, S., Saka, Y., Ebihara, K. and Arai, S.: 'High-reflectivity semiconductor/benzocyclobutene Bragg reflector mirrors for GaInAsP/InP lasers', 2001, *Japanese Journal of Applied Physics Part 1 - Regular Papers Short Notes & Review Papers*, **40**, (4A), pp.2269-77
- [36] Raj, M.M., Wiedmann, J., Saka, Y., Ebihara, K. and Arai, S.: 'Highly uniform 1.5 μ m wavelength deeply etched semiconductor / benzocyclobutene distributed Bragg reflector lasers', 2000, *Japanese Journal of Applied Physics Part 2-Letters*, **39**, (12B), pp.L1297-9
- [37] Wiedmann, J., Raj, M.M., Ebihara, K., Matsui, K., Tamura, S. and Arai, S.: 'Deeply etched semiconductor / benzocyclobutene distributed Bragg reflector laser combined with multiple cavities for 1.5 μ m-wavelength single-mode operation', 2001, *Japanese Journal of Applied Physics Part 1 - Regular Papers Short Notes & Review Papers*, **40**, (6A), pp.4031-7
- [38] Krauss, T., Vögele, B., Stanley, C.R. and De La Rue, R.M.: 'Waveguide microcavity based on photonic microstructures', 1997, *IEEE Photonics Technology Letters*, **9**, (2), pp.176-8
-

Chapter 2

Refractive Index

The dependence of emission spectrum on wavelength arises, in all single-mode sources, from variation of refractive index with temperature. The origins and characteristics of refractive index, its dispersion and temperature dependence are discussed for semiconductor and dielectric materials, with particular reference to polymers.

2.1 Electromagnetic Parameters

2.1.1 Electric Permittivity

A medium subjected to an electric field \mathbf{E} forms an internal *electric polarisation* field \mathbf{P} as electronic (and perhaps also orientational and ionic) dipoles are induced. Until equilibrium is reached, a *displacement current* can be considered to flow. If free charge carriers are present, the familiar *conduction current* will also flow.

James Clark Maxwell introduced the concept of displacement current $\partial\mathbf{D}/\partial t$ as the time derivative of the fictitious *displacement field* \mathbf{D} :

$$\mathbf{D} = \varepsilon_0 \mathbf{E} + \mathbf{P} . \tag{E2-1}$$

\mathbf{D} is simply the resultant of the applied and induced fields, that is, the field that would be measured in the medium. In vacuum, \mathbf{D} and \mathbf{E} are identical except that in SI units they are measured differently so that $\mathbf{D} = \varepsilon_0 \mathbf{E}$ (\mathbf{D} and \mathbf{P} have units of C/m^2 , while \mathbf{E} is given in V/m). The constant of proportionality ε_0 is called the *permittivity of free space* and is equal to $8.85419 \times 10^{-12} \text{ F}/\text{m}$. In a medium, however, \mathbf{P} is nonzero and is given, on a macroscopic scale, by

$$\mathbf{P} = (\varepsilon - \varepsilon_0) \mathbf{E} \tag{E2-2}$$

where ε is the permittivity of the medium, usually expressed relative to the permittivity of free space as *relative permittivity* $\varepsilon_r = \varepsilon/\varepsilon_0$. A medium's relative permittivity is also known as its *dielectric constant*.

Substituting this in to (E2-1) gives us an alternative form

$$\mathbf{D} = \varepsilon_r \varepsilon_0 \mathbf{E} = \varepsilon \mathbf{E} . \tag{E2-3}$$

In isotropic media, such as non-crystalline solids, fluids and or cubic crystals, \mathbf{E} , \mathbf{P} and so \mathbf{D} are parallel and ε is a scalar, but in more general anisotropic media this is not the case and ε is a

rank-2 tensor, causing birefringence. Certain materials are also non-linear: permittivity is a function of applied field.

The displacement current can be thought of as an elastic response which a material has to an applied electric field. As the electric field is increased, a charge displacement is built up in the material, and this is released when the electric field is decreased. D is proportional to E with a constant of proportionality given by the permittivity of the material.

Permittivity therefore tells us how much electrostatic energy can be stored per unit of volume when unit voltage is applied. If a material with a high dielectric constant is placed in an electric field, the displacement field will be large and the magnitude of applied field will be measurably reduced within the volume of the dielectric. This fact is commonly exploited to increase the rating of capacitors.

Material behaviours can be classified according to their permittivity. A ‘perfect’ dielectric is a material that shows displacement current only, so it stores and returns electrical energy with no loss. When the conduction currents are not negligible the medium is termed ‘lossy’ and the total current density flowing is:

$$\mathbf{J}_{tot} = \mathbf{J}_c + \mathbf{J}_d = \sigma \mathbf{E} + j\omega \epsilon_0 \epsilon_r \mathbf{E} = j\omega \epsilon_0 \epsilon^* \mathbf{E} \quad (\text{E2-4})$$

where σ is the conductivity of the medium and ϵ^* is its *complex permittivity*. It can be seen that permittivity is to displacement current somewhat what conductivity is to conduction current, except that the size of the displacement current is dependant on the frequency ω of the applied field \mathbf{E} : there is no displacement current in a constant field. In this formalism the complex permittivity ϵ^* is defined as:

$$\epsilon^* = \epsilon_r - j \frac{\sigma}{\epsilon_0 \omega} \quad (\text{E2-5})$$

Materials whose complex permittivity has a negative real part are considered metals (in which no propagating electromagnetic waves exist), and those with a positive real part are dielectrics. The imaginary part of ϵ^* represents losses if negative and gain if positive.

For real materials, both the real and imaginary parts of the permittivity are actually functions of frequency ω . This leads to dispersion of signals containing multiple frequencies and such materials are called *dispersive*. This frequency dependence reflects the fact that a material's polarization does not respond instantaneously to an applied field, but does so by a number of non-instantaneous mechanisms.

On a microscopic scale, there are distinct regions of quantum-mechanical atomic and molecular interactions that account for the macroscopic behaviour labelled permittivity. At low

frequencies in polar dielectrics, molecules are polarised by applied electric fields and certain rotations may be resonant. At intermediate frequencies rotation is too slow to keep up but vibrations of covalent bonds are resonant. At high frequencies, all molecular motions are too slow and energy is absorbed by electrons only. Frequencies above these resonances, which are typically in the ultraviolet, experience very little absorption in dielectrics.

When studying narrow frequency ranges it is often reasonable to approximate dielectric constant as frequency-independent.

2.1.2 Magnetic Permeability

Sub-atomic charges such as protons and electrons can be thought of as tracing out tiny circuits and behaving as tiny magnetic moments. They respond to external magnetic field intensities \mathbf{H} and give rise proportionally to a magnetic moment, or *magnetization* \mathbf{M} . The resultant *magnetic flux density* \mathbf{B} in a material (also known as the *magnetic induction*) is given by

$$\mathbf{B} = \mu_0 \mathbf{H} + \mathbf{M} \quad (\text{E2-6})$$

In vacuum, \mathbf{B} and \mathbf{H} are identical except that in SI units they are measured differently so that $\mathbf{B} = \mu_0 \mathbf{H}$ (\mathbf{B} and \mathbf{M} have units of Tesla, while \mathbf{H} is given in A/m). The constant of proportionality μ_0 is called the *permeability of free space* and is equal to $4\pi \times 10^{-7}$ Henrys per metre (H/m). In a medium, however, \mathbf{M} is nonzero and is given, on a macroscopic scale, by

$$\mathbf{M} = (\mu - \mu_0) \mathbf{H} \quad (\text{E2-7})$$

where μ is the permeability of the medium, often expressed relative to the permeability of free space as *relative permeability* $\mu = \mu_r \mu_0$.

Substituting this in to (E2-6) gives us an alternative form

$$\mathbf{B} = \mu_r \mu_0 \mathbf{H} = \mu \mathbf{H} \quad (\text{E2-8})$$

Permeability is the degree of magnetisation of a material in response to a magnetic field. It can be thought of as a 'resistance to magnetic flux' – whereas materials with high conductivity let electric current through easily, materials with high permeabilities allow flux through more easily than others. For non-ferromagnetic substances μ_r is effectively unity.

2.1.3 Speed of Light

Permittivity and permeability together define the speed of light. In a medium it should be recalled that both ϵ and μ are functions of frequency, and sometimes also of direction. If v is the

phase velocity (the speed at which fronts of a given phase travel) of radiation of a specific frequency in a specific material in a specific direction,

$$v = \frac{1}{\sqrt{\epsilon\mu}} \tag{E2-9}$$

In a vacuum, all electromagnetic radiation travels at the same speed, 299,792,458 metres per second, denoted by c .

$$c = \frac{1}{\sqrt{\epsilon_0\mu_0}} \tag{E2-10}$$

2.2 Origins and Definitions

2.2.1 Origins

An electromagnetic wave propagating in a medium displaces the charges of each atom (primarily the electrons) away from equilibrium by an amount proportional to the permittivity and the field intensity. The magnetic field also has an effect but it is negligibly small in comparison. Below resonance this oscillation of charges lags the driving wave slightly. The resultant of the incident and re-radiated waves is a wave with the same frequency but shorter wavelength than the original, apparently the original wave slowed down. This is the origin of the concept of refractive index.

Above resonance the amplitude of forced oscillation quickly becomes negligible. At resonance itself, the amplitude peaks and phase lag is 90° . The total re-radiated field, the sum of contributions from dipoles around the axis of propagation, each with an extra phase lag which increases with the distance from the axis at which it originated, is then 180° out of phase and this destructive interference can be interpreted as absorption.

Denser materials have a greater density of re-radiators so that the re-radiated amplitude is larger and the original propagating field will appear to be more slowed down. This means denser materials are generally also more optically dense. However, other effects influence refractive index, especially the polarisability of the materials' charge clouds – high polarisability leads to large re-radiated fields, faster phase translation and so increased refractive index.

2.2.2 Definitions

A material's refractive index n is defined as the factor by which electromagnetic radiation is slowed down when it travels inside the material, relative to in a vacuum. Taking v as the phase

velocity of radiation of a specific frequency travelling in a given direction in a specific material, the refractive index is given by

$$n = \frac{c}{v} \tag{E2-11}$$

Substituting in (E2-9) and (E2-10) we find n can also be expressed in terms of the material's permeability μ and permittivity ϵ .

$$n = \frac{c}{v} = \sqrt{\epsilon_r \mu_r} \approx \sqrt{\epsilon_r} \tag{E2-12}$$

where the approximation holds for non-magnetic materials.

Refractive index is generally greater than one, increasing with density. However, at certain frequencies (e.g. near absorption resonances, and for x-rays), n can be less than one. This does not contradict the theory of relativity, which holds that no information-carrying signal can ever propagate faster than c , because the phase velocity is not the same as the *group velocity*, also known as the *signal velocity*.

The group velocity is the rate that the *envelope* of the waveform is propagating; that is, the rate of variation of the amplitude of the waveform. It is the group velocity that defines the rate at which information and energy may be transmitted by the wave; the velocity at which a pulse of light travels down an optical fibre.

A 'group velocity refractive index', or *group index* is defined

$$n_g = \frac{c}{v_g} = n + v \frac{dn}{dv} = n - \lambda \frac{dn}{d\lambda} \tag{E2-13}$$

where v_g is the group velocity and v is frequency. This value should not be confused with the *phase index* n , which is always defined with respect to the phase velocity.

Often it is the case that a propagating electromagnetic wave overlaps regions of different refractive indices. The wave is said to see an *effective refractive index* which is a weighted combination of the indices.

Both group index and effective index can differ significantly from phase index. The same can be said of their rates of change with temperature.

2.2.3 Dispersion and Absorption

Section 2.1.1 described how permittivity is dependent on frequency. Because refractive index depends on permittivity, it also varies with frequency. This dispersion can severely limit optical fibre communications by causing pulses of light to spread out as they travel. In general, in

regions of the spectrum where a material does not absorb, its refractive index decreases with wavelength, as permittivity also falls. Near absorption peaks, the refractive index increases with wavelength.

Just as permittivity may, refractive index may be defined as a complex number, with the imaginary part of the number representing the absorption of the material. The real and imaginary parts of the complex refractive index are related by the *Kramers-Kronig* relations.

2.2.4 Polarisability and Density

When photons impinge on a material but are not resonant with any energy transition, a subtler effect than absorption obtains. A dielectric subjected to an electric field forms an internal field as electronic, orientational and ionic dipoles are induced. An incident electromagnetic wave subjects the dielectric charges to time-varying electric and magnetic forces,

$$\mathbf{F}_{electric} = q\mathbf{E} \tag{E2-14}$$

$$\mathbf{F}_{magnetic} = q(\mathbf{v} \times \mathbf{B}) \tag{E2-15}$$

where q is charge and \mathbf{v} is its motion vector. Of these the magnetic force is negligible, and most effects can be understood in terms of electric field alone. There is a further simplification in that at optical frequencies the only polarisation mechanism fast enough to follow the electric field is the electronic one.

If the *polarisability* α of a material is a property that quantifies the ease of distortion of the electron cloud of a molecular entity by an electric field, the dipole moment of an individual molecule subject to an electric field is given by

$$\mathbf{p} = q\mathbf{x} = \alpha\mathbf{E} \tag{E2-16}$$

where \mathbf{x} is the displacement of the centre of negative charge from the centre of positive charge. The dipole moment per unit volume is the electric polarisation \mathbf{P} and, recalling (E2-2), is given by

$$\mathbf{P} = N\mathbf{p} = N\alpha\mathbf{E} = (\epsilon - \epsilon_0)\mathbf{E} = \epsilon_0(\epsilon_r - 1)\mathbf{E} \tag{E2-17}$$

where N is the number of dipoles per unit volume. Taking (E2-12) we can say that for non-magnetic materials

$$\epsilon_r - 1 \approx n^2 - 1. \tag{E2-18}$$

Substituting this back into (E2-17):

$$N\alpha = \varepsilon_0(n^2 - 1) \quad (\text{E2-19})$$

Rearranging:

$$n = \sqrt{1 + \frac{N\alpha}{\varepsilon_0}} \quad (\text{E2-20})$$

This equation shows how polarisability and density contribute to refractive index in non-magnetic materials and will be used later, in the consideration of thermal effects.

2.2.5 Plasma Index Contribution

The presence of free carriers in a material leads to an additional contribution to refractive index simply by increasing polarisability and so changing the dielectric constant. The change in refractive index induced by a free carrier density N_e is

$$\Delta n_r = -\frac{N_e e^2}{2m^* \varepsilon_{r0} \varepsilon_0 \omega^2} \quad (\text{E2-21})$$

where m^* is the appropriate electronic mass, the effective mass in a semiconductor. As free electrons or holes are added to a semiconductor, the refractive index is reduced.

The emission wavelength of directly-modulated laser-diodes changes as the carrier density oscillates around equilibrium at abrupt changes in drive current. It overshoots on both rising and falling edges, causing blue and red-shifts respectively. This can cause inter-symbol interference in optical communications systems and is called *dynamic chirp*. The steady-state difference between high and low signals, due to heating, is called *static chirp*.

2.3 Absorption and Refraction

2.3.1 IR Absorption in Semiconductors

When a photon of a particular energy is incident on an atom it may excite an electron into a quantum-mechanically higher energy state. In the solid state, the electrons of neighbouring atoms and molecules interact so that instead of distinct energy levels broad bands are formed. The nature of these bands, their degree of filling with electrons and their separation in energy determines many electrical and optical properties of the material.

The continuum of bound states is known as the *valence band*. The continuum of unbound, free states is known as the *conduction band*. In electrically-conducting solids these bands overlap and the Fermi level, i.e. that energy up to which all states would be filled at absolute

zero of temperature, is within the conduction band. This means there is a permanent population of free electrons in the material, providing high optical reflectivity at all wavelengths. In insulators, the bands are separated by more than thermal energies and the Fermi energy is located within the valence band, so that negligibly few electrons are free. Semiconductors lie between the two, having conduction and valence bands separated by a moderate band gap, and Fermi energies lying near the top of the valence band.

Electrons in semiconductors can make transitions from one band to another by emitting or absorbing photons of energy corresponding to the energy difference between the bands. The amount of *electronic absorption* becomes dependent upon the size of the energy gap at any given temperature, and the absence of impurities. An electronic '*absorption edge*' (**Figure 2-1**) exists at the band-gap energy. At frequencies close to this a change in band gap by a fraction of an electron volt can change the absorption coefficient by nearly four orders of magnitude.

Because the bands are broad in energy, a semiconductor has a very broad optical emission spectrum, much broader than the narrow lines emitted from single atoms in a gas.

In crystals energy and momentum can be exchanged with electrons via quanta of thermal lattice vibrations, or *phonons*. These play a key role in electronic absorption because photon momentum h/λ is always small compared to phonon momentum h/a (a being the lattice constant) so any change in electronic momentum necessary to make a transition and absorb a photon must come through the agency of a phonon or impurity. Transitions in such *indirect band-gap* semiconductors are comparatively unlikely, so active materials for semiconductor lasers must have a *direct band-gap*, where absorption and emission can occur without mediation by phonons.

Some phonons create localised dipoles which interact with long optical wavelengths and bring about *lattice absorption*. Conservation of momentum requires that phonon momentum h/a is equal to photon momentum h/λ , but because phonon momentum is large compared to that of photons two or more photons are necessary. Lattice absorption defines the long-wavelength transparency limit of semiconductor materials, usually around $10\mu\text{m}$.

A third possible absorption mechanism, *free-carrier absorption*, involves electronic transitions between initial and final states within the conduction band. It involves scattering by phonons or charged impurities. Because the conduction band is not, in general, densely populated in semiconductors this is not usually a significant contributor.

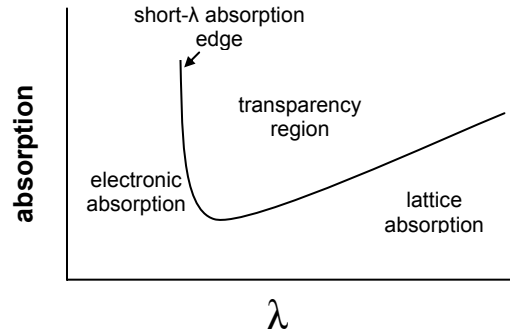


Figure 2-1 *Infra-red absorption in semiconductor*

The transparency region is bounded by electronic absorption at the short-wavelength limit and lattice absorption at the long-wavelength limit.

2.3.2 Kramers-Kronig Relations

The relation between the real and imaginary parts of a certain class of complex-valued functions is described by the *Kramers-Kronig relations*. For them to apply, a function $f(\omega)$ must represent the Fourier transform of a linear, finite and causal physical process. If we write

$$f(\omega) = f_1(\omega) + if_2(\omega) \quad (\text{E2-22})$$

where f_1 and f_2 are real-valued "well-behaving" functions, then the Kramers-Kronig relations are

$$f_1(\omega) = \frac{2}{\pi} \int_0^{\infty} \frac{\omega' \cdot f_2(\omega')}{\omega^2 - \omega'^2} d\omega'$$

$$f_2(\omega) = \frac{2\omega}{\pi} \int_0^{\infty} \frac{f_1(\omega')}{\omega^2 - \omega'^2} d\omega'$$

(E2-23)

The Kramers-Kronig relations are most often applied to the permittivity $\epsilon(\omega)$ of materials, which represents their response to an applied electric field (compare (E2-5) with (E2-22)). This response is causal because polarisation does not respond instantaneously to applied field, is finite in that a finite field obtains a finite response, and linear in that the polarisation is proportional to the field.

The real part of ϵ is related to refractive index, and the imaginary part to loss. (E2-23) shows that absorption and refraction are not independent phenomena. It is possible to deduce refractive index given full knowledge of the absorption spectrum, and *vice versa*.

2.3.3 Refractive Index near the Band-Gap Energy

Just below the band gap energy semiconductor material is substantially transparent. As the photon energy approaches the band gap, refractive index increases. Although the absorption has

a sharp edge at the band gap, the consequent rise in refractive index is spread out over the energies approaching the band gap energy.

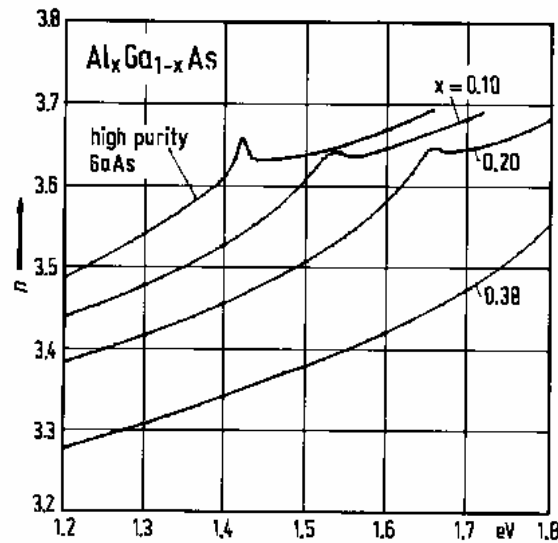


Figure 2-2 Refractive index for $Al_xGa_{1-x}As$. (from [1])

1.2eV corresponds to 1033nm wavelength, 1.8ev to 689nm.

Figure 2-2 shows refractive index of AlGaAs alloys and GaAs. In each case refractive index rises as the photon energy approaches the band gap energy. The materials with larger band gap energies also tend to have lower refractive index at any given photon energy in the transparent region because it is further from the band gap energy. This difference in refractive indices is widely utilised for making waveguides in edge emitting lasers and distributed Bragg mirrors in VCSELs, and it is convenient that the lower-index layers, which can form the cladding of the guides, are also the ones with the larger band gaps and hence do not absorb at the wavelength of interest. Generally material with smaller band gap and consequently higher refractive index is used for the active parts of the device, which are also usually in the core of the waveguide such that the region with gain has the highest optical field.

2.4 Thermal Effects

2.4.1 Band-Gap Renormalization

It is usually can be assumed that band-gap energy E_g does not itself depend on carrier density. However, close to E_g , where many optoelectronic devices operate, this is not a safe assumption.

When electron-hole pairs are created in the presence of mobile charge, the existing charge can move to reduce the energy of the system in a *screening* process. As a result the energy required to create an electron-hole pair is reduced. As far as optical transitions are concerned this gives an effective reduction of the band gap energy when the material contains large numbers of

carriers. This is called *band-gap renormalization*. It is not the same as the exciton interaction, which is between an excited electron and the hole it vacates.

Figure 2-3 gives some experimentally-determined band-gap vs. carrier density data and shows the characteristic variation common to all semiconductors.

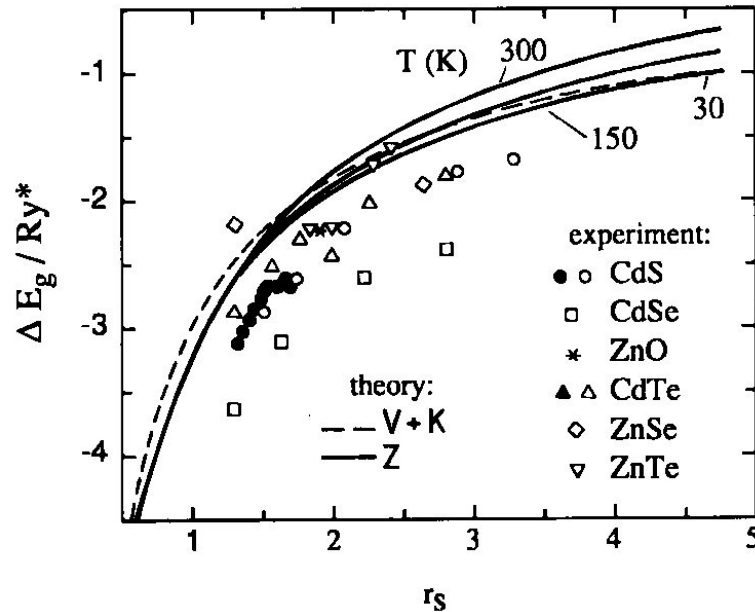


Figure 2-3 Band gap renormalisation theory and experiment [2]

Band-gap reduction is in units of the exciton binding energy, exciton Rydbergs ($\sim 4\text{-}5$ meV in GaAs). Carrier densities are expressed in terms of the average inter-particle separation, r_s . $r_s = 1$ corresponds to a plasma density of about 1.6×10^{17} cm $^{-3}$, at which band-gap shrinkage is approximately 15 meV.

High densities of electrons and/or holes are common in doped layers or inside forward-biased light-emitting or laser diodes and renormalization effects are commonly observable. An important example is the effect of increasing temperature: carrier density increases and so the band-gap energy decreases, red-shifting the emission spectrum.

2.4.2 Thermal Index changes

Refractive index at photon energies below the band gap changes with temperature along with the band gap energy. A simple estimate can be made by assuming the whole refractive index spectrum shifts as the band gap energy shifts; such an assumption is not exactly correct, because the form of the absorption spectrum - and hence the refractive index spectrum - changes somewhat with temperature, but it is sufficient as a first approximation. We can see, for example, from **Figure 2-2** that just below the band gap energy, the change in index with photon energy is ~ 0.05 for 0.1 eV change in photon energy. Taking the band gap energy change with temperature to be a reduction of ~ 0.4 meV/K, we therefore expect $\sim 0.4 \times 10^{-3} \times 0.05/0.1 = 2 \times 10^{-4}$ K $^{-1}$ change in refractive index; note that this change is an increase in refractive index with increasing temperature, because the band gap energy is becoming smaller with increasing

temperature. Such changes are large enough, for example, to give shifts in the wavelengths of semiconductor lasers with temperature as the effective optical length of the cavity changes.

2.4.3 Thermo-Optic Effect

The dependency of refractive index n on temperature T , dn/dT , is called the *thermo-optic effect* (TOE) and is present in all transparent materials including dielectrics, semiconductors, and organic films. dn/dT can be positive (e.g. silica, semiconductors) or negative (e.g. polymers) depending on the competing factors of density (N particles per unit volume) and polarisability (α), which are themselves functions of temperature.

An increase in polarisability, due to increased free charge carriers or an expansion of the molecular electron clouds, will increase the dielectric constant and hence refractive index.

Most materials expand on heating, as their molecules acquire heat energy and increase their kinetic energy or the amplitude of their oscillations and so move further apart. The *coefficient of thermal expansion* (CTE) is used to describe this in solids. CTE is a material property which depends on the molecules' masses and the means of absorbing energy open to them.

As temperature increases the number of molecules or atoms per unit volume N will decrease. Fewer polarisable entities per unit volume means a smaller polarisation field \mathbf{P} , so smaller dielectric constant and decreased refractive index.

To relate polarisability and CTE to refractive index we recall (E2-20):

$$n = \sqrt{1 + \frac{N\alpha}{\epsilon_0}} \quad (\text{E2-24})$$

Since $n(\alpha, N)$ and $\alpha(T)$ and $n(T)$, we differentiate n with respect to T thus

$$\frac{dn(N, \alpha)}{dT} = \frac{\partial n}{\partial N} \frac{dN}{dT} + \frac{\partial n}{\partial \alpha} \frac{d\alpha}{dT} \quad (\text{E2-25})$$

Dealing with the terms on the right separately:

$$\begin{aligned} \frac{\partial n}{\partial \alpha} \frac{d\alpha}{dT} &= \frac{1}{2} \left(1 + \frac{N\alpha}{\epsilon_0} \right)^{-\frac{1}{2}} \left(\frac{N}{\epsilon_0} \right) \frac{d\alpha}{dT} = \frac{N}{2\epsilon_0 n} \frac{d\alpha}{dT} \\ \frac{\partial n}{\partial N} \frac{dN}{dT} &= \frac{1}{2} \left(1 + \frac{N\alpha}{\epsilon_0} \right)^{-\frac{1}{2}} \left(\frac{\alpha}{\epsilon_0} \right) \frac{dN}{dT} = \frac{\alpha}{2\epsilon_0 n} \frac{dN}{dT} \end{aligned} \quad (\text{E2-26})$$

where we simplify in each case by substituting (E2-24) back in. Substituting these terms in to (E2-24) we obtain, finally

$$\frac{dn}{dT} = \frac{1}{2\varepsilon_0 n} \left(\alpha \frac{dN}{dT} + N \frac{d\alpha}{dT} \right) \quad (\text{E2-27})$$

dN/dT is usually negative because density typically *decreases* with increasing temperature, whereas $d\alpha/dT$ is usually positive because polarisability typically *increases* with increasing temperature. These two effects compete to determine the actual behaviour of the refractive index with temperature.

Close-packed crystal structures such as semiconductor crystals (e.g. InP) and ionic materials (e.g. LiF) have high thermal expansivity and the density effect dominates, leading to negative dn/dT . Less structured materials (e.g. polymers, Al_2O_3) have lower thermal expansivity and polarisability dominates, leading to positive dn/dT .

Table 2-1 sets out TOCs for some common optical materials.

Table 2-1 Example refractive indices and TOCs

Material	Refractive Index	dn/dT ($^{\circ}\text{C}^{-1}$)
Silica (SiO_2)	1.5	10^{-5}
Silicon (Si)	3.5	1.8×10^{-4}
Sol-Gels	1.2 to 1.5	10^{-5}
Polymers	1.3 to 1.7	-1 to -4×10^{-4}
Indium Phosphide (InP)	3.1	0.8×10^{-4}
Gallium Arsenide (GaAs)	3.4	2.5×10^{-4}

[1] Aframowitz, M.A., *Solid State Communications*, 1974, **15**, (59)

[2] Klingshirn, C. F.: *Semiconductor Optics*, 1995, Springer, Berlin

Chapter 3

Grating Drift Control

Drift-engineering of distributed Bragg reflector gratings, including athermalisation, is discussed. The technique depends on integration of material with differing thermo-optic coefficient, such as optical polymer, within the grating. Test devices are found to show a small but significant reduction in modal drift.

3.1 Introduction

Several drift control strategies have been mentioned in the introduction. This investigation concerns only those involving integral drift-engineered Bragg gratings. The original work on such gratings was done by Gefan Huang, a colleague in the author's research group, formerly of the University of Bristol, now the Photonic Communications Systems group of Cambridge University Engineering Department. The work presented in this dissertation developed from a modelling requirement for these gratings and they are consequentially a logical entry point. In this chapter they are introduced, some design considerations developed and results from a prototype motivate subsequent investigation.

3.2 Bragg Condition and Drift

For reflections from a series of refractive-index variations to interfere constructively the waves reflected from successive reflecting planes inside the structure must be in phase with each other. This means the path difference for successively-reflected waves must be a whole number of wavelengths. This is usually achieved with a periodic structure where the period of the variation must be a whole number of half-wavelengths,

$$\Delta = m \frac{\lambda}{2} \tag{E3-1}$$

where Δ is the period, m is now the grating order (the number of half-wavelengths per period), and λ is effectively the average wavelength in the medium. This is a Bragg reflector.

If a rectangular two-phase grating is assumed (E3-1) can be written without resorting to average wavelength:

$$l_1 n_1 + l_2 n_2 = m \frac{\lambda_{\text{Bragg}}}{2} \tag{E3-2}$$

where l_1 and l_2 and n_1 and n_2 are the lengths and refractive indices, which may be *effective* refractive indices, of the two materials making up each period, and λ_{Bragg} is the free-space wavelength at which all the reflections from the grating add up in phase – the *Bragg wavelength*.

Both l and n are functions of temperature T . The different thermo-optic coefficients (TOCs, dn/dT) of the two materials cause a relative change in optical lengths of the two materials individually and of the period as a whole. The rate of physical, thermal expansion dl/dT is the product of the coefficient of linear thermal expansion (CTE) and the length. For optical materials TOCs are typically of the order $10^{-4}/^\circ\text{C}$ and CTEs typically $10^{-6}/^\circ\text{C}$. Thermal expansion can therefore be neglected and l assumed independent of temperature, particularly for short gratings. Differentiating (E3-2) with respect to temperature gives the drift rate of the Bragg reflection peak:

$$\frac{d\lambda_{\text{Bragg}}}{dT} = \frac{2}{m} \left(l_1 \frac{dn_1}{dT} + l_2 \frac{dn_2}{dT} \right) \tag{E3-3}$$

3.3 Bragg Drift Tuning

3.3.1 Zero-Drift Condition

If we require $d\lambda_{\text{Bragg}}/dT = 0$ m/°C then (E3-3) gives the athermalisation condition:

$$\frac{l_1}{l_2} = - \frac{dn_2/dT}{dn_1/dT} \tag{E3-4}$$

This can be substituted back in to (E3-2) to obtain l_1 and l_2 . The mathematics dictates that one of the thermo-optic coefficients has to be negative for this condition to be physical. All semiconductors have positive dn/dT , but air is slightly negative and many organic materials including the optical polymer benzocyclobutene (BCB, see §9.4.4) are more so.

Recall that the period Δ is given by

$$\Delta = l_1 + l_2 \tag{E3-5}$$

and l_1 and l_2 can vary continuously within the period length. In two-material gratings it is usual to have a quarter-wavelength of each to make up one period, but some leeway is possible.

Grating drift athermalisation is posited on using this condition to stabilise the optical length of the grating period over temperature by constructing each period out of two materials with opposite signs of dn/dT . As one expands optically, the other contracts, maintaining the optical length of the period.

3.3.2 Design for Specific Reflector Drift

As well as athermalisation (zero-drift) it is possible to design for particular grating drift rates, by rearranging (E3-3) to isolate l_1 and l_2 and substituting back into (E3-2) to obtain

$$l_2 = \frac{m}{2} \left(\frac{\lambda_{Bragg} \frac{dn_1}{dT} - n_1 \frac{d\lambda_{Bragg}}{dT}}{n_2 \frac{dn_1}{dT} - n_1 \frac{dn_2}{dT}} \right) \quad (\text{E3-6})$$

$$l_1 = \frac{m}{2} \left(\frac{\lambda_{Bragg} \frac{dn_2}{dT} - n_2 \frac{d\lambda_{Bragg}}{dT}}{n_1 \frac{dn_2}{dT} - n_2 \frac{dn_1}{dT}} \right). \quad (\text{E3-7})$$

If a grating with a reflectivity peak at wavelength λ_{Bragg} and drift $d\lambda_{Bragg}/dT$ is desired and n_1 , n_2 , dn_1/dT and dn_2/dT are known, these two equations can be used to obtain appropriate l_1 and l_2 .

3.3.3 Design Tool

For a given pair of materials and desired Bragg wavelength, the optical length of the grating period is fixed but reflection-peak drift rate can be varied over some range by varying the relative sizes of l_1 and l_2 . The limits of the range are defined by having a ‘grating’ made entirely from either material. This is shown in **Figure 3-1**.

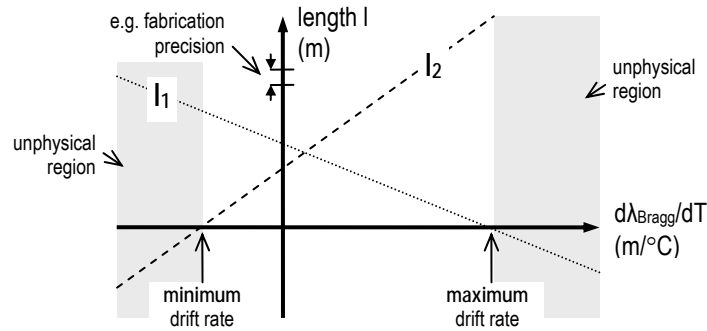


Figure 3-1 Illustrative variation of l_1 and l_2 with desired Bragg-drift rate for a given Bragg wavelength

The slopes and intercepts of the lines for the two materials depend on their refractive indices and TOCs. As the length of one material increases the other decreases to maintain the same grating period. The form of the lines is invariant with the Bragg wavelength and the grating order except that the vertical scale changes. To obtain zero drift it is necessary to have one material with negative TOC; otherwise zero drift lies in an unphysical zone requiring negative lengths.

Such plots are easily implemented in a spreadsheet, in to which various values can be input (**Table 3-1**). They are useful for several reasons. First, they show the range of available drift rates available. Second, they show how the grating length, which may be a design consideration, will vary with drift rate. Third, they show how l_1 and l_2 vary relative to one another against drift rate, so that drifts where the two lengths are very different and may be difficult to fabricate can be avoided. Lastly, if the grating fabrication precision is known, the plot gives an idea of the sensitivity of drift rate to length errors.

Table 3-1 Selection of material properties

Material or Structure	Refractive Index n at 20°C and 1320nm	dn/dT (1/°C)
InP	3.2	0.000202
BCB	1.52	-8.00E-05
SiO ₂	1.5	1.01E-05
dry air	1.000268	-7.87E-07
AlAs	2.92	1.46E-04
Al oxide	1.6	1.01E-05
GaAs	3.3	1.46E-04
7QW InGaAsP device	3.487	2.98E-04

3.4 Test Device

3.4.1 Grating Parameters

In DFBs it is usual to have a very small variation in index in a plane just above the waveguide. Only a tail of the mode sees this (see **Figure 3-2a**) but because such gratings extend the full length of the device the weak interaction is sufficient to give a strong total reflection. DBRs can be similar, but two problems arise if the use of low or negative dn/dT materials is required.

Firstly, the propagating mode in **Figure 3-2a** sees an effective refractive index that is the average refractive index across the mode profile. If only a fraction of such a mode overlaps a shallow trench filled with negative-TOC material the *effective* TOC is likely to remain positive, rendering athermalisation impossible. A drift reduction is still possible.

Secondly, optical materials with negative TOC - air, silica (SiO) and various polymers - all present a large refractive index contrast with the semiconductor crystal of laser diodes. Used to fill shallow trenches, these materials tend to cause the propagating mode profiles to change shape to avoid them.

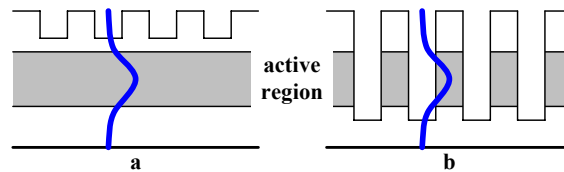


Figure 3-2 Schematic of mode energy distribution in an edge-emitting laser diode waveguide with a) a normal Bragg grating b) a deep grating

It is necessary to use a deeply-etched trench design as in **Figure 3-2b**, so that the light in the cavity is forced to traverse the material filling the trenches. Unfortunately, the high index contrast inevitably leads to very broad grating reflectivity peak, but this can be ameliorated by using higher grating orders.

Gefan Huang developed two athermal deep grating designs in which the trenches were filled with BCB (**Table 3-2**).

Table 3-2 Gefan Huang's 1310nm athermal grating parameters

16th-order grating, 7 periods:	
l_{polymer}	3742.4 nm
$l_{\text{semiconductor}}$	1496.96 nm
Refractive-index parameters:	
n_{polymer}	1.52
$n_{\text{semiconductor}}$	3.2
$\text{TOC}_{\text{polymer}}$	$-8 \times 10^{-5} / ^\circ\text{C}$
$\text{TOC}_{\text{semiconductor}}$	$2.02 \times 10^{-4} / ^\circ\text{C}$

Figure 3-3 shows the range of drift rates available with these materials.

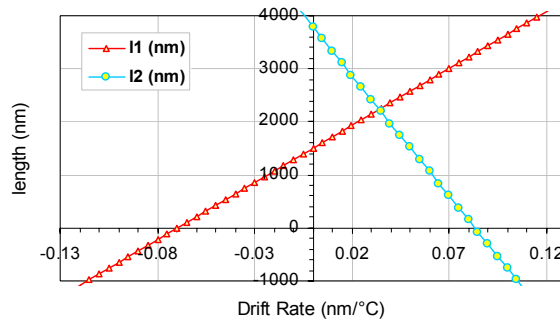


Figure 3-3 Drift rate vs. composition of one 16th-order 1310nm grating period constructed from BCB and InP (as in Table 3-2)

Real example of Figure 3-1. Drift rates from -0.071 to +0.083 nm/°C are available. For zero drift, the material proportions are as given in Table 3-2.

Figure 3-4 shows the theoretical reflectivity spectrum for the 16th-order mirror, as seen from an InP waveguide.

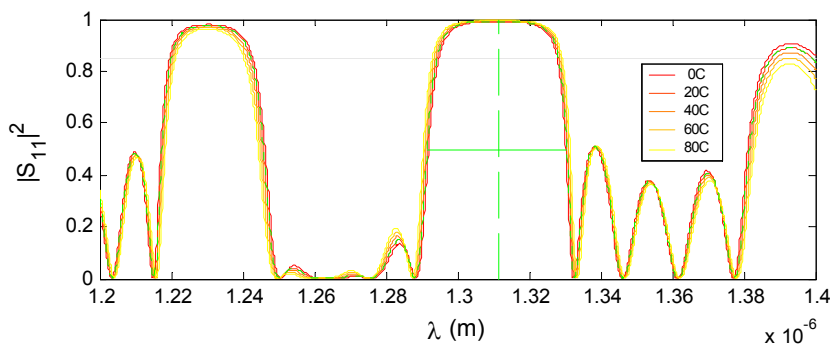


Figure 3-4 Athermal powerreflectivity spectrum for 1310nm 16th-order grating specified in Table 3-2, for five temperatures.

This is an ideal case – in practice maximum reflectivity will be limited by diffractive loss in the polymer sections, where there is no wave-guiding. Note the broad reflectivity peak (40nm) despite the high grating order.

3.4.2 Base Device

Two InP-based FP data-communications lasers with integrated spot-size converters were modified by Gefan Huang to incorporate deeply-etched athermalised gratings. Etching in the passive waveguide section of the spot-size converter meant that problems caused by etching through active layers were avoided. The trenches were fabricated using focussed ion beam etching (FIBE) and filled in with BCB polymer. The peak FP emission wavelength of these devices was approximately 1310nm, the grating design wavelength.

The total length of each device was 500 μm . A 250 μm MQW InP active section fed in to a 200 μm taper, which forced the optical transverse mode to expand into an underlying passive waveguide section with mode size well matched to that of single-mode fibre. The passive waveguide extended the full length of the device, and it is in the last 50 μm of this that the gratings were etched.

3.4.3 Focussed Ion Beam Etching

3.4.3.1 Overview

The semiconductor industry has developed a number of methods of selectively removing material, which are combined with successive deposition and crystal growth stages to create epitaxial structures. Of these, focussed ion-beam etching (FIBE) (**Figure 3-5**) is unique as a prototyping tool due to its single-step nature and ability to combine etching with imaging functions and even deposition of conducting and insulating structures.

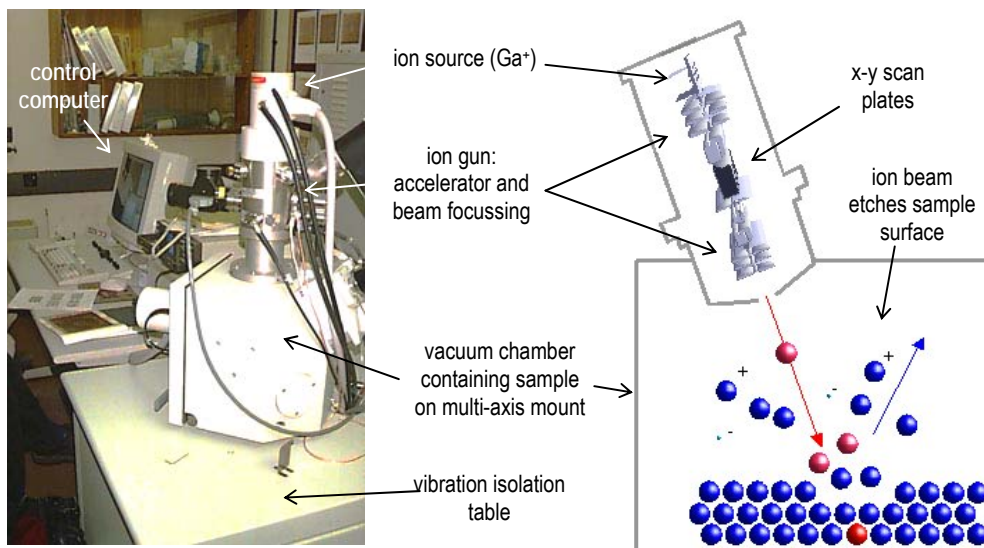


Figure 3-5 Cambridge Department of Materials Science Device Materials Group focussed Ion Beam (FIB) machine

The FIB system is similar to a SEM but uses Ga^+ ions rather than electrons in order to knock atoms out of semiconductor crystal. 10nm etch resolution is possible.

A focused ion beam system is similar to a scanning electron microscope, except that instead of using an electron beam a beam of heavy ions is scanned across the sample. The ions are created from a liquid metal source, usually gallium, and accelerated through electrostatic grids. Magnetic fields are used as ion optics, focusing and conditioning the beam. Electrostatic plates in two axes are used to steer the beam. They can be operated to produce raster scans or other programmed beam-paths.

Imaging using secondary electrons provides surface information with similar resolution to that obtainable from a scanning electron microscope (SEM) - the beam spot size available from modern systems is less than 10nm.

Gallium ions are 140 000 times more massive than electrons, so, unlike a SEM, a FIB can be used to knock atoms out of a sample surface such as a semiconductor crystal. Because work pieces can be imaged and etched on the same platform, it is possible to specify an area to be etched simply by drawing on a displayed image. Structures such as reflectors and gratings can be easily defined, even non-normal to the surface, and modifications such as electrical contact separation can be performed. In such cases it is possible to conduct real-time resistance monitoring as the etch progresses.

By using other ions, conducting platinum and insulating amorphous silicon dioxide can be deposited, and dopants implanted into semiconductor structures.

The FIB provides a means of performing materials studies and device fabrication processes which would otherwise be impossible or unreasonably time-consuming. The model operated by the Device Materials Group and used in this investigation is a commercially-available FEI FIB 200 system funded by the UK Engineering and Physical Sciences Research Council.

3.4.3.2 Etch Specification

Etch patterns are specified to the FIB control software as 1024×1024 pixel 8-bit greyscale bitmap images, non-white pixels indicating an area to be etched. The sample must be carefully aligned with the etch pattern image before etching commences. This working area represents 1/16 of the image field, which is 4096×4096 pixels. Etch resolution is the same as image resolution.

A consequence of this procedure is that maximum etch resolution is frequently limited to 1/4096 of the image field width at a given magnification, rather than by the spot size. That is, available resolution increases proportionally with magnification until the 10nm limit is reached (**Table 3-3**), corresponding to a field width of 40.96µm. This is because of the finite voltage resolution of the X-Y plates.

Table 3-3 Available etch resolutions and magnifications

magnification (thousands)	image field width (μm)	dimension of working area (μm)	etch resolution (nm)
0.0398	7630	1907.500	1862.8
0.239	1270	317.500	310.1
0.350	869	217.250	212.2
0.500	608	152.000	148.4
0.650	468	117.000	114.3
0.800	380	95.000	92.8
1.00	304	76.000	74.2
1.20	253	63.250	61.8
1.50	203	50.750	49.6
2.00	152	38.000	37.1
2.50	122	30.500	29.8
3.50	86.9	21.725	21.2
5.00	60.8	15.200	14.8
6.50	46.8	11.700	11.4
8.00	38.0	9.500	10.0
10.0	30.4	7.600	10.0
12.0	25.3	6.325	10.0
15.0	20.3	5.075	10.0
20.0	15.2	3.800	10.0
25.0	12.2	3.050	10.0
35.0	8.69	2.172	10.0
50.0	6.08	1.520	10.0
65.0	4.68	1.170	10.0
80.0	3.80	0.950	10.0
100	3.04	0.760	10.0

Other important etch parameters are the time the beam *dwells* at each point on its path (μs) defining the scanning speed of the beam, the percentage overlap between dwell-points, the beam current (nA), which defines the intensity of the beam, and the total etch time. Beam current and etch time may be aggregated into a beam ‘dose’ ($\text{nJ}/\mu\text{m}^2$).

3.4.3.3 Etch Considerations

As well as trading off resolution and working area the experimenter using FIB equipment to make deep trenches must be aware of three other issues.

One is the nature of possible etching errors. These generally manifest themselves as *beam drift*, so that the longer the etch period the greater the error. Both etch depth and extent can be seriously affected, more so at small scales. Each etch may be subject to different drift so that when creating extended fine-resolution structures by means of a series of etches a *stitching error* may be introduced.

Second, there are potential problems arising from etching through active layers. Laser diodes have complex current-confinement structures and etching through them, as may be the case with deep gratings, may introduce parallel current paths. This may increase threshold to the point of preventing lasing. It is possible that this can be prevented by depositing insulating material on the sidewalls prior to their exposure to air but this has not been tested.

Thirdly, etched atoms are evacuated from the etch area only by their own motion. In confined spaces such as a high aspect-ratio trench there can be significant *redeposition*, in which the etched atoms condense on the sides of the trench. The maximum practically-achievable aspect ratio is about 30:1.

3.4.4 Polymer Infill

Optical polymers have attracted interest from various quarters for their low material and processing costs, their flexibility as a material system for integrating optical functions, and their unique properties.

Benzocyclobutene was originally synthesised as a low-k dielectric but because of its availability and good mechanical properties has been extensively studied by groups interested in using organic materials in optical applications. Sustained interest over the last decade has brought forth a number of polymer systems with greatly improved optical properties but at the time of this investigation none were readily available.

Grating athermalisation depends on integration of negative-TOC materials and the subject of optical polymers will be returned to later in this dissertation. At this point it is sufficient to say that following etching of deep trenches, BCB polymer in solution was applied to the test devices with a pipette and cured in an oven at 100°C. Other workers, notably Raj *et al* [1], have reported similar BCB-infilled deep gratings, but not in the context of drift control.

3.4.5 Observations

The modified devices were found to be two-moded, lasing at 1287nm and 1293nm. The separation of these modes is much greater than the mode spacing so they can be attributed to the reflection grating. However, the sub-threshold emission spectrum (**Figure 3-6**) shows features which can not be matched with the grating reflection spectrum as designed (see **Figure 3-4**).

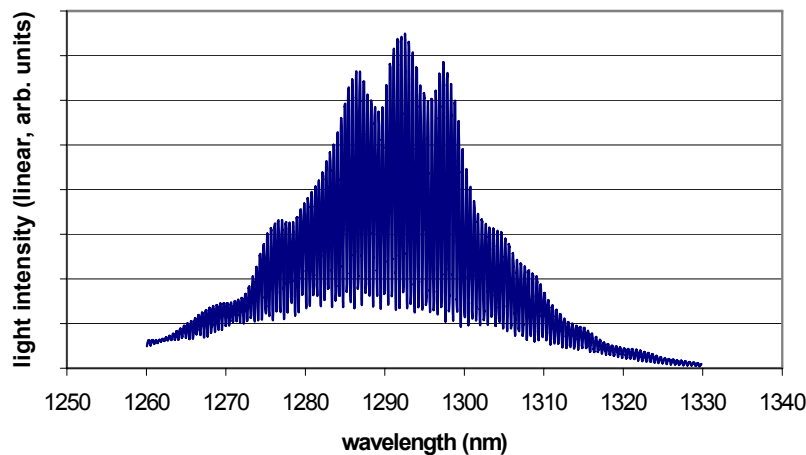


Figure 3-6 Sub-threshold spectrum – 20mA, 20°C (device 1)

It must be surmised that the refractive indices used in the design phase are not accurate and the reflectivity peak is not where it is expected to be. None of the peaks in the emission envelope can be identified as the main reflectivity peak, which must be tens of nanometres across. However, it can be seen from **Figure 3-4** that these side lobes, if that is what they are, are also expected to be well athermalised.

Drift rate of the lasing mode was measured before and after infilling of the deep grating with BCB. A 10% reduction in drift rate was observed (**Figure 3-7**).

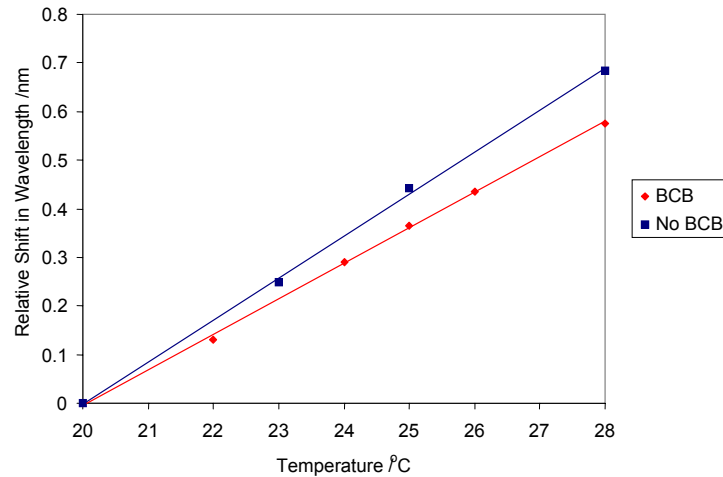


Figure 3-7 Measured wavelength of lasing mode of test device (1) vs. temperature after etching, before and after inclusion of BCB polymer

It is not possible to explain this reduction in drift rate in terms of the theory used to arrive at this design. Partial elimination of drift indicates that other, unconsidered mechanisms are at work. To better study the reflectors a computer simulation was developed, which is the subject of the next chapter, although some of its output (**Figure 3-4**) has been used here.

-
- [1] Raj, M. M., Wiedmann, J., Toyoshima, S., Saka, Y., Ebihara, K. and Arai, S.: 'High-reflectivity semiconductor / benzocyclobutene Bragg reflector mirrors for GaInAsP / InP lasers', *Japanese Journal of Applied Physics Part 1-Regular Papers Short Notes & Review Papers*, **40**, (4A), pp.2269-77

Chapter 4

Reflector Model Development

A numerical model based on the Transfer Matrix Method (TMM) is developed in Mathworks' Matlab environment. It is used to investigate anomalous test results from previously-fabricated athermal grating devices.

4.1 Bragg Reflector Model Requirements

A computational model was used to investigate the anomalous wavelength drift of the devices with BCB-infilled DBRs. As an investigative simulation tool it necessarily must include temperature and wavelength effects. As a potential prototyping tool, speed, simplicity and flexibility were desired characteristics.

There exist exact expressions for the complex reflectivity as a function of wavelength near the Bragg wavelength for quarter-wave Bragg reflectors [1]. Unfortunately, for more general cases no such expressions exist. Non-quarter-wave gratings, or gratings away from their design temperature, which do not strictly satisfy the Bragg condition at any optical wavelength, are such general cases (see, e.g. **Figure 8-27**). The highly differential optical expansion of the organic and inorganic grating elements is likely to exacerbate this as well as making equation (E3-2) unreliable as a means of predicting the location of the reflection maximum. Furthermore, it is useful for an investigative tool to be capable of accurately predicting the mirror reflection spectrum at many wavelengths and for arbitrary structures, including organic-inorganic reflector stacks away from their design temperature. Therefore it was considered necessary to use a numerical technique.

This chapter covers the issues relating to the development of such a model and describes the model itself and its validation.

4.2 Reflectivity and Transmissivity

The boundary conditions for traveling electromagnetic waves incident at a sharp interface between two media are:

- i) **E** and **H** parallel to the surface are equal on both sides of the interface,
- ii) **D** and **B** normal to the surface are equal on both sides of the interface.

Consideration of these conditions and the wave impedances $Z (=E/H)$ leads to expressions for the *Fresnel coefficients* for reflection and transmission of plane waves at planar surfaces. For the special case of normal incidence (**Figure 4-1**) the fractions of the incident field amplitude reflected and transmitted, *reflectance* r and *transmittance* t , are given by:

$$r = \frac{n_1 - n_2}{n_1 + n_2} \tag{E4-1}$$

$$t = \frac{2\sqrt{n_1 n_2}}{n_1 + n_2} \tag{E4-2}$$

where n_1 and n_2 are the refractive indices of the incident and transmitting materials, respectively.

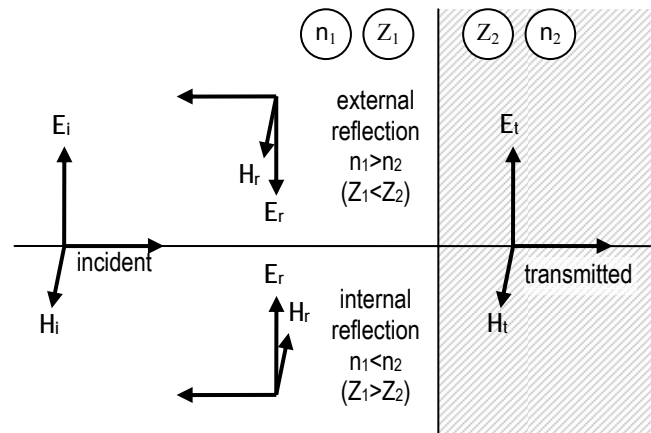


Figure 4-1 Normal reflection from a plane boundary

Poynting vector $\mathbf{\Pi} = \mathbf{E} \times \mathbf{H}$ and $\mathbf{\Pi}$ is parallel to wave-vector \mathbf{k} , in an isotropic medium. Note the 180° phase change for external reflection.

Note that in the expressions given here field amplitudes are normalised by power flow, so that the complex conjugate $a \cdot a^*$ of the field amplitude a gives the intensity. Were this not so, (E4-2) would take its more common form in which the numerator is $2n_1$, which is correct for the incident medium only. By using normalised amplitudes, *reflectivity* R and *transmissivity* T , which deal with power flow, can be written

$$R = r^2 \tag{E4-3}$$

$$T = t^2 \tag{E4-4}$$

In practice changes in refractive index along waveguides are often continuous, and furthermore are not really plane boundaries since the propagating wavefront is not itself planar. However these assumptions permit quick and reasonable estimates of reflectivity to be made, and they can be ameliorated by using effective indices.

4.3 Multiple Reflections in Dielectric Stacks

4.3.1 Network Analysis

As in electrical circuits, optical elements can be characterised as having one or more *terminals*, or end points. A collection of connected elements is a *network*. A network has internal circuit elements connected together at *nodes* and external terminals to give access to the network. Each pair of terminals used to connect a stimulus or termination is called a *port*, and a network with n ports is called *n-port*. Terminals may be common to more than one port, so an *n-port* network does not necessarily have $2n$ external terminals.

Network analysis often requires the connection of several networks to form a larger unit representing the structure to be analysed. Where the output port of one network is connected to the input port of a second this is called a *cascade* connection. The series of material interfaces in a dielectric reflector stack can be viewed in this way.

A first-principals approach to analysing the behaviour of such structures is to postulate an incoming wave and follow its transmission and reflection through multiple interfaces, adjusting its amplitude by factors of the appropriate transmittances and reflectances and incrementing its phase using the appropriate lengths and propagation constants at each step. *Signal flow graphs* are a tool which can simplify this process somewhat.

It is, fortunately, also possible to use network *scattering* and *transmission parameters* which, as we shall see, reduce the analysis of axial optical structures with many impedance discontinuities to simple matrix multiplication.

4.3.1.1 Scattering Parameters

Incoming waves are ‘scattered’ by a network and their energy partitioned between all possible outgoing waves. The scattering parameters are fixed properties of the network which describe how the energy couples between each pair of ports or transmission lines connected to the circuit.

An *n-port* network has n ports into which power can be fed and from which power can be taken. In general, power can pass from any port to any other port, so there are n incoming waves and n outgoing waves. Power can also be reflected by a port, so the input power to a single port can be partitioned into outgoing waves from all the ports of the network.

The n incoming wave complex amplitudes are usually designated by the n complex quantities a_j , and the n outgoing waves are designated by the n complex quantities b_i (**Figure 4-2**). Provided the outputs are linearly related to the inputs we can say

$$b_i = \sum_j S_{ij} a_j \tag{E4-5}$$

where S_{ij} are the scattering parameters. To measure a particular S_{ij} all inputs except a_j must equal zero, i.e.

$$S_{ij} = \left. \frac{b_i}{a_j} \right|_{a_k=0, k \neq j} \quad (\text{E4-6})$$

This is equivalent to terminating all other ports in their characteristic impedances to prevent reflections.



Figure 4-2 Key to wave designations in two-port network scattering parameters
Incoming waves a_i , outgoing waves b_i .

Associated with each port is the notion of a *reference plane* at which the wave amplitude and phase is defined. Usually the reference plane associated with a certain port is at the same place with respect to incoming and outgoing waves.

If the incoming wave quantities are assembled into an n -vector \mathbf{A} and the outgoing wave quantities into an n -vector \mathbf{B} the outgoing waves are expressed in terms of the incoming waves by the matrix equation $\mathbf{B} = \mathbf{S}\mathbf{A}$, where \mathbf{S} is an n by n square matrix of complex numbers called the *scattering matrix*. This completely determines the behaviour of the network. The elements of this matrix are the S-parameters, which are in general frequency-dependent, although this tends to be only implied in formulae. Another unstated assumption tends to be that complex gain (i.e. gain and phase) is to be used, with the wave amplitudes a_j and b_i normalised with respect to power, so that the incoming power is $a_j a_j^*$ and the outgoing power is $b_i b_i^*$, regardless of port impedance. For this reason S-parameters are sometimes called *complex* scattering parameters. The total net power flowing in to a port j is given by

$$P_j = a_j a_j^* - b_j b_j^* \quad (\text{E4-7})$$

The matrix equation for a 2-port network, such as a partial mirror, in optics, is

$$\begin{pmatrix} b_1 \\ b_2 \end{pmatrix} = \begin{pmatrix} S_{11} & S_{12} \\ S_{21} & S_{22} \end{pmatrix} \begin{pmatrix} a_1 \\ a_2 \end{pmatrix} \quad (\text{E4-8})$$

The four complex quantities making up the scattering matrix actually contain eight separate numbers; the real and imaginary parts, or the modulus and the phase angle, of each of the four complex scattering parameters. In each case the scattering parameter describes a ratio of

normalised input to normalised output and as such has a direct and intuitive physical interpretation:

- S_{11} is the reflection coefficient of the input,
- S_{22} is the reflection coefficient of the output,
- S_{21} is the forward transmission gain,
- S_{12} is the reverse transmission gain (from output to input).

Take the case of an incoming wave a_1 on port 1. If the output port, port 2, is connected to a matched impedance giving rise to no reflections then there is no input wave on port 2. a_1 gives rise to a reflected wave $S_{11}a_1$ at port 1 and a transmitted wave $S_{21}a_1$ output at port 2. Although it is clear mathematically, it is important to note the import of the subscripts: the parameter S_{21} , for example, gives the ratio of the output on port 2 to the incident wave to port 1, not vice versa as might be assumed. In general, the S-parameters can be interpreted as relating the power and phase leaving each port given an input at one, with their relative magnitudes determining how the input power splits between the possible output paths.

In a *lossless* network, the output power must equal the input power and so in the case described $|S_{11}|^2 + |S_{21}|^2 = 1$ and $|S_{22}|^2 + |S_{12}|^2 = 1$. This would not be the case for a network containing gain or loss.

A *reciprocal* S-matrix has symmetry about the leading diagonal and is obtained for networks which appear the same to waves incident from any direction, i.e. $S_{ij} = S_{ji}$ and interchanging the input and output ports does not change the transmission properties. Many optical components can be represented by reciprocal two-port networks.

4.3.1.2 Transmission Parameters

Another important matrix that relates the normalised amplitudes is the *transmission matrix*, which expresses the inputs and outputs at a given port in terms of those at the others. For a two-port case:

$$\begin{pmatrix} A_1 \\ B_1 \end{pmatrix} = \begin{pmatrix} T_{11} & T_{12} \\ T_{21} & T_{22} \end{pmatrix} \begin{pmatrix} A_2 \\ B_2 \end{pmatrix} \tag{E4-9}$$

Transmission parameters uniquely suited to calculating the performance of cascaded systems, taking into account reflections. Take, for example, the simple two-port network from cascaded in series with itself shown in **Figure 4-3**.

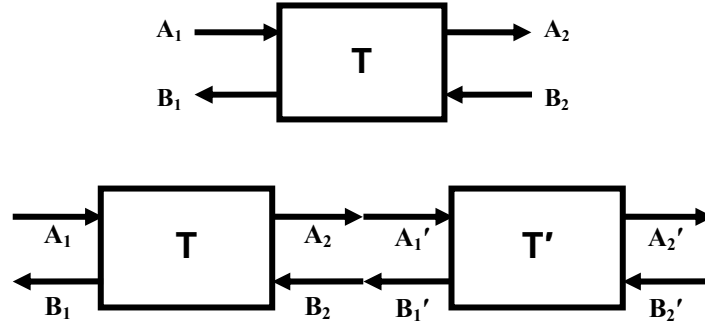


Figure 4-3 Top: wave designations in two-port network transmission parameters, Bottom: T-parameterised two-port networks in series

Right-going waves A_i , left-going waves B_i . The transmission matrix of the cascaded networks can be obtained by matrix multiplication of their T-matrices T and T' .

It is easy to relate the incoming and outgoing waves at the left-hand edge of the network to those at the far end, simply by multiplying the transmission matrices together:

$$\begin{pmatrix} A_1 \\ B_1 \end{pmatrix} = \begin{pmatrix} T_{11} & T_{12} \\ T_{21} & T_{22} \end{pmatrix} \begin{pmatrix} A_2 \\ B_2 \end{pmatrix} = \begin{pmatrix} T_{11} & T_{12} \\ T_{21} & T_{22} \end{pmatrix} \begin{pmatrix} A'_1 \\ B'_1 \end{pmatrix} = \begin{pmatrix} T_{11} & T_{12} \\ T_{21} & T_{22} \end{pmatrix} \begin{pmatrix} T'_{11} & T'_{12} \\ T'_{21} & T'_{22} \end{pmatrix} \begin{pmatrix} A'_2 \\ B'_2 \end{pmatrix} \quad (\text{E4-10})$$

The transmission-matrix description therefore excels at modelling systems that incorporate multiple cascaded sections with noticeable reflections, such as, in optics, stacks of dielectric interfaces. Given a set of system components represented by transmission matrices \mathbf{A} , \mathbf{B} , ... \mathbf{Z} , the transmission matrix representing the cascaded combination of all the elements is constructed by simply forming the matrix-multiplication product of all the elements: $\mathbf{AB}\dots\mathbf{Z}$. If the single unit \mathbf{A} was repeated n times in a cascade of itself, the overall transmission matrix would be simply \mathbf{A}^n . In either case the resulting combined transmission matrix properly represents all the transmission gains and all the internal reflections associated with the combination of system components.

Note that although matrix multiplication is *associative*, i.e. $\mathbf{T}_1\mathbf{T}_2\mathbf{T}_3\mathbf{T}_4 = (\mathbf{T}_1\mathbf{T}_2)(\mathbf{T}_3\mathbf{T}_4) = (\mathbf{T}_1\mathbf{T}_2\mathbf{T}_3)\mathbf{T}_4$ etc., it is not, in general, *commutative*, i.e. $\mathbf{T}_1\mathbf{T}_2 \neq \mathbf{T}_2\mathbf{T}_1$. When cascading T-matrices it is necessary to choose a reference plane to begin at and work outwards, multiplying successive component T-matrices together in the order encountered.

Given S-parameter descriptions of several components, each S-parameter description can be converted to a transmission-matrix description and then multiplied together with all the transmission matrices corresponding to the cascaded system components. The result is a transmission-matrix description of the whole system, which can itself be converted back to scattering-matrix form. **Table 4-1** summarises the relations between S and T matrices for normalised amplitudes.

Table 4-1 Comparison of S and T parameter approaches (from Coldren and Corzine [2])

SCATTERING MATRIX		TRANSMISSION MATRIX	
<i>definitions:</i>			
$\begin{pmatrix} b_1 \\ b_2 \end{pmatrix} = \begin{pmatrix} S_{11} & S_{12} \\ S_{21} & S_{22} \end{pmatrix} \begin{pmatrix} a_1 \\ a_2 \end{pmatrix}$		$\begin{pmatrix} A_1 \\ B_1 \end{pmatrix} = \begin{pmatrix} T_{11} & T_{12} \\ T_{21} & T_{22} \end{pmatrix} \begin{pmatrix} A_2 \\ B_2 \end{pmatrix}$	
$b_1 = S_{11}a_1 + S_{12}a_2$ $b_2 = S_{21}a_1 + S_{22}a_2$		$A_1 = T_{11}A_2 + T_{12}B_2$ $B_1 = T_{21}A_2 + T_{22}B_2$	
<i>relations to r and t:</i>			
$r_{12} = \left. \frac{b_1}{a_1} \right _{a_2=0} = S_{11}$	$r_{21} = \left. \frac{b_2}{a_2} \right _{a_1=0} = S_{22}$	$r_{12} = \left. \frac{B_1}{A_1} \right _{B_2=0} = \frac{T_{21}}{T_{11}}$	$r_{21} = \left. \frac{A_2}{B_2} \right _{A_1=0} = -\frac{T_{12}}{T_{11}}$
$t_{12} = \left. \frac{b_2}{a_1} \right _{a_2=0} = S_{21}$	$t_{21} = \left. \frac{b_1}{a_2} \right _{a_1=0} = S_{12}$	$t_{12} = \left. \frac{A_2}{A_1} \right _{B_2=0} = \frac{1}{T_{11}}$	$t_{21} = \left. \frac{B_1}{B_2} \right _{A_1=0} = \frac{\det \mathbf{T}}{T_{11}}$
$\mathbf{S} = \begin{bmatrix} r_{12} & t_{21} \\ t_{12} & r_{21} \end{bmatrix}$		$\mathbf{T} = \frac{1}{t_{12}} \begin{bmatrix} 1 & -r_{21} \\ r_{12} & t_{12}t_{21} - r_{12}r_{21} \end{bmatrix}$	
$\det \mathbf{S} = S_{11}S_{22} - S_{12}S_{21} = r_{12}r_{21} - t_{12}t_{21}$		$\det \mathbf{T} = T_{11}T_{22} - T_{12}T_{21} = \frac{t_{21}}{t_{12}}$	
<i>relation to T matrix:</i>		<i>relation to S matrix:</i>	
$\mathbf{S} = \frac{1}{T_{11}} \begin{bmatrix} T_{21} & \det \mathbf{T} \\ 1 & -T_{12} \end{bmatrix}$		$\mathbf{T} = \frac{1}{S_{21}} \begin{bmatrix} 1 & -S_{22} \\ S_{11} & -\det \mathbf{S} \end{bmatrix}$	

4.3.2 Scattering Matrix by Multiplication of Transmission Elements

Starting by deriving S-matrices for the most basic network elements (after Coldren and Corzine [3]) it is possible to obtain their T-matrices and hence the building blocks for complex networks.

4.3.2.1 Dielectric Interface

The location of the reference planes for a network is part of its definition and so we are free to place them wherever convenient. Considering an interface between two media as a two-port

network, it is most convenient to locate both reference planes at the interface itself, giving the network zero length.

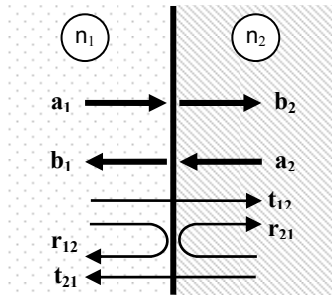


Figure 4-4 Normally-incident plane waves at a dielectric interface

Interpreting this as a two-port network we place the reference planes of both ports at the physical interface, giving the scattering junction zero length. This placement is part of the definition of the network and so is arbitrarily variable – it is done this way purely for our own convenience.

We can construct the scattering parameters as follows:

$$S_{11} = \left. \frac{b_1}{a_1} \right|_{a_2=0} = r_{12} = \frac{n_1 - n_2}{n_1 + n_2} \quad (\text{E4-11})$$

By reciprocity reflection is the same on both sides of the interface apart from a π phase shift on the external reflection, whichever that is. The second equality is true in waveguides for weakly-guided dielectric modes but in more strongly-guided cases the refractive indices n_1 and n_2 should be replaced by the *effective refractive indices* seen by the mode, \bar{n}_1 and \bar{n}_2 .

$$S_{22} = \left. \frac{b_2}{a_2} \right|_{a_1=0} = r_{21} = -(-r_{12}) = -S_{11} \quad (\text{E4-12})$$

By reciprocity it is necessary that $r_{12} = -r_{21}$ and reflection magnitude $|r|$ is the same in both directions. This also applies to transmission, $t_{12} = t_{21} = t$, hence

$$S_{12} = S_{21} = t = \sqrt{1 - r^2} \quad (\text{E4-13})$$

where the second equality is provided by power conservation:

$$t^2 + r^2 = 1. \quad (\text{E4-14})$$

This is always valid for plane waves because there can be no loss in zero length but for guided waves this implies that the transverse mode profiles are the same: in fact if the modes do not match there can be *scattering loss*.

Using equations (E4-11), (E4-12) and (E4-13) we can construct the scattering matrix for this element:

$$\mathbf{S} = \begin{pmatrix} r_{12} & t_{12} \\ t_{12} & -r_{12} \end{pmatrix} \quad (\text{E4-15})$$

Using the relations set out in Table 1-1 this can be converted to the transmission matrix:

$$\mathbf{T} = \frac{1}{t_{12}} \begin{pmatrix} 1 & r_{12} \\ r_{12} & r_{12}^2 + t_{12}^2 \end{pmatrix} \quad (\text{E4-16})$$

Where there is no scattering loss at the interface, T_{22} becomes equal to one.

4.3.2.2 Transmission Line

In the case of a length of transmission line with no discontinuities, the variables are related from one reference plane to the other simply by phase changes.

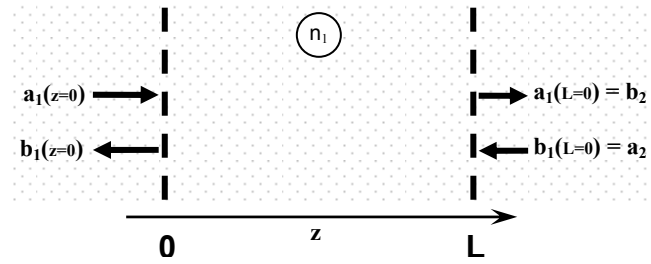


Figure 4-5 Transmission line with no discontinuities

The reference planes are placed a distance L apart.

If we use a complex propagation constant \tilde{k} where

$$\tilde{k} = k + jk_i \quad (\text{E4-17})$$

then mode propagation a distance L results in a phase shift $-kL$ and a growth rate k_iL :

$$\begin{aligned} b_2 &= a_1(L) = a_1(0)e^{-j\tilde{k}L} = a_1e^{-j\tilde{k}L} \\ a_2 &= b_1(L) = b_1(0)e^{+j\tilde{k}L} = b_1e^{+j\tilde{k}L} \end{aligned} \quad (\text{E4-18})$$

Thus

$$S_{12} = S_{21} = e^{-j\tilde{k}L} \quad (\text{E4-19})$$

Where there is no gain or loss, $k_i = 0$ and k can be used instead of \tilde{k} . Note that aforementioned scattering loss can not be represented by the complex propagation constant, except by defining some distributed equivalent.

The remaining two scattering coefficients are readily obtained by recalling that with no discontinuities there is no coupling between backward and forward-propagating waves, so

$$S_{11} = S_{22} = 0 \quad (\text{E4-20})$$

Using equations (E4-19) and (E4-20) we can construct the scattering matrix for this element:

$$\mathbf{S} = \begin{pmatrix} 0 & e^{-j\phi} \\ e^{-j\phi} & 0 \end{pmatrix} \quad (\text{E4-21})$$

where $\phi = \tilde{k}L$. Using the relations set out in Table 1-1 this can be converted to the transmission matrix:

$$\mathbf{T} = \begin{pmatrix} e^{j\phi} & 0 \\ 0 & e^{-j\phi} \end{pmatrix} \quad (\text{E4-22})$$

4.3.2.3 Constructing reflection gratings using TMM

At the Bragg wavelength the period of a reflection grating is half the average optical wavelength in the medium. For rectangular gratings with alternating layers of materials of different refractive index there are two discontinuities per period, each with the same reflectivity R . The reflections from all the discontinuities arrive back at the start of the grating in phase, interfering constructively to produce a large total reflection.

Away from the Bragg wavelength reflections from deeper in the grating return with progressively greater phase mismatch. This happens faster the further the wavelength is deviated from the Bragg wavelength, causing a roll-off in net reflectivity. The longer the grating, the more mismatched the reflection from the farthest interface and the faster the roll-off.

If the interface reflectivity is small the incident field at the last interface is similar to that at the first discontinuity and the net grating reflectivity can be taken as $2mR$, where m is the number of periods. If R is larger the field will fall off significantly along the length of the grating and the problem is more difficult.

A transmission-matrix approach renders it relatively simple. By deriving the scattering parameters for a single period of the grating, converting to a transmission matrix and raising to the n^{th} power where n is the number of periods in the grating, using separate T-matrices for the

initial and terminal interfaces as necessary, we can rapidly obtain reflectivity and transmissivity at any given wavelength.

By repeating the calculation for a range of wavelengths a reflectivity spectrum can be constructed. By including temperature dependencies in the grating specification the effect of temperature on this spectrum can also be studied.

Whether in edge-orientated or vertical configurations, all semiconductor lasers utilising reflection gratings place them normal to the device axis. Where the dielectric interfaces extend uniformly across the mode profile the interface reflectance can be calculated simply using (E4-1). This is typically true for VCSELs but not for edge-emitters, where there is stronger wave guiding and fabrication limitations mean that typically only part of the mode profile will overlap the refractive index variation. In this case it is necessary to use the effective indices \bar{n} seen by the propagating mode on either side of the interface. Even so, this will only be approximate because the transverse grating mode will in fact be something in between those which would exist for uniform waveguides of \bar{n}_1 and \bar{n}_2 . Edge-emitting configurations allow other means of introducing a periodic variation in the waveguide, but we are concerned primarily with refractive index.

For non-rectangular grating profiles with gradual changes in refractive index coupled-mode theory is required.

4.4 Model Code Structure

An approach based on the transmission-matrix method (TMM) was implemented in Matlab code. In this section a description of the key areas is given – the code itself is provided on an accompanying CD.

4.4.1 Introduction to Matlab

Matlab is commercially-available software from The Mathworks, Inc. It is a numerical modelling environment based on matrix mathematics. Data is stored in named n-dimensional structures, which may be single variables, vectors, matrices or arrays. As well as a range of built-in mathematical, analytical and graphical functions, programming commands are also available, including logical tests, conditional execution, loops, and a structured data space which keeps variables used by different functions separate.

Variables are passed to *functions*, which are self-contained pieces of code, at the time they are called. They are a useful means of organising and re-using code and are the form in which Matlab programs are written. Programs consisting of a top-level function calling many

subsidiary functions may be spread over several files or contain all their code in a single file. Subfunctions contained in the same file are not available outside execution of that top-level function.

The version used in this investigation was 6.5, release 13.

4.4.2 Overview

The user is required to construct a matrix in Matlab describing the dielectric stack to be modelled. It includes physical lengths, refractive indices, TOCs and initial and terminal interfaces.

CTE is not modelled, on the assumption that length scales will be such that it is negligible. Dispersion is not included either, on the assumption that wavelength ranges will typically be small enough that the effect is negligible. The refractive indices can be complex, which in principle allows inclusion of gain and loss, apart from scattering loss at mode mismatches at interfaces. Gain might well be expected to vary over the typical wavelength ranges however, so that exploiting this possibility would require the inclusion of dispersion of the complex refractive index in the model and stack specification.

The stack specification matrix is accompanied by a small vector specifying the number of periods, the temperature at which the given refractive indices are defined and the temperature at which data should be plotted, if at all.

The temperature and wavelength ranges to be covered are also specified by the user at this point, formatted in a third matrix. If a single temperature and wavelength is specified the code will run in 'single shot' mode, skipping all graphing and data analysis functions. This is useful when calling the code from another program.

Once set running the code generates a set of working matrices in which various data are stored, such as interface reflectivity, position of peak reflectivity at each temperature, loop counters and many others. If the code is not running in single-shot mode it begins looping through the specified wavelengths and temperatures, calculating the grating scattering parameters at each.

The algorithm implementing TMM lies at the heart of the code. Using the dielectric stack specification supplied by the user it builds up a grating transmission matrix from the basic dielectric interface and transmission line elements described in the preceding sections, thus maximising flexibility and generality – wholly arbitrary stack structures can be built up. If necessary, minor modifications to the code at this point would allow inclusion of scattering losses.

Single-shot mode exits with a single S-matrix at this point, from which reflectances and transmittances may be extracted. Plot mode measures key properties of the modelled spectra including position of reflectivity peak, position of zero reflection phase, upper and lower 3dB bands of the reflection peak, drift rates with temperature of all these, phase slope at peak reflectivity, phase slope at zero reflection phase, bandwidth, and locations of all reflection peaks (main and subsidiary).

When the program exits all the working matrices are erased from the Matlab environment, leaving only specified output matrices containing the above data.

The program has a third mode of operation designed to facilitate investigation of paired gratings, such as DBRs at either end of a laser cavity. In this mode two stack specifications are input as an array, the resulting reflection spectra are multiplied together and the same measurement routines applied to the combined spectrum.

Figure 4-6 diagrams data flow in the function code.

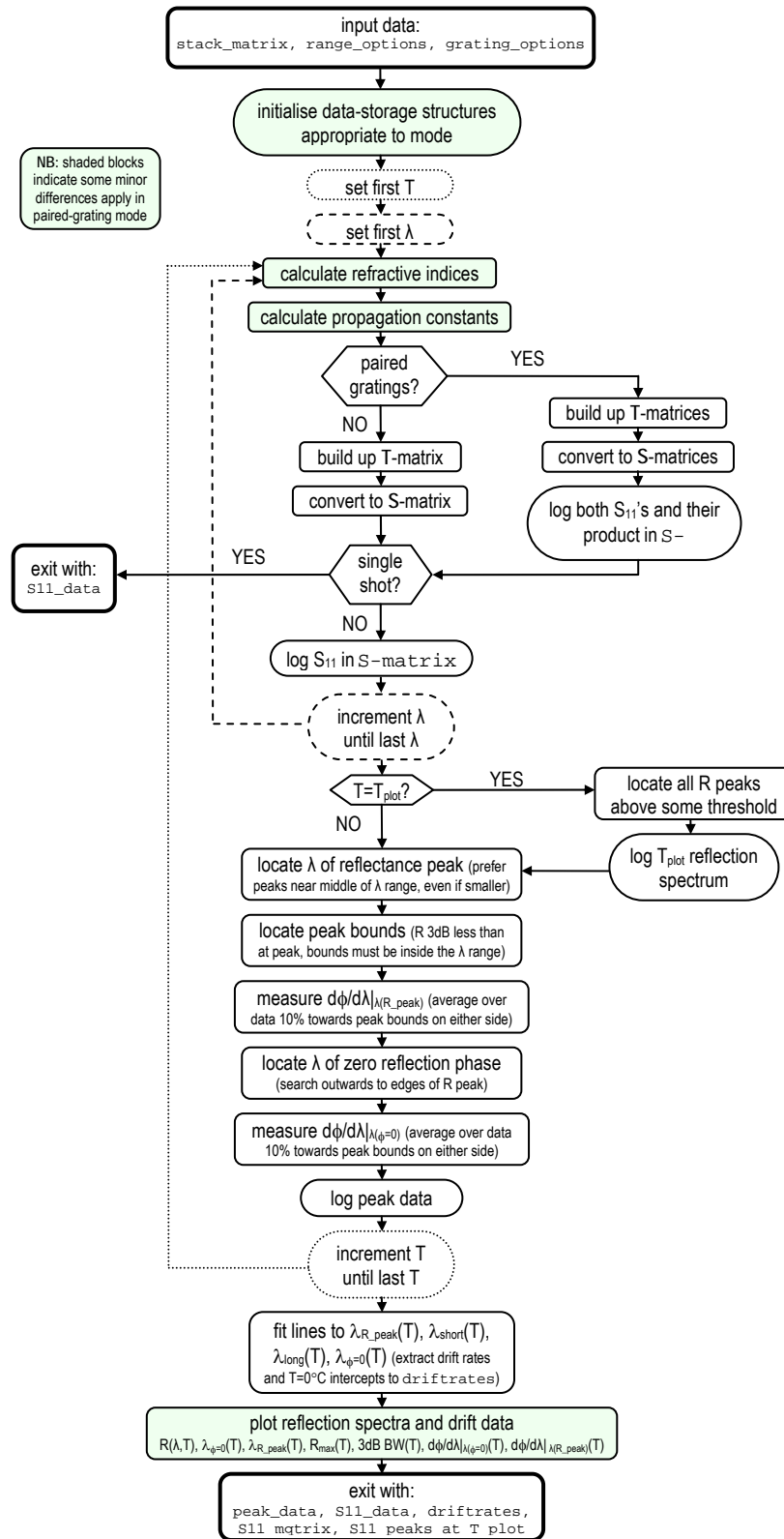


Figure 4-6 Schematic of data flow and operating structure of TMM model code

The main variables, conditional paths and structures are included here. Many more exist but are not important to comprehension of the general operation of the program. In particular the exact *modi operandi* of the various subfunctions are not made explicit. Knowledge of these can be of importance in evaluating results and detailed descriptions are given in a following section.

4.4.3 Assumptions

Four important assumptions are made at this level:

1. Chromatic dispersion is negligible.
2. The input wave is monochromatic and continuous, with no modulation on phase or amplitude. The model is strictly steady-state.
3. Thermal expansion of the grating elements is not significant. In most cases it is true that the changing refractive indices completely dominate any temperature-related phenomena, but in the case of very long gratings the whole might be considered to thermally expand with the substrate.
4. Because the Fresnel perpendicular plane-wave reflection and transmission coefficients are used in calculating the grating S parameters, the model assumes that refractive index changes occur in the form of infinite planar interfaces between homogeneous materials. Using effective refractive indices ameliorates this problem.

The model will work for any regular rectangular grating and can approximate non-rectangular gratings with some success. In the case of deep Bragg gratings the model requires two further assumptions:

1. Because the deep trenches of such devices cut right through the waveguide, n_{eff} in the trenches is the same as n of the trench infill material. This is believed to be a safe assumption as nearly all the mode energy passes through the trench rather than just the tail of the mode as in a normal grating.
2. Diffractive loss due to the lack of wave-guiding structure in the trenches is negligible. This is not a good assumption as this has significant effects. Including such losses is a matter for further work.

4.4.4 Input and Output Data Structures

This is intended as a brief guide for the user. The program is called thus:

```
[S11_data, peak_data, S11_matrix, driftrates, S11_peaks_at_T_plot] =
    TM_BG_model_TG( stack_matrix, range_options, grating_options,
    savetag);
```

In Matlab the names in the square brackets are assigned to the outputs of the program, the program itself has a name (TM_BG_model_TG in this case) independent of its file name, and the variables names in the round brackets are those to be passed to the program on its initialisation.

Define some variables contained in the input data structures:

- **N** - number of grating elements
- **l1**, **l2** - normal thicknesses of materials of refractive indices n_1 , n_2 (m)
- **n1_def**, **n2_def**, ... - refractive index n_1 of material 1 (usually semiconductor) and refractive index n_2 of material 2 (usually polymer)
- **T_def** – temperature (°C) at which **n1_def**, **n2_def** are defined (usually room temperature)
- **dn1dT**, **dn2dT**, ... - rates of change dn/dT of refractive indices of materials 1 and 2 with temperature (i.e. the thermo-optic coefficients) (/°C)
- **low_T**, **high_T**, **Tstepsize** - temperature range to scan (°C) and size of step to use (plot mode only)
- **short_W**, **long_W**, **Wstepsize** - range of free-space wavelengths to scan (m) response for and size of step to use (plot mode only)
- **T_plot** - temperature (°C) at which to plot reflection spectrum and related data (plot mode only)
- **savetag** - a string, e.g. 'alice', which will be used as the root of the filenames the output matrices and plots are saved under

Table 4-2 sets out the structures of the input matrices, using formats Matlab would accept. Examples are given which specify a typical DFB structure and suitable wavelength and temperature ranges.

Table 4-2 Input data structures to TMM model

Input structure (with example)	Notes
<pre>grating_options = [N, T_def, T_plot] grating_options = [1371, 20, 20];</pre>	<p>Specifies number of periods N (the period is defined in <i>stack_matrix</i>). T_{def} is the temperature for which refractive indices are given. T_{plot} specifies the temperature at which to plot spectra and should be omitted for single-shot use</p>
<pre>range_options = [low_T, Tstepsize, high_T; short_W, Wstepsize, long_W] range_options = [10, 20, 80; 1390e-9, 0.1e-9, 1410e-9];</pre>	<p>Specify the temperature and wavelength windows and the scan resolution within them.</p> <p>Note that to avoid quantisation errors on measurements of some low drift rates $W_{stepsize}$ may need to be as little as 1/2000 of the width of the frequency window. Unfortunately this will increase the model run time to several minutes.</p> <p>To run in single-shot mode use 1 column only to specify a single temperature and wavelength.</p>
<pre>stack_matrix = [NaN, 11, 12, K ln, NaN; nstart_def, n1_def, n2_def, K nn_def, nend_def; dnstartdT, dn1dT, dn2dT, K dnndT, dnenddT] stack_matrix = [0, 109.372e-9, 109.414e-9, 0; 3.20112, 3.20112, 3.19886, 3.20112; 2.02e-4, 2.02e-4, 2.02e-4, 2.02e-4];</pre>	<p>Any number of layers can be specified. Top row specifies length of each layer (the first and last columns specify the environment so no length is specified). Middle row specifies refractive index n_{def} at reference temperature T_{def} for each layer. Bottom row specifies dn/dT of each layer.</p> <p>Note that the grating T-matrix is calculated left-to-right in the stack definitions, so which way round a grating specification is can be significant, especially regarding the phase of the reflection.</p>
<pre>grating_options = {[N_1, N_2], [T_def_1, T_def_2], T_plot} stack_matrix = {stack_matrix_1, stack_matrix_2}</pre>	<p>A pair of gratings can be specified by setting up the input arguments as arrays, thus.</p>

Table 4-3 sets out the structures of the output matrices. Apart from the names of the output structures, it does not use a Matlab-compatible format.

Table 4-3 Output data structures from TMM model

Output structure	Notes
$\text{peak_data} = \begin{bmatrix} T_1 & T_2 & \Lambda & T_n \\ \lambda_{\text{peak}} & \Lambda & \Lambda & \Lambda \\ S_{11} _{\text{max}} & \Lambda & \Lambda & \Lambda \\ \frac{d\phi}{d\lambda} _{ S_{11} _{\text{max}}} & \Lambda & \Lambda & \Lambda \\ BW & \Lambda & \Lambda & \Lambda \\ \lambda_{\text{short}} & \Lambda & \Lambda & \Lambda \\ \lambda_{\text{long}} & \Lambda & \Lambda & \Lambda \\ \lambda_{\phi=0} & \Lambda & \Lambda & \Lambda \\ \frac{d\phi}{d\lambda} _{\lambda_{\phi=0}} & \Lambda & \Lambda & \Lambda \end{bmatrix}$	<p>Plot & paired-grating modes only. Matrix of 9 rows recording data about the reflection peak at each temperature: temperature T, free-space wavelength λ_{peak} of reflection peak, peak reflectance $S_{11} _{\text{max}}$, phase slope at reflection peak $d\phi/d\lambda$, 3dB width of reflection peak BW, short-wavelength bound λ_{short}, long-wavelength bound λ_{long}, location of zero reflection phase $\lambda_{\phi=0}$, phase slope at zero reflection phase.</p> <p>Inside the program this structure is given the name <code>output_T</code>.</p>
<p>S11_data = S_{11} in single - shot mode = $\begin{pmatrix} \lambda_1 & \lambda_2 & K & \lambda_n \\ S_{111} & S_{112} & K & S_{11n} \end{pmatrix}$ in plot mode = $\begin{pmatrix} \lambda_1 & \lambda_2 & K & \lambda_n \\ S_{11}(\lambda_1)_{\text{product}} & S_{11}(\lambda_2)_{\text{product}} & K & S_{11}(\lambda_n)_{\text{product}} \\ S_{11}(\lambda_1)_{\text{grating}_1} & S_{11}(\lambda_2)_{\text{grating}_1} & K & S_{11}(\lambda_n)_{\text{grating}_1} \\ S_{11}(\lambda_1)_{\text{grating}_2} & S_{11}(\lambda_2)_{\text{grating}_2} & K & S_{11}(\lambda_n)_{\text{grating}_2} \end{pmatrix}$ in paired - grating mode</p>	<p>Reflectance data: a single S_{11} in single-shot case. Otherwise a matrix of 2 rows: λ on row 1 and S_{11} at T_{plot} on row 2. If the program is run in paired-grating mode then it returns a matrix of 4 rows: λ, product of the two grating reflectances $S_{11}(\lambda)_{\text{product}}$, reflectance of first grating $S_{11}(\lambda)_{\text{grating}_1}$ and reflectance of second grating $S_{11}(\lambda)_{\text{grating}_2}$, all at T_{plot}. There is one column per surveyed wavelength.</p>
$\text{driftrates} = \begin{bmatrix} \frac{d\lambda_{S_{11}\text{-peak}}}{dT} & \lambda_{S_{11}\text{-peak}} _{T=0} \\ \frac{d\lambda_{\text{long}}}{dT} & \lambda_{\text{long}} _{T=0} \\ \frac{d\lambda_{\text{short}}}{dT} & \lambda_{\text{short}} _{T=0} \\ \frac{d\lambda_{\phi=0}}{dT} & \lambda_{\phi=0} _{T=0} \end{bmatrix}$	<p>Plot & paired-grating modes only. Matrix of 4 rows by 2 columns: average drift rates (column 1) and wavelength at zero °C (λ-intercept) (column 2) of reflectance peak, upper and lower reflectance-peak bounds, zero-reflection-phase wavelength. Average drift rate is found by fitting a straight line to the data, which may be quantised to some degree.</p>
$\text{S11_matrix} = \begin{bmatrix} S_{11}(\lambda_1, T_1) & S_{11}(\lambda_1, T_2) & \Lambda & S_{11}(\lambda_1, T_{\text{num}_T}) \\ S_{11}(\lambda_2, T_1) & S_{11}(\lambda_2, T_2) & & M \\ & M & O & M \\ S_{11}(\lambda_{\text{num}_\lambda}, T_1) & \Lambda & \Lambda & S_{11}(\lambda_{\text{num}_\lambda}, T_{\text{num}_T}) \end{bmatrix}$	<p>Plot & paired-grating modes only. Matrix recording complex S_{11} at every T and λ point in the search space. It has one row per surveyed wavelength, and one column per surveyed temperature. In paired-grating mode each S_{11} is the product of the two complex reflectances.</p>
$\text{S11_peaks_at_T_plot} = \begin{bmatrix} \lambda_{\text{peak}_1} & \lambda_{\text{peak}_2} & \Lambda & \lambda_{\text{num_peaks}} \\ S_{11} _{\text{peak}_1}^2 & S_{11} _{\text{peak}_2}^2 & \Lambda & S_{11} _{\text{num_peaks}}^2 \\ 1 & 2 & \Lambda & \text{num_peaks} \end{bmatrix}$	<p>Plot & paired-grating modes only. Matrix of 3 rows recording the wavelengths (top row) and magnitudes (second row) of major reflectivity peaks ($S_{11} ^2$ peaks) at T_{plot}. The third row contains the indices of the peaks.</p> <p>If no peaks are detected the matrix will be a column of three zeros. The detection threshold is set as the internal variable</p> <p style="text-align: center;"><code>S11mag2_peak_detection_level</code></p> <p>which is by default is set at $R=0.7$.</p>

Further data structures internal to the program may be of importance to anyone seeking to make modifications. Here follows a brief description of the most important, others are annotated in the code itself.

The output structure `peak_data` is internally referred to as `output_T`. During each temperature loop the structure `output_lambda` is used to store the scattering-parameter data for each wavelength which, for `T_plot` only, is output in `S11_data`.

Before calculating any single-period transfer matrix all the reflection and transmission coefficients are calculated and logged in `r_t_matrix`, a structure of four rows containing, from top to bottom, r_{12} , t_{12} , r_{21} , and t_{21} for each material interface in the grating specification. The first column contains the coefficients for the interface between the surrounding material and the first material of the period, the next column contains those for the next element-element interface, etc., until the last-element to surrounding-medium interface in the penultimate column. The last column contains the interface between the last element of a period and the first element of the next.

4.4.5 Construction of Grating T-matrix

This is the core routine of the program and is performed for every combination of wavelength and temperature. Fundamentally, no assumptions are made about the form of the grating except that it is rectangular and does not suffer scattering loss at the interfaces. The code contains the general **T**-matrices for dielectric interfaces and transmission-line segments ((E4-16) and (E4-22)) and from these **T**-matrices for any rectangular grating can be constructed, from a single dielectric interface upwards.

Any number of periods is allowed, and periods can contain any number of layers. It is possible to define aperiodic gratings (e.g. chirped gratings) by specifying them as single-period gratings with an unusually long ‘period’.

Figure 4-7 illustrates how this is implemented.

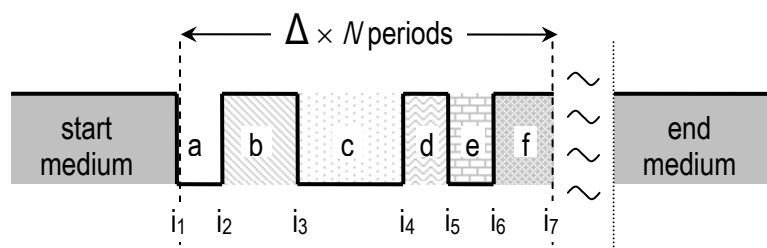
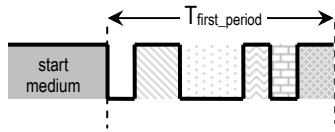


Figure 4-7 Example grating structure

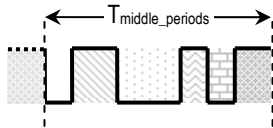
One period Δ of this grating consists of 6 layers, and so 6 bulk intervals, $a-f$. Interfaces are slightly more involved. There are 5 interfaces internal to each period, i_2-i_6 . For the first period, i_1 is the very first interface of the grating and is start-medium-to- a . In subsequent periods $i_7=i_1, f$ to a . In the last period, i_7 is f -to-end-medium.

Before calculating the total grating **T** matrix the program creates three intermediate **T**-matrices:

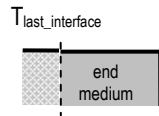
- $T_{\text{first_period}}$ for the first period including the very first interface



- $T_{\text{middle_periods}}$ for the bulk intervals and internal interfaces of the other periods, including at the beginning the interface from the last layer of the preceding period



- $T_{\text{last_interface}}$ for the final interface, between the last layer of a period and the end medium.



The total grating T-matrix is then given by

$$T_{\text{grating}} = T_{\text{first_period}} \times T_{\text{period}}^{N-1} \times T_{\text{last_interface}}$$

(E4-23)

where N is the specified number of periods.

4.4.6 Data Analysis Routines

4.4.6.1 Location of Reflection Peak

It is sometimes the case that the reflection peak of interest in a reflection spectrum is not the largest in the wavelength window. This may come about as a grating moves off the Bragg condition with changing temperature, or perhaps harmonics of the Bragg wavelength are visible on either side. To reduce the amount of user intervention required by the program, the peak-location algorithm gives preference to peaks more central in the window, even if they are smaller.

Specifically, the code identifies all the peaks above a certain reflectivity threshold (subfunction `s11_trace_peaks`), set at 0.85 of the maximum reflectivity present by default, and chooses the one nearest the centre of the wavelength window. This threshold is drawn in the plot of reflectivity spectrum which is one of the program outputs. It can be modified by editing the internal variable `detection_threshold`.

Peaks are identified as surveyed wavelengths at which there are local maxima in reflectivity. Specifying a higher density of survey wavelengths will therefore reduce quantization errors.

4.4.6.2 Location of Limits of Reflection Peak

Subfunction `find_3dBBW` works outwards in wavelength from the identified reflection peak until reflectivity falls below half (3dB) of the peak value. It looks on the short-wavelength side of the peak first, then the long-wavelength side. If it encounters the edge of the wavelength window before finding either boundary then the edge of the wavelength window is recorded at the peak boundary. This behaviour is not perfectly logical, but simplifies the coding.

Athermalised reflection peaks such as are studied in this investigation are frequently found to become wider or narrower even while remaining stationary. Such boundary-drift is often very small and quantisation errors are easily introduced if an insufficient density of wavelengths is scanned, because the first wavelength at which the reflectivity falls below the 3dB level has to be taken as representing the edge of the peak. To combat this problem the algorithm takes this point and the point immediately preceding, at which reflectivity is above the 3dB level. It calculates a straight line intersecting the two points and finds its intercept on the 3dB level, recording that as the 3dB boundary.

A second function, `find_BWnull2null`, is included in the code but not called. It finds bandwidth by measuring between the reflectivity nulls on either side of the peak, or to be exact, between the first surveyed wavelengths falling beyond the nulls. It does not attempt any interpolation. To use it, it is necessary to substitute its name at the point in the program where `find_3dBBW` is called.

4.4.6.3 Location of Zero Reflection-Phase

There is zero phase change on reflections at the Bragg wavelength of a Bragg grating. Gratings which do not fulfill the Bragg condition may have reflection peaks but these do not necessarily coincide with the wavelength of zero reflection phase. It is important in this investigation to relate reflectivity-spectrum drift rate to the slope with wavelength of the reflection phase. The drift rate of the zero-phase wavelength is most appropriate measure of drift rate in this case.

Subfunction `zero_phase_locator` operates very similarly to that locating the limits of the reflection peak. Beginning at the reflection peak, it works outwards to shorter wavelengths testing the reflection phase at each to see if it has changed sign. If it reaches the wavelength identified as the short-wavelength boundary it returns to the wavelength of the peak and resumes its search in the opposite direction, out to longer wavelengths. When it finds the zero-crossing it conducts a linear interpolation to better locate the exact zero-phase wavelength. If it reaches the long-wavelength bound without finding a zero crossing, it records `NaN` (Not a Number).

4.4.6.4 Measurement of Phase Slopes

Subfunction `linear_phase_slope_fit` takes a surveyed wavelength – either that identified as the reflectivity peak or that nearest that recorded as locating zero reflection phase – and extracts part of the reflectivity spectrum on either side. Specifically, it takes 10% of the surveyed wavelengths between the start point and the long and short-wavelength bounds. From this complex reflectivity data it extracts the phase information and fits a straight line to it, returning the phase slope in radians per nanometer as its output.

4.4.6.5 Calculation of Drift Rates

The reflection-peak wavelength, the zero-reflection-phase wavelength and the short and long-wavelength boundaries of the reflection peak are all located at each surveyed temperature and recorded in the matrix `peak_data`, referred to internally as `output_T`. When the temperature survey is complete this information is passed to a function `linear_drift_fits` which performs a straight-line fit to each of these quantities, using Matlab's built-in `polyfit` function. Temperature-dependent drift rates are not captured, therefore – the user must plot the data in `peak_matrix` if such behaviour is looked for.

Assuming linear fits are valid, it is good practice to maximise both the range of temperatures surveyed and the density of wavelengths. Both of these actions will reduce the probability of quantisation error of the drift rates. Note also that if the `find_3dB` subfunction did not find 3dB bounds, e.g. if the edge of the reflection peak moved out of the wavelength window, the peak boundary will have defaulted to the edge of the wavelength window and the fitted drift rate will not be useful

4.5 Test and Verification

4.5.1 Characteristics of Reflection Spectra

On either side of the designed reflectivity peak there exist other peaks at harmonics of the Bragg wavelength, with a number of sidelobes lying in between. The highly-structured Bragg grating reflectivity spectrum of Gefan Huang's 16th-order 1310nm athermal InP-BCB grating, shown in **Figure 3-4**, is a good example. Higher order gratings produce narrower and more closely spaced peaks. The 'sharpness' of the peak is determined by the number of periods – the longer the grating the faster and more complete the destructive interference away from the central wavelength. In high-contrast gratings little light may penetrate beyond the first few periods so that adding more periods has no effect on peak width except at the edges of the reflection peak where reduced reflectivity enables light to penetrate further.

The reflection phase increases smoothly with wavelength, through 2π radians across the reflection peak and its harmonics and through π across each sidelobe, describing an ‘inverse S’ shape in each case. The greater the grating contrast the more pronounced the ‘S’ shape. Phase drops discontinuously by π radians at reflectivity nulls. Phase is always zero at the Bragg wavelength, coinciding with the reflection peak – but only at the design temperature of the grating. For non-Bragg gratings (or Bragg gratings away from their design temperature) there is non-zero reflection phase at the wavelength of the peak reflectivity.

The TMM function by default produces plots of these characteristics including reflectivity and phase spectra, reflection-peak and zero-phase wavelengths against temperature, and phase slope (the rate of change of reflection phase with wavelength) at both, also against temperature.

4.5.2 Published Deep Gratings

Only one report concerning deeply-etched air gap gratings and giving both grating definitions and reflection spectra could be found (**Figure 4-8**). Although the reflection phase was not given there, modelled reflectivity is an exact match.

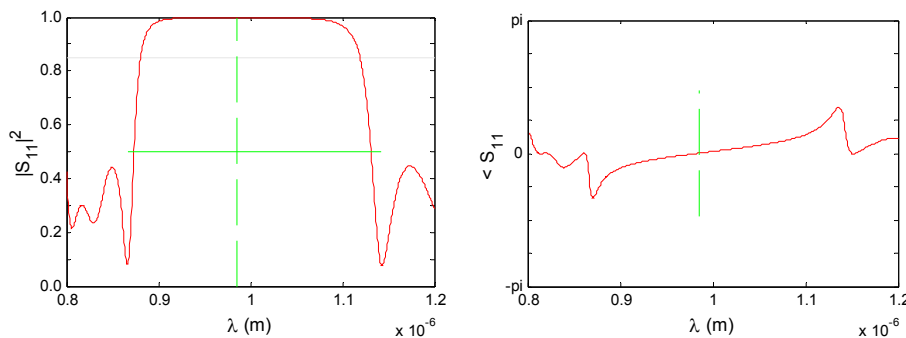


Figure 4-8 TMM model output for mirror structure described by Jambunathan et al [3]

Prepared using the grating parameters given in the published paper, the plot from which is reproduced in **Figure 4-13c**.

4.5.3 Typical DFB Parameters

To verify the model conclusively it would be necessary to obtain the parameters of a real device, input them to the model and compare the output with measurements. Although there is much publicly-available material on holographically-imprinted sinusoidal gratings, much of it concerns novel devices and in fact no literature giving both grating dimensions and complex reflection spectra could be found. The TMM approach is nevertheless an established and well-accepted tool and it was considered sufficient initially to check the model’s outputs against typical DFB spectra, which though sinusoidal are both familiar and entirely determined by the grating. As will be seen later in discussion of investigations the model was never falsified and in several cases its results were confirmed by measurements.

It is usual to discuss Bragg gratings with small index variations in terms of the fraction of field amplitude reflected per unit length, known as the *coupling coefficient* κ . For a DFB laser the product κl of the coupling coefficient with the grating length is typically 1 to 2. For a sinusoidal variation Gowar [4] gives

$$\kappa = \frac{\pi \Delta n}{\lambda_0} \tag{E4-24}$$

where Δn is the difference between the maximum and minimum refractive indices and λ_0 is the free-space wavelength satisfying the Bragg condition of the grating. Taking typical DFB laser diode lengths of 200-300 μm it is possible to obtain from this information representative estimates of Δn and of the number of periods N . Table 1-4 sets out Δn and N for a selection of DFB configurations. Since index contrast in a DFB is very small the mean refractive index of the grating is given as n_0 ; 3.35 is reasonable for GaAs and 1.5 for silica glass.

Table 4-4 Four representative DFB configurations, each with three possible κl products

	κl	Δn	N
$n_0 = 3.35$	1.00	0.0020	1031
$l = 200 \mu\text{m}$	1.50	0.0030	1031
$\lambda = 1300 \text{ nm}$	2.00	0.0040	1031
$n_0 = 3.35$	1.00	0.0013	1546
$l = 300 \mu\text{m}$	1.50	0.0020	1546
$\lambda = 1300 \text{ nm}$	2.00	0.0027	1546
$n_0 = 1.50$	1.00	0.0013	692
$l = 300 \mu\text{m}$	1.50	0.0020	692
$\lambda = 1300 \text{ nm}$	2.00	0.0027	692
$n_0 = 3.35$	1.00	0.0016	1297
$l = 300 \mu\text{m}$	1.50	0.0024	1297
$\lambda = 1550 \text{ nm}$	2.00	0.0032	1297

Taking $n = n_0 \pm (\Delta n/2)$ for n_1 and n_2 , the indexes of alternate layers, the length of each quarter-wave layer is calculated using the Bragg condition:

$$l_i = \frac{\lambda_0}{4n_i} \tag{E4-25}$$

Figure 4-9 shows the S_{11} magnitude plots produced using the model with the twelve configurations tabulated above. Qualitatively the plots appear convincingly similar to sub-threshold DFB emission spectra.

As expected it is seen that if the length of the grating is increased the width of the reflectivity peak is reduced – more periods mean that away from the Bragg condition the reflected waves begin to interfere destructively sooner. In the silica glass case ($n_0=1.5$) the stop band is broader because each period is longer so there are fewer periods. As κl is increased peak reflectance

also increases, quite reasonably. In these low-contrast gratings the field intensity does not change quickly as it penetrates the structure, so with two refractive-index interfaces per period one would expect the peak reflectivity to approach the product $2Nr$, especially for short gratings. Reflectivity r is given in (E4-1) and for the 200 μm , 1031-period, $\kappa l=1.0$ GaAs case in **Figure 4-9** below (top left) is $\pm.298 \times 10^{-3}$, giving $2Nr = 0.62$, a little more than what the model predicts. The discrepancy is due to the length of the grating which is sufficient that later periods see a significantly weaker field than early ones. As the number of periods N and coupling coefficient κ increase such an estimate tends to overshoot more, but it does offer some extra confirmation of the model.

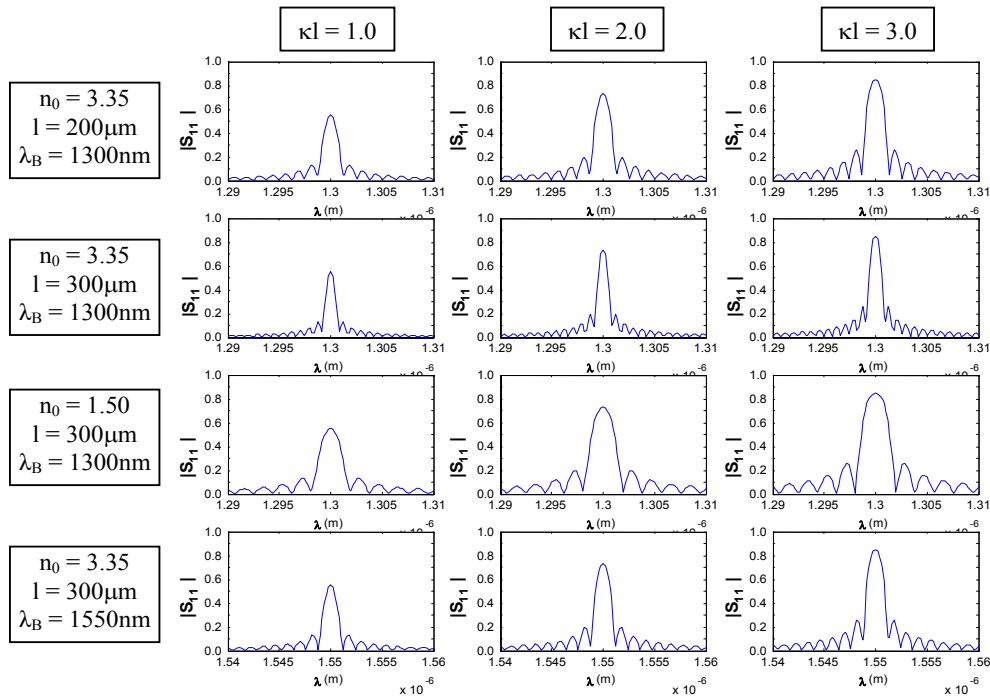


Figure 4-9 Reflectance r spectra produced by the TMM model using the DFB configurations in Table 1-4

The four rows in the figure correspond to four grating configurations, and the three columns represent increasing values of κl .

4.5.4 Loss in Deep Bragg Gratings

Several studies have shown that in deep-etch DBRs the main form of loss is due to diffraction of the propagating mode in the trenches, so that only a fraction of the light launched across the gap is coupled into the waveguide on the opposite side.

The size of this loss depends upon the size of the propagating mode, its wavelength, the refractive index contrast at the waveguide-airgap interface, the number of air gaps and the length of the air gaps.

The mode size may be determined by relatively simple electromagnetic simulation of the laser structure or in terms of the waveguide dimension and the proportion of mode energy contained within it, known as the *confinement factor* Γ . This is derived by Botez [5] as:

$$\Gamma = \frac{2v^2}{1 + 2v^2} \tag{E4-26}$$

where v is ‘normalised frequency’:

$$v = \frac{\pi d}{\lambda} \sqrt{n_{active}^2 - n_{passive}^2} \tag{E4-27}$$

where d is the thickness of the active region (**Figure 4-10**).

It is worth noting in passing that in bulk active regions, what has been referred to previously as material gain is in fact a net gain g_{net} dependent on the confinement factor, where

$$g_{net} = \Gamma \cdot g_{active} \tag{E4-28}$$

The inclusion of quantum wells further complicates this relationship.

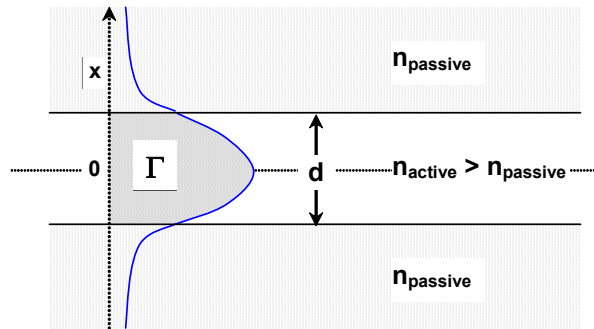


Figure 4-10 Schematic energy distribution of the TE_0 mode propagating inside a laser cavity of thickness d .

The curve is approximately Gaussian.

Given the mode confinement factor, the width of the laser cavity and that the TE_0 mode energy distribution across the laser cavity is approximately Gaussian it is possible to obtain an estimate of the mode size for use in diffraction loss calculations. The Gaussian curve is given by

$$F(x) = \frac{1}{\sigma_x \sqrt{2\pi}} \exp\left(-\frac{(x - \mu_x)^2}{2\sigma_x^2}\right) \tag{E4-29}$$

where $F(x)$ is the mode power density with distance x from the cavity axis, μ_x is the mean of the distribution (zero in this case) and σ_x is a measure of the width of the curve which in a

statistical context would be the standard deviation of the sample. The term to the left of the exponent is to normalise the area under the curve to unity. (E4-29) is plotted in **Figure 4-11**.

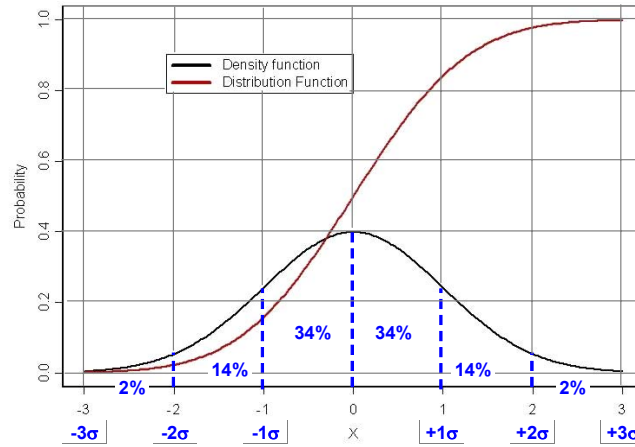


Figure 4-11 Standard Gaussian (normal) distribution with mean 0, variance 1, and the cumulative integral beneath it.

First we must recognise that

$$\frac{\Gamma}{2} + \frac{1}{2} = \Phi(z) \tag{E4-30}$$

where $\Phi(z)$ is the standard cumulative normal probability distribution, a parameter not available in simple analytic form but widely tabulated in statistics texts, where one can look up Φ and obtain the corresponding z . Because these tables are drawn up for standard Gaussians with zero mean and unity standard deviation z is normalised such that

$$z = \frac{x - \mu_x}{\sigma_x} \tag{E4-31}$$

$$\sigma_x = \frac{x - \mu_x}{z}$$

We have $z, \mu_x = 0$ and $x = d/2$ so this equation gives us σ_x . Recalling (E4-29), the maximum of the curve is at $x = 0$:

$$F(x = 0) = \frac{1}{\sigma_x \sqrt{2\pi}} \tag{E4-32}$$

Say we wish to know the width of the mode at some fraction B of its peak power, for instance its 3dB width, we can now rearrange (E4-29) to make x the subject, putting σ_x from (E4-31), $\mu_x = 0$ and $F(x) = B \cdot F(x=0)$:

$$x = \sqrt{2\sigma_x^2 \ln\left(\frac{1}{B}\right)} \tag{E4-33}$$

This can be used this as an estimate of field radius for use in Gaussian-beam expansion and coupling formulae, as used by Kasunic [6] (drawing heavily on Hall *et al* [7]), and the simpler approach of Baba *et al* [8] (drawing on Marcuse [9]).

In this second approach, the reflectivity R of the grating is reduced by a coupling efficiency factor η :

$$R_{eff} = R \cdot \eta \quad (\text{E4-34})$$

The efficiency η is calculated considering the grating as a whole and is given by

$$\eta = \frac{1}{\sqrt{1 + \left(\frac{L_{eff}}{\pi n w}\right)^2}} \quad (\text{E4-35})$$

Here n is the index of the DBR averaged over its length, w is the half-width (typically 0.4) of the mode in wavelengths at $1/e^2$ of its maximum power, and L_{eff} is in this case a parameter describing how far light penetrates into the DBR in wavelengths, given by the sum

$$L_{eff} = \frac{1}{n} \left[n_a l_a + \sum_{i=1}^N \left\{ (n_s l_s + n_a l_a) \left(\frac{n_a}{n_s}\right)^{2i} \right\} \right] \quad (\text{E4-36})$$

where a two-material deep grating is assumed with N periods of length $l_a + l_s$, and $n_a l_a$ & $n_s l_s$ are the refractive index and length of, respectively, air and semiconductor intervals in each period. Air gaps are presumed but any infill may be specified.

Since this method starts from R derived using TMM and multiplies it by a real number, it will not change the mirror phase. However, it must be noted that diffractive losses can in fact alter the mirror phase from the no-loss case, especially away from the Bragg wavelength, by changing the number of periods seen by reflected light. To account for this, loss must be taken into account when calculating R for individual periods of the DBR, using Kasunic's more complicated method or perhaps adapting the method above. The ultimate method is of course finite-difference time-domain (FDTD) electromagnetic modeling such as that carried out by Jambunathan *et al* [3]. FDTD is computationally demanding and slow but probably represents the 'gold standard'.

The results obtained by these workers (**Figure 4-12**) reveal the significance of diffractive losses in deep DBR structures.

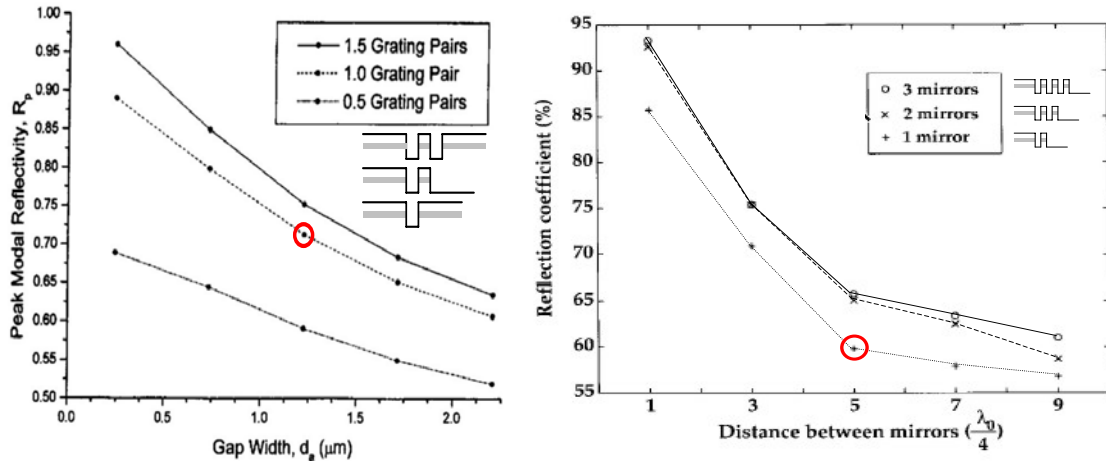


Figure 4-12 Power reflectivity R at 980nm for deep air-gap gratings.

The horizontal scales are nearly equal. The two directly comparable structures are circled. Note that reflectivity R obtained using Kasunic’s Gaussian beam model is slightly higher than Jambunathan’s, obtained using FDTD.

LEFT – R of 0.5, 1 and 1.5 quarter-wave grating periods vs. air-gap length, including diffraction losses, modelled using Gaussian beam optics [6].

RIGHT – R of 1, 2 and 3 380nm thick mirrors vs. length of air gaps between them, modelled using FDTD method [3].

Key points to note are the rapid saturation of mirror reflectivity with increasing number of periods, and the convergence of reflectivity toward the single facet case as air gap increases. Jambunathan also produced example plots of reflectivity spectra of different grating structures, with results from TMM (lossless) also plotted for comparison (**Figure 4-13**).

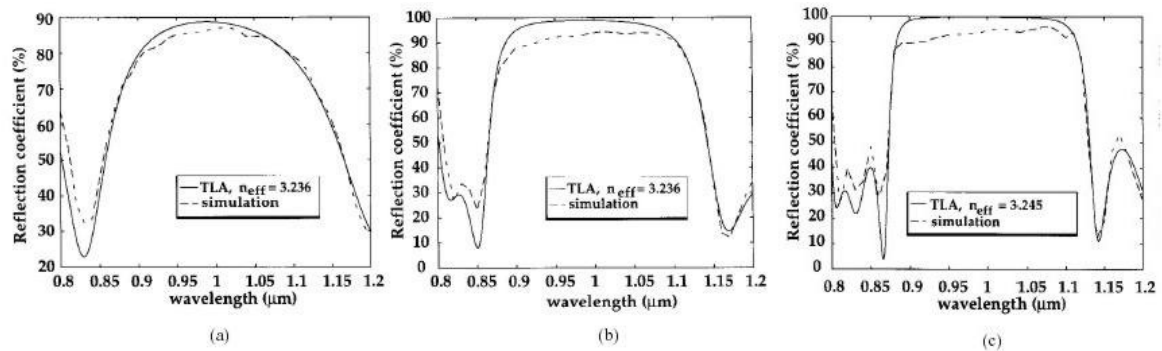


Figure 4-13 Reflectivity vs. wavelength, for 980nm Bragg condition grating with 380nm mirrors separated by deeply etched $\lambda/4$ air gaps, with one, two and three mirrors, from left to right.

Modelled using FDTD method (dotted line) and TMM (solid line) [3].

Figure 4-13 shows that increasing N from 1 to 3 sharpens up the Bragg peak while predicted R at the 980nm Bragg wavelength remains constant. Note that the FDTD data agrees well with TMM in wavelength, but less well in reflectivity. At short wavelengths in particular, diffractive losses are greater so fewer reflections contribute to destructive interference at the edge of the Bragg peaks, which become shallower as a result. Keeping the number of mirrors constant at 3

and increasing the air gap in half-wavelength steps shows how losses increase radically with increasing air gap width (**Figure 4-14**):

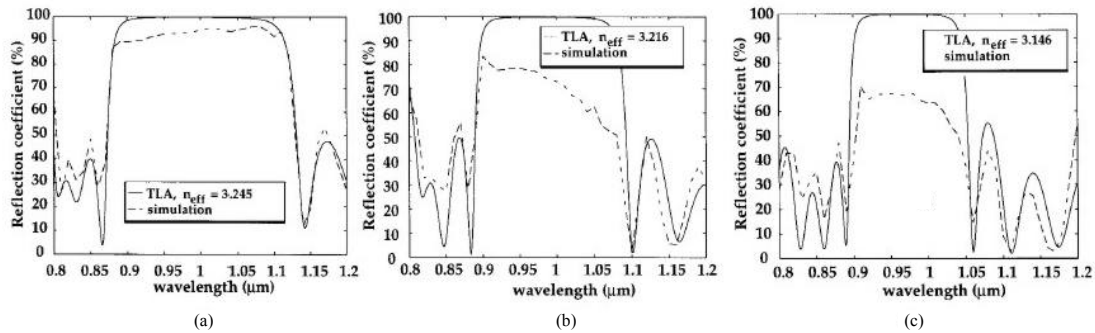


Figure 4-14 Reflectivity vs. wavelength, for 980nm Bragg condition grating with three 380nm mirrors separated by deeply etched $C\lambda/4$ air gaps, where $C=1, 3, 5$ from left to right.

Modelled using FDTD method (dotted line) and TMM (solid line) [3].

Jambunathan makes a further demonstration showing the influence of competing effects on diffraction losses. Taking three 380nm mirrors with $n=3.45$ and fixing the phase length of a period at 10.5 wavelengths, the refractive index of the material in the troughs is varied. As index increases, the index contrast decreases so classical plane reflectivity is reduced. Simultaneously, the lower contrast reduces the diffraction of the mode and the mirrors also move closer together optically, both of which cut diffraction loss and so increase effective reflectivity. **Figure 4-15** shows how these effects nearly balance each other up to a dielectric index of ~ 2.3 . It may be concluded that infilling trenches with silica ($n=1.6$) or BCB ($n=1.52$) for drift control will not much affect reflectivity.

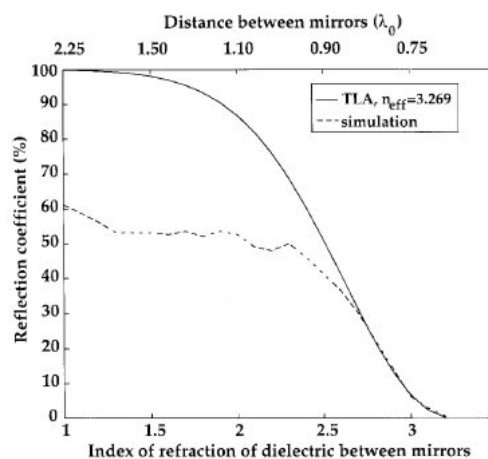
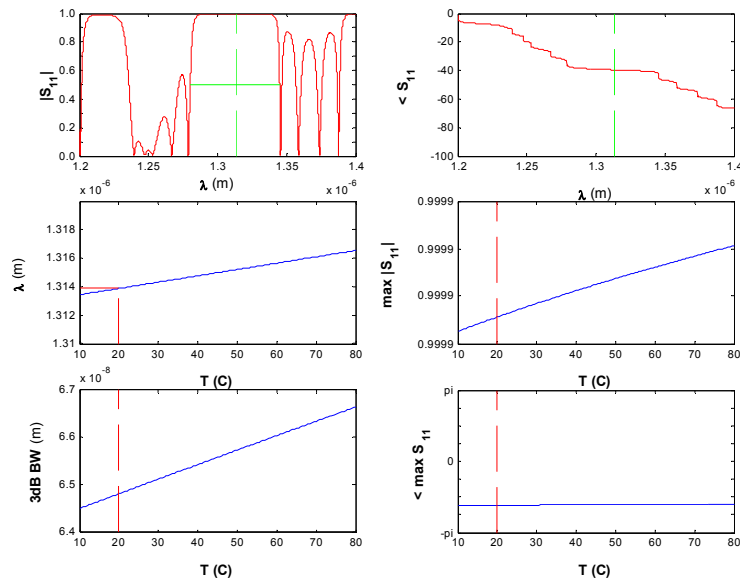


Figure 4-15 Reflectivity vs. infill material refractive index, for 980nm wavelength, with three 380nm thick mirrors separated by deeply etched $9\lambda/4$ air gaps.

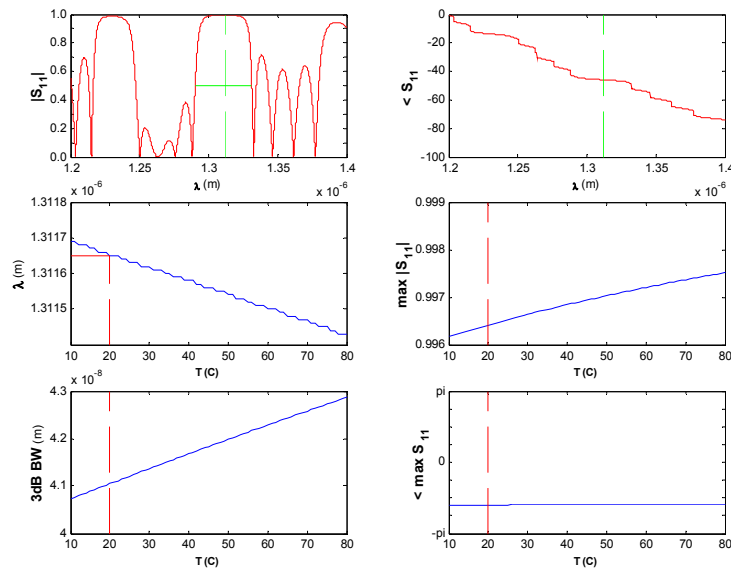
Modelled using FDTD method (dotted line) and TMM (solid line) [3].

4.5.5 Application to Athermal Mirror Test Device

Chapter 3 described a prototype athermal device utilising a zero-drift Bragg grating constructed by infilling deeply-etched air gaps with polymer material possessing negative thermo-optic coefficient. Despite implementing an athermal grating only a 10% reduction in emission wavelength drift-rate was observed between etching the trenches and filling them with the optical polymer. The TMM model was used to attempt an explanation.



(a) without polymer infill



(b) with polymer infill

Figure 4-16 Reflection spectra and temperature-dependence data for air-gap grating of 16th order and 1310nm reflection peak designed to be athermalised by infilling with BCB polymer

(a) without polymer infill, drift is 0.044nm/°C

(b) with polymer infill, drift is -0.0036nm/°C

Before the polymer infill the grating might not be expected to work – the reflection spectrum would change and the grating would not be athermalised. **Figure 4-16a** shows the modelled reflection spectrum for this air-gap grating, with a reflection peak only slightly displaced. Its drift rate is a factor of 12 greater than when the polymer is used, so the result of observed 10% reduction in drift rate of the device lasing mode therefore can not be attributed solely to the reflection-peak drift rate. If the drift of the Bragg peak by itself determined the mode drift rate, a much greater reduction would in this case be observed. Another factor must contribute to the rate of drift of modes in this device.

-
- [1] Babic, D.I. and Corzine, S.W.: ‘Analytic expressions for the reflection delay, penetration depth, and absorptance of quarter-wave dielectric mirrors’, *IEEE Journal of Quantum Electronics*, 1992, **28**, (2), pp.514-524
 - [2] Coldren, L.A. and Corzine, S.W.: *Diode Lasers and Photonic Integrated Circuits*, 2nd ed., 1995, ch.3, Wiley & Sons Ltd, London
 - [3] Jambunathan, R. and Singh, J.: ‘Design studies for distributed Bragg reflectors for short-cavity edge-emitting lasers’, *IEEE Journal of Quantum Electronics*, 1997, **33**, (7), pp.1180-1189
 - [4] Gowar, J.: *Optical Communication Systems*, 2nd ed., 1993, Prentice Hall, Hemel Hempstead
 - [5] Botez, D.: ‘Analytical approximation of the radiation confinement factor for the TE₀ mode of a double heterojunction laser’, *IEEE Journal of Quantum Electronics*, 1978, **QE-14**, pp.230-232
 - [6] Kasunic, K.J.: ‘Design equations for the reflectivity of deep-etch distributed Bragg reflector gratings’, *Journal of Lightwave Technology*, 2000, **18**, (3), pp.425-429
 - [7] Hall, D.G., Rice, R.R. and Zino, J.D.: ‘Simple gaussian-beam model for GaAlAs double-heterostructure laser-diode-to-diffused-waveguide coupling calculations’, *Optics Letters*, 1979, **4**, (9), pp.292-294
 - [8] Baba, T., Hamasaki, M., Watanabe, N., Kaewplung, P., Matsutani, A., Mukaiharu, T., Koyama, F. and Iga, K.: ‘A novel short-cavity laser with deep-grating distributed Bragg reflectors’, *Japanese Journal of Applied Physics Part 1 - Regular Papers Short Notes & Review Papers*, 1996, **35**, (2B), pp.1390-4
 - [9] Marcuse, D; *Light Transmission Optics*, Van Nostrand Reinhold (USA) 1982

Chapter 5

Cavity Mode Location Model

A second model based on the gain and resonance conditions for lasing is developed to study the drift of resonant modes within DBR cavities. It indicates that the high contrast of organic-inorganic athermal gratings renders them insufficiently selective to greatly influence lasing wavelength.

5.1 Motivation

The emission wavelength of a semiconductor laser may depend on combination of cavity length and gain spectrum as well as complex grating reflectivity. How these combine to select lasing modes and influence mode drift with temperature is determined by the exact configuration of the device.

In the previous chapter it has been shown that although the athermalised mirrors of the prototype low-drift device were athermally designed the 3dB width of their reflection peaks was approximately 300nm, allowing considerable scope for mode drift within the stationary reflection peak. Moreover, the wavelength of the peak was not as intended. It will be recalled however that some reduction of the wavelength drift rate was nevertheless observed.

In order to investigate this behaviour and identify the drift-reduction mechanism it was necessary to develop a computational method of locating and tracking resonant modes, in particular the lasing wavelength, in conjunction with data from the TMM reflector model.

5.2 Semiconductor Laser Active Structures

In a simple homojunction LED the n and p -doped regions are made of the same semiconductor and there is nothing to confine the light generated. This is not efficient and usually in laser diodes a double-heterojunction structure is used (**Figure 5-1**). The different bandgaps of the materials confine recombination to the active central region whose higher refractive index also helps confine light, forming an optic waveguide.

Guiding in the plane of the active region is implemented by self-focussing of laser filaments, by stripe-geometry current injection using the electrical contact or a structured insulating layer, by fabricating a long thin active volume using etching and epitaxial regrowth, or a combination of these.

Heterostructures are generally created by epitaxial crystal growth. Combined with lateral current confinement and wave guiding they effectively minimise active volume. Doing so increases current density and photon density, reducing the lasing threshold. Higher modulation rates, better thermal properties and improved mode structure are other benefits.

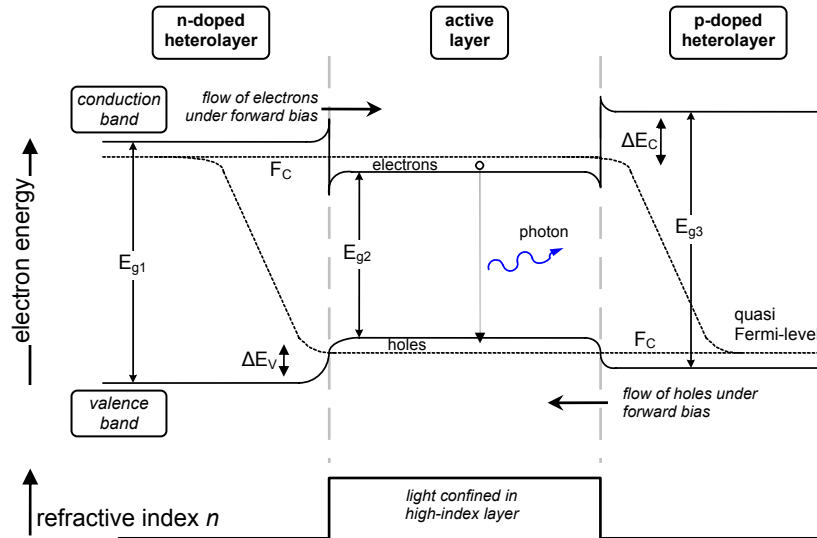


Figure 5-1 Band diagram of a double heterostructure under forward bias.

The quasi-Fermi levels serve as a reference on which to base the statistical behaviour of the carriers.

Heterostructures are often combined with *quantum wells*. Quantum wells (QWs) are very thin lattice-matched epitaxial layers doped such as to give deep potential wells in which electrons are confined. Electron energy is quantised in the vertical direction and the difference between quantum well energy levels can be used for the laser action instead of the bandgap, granting the ability to tune the output wavelength by altering the thickness of the well. Lasing action will occur between the lowest allowed quantum well state in the conduction band and the highest allowed quantum well state in the valence band, leading to some shortening of the wavelength. The efficiency of a quantum well laser is greater than that of a bulk laser due to the higher carrier density. The rate of change of optical gain coefficient with carrier density is also increased, narrowing the spontaneous emission spectrum and reducing chirp and random intensity noise (RIN).

More recently, *quantum dots* (QDs) have been a subject of intense research and are beginning to supplant quantum wells. Of the order of an electron's de Broglie wavelength in dimension (a few nanometres in semiconductors), these structures form potential wells which confine electrons and holes in three dimensions. Electrons in the quantum dot have quantised, discrete energy levels which can be controlled by changing the size and shape of the quantum dot and the depth of the potential. The density of states in a QD is sharper than for quantum wells.

5.3 Wavelength Drift in Laser Diode Cavities

All wavelength-selective phenomena in laser diodes influence the lasing wavelength, and all may depend upon temperature. The three main effects are gain-peak drift, mirror reflectivity drift and cavity expansion. The first may be explained in terms of the band gap, which arises from the quantum mechanics of electrons in the semiconductor crystal, the second and third in terms of refractive index changes and thermal expansion.

Given effective phase index n_{def} at a given wavelength and temperature (T_{def}) the effective index n_{eff} at any other temperature is given by:

$$n_{eff}(T)_{\lambda} = n_{def} + \frac{dn_{eff}}{dT} \cdot \Delta T \quad (\text{E5-1})$$

where $\Delta T = T - T_{def}$.

Similarly for cavity expansion: given a cavity has length L_{def} at a given temperature T_{def} the cavity's length at any other temperature is given by:

$$\begin{aligned} L(T) &= L_{def} + \frac{dL}{dT} \cdot \Delta T \\ &= L_{def} + L_{def} \cdot CTE \cdot \Delta T \\ &= L_{def} \cdot (1 + CTE \cdot \Delta T) \end{aligned} \quad (\text{E5-2})$$

where CTE is the coefficient of linear thermal expansion, 5.4×10^{-6} for GaAs at 300K [1]. Note that

$$\frac{dL}{dT} = L_{def} \cdot CTE \quad (\text{E5-3})$$

Table 5-1 gives these properties for a selection of semiconductors.

Table 5-1 Experimental values for the energy gap, its temperature coefficient, the refractive index temperature dependence, and linear thermal expansion coefficient for some semiconductors. From Oe et al [2].

Material	E_g (eV)	dE_g/dT ($\times 10^{-4}$ eV K $^{-1}$)	α_n ($\times 10^{-5}$ K $^{-1}$)	α_L ($\times 10^{-6}$ K $^{-1}$)	Reference
Ge	0.67	-3.7	6.9	5.5	a)
Si	1.1	-2.8	4.0	2.4	a)
AlAs	2.15	-4.0	4.6	5.0	b)
AlP	2.41	-3.7	3.6		b)
GaAs	1.42	-3.9	4.5	5.5	c)
GaSb	0.75	-3.7	8.2		c)
InP	1.35	-2.9	2.7	4.5	c)
InAs	0.36	-3.0		4.5	c)
InSb	0.17	-2.8	6.9	5.0	c)
CdTe	1.6 (1.7 K)	-4.1		5.5	d)
PbSe	0.28	5.1	-21		d)
HgTe	-0.3 ⁰⁰ (1.7 K)	5.0		4	d)

- a) Cardona, M., Paul, W. and Brooks, H., J. Phys. Chem. Solids 8, 204 (1959)
- b) Grimmeiss, H. G. and Monemar, B., Phys. Status Solidi A 5, 109 (1971)
- c) Landolt-Bornstein, Numerical Data and Functional Relationship in Science and Technology, (Springer, Berlin, 1982), Vol. 17/a, 17/f, 22/a
- d) Applied Solid State Science, Vol. 4, (Academic Press, New York, 1974)

These mechanisms are discussed in more detail in the following sections.

5.4 Resonance in Fabry-Perot Cavities

5.4.1 Resonance Condition

In laser cavities, as for any other kind of cavity, standing waves can form at wavelengths at which a whole number of half-wavelengths will fit inside (**Figure 5-2**). These wavelengths are the resonant modes of the laser. They are easily observable as the peaks under the output envelope of a Fabry-Perot laser diode. Expressed mathematically, the m^{th} resonance requires

$$L = m \frac{\lambda_{\text{medium}}}{2} = m \frac{\lambda}{2n} \tag{E5-4}$$

where L is the length of the cavity, m is the number of half-wavelengths, λ_{medium} is the wavelength in the medium, n is the refractive index in the cavity and λ is the wavelength in free space.

The symbol λ is used to indicate free-space wavelengths throughout this investigation. Where it is necessary to refer to the wavelength in a medium this is explicitly indicated.

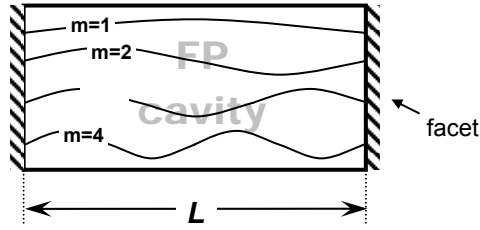


Figure 5-2 FP cavity with the first four possible resonances

The cavity has physical length L . Resonances have whole m , but number of half-wavelengths m can also be used as a measure of 'optical' length.

5.4.2 Mode Spacing

Starting from the resonance condition the spacing of adjacent modes can be worked out as follows. For mode m :

$$\lambda_m = \frac{2Ln}{m} \quad (\text{E5-5})$$

In terms of frequency ν :

$$\nu_m = \frac{mc}{2nL} \quad (\text{E5-6})$$

For the adjacent mode $m+1$:

$$\nu_{m+1} = \frac{(m+1)c}{2nL} \quad (\text{E5-7})$$

Taking the difference in resonant frequencies

$$\nu_{m+1} - \nu_m = \Delta\nu = \frac{mc}{2nL} \quad (\text{E5-8})$$

Now, from first principals:

$$\begin{aligned} \nu &= \frac{c}{\lambda} \\ \frac{d\nu}{d\lambda} &= -\frac{c^2}{\lambda^2} = \frac{\Delta\nu}{\Delta\lambda} \\ |\Delta\nu| &= \left| c \frac{\Delta\lambda}{\lambda^2} \right| \end{aligned} \quad (\text{E5-9})$$

Substituting (E5-8) in for $\Delta\nu$ and rearranging gives us the mode spacing $\Delta\lambda$:

$$\Delta\lambda = \frac{\lambda^2}{2nL} \tag{E5-10}$$

Edge-emitting laser cavities tend to be long in terms of wavelengths and the modes are very closely spaced, typically being of the order of nanometers apart. This is narrow compared to the gain spectrum and this is why FP lasers emit many modes simultaneously. Where just one mode is isolated using a grating as a wavelength-selective mirror the modes tend to drift at a different rate to the reflection peak, leading to abrupt hops in emission wavelength from one mode to the next. Both of these effects can be problematic in optical communications systems. In contrast, VCSELs have cavities only a few wavelengths long and their mode spacing can be hundreds of nanometers. This is wide compared to the width of the gain region and guarantees single-modedness. In any case, mode spacing plays an important role in selecting the lasing mode from amongst those available.

Measuring the mode spacing is also one way of discovering the effective group index.

5.4.3 Cavity Phase Length

An analysis of optical cavity length vs. temperature and wavelength provides means of verifying the models, and will also be useful in calculating mode drift rates later.

To begin, take cavity length L which is a function of temperature T only.

$$L(T) = L|_{T_{def}} + L|_{T_{def}} CTE [T - T_{def}] \tag{E5-11}$$

where T_{def} is some arbitrary, nearby temperature at which L has been measured.

We assume that L is a linear function of T , i.e. that CTE is a constant and not a function of T itself. This is a reasonable assumption in the temperature range of interest, 0-100°C, but in practice T_{def} should be not too far removed from T , preferably in the middle of the range of T , and CTE should also be measured at T_{def} .

Secondly, take cavity refractive index n , which we will assume is a linear function of both temperature and wavelength (**Figure 5-3**). This is a reasonable assumption for dielectric material, but less so for semiconductors near the band-gap energy, where n is certainly a higher-order function of T . However, an approximation is still possible.

Define $n(T)$ at a given wavelength using the thermo-optic coefficient dn/dT :

$$n(T)|_{\lambda} = n|_{T_{def}} + \frac{dn}{dT} [T - T_{def}] \tag{E5-12}$$

and $n(\lambda)$ at a given temperature:

$$n(\lambda)|_T = n|_{\lambda_{def}} + \frac{dn}{d\lambda} [\lambda - \lambda_{def}] \quad (\text{E5-13})$$

where λ_{def} , like T_{def} , is some arbitrary wavelength at which n is known. It too is best located near the middle of the range, of wavelengths in this case, to minimise any deviation from the linear approximation.

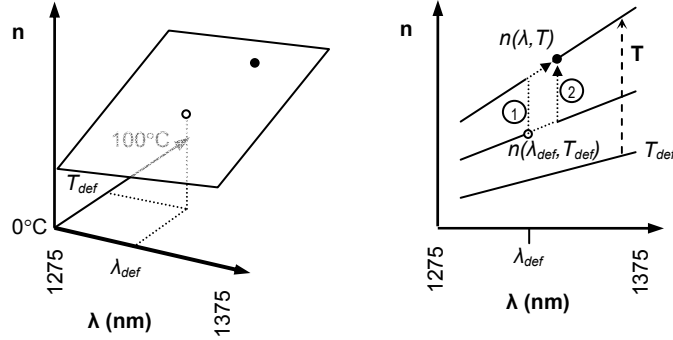


Figure 5-3 Cavity refractive index vs. T and λ (left) and vs. λ only, for several T (right)

n is assumed linear in both wavelength and temperature in the ranges indicated, thus a plot if it gives a plane. Also indicated are the ideal locations of T_{def} and λ_{def} .

Figure 5-3 shows how from n at λ_{def} and T_{def} it is possible to find n at some other wavelength λ and temperature T by two routes: that marked as route one requiring knowledge of dn/dT at λ_{def} and of $dn/d\lambda$ at T , that marked as route two requiring knowledge of $dn/d\lambda$ at T_{def} and of dn/dT at λ .

Route 1:

$$\begin{aligned} n(\lambda, T) &= n|_{\lambda_{def}, T_{def}} + \frac{dn}{dT}\bigg|_{\lambda_{def}} [T - T_{def}] + \frac{dn}{d\lambda}\bigg|_T [\lambda - \lambda_{def}] \\ &= n|_{\lambda_{def}, T} + \frac{dn}{d\lambda}\bigg|_T [\lambda - \lambda_{def}] \end{aligned} \quad (\text{E5-14})$$

Route 2:

$$\begin{aligned} n(\lambda, T) &= n|_{\lambda_{def}, T_{def}} + \frac{dn}{d\lambda}\bigg|_{T_{def}} [\lambda - \lambda_{def}] + \frac{dn}{dT}\bigg|_{\lambda} [T - T_{def}] \\ &= n|_{\lambda_{def}, T} + \frac{dn}{dT}\bigg|_{\lambda} [T - T_{def}] \end{aligned} \quad (\text{E5-15})$$

Given these expressions we can proceed with an analysis of the phase-length of the cavity. Rearranging the resonance condition (E5-4) and making the functional dependencies explicit:

$$m(\lambda, T) = \frac{2 n(\lambda, T) L(T)}{\lambda} \quad (\text{E5-16})$$

By allowing it to vary continuously m can be used as a measure of optical length, rather than just a means of labelling resonances. By multiplying the number of half-wavelengths m by π we obtain the phase-length of the cavity.

Differentiating with respect to λ shows how this *cavity phase length*, m , varies with wavelength:

$$\begin{aligned} \frac{dm}{d\lambda}(\lambda, T) &= 2L|_T \frac{d}{d\lambda} \left[\frac{n(\lambda, T)}{\lambda} \right] \\ &= 2L|_T \left[\frac{1}{\lambda} \frac{dn}{d\lambda} \Big|_T - \frac{1}{\lambda^2} n|_{\lambda, T} \right] \\ &= -\frac{2}{\lambda^2} L|_T \left[n|_{\lambda_{def}, T_{def}} + \frac{dn}{dT} \Big|_{\lambda_{def}} [T - T_{def}] + \lambda_{def} \frac{dn}{d\lambda} \Big|_T \right] \\ &= -\frac{2}{\lambda^2} L|_{T_{def}} \left\{ 1 + CTE [T - T_{def}] \right\} \\ &\quad \cdot \left[n|_{\lambda_{def}, T_{def}} + \frac{dn}{dT} \Big|_{\lambda_{def}} [T - T_{def}] + \lambda_{def} \frac{dn}{d\lambda} \Big|_T \right] \\ &= -\frac{2}{\lambda^2} L|_{T_{def}} \left\{ 1 + CTE [T - T_{def}] \right\} \\ &\quad \cdot \left[n|_{\lambda_{def}, T} + \lambda_{def} \frac{dn}{d\lambda} \Big|_T \right] \end{aligned} \quad (\text{E5-17})$$

Note that here $\partial n(\lambda, T)/\partial \lambda$ has been written simply $dn/d\lambda|_T$. In the third line the long form of route 1 (E5-14) has been substituted in for $n|_{\lambda, T}$ and the result simplified. The route 1 expression is used because some $dn/d\lambda|_T$ terms cancel. In the third line (E5-11) is substituted in for $L|_T$. The final step is the same step that gives the short form of route 1.

Finally, differentiate with respect to λ to show how m varies with temperature:

$$\begin{aligned}
 \frac{dm}{dT}(\lambda, T) &= \frac{2}{\lambda} \frac{d}{dT} [n(\lambda, T) L(T)] \\
 &= \frac{2}{\lambda} \left[\left. \frac{dn}{dT} \right|_{\lambda} L|_T + n|_{\lambda, T} \left. \frac{dL}{dT} \right|_{\lambda} CTE \right] \\
 &= \frac{2L|_{T_{def}}}{\lambda} \left[\left. \frac{dn}{dT} \right|_{\lambda} + 2 \left. \frac{dn}{dT} \right|_{\lambda} CTE [T - T_{def}] \right. \\
 &\quad \left. + n|_{\lambda_{def}, T_{def}} CTE + \left. \frac{dn}{d\lambda} \right|_{T_{def}} [\lambda - \lambda_{def}] CTE \right] \\
 &= \frac{2L|_{T_{def}}}{\lambda} \left[\left. \frac{dn}{dT} \right|_{\lambda} + 2 \left. \frac{dn}{dT} \right|_{\lambda} CTE [T - T_{def}] + n|_{\lambda, T_{def}} CTE \right]
 \end{aligned} \tag{E5-18}$$

Note that here $\partial n(\lambda, T)/\partial T$ has been written simply $dn/dT|_{\lambda}$. In the second line $L|_{T_{def}} CTE$ has been substituted in for dL/dT (see (E5-11)). In the third line (E5-11) has been substituted in for $L|_T$ and the long form of route 2 (E5-15) substituted in for $n|_{\lambda, T}$, followed by some simplification. The route 2 expression is used because some $dn/dT|_{\lambda}$ terms cancel. The final step is the same step that gives the short form there.

If we evaluate (E5-18) with representative values ($n_{1300\text{nm}, 20^\circ\text{C}} = 3.2$, $dn/dT_{1300\text{nm}} = 2.02 \times 10^{-4}/^\circ\text{C}$, $T - T_{def} = 50^\circ\text{C}$ (i.e. worst-case), $CTE = 5.4 \times 10^{-6}/^\circ\text{C}$) we find that the first term, $dn/dT|_{\lambda}$, makes by far the greatest contribution. The second and third terms contribute approximately 0.1% and 10% respectively. We can therefore approximate to

$$\frac{dm}{dT}(\lambda, T) \approx \frac{2}{\lambda} L|_{T_{def}} \left. \frac{dn}{dT} \right|_{\lambda} \tag{E5-19}$$

5.4.4 Temperature Sensitivity

Unlike the reflection spectrum of reflection gratings the wavelengths of resonant modes are available analytically. Continuing the above analysis, a simple algebraic trick will give a predicted modal drift rate for FP cavities:

$$\frac{d\lambda_m}{dT} = - \frac{dm}{dT} \frac{d\lambda}{dm} = - \frac{dm}{dT} \left(\frac{dm}{d\lambda} \right)^{-1} \tag{E5-20}$$

Substituting in (E5-17) and (E5-18):

$$\frac{d\lambda_m}{dT} = \lambda \frac{\left[\frac{dn}{dT} \Big|_{\lambda} + 2 \frac{dn}{dT} \Big|_{\lambda} CTE [T - T_{def}] + n|_{\lambda_{def}, T_{def}} CTE + \frac{dn}{d\lambda} \Big|_{T_{def}} [\lambda - \lambda_{def}] CTE \right]}{\left\{ 1 + CTE [T - T_{def}] \right\} \cdot \left[n|_{\lambda_{def}, T_{def}} + \frac{dn}{dT} \Big|_{\lambda_{def}} [T - T_{def}] + \lambda_{def} \frac{dn}{d\lambda} \Big|_T \right]} \quad (\text{E5-21})$$

We can see that mode drift in an FP cavity is independent of cavity length.

At $T=T_{def}$ and $\lambda=\lambda_{def}$ this reduces to

$$\frac{d\lambda_m}{dT} = \frac{\lambda \left(n|_{\lambda_{def}, T_{def}} CTE + \frac{dn}{dT} \Big|_{\lambda} \right)}{n|_{\lambda_{def}, T_{def}} + \lambda_{def} \frac{dn}{d\lambda} \Big|_T} \quad (\text{E5-22})$$

If, taking representative values for InP devices, there is a mode at $\lambda = 1320\text{nm}$, $n|_{\lambda_{def}, T_{def}} = 3.2$, $CTE = 5.4 \times 10^{-6}/^\circ\text{C}$, $dn/dT|_{1320\text{nm}} = 2.02 \times 10^{-4}/^\circ\text{C}$ and $dn/d\lambda|_{50^\circ\text{C}} = -1 \times 10^{-3}/\text{nm}$, then $d\lambda_m/dT = 0.09\text{nm}/^\circ\text{C}$, which is indeed consistent with the the range of drift rates commonly observed in InP-based devices.

5.5 Resonance in DBR Structures

5.5.1 Contribution of Reflector Phase

In a Fabry-Perot structure optical waves are internally reflected at both facets with no phase change. In DBR structures the reflections from either end of the cavity will, in general, be complex, i.e. exhibiting a phase change. How to include this in the resonance condition? If we express the resonance condition in terms of phase then it requires that there be a whole number of π of phase in the cavity:

$$m\pi = \beta L = \frac{2\pi}{\lambda_{medium}} L = \frac{2\pi}{\lambda} Ln \quad (\text{E5-23})$$

where β is the propagation constant of the wave, λ_{medium} is the wavelength in the medium, and the number of half-wavelengths m is constrained to whole numbers. It is then easy to include the reflection phases as $\angle S_{11}$ of each reflector.

$$\begin{aligned} m\pi &= \angle S_{11_1} + \angle S_{11_2} + \beta L \\ &= \angle S_{11_1} + \angle S_{11_2} + \frac{2\pi}{\lambda} Ln \end{aligned} \quad (\text{E5-24})$$

In general, reflection phase is not available analytically. However, it is available numerically and the TMM model can be invoked to supply it. It is for this purpose that the ‘single-shot’ mode exists in the TMM model.

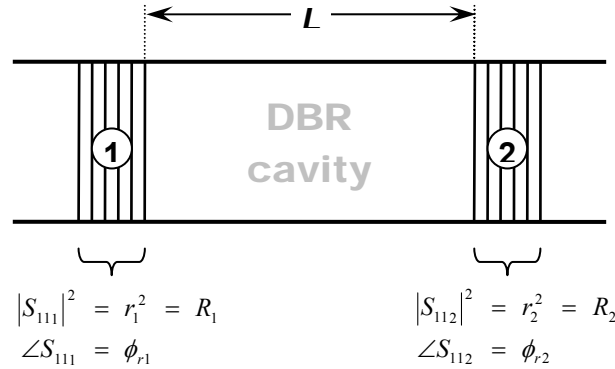


Figure 5-4 DBR cavity with complex reflectors

DBR cavity length is usually measured between the beginnings of the gratings. Reflectivity and reflection phase are also usually measured from the starts of the gratings, although in theory the reference plane could be placed anywhere in the waveguide.

5.5.2 The Phase Line

The two concepts of m – as resonance order and as optical length – can be combined in a single graph by plotting m against wavelength. Where the continuous line crosses integer m there exists a resonant mode. Because m is equal to phase divided by π , we call this the *phase line* (Figure 5-5).

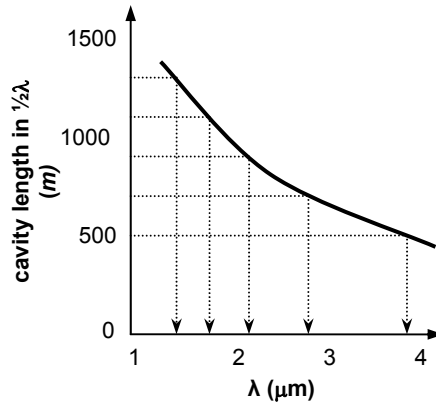


Figure 5-5 Illustrative phase line plot for a 250µm n=3.2 FP cavity

The FP resonances are located at integer m – starting from $m=500$ every 200th resonance is marked. As indicated by (E5-10) their spacing increases with wavelength, for a given cavity length. As indicated by (E5-17), optical cavity length in half-wavelengths m is proportional to $1/\lambda^2$

5.5.3 Temperature Sensitivity

With the addition of DBR reflectors a number of new factors are brought into play concerning temperature-dependence of the mode positions. As well as the cavity phase there is

the phase contribution of the reflectors, which changes across the reflection spectrum and drifts, more or less, with it.

If the phase contribution from each reflector is in the range $\pm\pi$ across the reflection peak this is equivalent to $\pm m$ on the phase line. This will not be a significant contribution to overall cavity optical length except for very short cavities of the order of a few wavelengths long. This is longer than most edge-emitting configurations but quite usual in VCSELs. However, it may not be necessary for the grating contribution to be so large in order to influence mode drift rate, which may occur due to small phase changes even where total phase length is large.

5.6 Mode Selection

5.6.1 The Gain Condition

Optical gain is present in a semiconductor when photon energy exceeds the band-gap but is less than the separation of the Fermi levels across the heterojunction, a situation which requires an inversion of the normal densities electrons and holes above and below the band gap - *population inversion*. When a laser diode is forward-biased the inverted carrier density increases, increasing gain, until some mode achieves the *gain condition* for lasing.

For lasing to occur, the round-trip optical gain experienced by the lasing filament inside the cavity, including losses at the end mirrors, must be equal to unity. It cannot be less than unity because the photon density would quickly fall, engendering less gain, so that lasing ceased. Neither can it exceed unity for long, because photon density quickly rises until the inverted carrier population is again depleted by stimulated emission at the same rate that it is replenished. Thus, under lasing conditions power input by drive current exactly equals optical and thermal power output, and increased drive current will simply lead to greater power output:

$$|S_{11}|_1 \cdot |S_{11}|_2 \cdot \exp\{2L(G - \alpha)\} = 1 \quad (\text{E5-25})$$

where $|S_{11}|_1$ and $|S_{11}|_2$ are the magnitudes of the complex electric field amplitude reflectivities of the cavity end mirrors, L is the length of the laser cavity, G is the optical gain per unit length of waveguide and α is the loss, similarly. $|S_{11}|^2$ would give the equivalent power reflectivities, and $\angle S_{11}$ would give the reflection phase.

Rearranging to isolate G and α , which are both functions of wavelength which peak around the band-gap energy but are not necessarily known:

$$(G - \alpha) = \frac{1}{2L} \ln \frac{1}{|S_{11}|_1 |S_{11}|_2} \quad (\text{E5-26})$$

Once a mode begins lasing, carrier density is clamped – any excess increases gain and is immediately converted to light. Thus, the first mode for which the gain condition is fulfilled will be the lasing mode. The only exception is when many modes experience near-identical gain simultaneously, such as may happen in long FP lasers.

5.6.2 Threshold Current

Threshold current I_{th} is the drive required to invert the carrier population in the diode and bring the carrier density and hence gain to a high enough level for the lasing condition to be met for some cavity mode (E5-25). I_{th} is increased by the existence of current leakage paths bypassing the p - n junction, and also by nonradiative recombination in the junction itself.

The rates of radiative and nonradiative spontaneous recombination increase with temperature, reducing the lifetime of carriers in the conduction band so more current is required to maintain carrier density. I_{th} can be shown to vary with temperature T as

$$I_{th}(T) = I_0 e^{\frac{T}{T_0}}, \quad (\text{E5-27})$$

where T_0 is a popular parameter for characterising devices, typically 150K for GaAs and 70K for InGaAs. High T_0 means less dependency on T . The increase in output power for a given increase in drive, the differential efficiency, also falls as temperature rises.

Threshold current density J_{th} is often a useful parameter for comparing different devices. J_{th} rises at short cavity lengths because of the increasing magnitude of the mirror losses relative to the gain. By using very strong mirrors this rise can be pushed to shorter cavity lengths.

Figure 5-6 shows how I_{th} and J_{th} typically vary with cavity length.

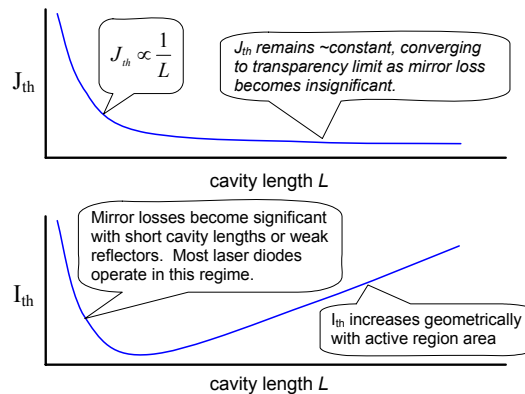


Figure 5-6 Schematic threshold current & current density vs. cavity length.

J_{th} rises at short cavity length L because of the large mirror losses.

5.6.3 Mode Selection

Depending on the device structure, any combination of the gain spectrum, the mirror reflectivity spectrum and the cavity length may dominate mode selection (see **Figure 1-5**).

The gain curve in semiconductors is wide, because transitions occur between bands rather than discrete energy states. The exact form of the gain curve depends on the material properties and structural configuration of the laser – bulk material, quantum wells, quantum wires and quantum dots all behave differently. Although the gain curve must be given due consideration, in general the designer uses other means of selecting a single mode.

Two options exist: either decrease the cavity length, increasing the mode spacing so that fewer modes fall inside the gain spectrum, or design a reflector to preferentially reflect a particular mode, ensuring all other modes experience higher losses so that the selected one is the first to reach unity roundtrip gain. These requirements are translated into single-mode device designs in a number of different ways.

In DFBs the reflection grating is distributed along the length of the cavity and it is as though many tiny cavities each have a single mode, defined by the grating period. In other words the grating defines both the resonant mode and the reflectivity peak so that they are automatically aligned. The emission wavelength is independent of any other consideration of cavity length or gain envelope (**Figure 5-7**).

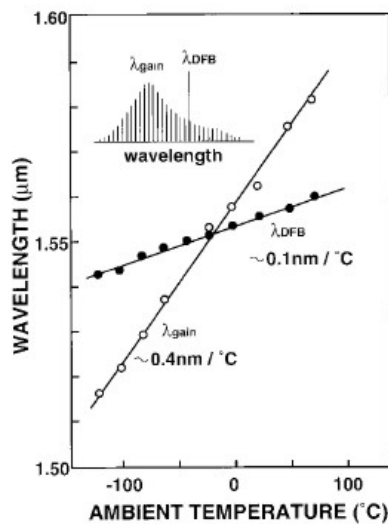


Figure 5-7 Drift with temperature of DFB lasing & gain peak wavelengths in a GaInAsP alloy system laser (Oe et al [2]).

The gain peak drifts at a different rate to the DFB wavelength, with consequences only for the threshold current.

In edge-emitting DBRs the end mirrors are used to select a mode. The desired mode and the reflector stop band may not drift at the same rate with temperature, in which case they may become de-aligned and another mode will rise to lase in place of the first.

In fact, it is often the case that a series of evenly-spaced modes will drift across a slower-moving reflection peak, each lasing while it crosses the peak. This results in a series of *mode hops* from long to short wavelength.

The gain spectrum also drifts with temperature due to bandgap renormalisation, typically moving to longer wavelengths at a rate of 0.5nm/°C. This is faster than the drift cavity resonances so mode hops are also seen in FP devices, this time from short to long wavelength.

The high-contrast reflector stacks of VCSELs have very wide reflectivity peaks, typically hundreds of nanometres. However, the cavity lengths are so short that the resonant modes are widely spaced relative to the DBR reflectivity peak, so that wavelength drift is largely that of the cavity resonances.

5.6.4 Least-Loss Mode

Where the gain-envelope is wide and slowly-varying over wavelength, compared to the reflection spectrum, its influence on mode selection is small compared to reflectivity. This is especially the case near the middle of the gain profile where desired output wavelengths are generally located. This is because the top of the gain curve may approximate flatness over narrow-enough wavelength ranges.

The lasing mode in such cases is selected by the reflectivity profile and the gain envelope can, on the whole, be neglected. Whichever mode experiences highest reflectivity, i.e. *least mirror loss*, can be assumed to require least gain to meet the round-trip condition, and therefore to be the lasing mode.

Although it would be preferable to include data on gain, for generality, the object of this investigation is the study of DBR emission-wavelength drift with temperature. The effect of the gain profile being negligible, rather than spend time implementing accurate gain curves for different material systems, device structures and drive currents it was decided to rely on this least-loss assumption.

A separate question is whether the least-loss mode will lase at all – the available gain is limited by thermal and other effects and must be sufficient for the least-loss mode to achieve the round-trip condition.

5.7 Mode-Locating Code

A Matlab function, `cavity_model`, was developed using the phase condition to locate modes in DBR structures and the gain condition to predict which will lase. $S_{11}(\lambda, T)$ for the gratings is not available as an analytic function modes have to be located numerically. The model places

mirrors on either side of a cavity, modelling the mirrors as complex reflectors using the TMM model described in Chapter 4. An approximation of a DFB can be attempted, although the TMM model will not account for active-grating phenomena and is intended for rectangular gratings. FP structures are handled as a special case of a DBR, in which facets replace gratings.

5.7.1 Overview

The user is required to construct a number of problem-definition matrices to be passed to the function when it is called. The temperature and wavelength ranges to be covered are formatted in one matrix. Another matrix contains a list of properties of the cavity. The function will also accept zero, one or two grating specifications, treating these cases, respectively, as facet-facet, facet-grating and grating-grating device configurations. Each dielectric-stack-definition matrix includes physical lengths, refractive indices, TOCs and initial and terminal interfaces. Each stack specification matrix is accompanied by a small vector specifying the number of periods and the temperature at which the given refractive indices are defined.

The function then begins looping through the specified temperatures, calculating the facet reflectivity at each, if appropriate. It is assumed that facet reflectivity is not wavelength-dependent.

At each temperature, the function steps through the specified wavelength range, calculating complex reflectivity for each reflector stack using the grating model in one-shot mode and checking to see if total cavity phase-length m has passed through an integer value. If so, the model uses a bisection method to go back and home in on a precise value for the mode wavelength before searching for the next mode.

By examining how $dm/d\lambda$ and Δm change with each bisection the model is able to discriminate between cases where m crosses an integer value smoothly and where it is discontinuous due to the π -radian drop at a reflectivity null. Once each mode is located to sufficient precision the gain condition is applied. Taking into account the mirror losses only, the net material gain ($G-\alpha$) required for lasing is calculated. This is recorded with the mode wavelength and the associated complex grating reflectivities.

Once all modes at a given temperature have been identified the mode requiring least material gain is assumed to be the lasing mode. This information is logged in a matrix containing the number of modes detected and information about the least-loss mode for each temperature.

When all temperatures have been scanned and the least-loss mode identified at each, a subfunction identifies drift-rate, mode hops and underlying drift-rate (i.e. between mode hops) of the least-loss mode.

The program creates a number of plots and exits, erasing all working matrices from the Matlab environment and leaving only three output matrices containing the above data. If plots are not required, they can be disabled by editing a switch internal to the program, they are on by default.

Figure 5-8 describes the program in flow-chart form.

5.7.2 Considerations

The lasing-mode at any temperature is taken to be the one which requires the least round-trip gain from the laser material to achieve unity gain, i.e. the least-loss mode. This is always the mode nearest the reflectivity peak of the mirror because the only factor which could modify this selection, wavelength-dependent gain, is not implemented. The least mirror-loss mode thus may not be the lasing mode, but as explained above it does provide a reasonably reliable indication in the case of DBR structures.

Care must be taken that the wavelength resolution is smaller than the minimum probable mode separation or some modes will not be detected. One of the output plots is a sample plot of m vs. λ at a specified temperature; this is provided to allow the user to check that all integer-crossings (i.e. modes) are detected.

Mode hops are detected by the excursions they introduce in drift rate. It is therefore necessary to ensure that the drift-rate ceiling for hop-detection is set appropriately. The default value is usually adequate for steps of 1°C or less, but another of the output plots shows the temperature-to-temperature drift rates with the excursion-detection ceiling, again so that the user can check it is set appropriately. It is necessary also to ensure that at least two wavelength steps fall between successive mode hops, or it becomes impossible to say what is a hop and what is basal drift.

For the cavity, complex refractive index is not used. Instead a gain model is specified in a subfunction. This subfunction is a place-holder only; flat gain is all it presently contains.

Thermal expansion of the cavity is included, but not of the grating, which is modelled by the TMM model, where it is assumed that thermal expansion of the grating elements is not significant.

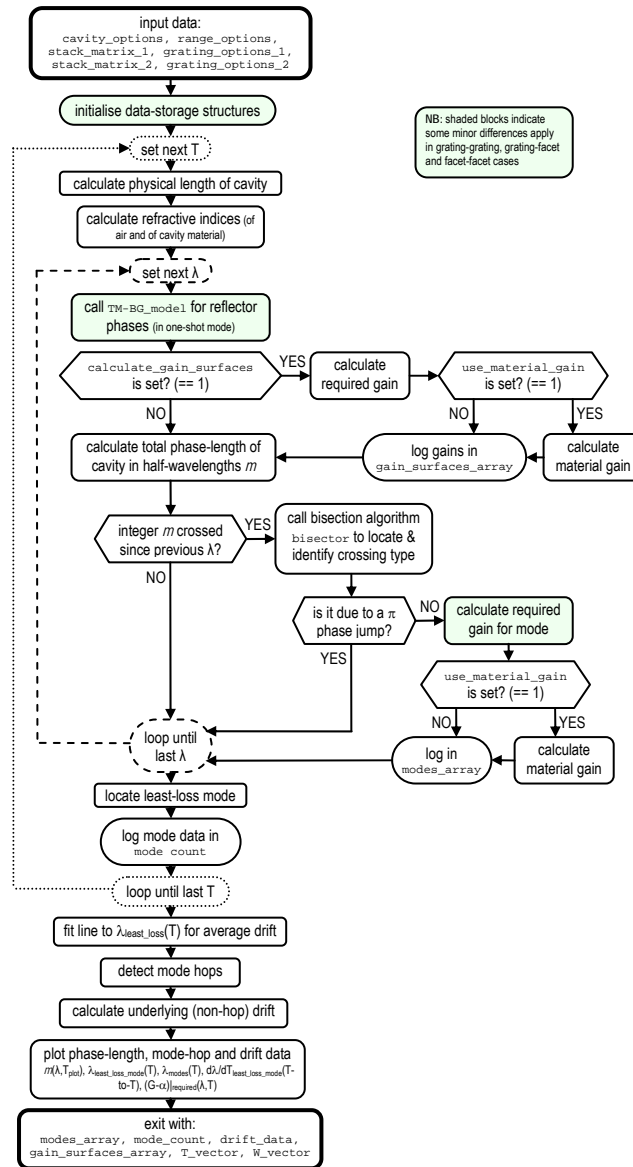


Figure 5-8 Schematic of data flow and operating structure of cavity model code

The main variables, conditionals and structures are included here. In particular the exact *modi operandi* of the various subfunctions are not made explicit. Knowledge of these can be of importance in evaluating results and detailed descriptions are given in a following section.

5.7.3 Input and Output Data Structures

This is intended as a brief guide for the user. The program is called thus:

```
[modes_array, mode_count, drift_data, gain_surfaces_array, T_vector,
W_vector] = cavity_model( cavity_options, range_options,
stack_matrix_1, grating_options_1, stack_matrix_2, grating_options_2,
savetag);
```

The names in the square brackets are assigned to the output matrices of the program, the function name is `cavity_model`, and the names in the round brackets are those of the variables to be passed to the program on its initialisation.

If the cavity to be modelled has one facet and one grating then only one grating definition is required and `stack_matrix_2` and `grating_options_2` can be omitted. If the cavity has facets at both ends then `stack_matrix_1` and `grating_options_1` can also be omitted. These grating-definition matrices have exactly the same form as in the TMM model, as does the `range_options` matrix. They are described again here for easy reference.

Define some variables contained in the input data structures:

- **N** - number of grating elements (specified for each grating separately)
- **l_def, l1, l2, ...** - axial lengths (m) at T_{def} of cavity material and of grating layers of materials 1, 2, etc (specified for each grating separately)
- **n_def, n1_def, n2_def, ...** - refractive indices at T_{def} of cavity material and grating materials 1, 2, etc. (specified for each grating separately)
- **T_def** - temperature ($^{\circ}\text{C}$) at which n_{def} , $n1_{def}$, $n2_{def}$ etc. are defined (usually room temperature) (specified for each grating separately)
- **dn/dT, dn1/dT, dn2/dT, ...** - rates of change with temperature ($/^{\circ}\text{C}$) of refractive indices of cavity material and grating materials 1, 2, etc. (dn/dT , i.e. the thermo-optic coefficients) (specified for each grating separately)
- **low_T, high_T, Tstepsize** - temperature range to scan ($^{\circ}\text{C}$) and size of step to use (need at least 2 steps to measure drift)
- **short_W, long_W, Wstepsize** - range of free-space wavelengths to search (m) and size of step (need at least one wavelength between adjacent cavity modes for correct detection)
- **T_plot** - temp ($^{\circ}\text{C}$) at which to plot sample of cavity phase-length vs. wavelength (cavity phase-length measured in half-wavelengths) and related data
- **savetag** - a string, e.g. 'alice', which will be used as the root of the filenames the output matrices and plots are saved under
- **CTE** - coefficient of thermal linear expansion of cavity material ($/^{\circ}\text{C}$),

$$(L|_{T_{def}} \cdot CTE = dL/dT)$$
- **precision** - precision to which the mode-location bisection algorithm locates the cavity modes' wavelengths (m)
- **ceiling** - threshold magnitude temperature-to-temperature lasing-mode wavelength drift rate ($\text{m}/^{\circ}\text{C}$) for hop detection: excursions occur when the mode hops (need at least 2 temperature steps between consecutive mode hops for measurement of underlying drift and mode-hop detection)

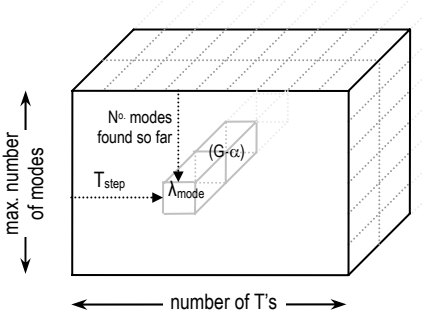
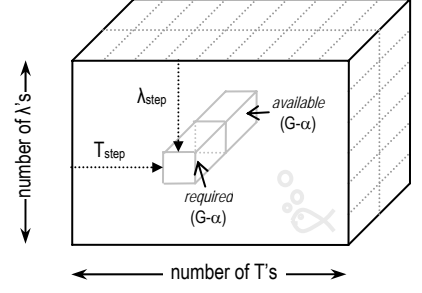
Table 5-2 sets out the structures of the input matrices, using formats Matlab would accept. Examples are given which specify a 200 μm cavity in GaAs, with offset Bragg reflectors at both ends and suitable wavelength and temperature ranges.

Table 5-2 Input data structures to cavity model

Input structure (with example)	Notes
<pre>grating_options_1 = [N_1,T_def_1] grating_options_2 = [N_2,T_def_2] grating_options_1 = [5,20]; grating_options_2 = [5,20];</pre>	<p>Specifies number of periods N (the period is defined in <i>stack_matrix</i>) and T_{def}, which is the temperature for which refractive indices are defined, for each grating.</p> <p>None, one or two grating definitions can be supplied to the program, which assumes a cleaves facet where no grating is defined.</p>
<pre>range_options = [low_T, Tstepsize, high_T; short_W, Wstepsize, long_W] range_options = [0, 2, 80; 1285e-9, 1e-9, 1320e-9];</pre>	<p>Specify the temperature and wavelength windows and the scan resolution within them.</p> <p>Note that to avoid mode detection errors $W_{stepsize}$ must be small enough to ensure at least one sample between adjacent resonant modes. Also, to avoid least-loss mode-hop and underlying-drift detection errors $T_{stepsize}$ must be small enough that at least two temperatures are sampled between mode hops.</p>
<pre>cavity_options = [n_def, dndT, l_def, CTE, T_def, precision, ceiling, T_plot] cavity_options = [3.2, 2.02e-4, 100e-6, 5.4e-6, 20, 0.01e-9, 0.6e-9, 20];</pre>	<p>Specify the cavity and various options in the program. Note that physical expansion is included, unlike in the TMM model. This is because in many edge-emitting DBR configurations the cavity is long compared to the gratings and physical expansion may be significant in it while remaining negligible in the gratings.</p>
<pre>stack_matrix_1 = [NaN, l1_1, l2_1, K, ln_1, NaN; nstart_def, n1_def_1, n2_def_1, K, nn_def_1, nend_def_1; dnstartdT, dn1dT_1, dn2dT_1, K, dnndT_1, dnenddT_1] stack_matrix_2 = [NaN, l1_2, l2_2, K, ln_2, NaN; nstart_def, n1_def_2, n2_def_2, K, nn_def_2, nend_def_2; dnstartdT, dn1dT_2, dn2dT_2, K, dnndT_2, dnenddT_2] stack_matrix_1 = [NaN, 1465.19e-9, 3699.6e-9, NaN; 3.2, 3.2, 1.52, 3.2; 2.02e-4, 2.02e-4, -0.8e-4, 2.02e-4]; stack_matrix_2 = [NaN, 1586.81e-9, 4006.71e-9, NaN; 3.2, 3.2, 1.52, 3.2; 2.02e-4, 2.02e-4, -0.8e-4, 2.02e-4];</pre>	<p>Specify the grating structures. None, one or two gratings can be defined.</p> <p>Any number of layers can be specified in each grating. Top row specifies length of each layer (the first and last columns specify the environment so no length is specified). Middle row specifies refractive index n_{def} at reference temperature T_{defn} for each layer. Bottom row specifies dn/dT of each layer.</p> <p>Note that the grating T-matrix is calculated left-to-right in the stack definitions, so which way round a grating specification is can be significant, especially regarding the phase of the reflection. The starting element is adjacent to the cavity material for both gratings.</p>

Table 5-3 sets out the structures of the output matrices. Apart from the names of the output structures, it does not use a Matlab-compatible format. This is because it is not necessary, and it is clearer in this case to use diagrams and regular mathematical layout.

Table 5-3 Output data structures from TMM model

Output structure	Notes
<p>modes_array =</p> 	<p>Array with one column for each temperature, each listing the wavelength (m) of each mode detected at that temperature. In the second plane are the corresponding gains (net /m) required for lasing.</p> <p>Because the number of modes detected in the wavelength window typically varies with temperature, the number of rows is equal to the maximum number of modes detected at any temperature, and there will be trailing zeroes in some columns (temperatures) where fewer modes were found.</p> <p>If the internal switch use_gain_spectrum is set equal to 1 then a third plane will contain the material gain at that wavelength and temperature. A gain model must be included under sub-function material_gain_model for this to work.</p>
<p>mode count =</p> $\begin{bmatrix} T_1 & T_2 & \Lambda & T_n \\ N^{o. \text{ modes}} & \Lambda & \Lambda & \Lambda \\ \lambda_{\text{least_loss}} & \Lambda & \Lambda & \Lambda \\ (G-\alpha)_{\text{required}} & \Lambda & \Lambda & \Lambda \\ \left(\frac{(G-\alpha)_{\text{required}}}{(G-\alpha)_{\text{available}}} \right) & \Lambda & \Lambda & \Lambda \end{bmatrix}$	<p>Number of modes found and information about least-loss mode at each temperature.</p> <p>Matrix with one column for each temperature, each column listing, in order, the temperature (°C), number of modes found, wavelength of least-loss mode (m), its required gain (net /m) and the required gain as a multiple of the material gain, which is found using sub-function material_gain_model.</p> <p>The 3 bottom rows are NaNs for any temperature where no modes are found. If use_gain_spectrum is set to zero, the material gain model is not used and the bottom row is zeros (except where NaN).</p>
<p>Drift_data =</p> $\left[\left. \frac{d\lambda_{\text{least_loss}}}{dT} \right _{\text{with_hops}} \quad \left. \frac{d\lambda_{\text{least_loss}}}{dT} \right _{\text{without_hops}} \quad \Delta\lambda_{\text{max}} \quad (\lambda - \lambda_{\text{fit}})_{\text{max}} \quad N^{o. \text{ hops}} \right]$	<p>Vector of key least-loss-mode drift parameters: drift with hops (m/°C), drift without hops (m/°C), maximum hop (m), maximum excursion from the best-fit line (m), number of hops. The number of hops may be zero. If not enough modes are found, measuring drift is impossible and the other measurements will be NaNs</p>
<p>Gain_surfaces_array =</p> 	<p>A two-layer array with one column for each temperature and one row for each wavelength. Layer 1 records the gain necessary (net /m) for lasing at each wavelength and temperature. This depends on the mirror reflectivity and cavity length. Layer 2 records the corresponding available material gain, but is all zeros if use_material_gain is not set.</p> <p>This array is maintained so that continuous gain surfaces are available for plotting, - gain is also recorded for each mode but this data is too unreliably-spaced for plotting.</p> <p>If the internal switch calculate_gain_surfaces is set equal to zero then required gain is not calculated at each survey point and the matrix returned contains only zeroes.</p>
<p>T_vector = [T₁ T₂ K T_n]</p>	<p>List of temperatures scanned (°C)</p>
<p>W_vector = [λ₁ λ₂ K λ_n]</p>	<p>List of wavelengths scanned (m)</p>

A number of working data structures internal to the program may be of importance to anyone seeking to incorporate modifications. In particular there is m_matrix: a matrix which records

cavity phase length in units of m for every coordinate in the search space. It has a column for each temperature and a row for each wavelength

Other working structures are annotated in the code itself.

5.7.4 Bisection Algorithm

The function steps through the wavelength window at each temperature, calculating cavity length in units of m each time and comparing it with the previous value. If it finds an integer value has been crossed it calls a subfunction `bisector` which uses a bisection method to localise precisely the crossing and which also attempts to decide whether the crossing is a resonance or due to a phase discontinuity.

`bisector` takes a wavelength exactly between the two wavelengths of the standard survey bracketing the integer-crossing, and determines in which half of the bisected wavelength step the integer-crossing lies. It then resets the boundaries to bracket that half and bisects them again, repeating this process until the difference between the boundaries is smaller than the figure specified in the input variable `precision`. If more than one integer crossing was bracketed by the original survey wavelengths the function will return invalid results, although it will run without errors. A minimum of five bisections are performed regardless of the precision, to assist discrimination of the kind of integer crossing involved.

This is achieved by examining the effect successive bisections have on the difference in m on either side of the integer-crossing, Δm , and also on the measured gradient $dm/d\lambda$. Steps down in m occur at zeros in the grating reflectance spectrum. A phasor diagram of the reflectance would show that as a zero-crossing is approached, moving from shorter to longer wavelengths, the reflectance phasor aligns itself with the positive real axis, shrinks to zero and re-emerges along the negative real axis, giving a downwards step in phase of π . This translates into a reduction in cavity-length contribution of $1m$ and as successive bisections home in on a step Δm tends to unity. For a continuum crossing the trend is to zero. Comparing the gradient $dm/d\lambda$ between successive bisections is a second discrimination method. For steps the phase gradient measured between the bisection boundaries doubles with each successive bisection. For continuum crossings the gradient stays more or less the same.

In some circumstances the discrimination algorithm can fail to make a positive identification. In such cases no mode is recorded because it is usually jumps that cause this. An error is reported to the Matlab command line without interrupting program execution.

5.7.5 Mode-Hop Detection

The least-loss mode may change several times over a temperature survey window as the cavity resonances drift relative to the reflectivity peak. The subfunction `least_required_gain_mode_analyzer` locates the mode hops, calculates the drift rate including hops, using a line of best fit, and without hops, taking an average of the temperature-to-temperature drift rates after excising those where a mode hop occurs. Finally it compiles a list of statistics about the mode hops including the maximum size of hop, the maximum wavelength excursion from the line of best fit, and the number of hops.

The temperature-to-temperature drift rates are calculated from the list of least-loss mode locations against temperature and each spike in drift rate is identified as a mode hop. The spikes are identified if they exceed a magnitude specified in the `ceiling` input variable. To assist the user in setting this appropriately one of the program outputs is a plot showing the temperature-to-temperature drift rates in relation to the ceiling value.

If the temperature resolution is not at better than half of the smallest temperature interval between hops then mode-hop detection becomes unreliable.

5.7.6 Test and Verification

The grating response from the example DBR specification in **Table 5-2** is given in **Figure 5-9**. It is obtained using the TMM model.

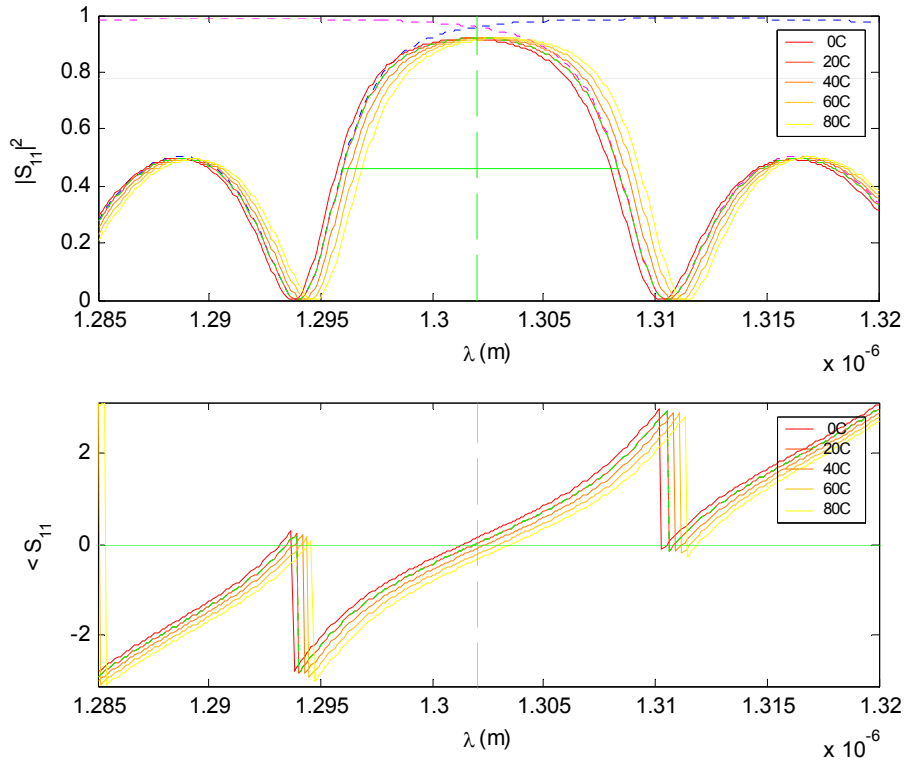


Figure 5-9 Reflectivity (top) and reflection-phase (bottom) spectra for combined gratings from Table 4-2

There are five lines in each set of axes, one for each of the indicated temperatures. The trace for T_{plot} (20°C in this case) is highlighted with a dashed line, the measured bandwidth is also indicated in the reflectivity plot, and the position of the reflectivity peak at 1302nm is indicated in both plots. The relatively narrow peak is obtained by overlapping the edges of two wider grating responses, also plotted as dashed lines for T_{plot} . λ_{peak} is partially athermalised and drifts at 0.02nm/°C.

When these gratings are combined with the example ranges and cavity specification from **Table 5-2**, the cavity model returns number of plot, shown in **Figure 5-10**, **Figure 5-11**, **Figure 5-12** and **Figure 5-13**.

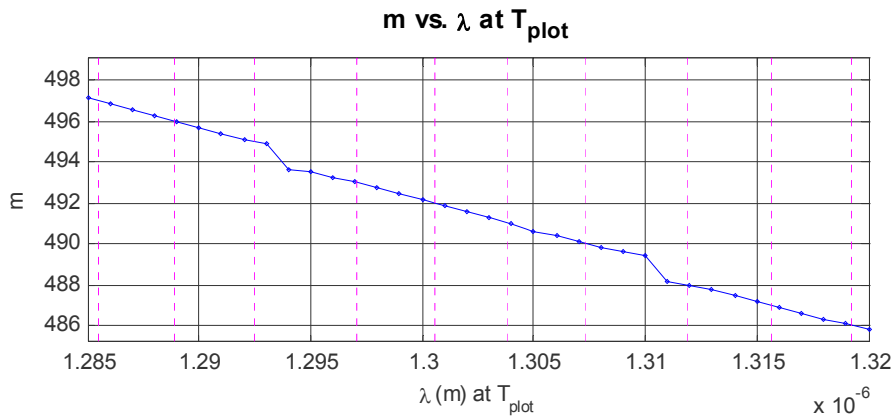


Figure 5-10 DBR cavity phase-length in half-wavelengths vs. wavelength, at T_{plot}

This 100 μm cavity is long compared to the phase-length of the gratings but the phase steps of π at the grating nulls are apparent and cause local perturbations in the mode spacing. Note that modes are located to better than the surveyed wavelength resolution, thanks to the bisection procedure.

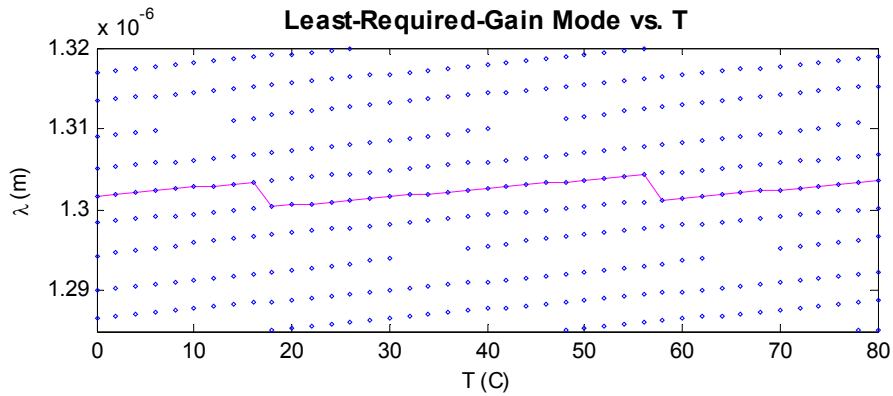


Figure 5-11 Wavelengths of all resonant modes over temperature.

The least-loss mode is highlighted. The modes all drift at $\sim 0.1\text{nm}/^\circ\text{C}$, twenty times as fast as λ_{peak} . As they overtake the slow-moving reflection peak their relative losses change and the least-loss mode changes to the one nearest the maximum reflectivity (least mirror loss). This manifests as mode hops.

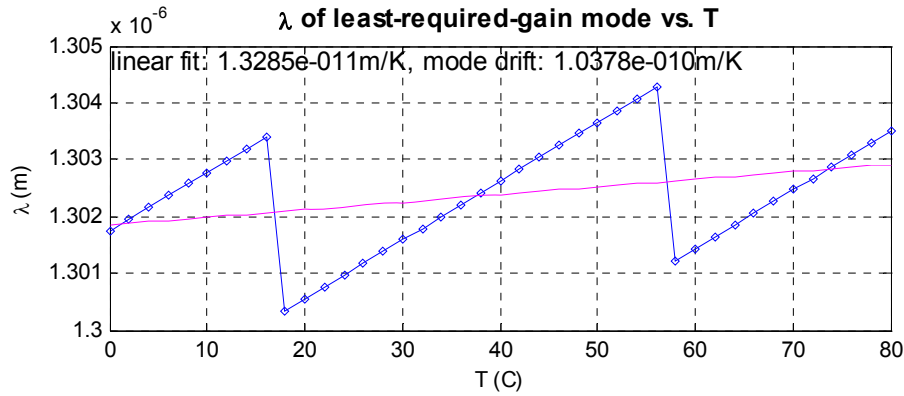


Figure 5-12 Wavelength of least-loss mode over temperature.

A zoomed-in version of **Figure 5-11**. A line of best fit is applied to the mode-position vs. temperature data to obtain drift *including* hops– if the temperature window is similar to the mode-hop interval this gradient is unlikely to be representative of the wider behaviour. The drift of the least-loss mode between mode hops is calculated by taking an average of temperature-to-temperature drift rates not including the mode hops.

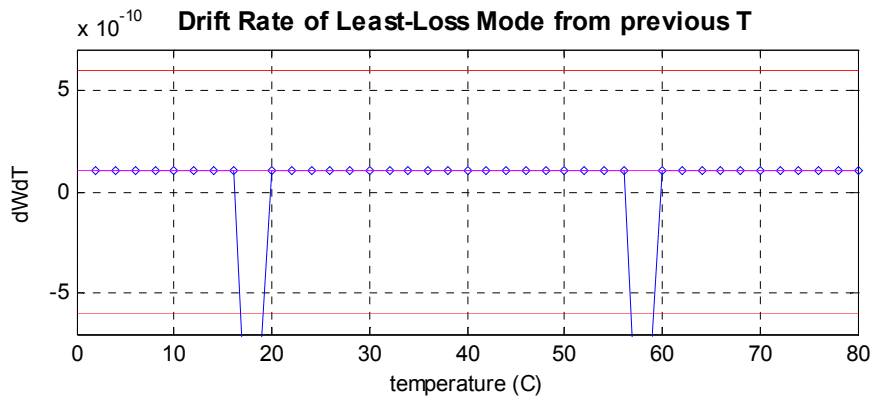


Figure 5-13 Temperature-to-temperature least-loss mode-drift rates

This plot is provided to assist the user in verifying that all the mode hops have been detected. The mode hops are apparent as excursions in drift rate which are identified if they cross a threshold set by the input variable `ceiling` ($\pm 0.6 \text{ nm}/^\circ\text{C}$ in this case). The underlying mode drift is calculated by taking the average of the remaining points.

The behaviour in all these plots is consistent with expectations.

Although the model is designed for DBR it handles FP cavities well except that it can not predict the lasing mode, because it does not have any knowledge of gain. **Figure 5-14** shows the phase-line and least-loss mode plots for this example cavity, as modelled with facets replacing the gratings.

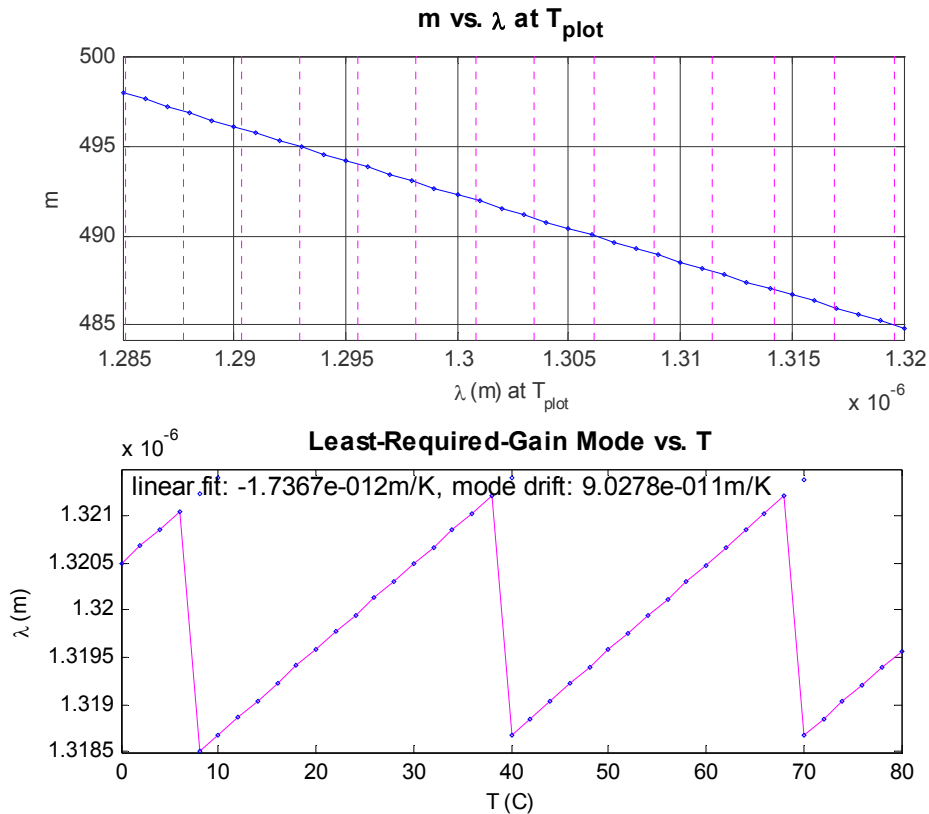


Figure 5-14 Phase-line (top) and least-loss mode (bottom) plots for example cavity from **Table 5-2**, modelled as an FP device with cleaved facets

Top: Note that the modes are now evenly spaced. The cavity is exactly the same as the one used in **Figure 5-10** but with facets instead of reflectors.

Bottom: The survey window for least-loss mode location is deliberately small in order to obtain the drift rate at 1320nm.

If facets are specified as end-mirrors, the first mode is taken as the least-loss mode. If, therefore, the short-wavelength edge of the wavelength window is adjusted to just short of 1320nm, the drift rate (not-including hops) can be compared to the sample evaluation of (E5-22), which predicted a drift rate of $0.090\text{nm}/^\circ\text{C}$.

The drift rate reported by the cavity model, shown in **Figure 5-14** (bottom), is also $0.090\text{nm}/^\circ\text{C}$. That this value is confirmed by the mathematical analysis is a convincing verification of the model, at least as far as FP behaviour is concerned.

5.7.7 Application to Athermal Mirror Test Device

The original athermal-mirror test device was fabricated from an FP cavity with a spot-size converter for efficient coupling to optical fibre. The cavity length was $500\mu\text{m}$. An analysis was made using the cavity model, attempting to explain the observed 10% mode-drift reduction, obtained after infilling the grating air gaps with BCB, compared to the drift rate with air gaps only. **Figure 5-15** plots modelled least-loss mode against temperature.

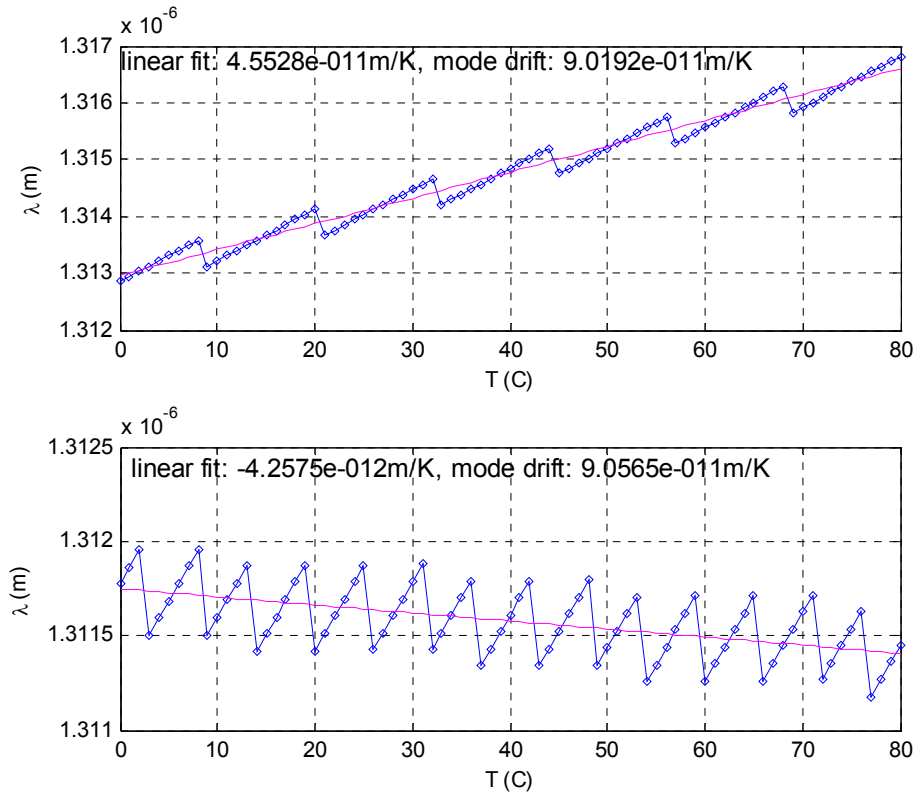


Figure 5-15 Wavelength of least-loss mode over temperature for athermal-mirror test device after etching, before (top) and after (bottom) infilling with BCB

The infilled mirror is well-athermalised so that average drift rate (including hops) is very low. Because of the long cavity, mode spacing is small and mode-hops are frequent and small.

Because of the small mode spacing, the predicted emission mode tracks the athermalised reflector peak closely via a series of small ($\sim 0.5\text{nm}$) mode hops. The mode drift rates before and after infilling are $0.0902\text{nm}/^\circ\text{C}$ and $0.0906\text{nm}/^\circ\text{C}$, a difference of less than 1%. The mean drift is $0.0455\text{nm}/^\circ\text{C}$ before and $-0.0043\text{nm}/^\circ\text{C}$ after, but no observation of this reduction was reported.

The modelled drift rates do not at all explain the observed drift reduction and it must be that some other mechanism is at work.

-
- [1] *C.R.C. Handbook of Chemistry and Physics*, 78th ed., 1999, CRC Press, USA
 [2] Oe, K. and Asai, H.: 'Proposal on a temperature insensitive wavelength semiconductor laser', *IEICE Transactions on Electronics*, 1996, **E79-C**, (12), pp.1751-1759

Chapter 6

Offset Grating Concept

DBRs with symmetrically-offset reflection spectra are examined as a means of increasing grating selectivity and reducing wavelength drift. They are found highly effective but suffer from unavoidable mode hopping.

6.1 Improving Wavelength Selectivity

In Chapter 3 engineered mirror-drifts were discussed, including fully-athermal mirrors. One of the problems observed was the freedom of resonant modes to drift within the broad reflectivity peak, itself brought about by the high-contrast grating materials necessary for engineering low drift. A possible method of increasing wavelength selectivity is to detune the gratings at either end of the cavity so that only the opposite edges of their reflectivity peaks overlap.

The gain condition for lasing (see (E5-25)) includes a term which is the product of the reflectivities at either end of the cavity. The product is therefore taken as a physically meaningful way of looking at the combined reflectivities. The two-grating mode in the TMM model (Chapter 4) was implemented specifically for this investigation.

The optimum degree of overlap is determined by the trade-off between obtaining high peak reflectivity and good selectivity. This is assisted by having sharply-defined peaks, such as are produced by high-order gratings.

6.2 Design Issues

6.2.1 Mode Hops

Improved grating wavelength selectivity will not by itself eliminate mode hops, which will occur as the reflection peak and the modes drift relative to each other. The only way to eliminate mode hops is to stabilise cavity length or have the grating reflectivity peak drift in synchrony with a particular mode, as in a DFB.

Mode hops as discussed so far are thermally induced. As temperature changes, the relative optical densities of the elements of the device change and if, as it likely for an edge-emitting device, the mode spacing is less than the reflection peak bandwidth, at some temperatures two modes on either side of the peak will have equal net gain. At this point the laser energy is

randomly partitioned between the two modes on a very short timescale, introducing significant intensity noise. This closes the eyes of the signal-time plot and operation of a communications laser in this condition therefore has a negative impact on the available bandwidth-distance product. A communications system not designed for this worst-case scenario will suffer a spike in bit error rate (BER).

Although the gain envelope can select between two modes with equal mirror loss it can not prevent this phenomenon: it is not necessary that the modes both have the same mirror loss, only that the net effect when material gain is included is equal, i.e. that greater mirror loss is balanced by lesser material gain, or *vice versa*.

If the laser is directly modulated another effect can also come into play. At temperatures where the two highest net mode gains are very similar, the modulation itself changes the refractive index of the active region by means of the plasma index contribution, changing the carrier density and shifting the cavity resonances. This can result in one mode lasing on high signals and another on low signals, swapping to and fro with each signal transition (**Figure 6-1**). The modes need not necessarily be adjacent but practically they always are.

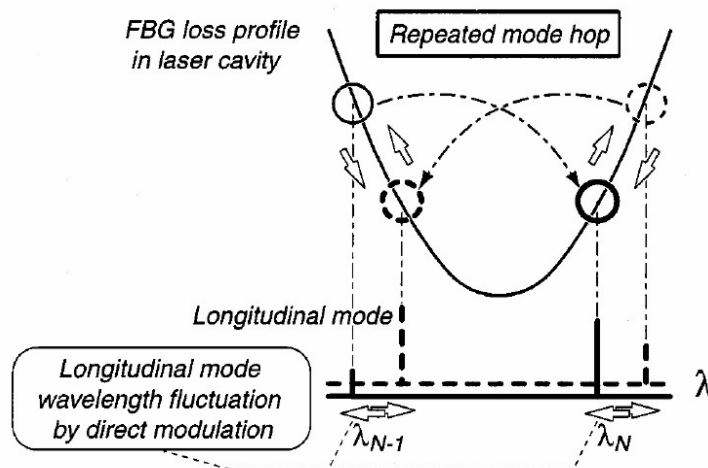


Figure 6-1 Repeated mode hopping under modulation (from Sato et al [1])

A 'high' signal changes the refractive index of the active region compared to for a 'low' signal by the plasma index contribution or by resistive heating. The resulting change in cavity resonance wavelengths and their net gains may be sufficient to select one over another, leading to a mode hop.

Intensity noise arises in the short crossover period when the modes have equal gain but this occurs at the edge of the signal eye. More significant is the severe limit this modulation-driven hopping can place on transmission distance and/or communications bandwidth due to inter-symbol interference (ISI) after fibre dispersion.

A high signal will cause a blue-shift of the cavity modes as refractive index temporarily decreases, selecting the redder of the two competing modes. Dispersion in silica glass is

greatest towards the blue end of the spectrum; therefore the redder, high-signal pulses will travel faster than the bluer, low signals. At slower modulation rates, high signals may elevate the cavity temperature, increasing refractive index and red-shifting the modes.

The severity of the ISI depends on the size of the mode hop, which is equal to the mode spacing. A small difference in wavelengths naturally suffers less dispersion than a large one, and short-duration symbols will suffer proportionally more than longer ones from the same amount of dispersion. Although small mode hops appear desirable thereby, they are necessarily accompanied by denser mode spacing, so that there are more hops over the same temperature range.

6.2.2 Athermal Reflection Peak

As described previously, it is possible to perfectly stabilise the Bragg wavelength of an organic-inorganic hybrid grating. However, its bandwidth, as a function of grating contrast, remains temperature-dependent. Overlapping opposite limbs of reflection peaks will in general give a resultant reflection peak whose bandwidth and magnitude both are temperature-dependent, but whose wavelength is not.

This peak must be wider than the mode spacing else temperatures will exist where no mode lies in the high-reflectivity region and where threshold current will increase significantly, possibly beyond the possibility of lasing. It should preferably also be wide enough compared to the mode spacing that no large variations in threshold occur between mode hops. The wider the peak is, however, the wider the range of temperatures over which SMSR approaches zero and mode partition noise occurs. The optimum peak would be a top-hat function with width equal to the mode spacing.

6.3 Offset Grating Devices

6.3.1 Design Procedure

Detuned grating-pairs were investigated. The general design is illustrated by **Figure 6-2**.

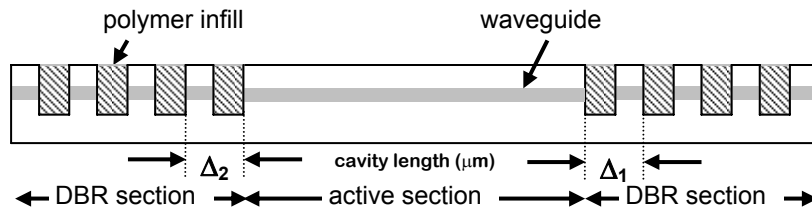


Figure 6-2 Schematic device configuration for offset-grating wavelength-confinement approach

The reflectivity peaks of the athermal end reflectors are detuned so that overlap is as narrow as possible, in order to improve wavelength selectivity, $\Delta_1 \neq \Delta_2$.

The design procedure was as follows. Example figures are given in parentheses (for polymer refractive index $n = 1.5$ at 20°C and 1320nm , polymer TOC = $-2 \times 10^{-4}/^\circ\text{C}$, semiconductor $n = 3.2$, TOC = $+2 \times 10^{-4}/^\circ\text{C}$):

1. Find athermal proportions (for first-order 1320nm grating $l_{\text{polymer}} = 141\text{nm}$ and $l_{\text{semiconductor}} = 139\text{nm}$)
2. Set desired grating order ($m = 2$, corresponding to $l_{\text{polymer}} = 282\text{nm}$ and $l_{\text{semiconductor}} = 278\text{nm}$)
3. Plot reflection spectrum
4. Adjust grating order m to bring reflection peak on to 1320nm ($m = 2.01$, corresponding to $l_{\text{polymer}} = 283\text{nm}$ and $l_{\text{semiconductor}} = 279\text{nm}$)
5. Split grating order to diverge mirror peaks and create two grating definitions, one red-shifted and one blue-shifted, overlapping in the middle (**Figure 6-4**) ($m \pm 0.213$ corresponds to $l_{\text{polymer}} = 313\text{nm} \ \& \ 253\text{nm}$ and $l_{\text{semiconductor}} = 310\text{nm} \ \& \ 250\text{nm}$)
6. Adjust numbers of periods in gratings to improve sharpness of overlap peak and/or preferential light emission (10 & 9 periods, respectively)

6.3.2 Use of Grating Order m

Note that to obtain a particular grating order m one simply takes the first-order dimensions and multiplies by m . If m is a whole number one will obtain harmonics, at the design wavelength, of the fundamental reflectivity peak. Fractional m is essentially equivalent to adjusting the Bragg wavelength of the grating, shifting the reflectivity peak and its harmonics. It is important to understand that, this being so, m does not represent an extra degree of freedom for the grating designer, only an alternative way of representing λ_{Bragg} .

Figure 6-3 demonstrates this equivalence with a 5-period InP-BCB reflector.

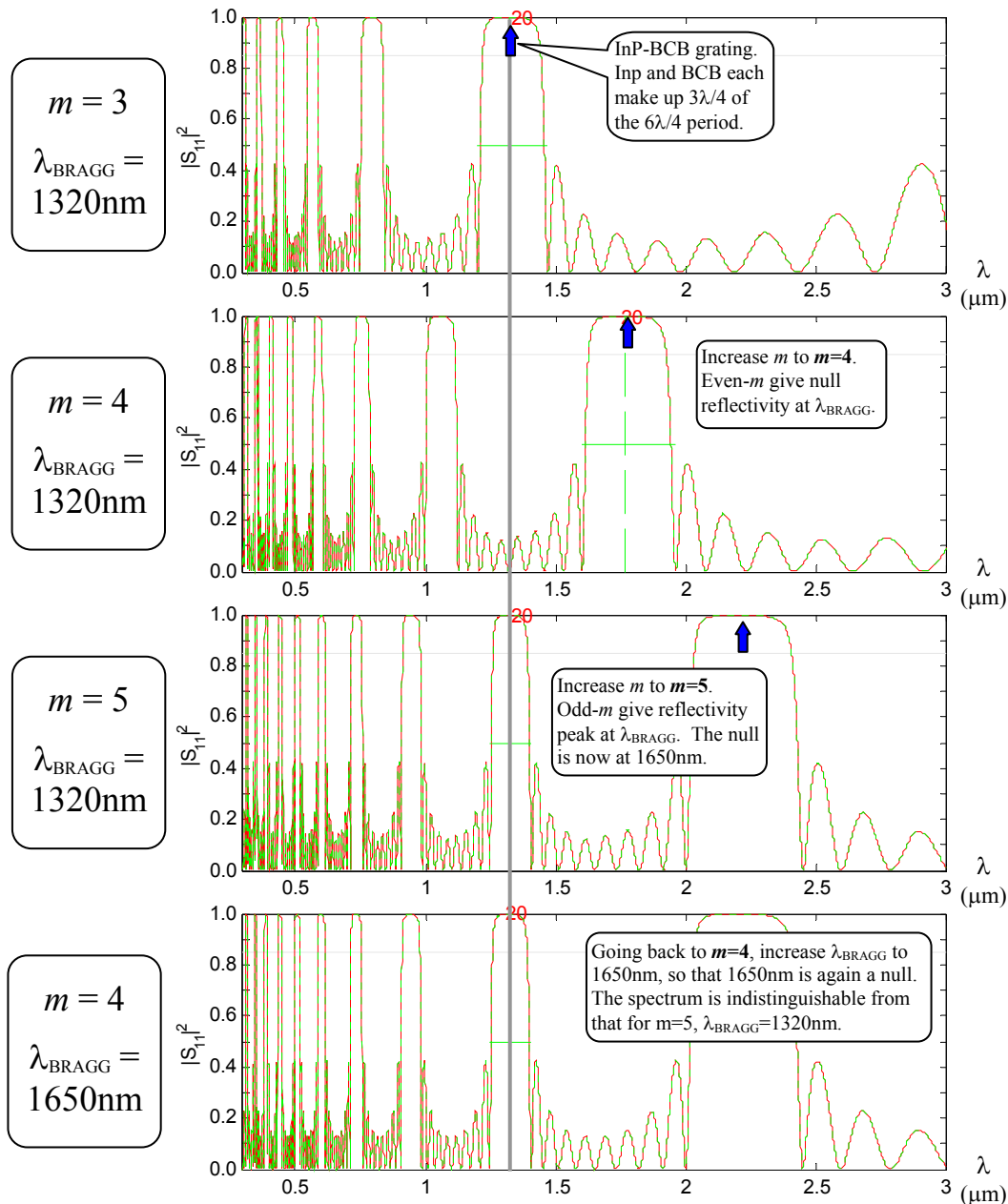


Figure 6-3 Equivalence of grating order m and λ_{Bragg}

6.3.3 Character of Overlap-Peaks

Figure 6-4 plots the example grating responses from §6.3.1 over 100°C . With increasing temperature the polymer's refractive index decreases, whereas the semiconductor index increases. Grating contrast increases and the reflectivity peak bandwidths increase (from around 300nm at 20°C). The peak positions are stable so the overlap region grows, the resultant reflectivity peak's 3dB width increasing from approximately 10 to 20nm and its magnitude from 0.8 to 0.95 . The position of the overlap peak is also stable against temperature.

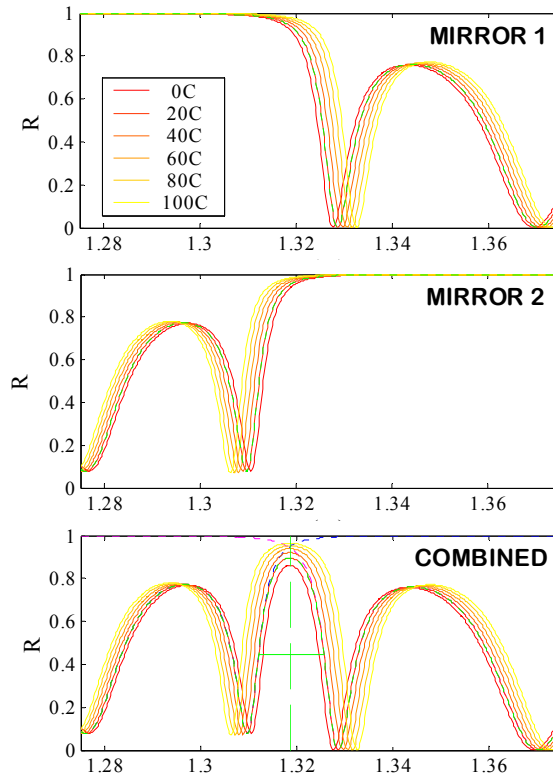


Figure 6-4 Individual and combined reflectivity spectra of offset grating pair

The organic-inorganic hybrid gratings are athermal. Parameters as follows: at 20°C and 1320nm polymer refractive index $n = 1.5$, polymer TOC = $-2 \times 10^{-4}/^{\circ}\text{C}$, semiconductor $n = 3.2$, semiconductor TOC = $+2 \times 10^{-4}/^{\circ}\text{C}$, grating dimensions are $l_{\text{polymer}} = 313\text{nm} \ \& \ 253\text{nm}$ and $l_{\text{semiconductor}} = 310\text{nm} \ \& \ 250\text{nm}$, with 9 & 10 periods for mirrors 2 & 1 respectively (approximately 2nd-order).

Although the sidelobes in **Figure 6-4** appear large, in practice they are unlikely to cause problems as long as the reflection peak is aligned with the gain peak. This is not quite as easy as it at first seems - the gain peak may drift up to 40nm over 80°C, which is a little less than the separation of the first sidelobes on either side. The fact that the main peak grows larger with temperature means that if it is placed at slightly longer wavelengths than the gain peak at the minimum operating temperature, it will continue to select the least-loss mode throughout the temperature range. Alternatively, using fewer grating periods will broaden the peak but move the sidelobes further away.

The edges of the grating reflection peaks, usually of small importance, here assume much greater significance because it is they that overlap to give a resultant peak. Using the TMM method an investigator finds almost unlimited ability to sharpen the edges of the grating peaks by increasing the number of periods. It is doubtful whether in reality any improvements could be realised with such long gratings. This is not because at such high contrasts very little light penetrates further than a handful of periods – outside the stop band light penetration can be much greater – but because of scattering losses. Using ten periods to sharpen up the reflectivity overlap is therefore probably not an option in practice.

Scattering losses can, however, be minimised in edge-emitters by keeping the unguided sections, that is the air-gaps infilled with polymer, as short as possible. Chapter 3 showed that, for a given polymer, only one proportion of polymer to semiconductor could athermalise a grating period. Minimising the unguided intervals therefore depends of choice of polymer infill. The larger the polymer TOC the shorter the polymer interval necessary to athermalise a given length of semiconductor.

6.3.4 Wavelength Confinement

The above offset grating pair was modelled on either side of a $200\mu\text{m}$ cavity using the cavity model code to locate resonant wavelengths over temperature.

As the optical length of the cavity increases with temperature the resonant modes drift across the reflectivity peak and the lasing mode hops from cavity resonance to cavity resonance as successive modes become least-loss. The size and frequency of the hops depends on cavity length and peak width. In this case the peak is considerably wider (10-20nm) than the mode spacing (1.36nm, for a $200\mu\text{m}$ cavity with refractive index 3.2) but the curvature at the peak is significant, minimising the possibility of dual-modedness. The emission wavelength is confined within a 1.36nm window centred on the reflection peak, which is athermal. **Figure 6-5** shows the confined wavelength in comparison with a typical DFB wavelength-temperature characteristic.

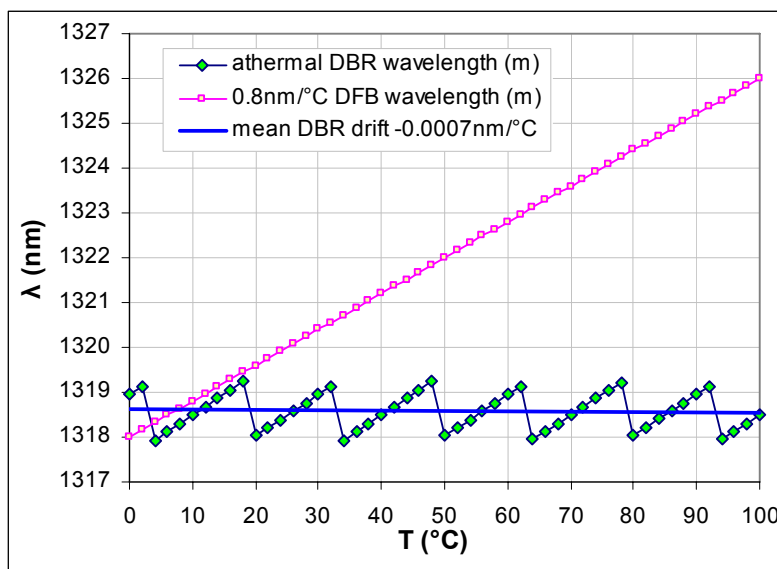


Figure 6-5 Emission wavelength vs. temperature of DBR with $200\mu\text{m}$ cavity and offset gratings as described in Figure 6-4. A typical DFB drift is shown for comparison.

The confined wavelength is confined to a 1.37nm window centred on 1318.6nm across the full temperature range from 0 to 100°C . Over the same temperature range a typical DFB drifts by 8nm. If 1.37nm is taken as the drift with the offset gratings, the DFB can be said to drift six times faster. Note that mean DBR drift, i.e. drift including mode hops, is negative.

A longer cavity would reduce the size of the mode hops, a 300 μm cavity, for instance, at 1320nm would have mode spacing of 0.09nm. For the cavity above we can look at worst, typical and best-case scenarios for the effect of mode hopping.

Take a 1.36nm mode hop, assuming non-dispersion-shifted single-mode fibre (SMF) and 25% symbol overlap tolerance. At 2.5Gb/s signalling rate a 100ps overlap of high and low signals is permissible. At 100Gb/s a 2.5ps overlap is allowed.

- Good case: 1270nm operating wavelength, dispersion of -1ps/nm-km, calculate mode hop $\Delta\lambda$ for a 350 μm $n=3.5$ cavity to be =0.658nm
→ transmission distance is 152km at 2.5Gb/s, 38.0km at 100Gb/s
- Typical case: 1300nm operating wavelength, dispersion of 3.5ps/nm-km, mode hop for a 300 μm $n=3.5$ cavity to be $\Delta\lambda=0.842\text{nm}$
→ transmission distance is 33.9km at 2.5Gb/s, 8.48km at 100Gb/s
- Worst case: 1330nm operating wavelength, dispersion of 21ps/nm-km, mode hop for a 200 μm $n=3.5$ cavity to be $\Delta\lambda=1.85\text{nm}$
→ transmission distance is 2.57km at 2.5Gb/s, 0.644km at 100Gb/s

It is apparent from **Figure 6-5** that the underlying drift rate of the resonant modes in the DBR is greater than that of the DFB. Why is this? In DFBs grating drift is identical with cavity mode drift but this is not an explanation in itself. The only possible cause is the gratings.

In a DFB the reflection phase of the fundamental resonance is zero, as this resonance necessarily fulfils the Bragg condition for the grating. In a DBR the grating phase contribution is not necessarily zero and across a reflection peak becomes more positive with wavelength, whereas the cavity phase length decreases. Across the reflection peak therefore the effect of the grating is to reduce the total phase slope, so that optical expansion of the cavity causes the resonant modes to (locally) drift faster. If the grating is not athermal, the grating drift will also affect mode drift.

If the cavity is very short, or the grating peak very narrow, the total phase slope could even be positive. That is, the cavity optical length (as measured in half-wavelengths) could increase with wavelength and mode drift could be negative.

Figure 6-6 illustrates this effect.

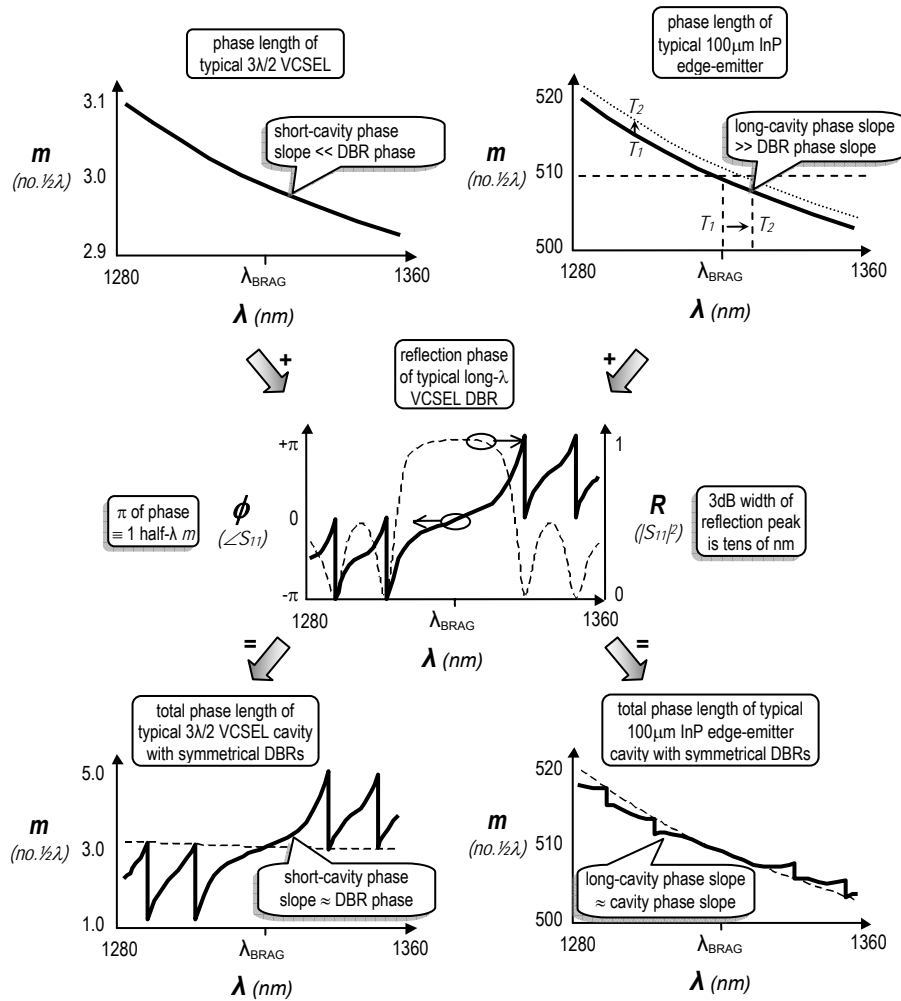


Figure 6-6 Contribution of DBR mirrors to total cavity phase length

Long and short-cavity cases are shown, on the right and left respectively. The same short, high-contrast grating is added to the ends of the cavity in both cases. For very short cavities the grating contribution is the more significant, for longer cavities the cavity phase dominates. The effect of temperature change on mode location is illustrated for the long FP cavity (top right). Given DBRs the phase-slope across the reflectivity peak is reduced compared to the FP case and a change in cavity refractive index results in an increased mode drift. In the short-cavity case a negative mode drift could be produced, depending on the response of the grating to changing temperature.

6.3.5 Single-Mode Device Modification

If athermalised gratings are left aside, the offset-grating approach can also be used simply to make a long FP cavity single-moded. It is the most straightforward way of using a FIBE machine to achieve this end, because the deep trenches required are compact and rather insensitive to etch depth, which is a difficult parameter to control.

This was attempted with one device as a partial proof-of-concept. The device and its specifications were provided by Yao-Lin Huang of the Industrial Technology and Research Institute (ITRI) of Taiwan.

The parameters of the device used in the grating design were as follows: one high-reflectivity coated (HR) facet and one cleaved facet, 1310.6nm peak gain wavelength, effective refractive index 3.243. Cavity length was 250 μ m.

The grating design developed was third-order with an offset of 0.35 ($m=3\pm 0.35$) (**Figure 6-7**). The gratings had four periods, each period having a $5\lambda/4$ semiconductor ‘tooth’ and a quarter-wave air gap, this to minimise scattering losses. The actual measurements were as follows. Blue-shifted mirror: $l_{\text{air}} = 289\text{nm}$, $l_{\text{semiconductor}} = 446\text{nm}$. Red-shifted mirror: $l_{\text{air}} = 366\text{nm}$, $l_{\text{semiconductor}} = 564\text{nm}$. The overlap bandwidth was modelled as 19nm.

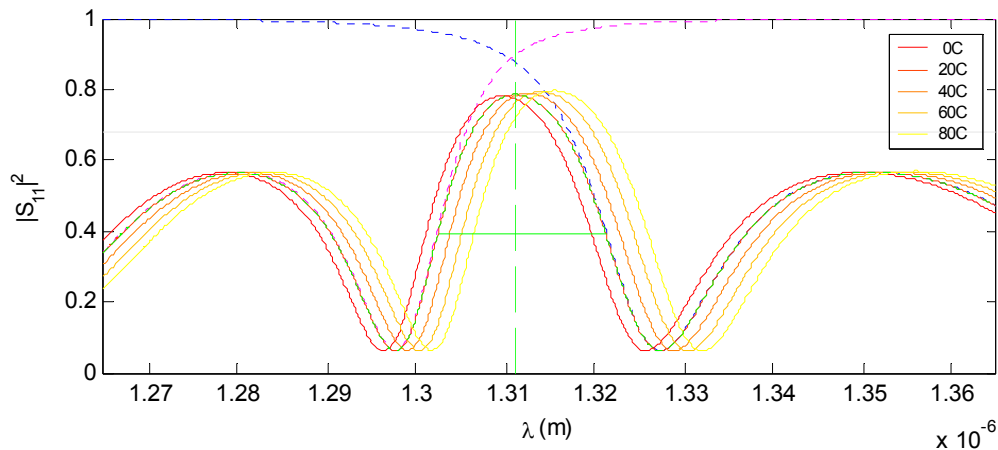


Figure 6-7 Overlapped reflectivity peak designed for proof-of-concept single-mode FIBE modification of FP device

Air-gap grating with no special thermal properties. $N=4$ for both gratings, $n_{\text{eff}}=3.243$, $m=3\pm 0.35$. Each period consists of a $5\lambda/4$ semiconductor ‘tooth’ and a quarter-wave air gap. The air gap is minimised to reduce scattering losses due to lack of wave-guiding in the air gaps. Drift rate is 0.072nm/ $^{\circ}$ C. Highlighted is the plot for 20 $^{\circ}$ C.

Following etching it was found that threshold current was very high. Investigation revealed that the peak gain at room temperature was in fact at 1333nm (**Figure 6-8**), whereas 1310nm, used in the grating design, was only the wavelength at which n_{eff} has been measured. **Figure 6-7** shows that peak gain therefore falls very close to a reflectivity minimum. This was identified as the cause of the unexpectedly high threshold current.

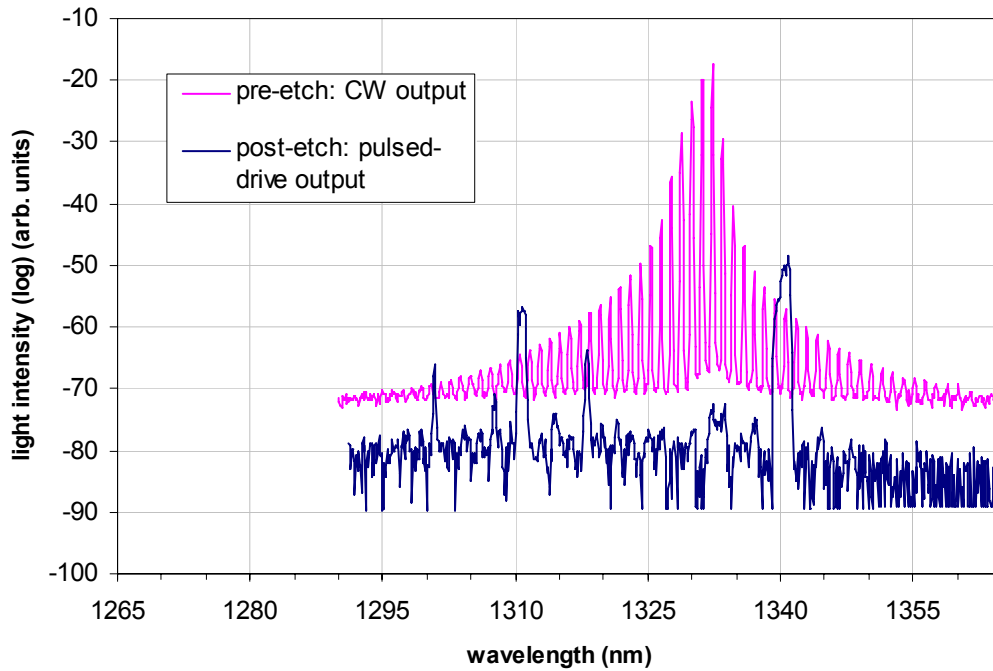


Figure 6-8 Output spectrum of device before and after FIB etching (20°C, $\sim I_{th} + 10mA$)

The wavelength axis is chosen to assist comparison with **Figure 6-7**, in which a grating reflectivity null is seen to lie at 1327nm, very close to the gain-envelope peak of 1333nm observed here in the FP output, pre-etch.

It was found that under high drive currents (see §6.3.6 for procedure) several lasing modes could be observed, the two principal of which were interpreted as corresponding to the reflectivity peak and long-wavelength sidelobe, both slightly shifted towards the gain peak as would be expected due to the slope of the gain envelope. It is reasonable to suppose that similar net gain applies at both locations – although mirror loss is greater in the sidelobe, material gain is also greater.

Given that the peak gain wavelength drifts at 0.5nm/°C and the reflection peak at 0.072nm/°C, and assuming that the sidelobes also drift at 0.072nm/°C, heating the device to 63°C was expected to bring the gain peak in to line with the long-wavelength sidelobe. It was hoped that this would enable demonstration of CW single-modedness, unfortunately our collaborator returned to Taiwan, with ITRI's devices, before this could be attempted.

6.3.6 Pulsed-Drive Investigation

Devices may for many reasons have threshold currents so high that driving them above threshold risks catastrophic damage from resistive heating. Obtaining LIV data and output spectra is often particularly desirable in such cases, including this one, in order to facilitate diagnosis of the problem.

Driving the laser with a low duty-cycle high-current pulse reduces the risk of thermal damage by allowing heat to dissipate between pulses. The duty cycle must be as low as possible consistent with obtaining sufficient power for a measurement - a duty cycle of 1% will give 1% of the equivalent CW power. The pulses must be square, so that increasing the drive current gives a proportional increase in power delivered to the device. They must be sufficiently wide not to suffer much attenuation by small impedance mismatches – long pulses contain low frequencies which are not reflected so readily. However the pulses must not be so long as to risk catastrophic heating.

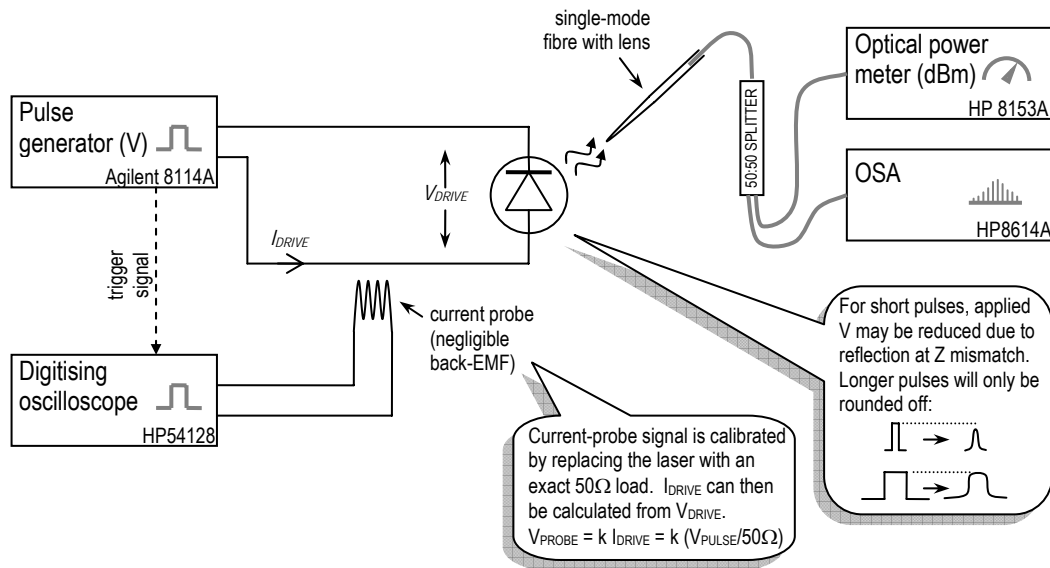


Figure 6-9 Experimental set-up for pulsed-mode LIV and spectral measurements

In this investigation an 800ns pulse on a 4ms period was used, representing a 0.02% duty cycle. The current-probe calibration showed a 5V drive pulse registered a 50.625mV probe voltage, giving a probe constant of 1.975mA/mV.

The voltage across the laser diode is

$$V_{DRIVE} = V_{JUNCTION} + I_{DRIVE} R_{SERIES} \tag{E6-1}$$

where R_{SERIES} is typically of the order 3Ω and $V_{JUNCTION}$ is determined by the bandgap energy and so can be calculated from the output wavelength. It can be expected to be in the region of 1V.

Where current probes are used to contact a device they may include an impedance-matching resistor. A 47Ω resistor will match between a 50Ω transmission line and a 3Ω diode.

6.4 Conclusions

Offset, athermal Bragg reflectors can effectively confine lasing wavelength within a very small wavelength window, limited by the longitudinal mode spacing. They are a simpler and cheaper method than others so far proposed or implemented. The same technique can also potentially be applied without athermal gratings to obtain single-mode operation from FP devices. Mode hopping, however, is a source of concern. The size of mode hops can be minimised to prevent limitation of transmission distance by ISI after fibre dispersion, but the danger of severe intensity noise at mode-hops remains.

A possible solution to this has been discussed by Sato *et al* [1] in relation to a laser diode operated with an external cavity and a fibre Bragg grating. It depends on exploitation of the nonlinear gain suppression (NGS) effect, which introduces hysteresis to mode hopping – i.e. mode hops occur at different temperatures on the way up and the way down - and eliminates both mode partition noise and hopping under modulation.

Two effects, carrier heating and spectral hole-burning, deplete the carriers at energy levels around the lasing energy (**Figure 6-10**).

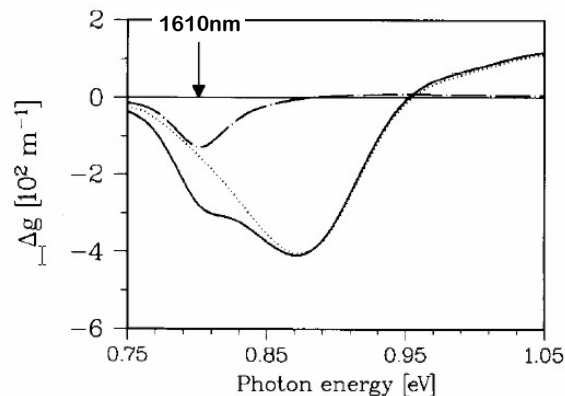


Figure 6-10 Calculated change of the gain spectrum vs. photon energy from Illatzen *et al* [2]

The three curves show the contributions from spectral holeburning (dash-dotted), carrier heating (dotted) and the combined effect (solid). The arrow indicated the lasing energy, which is taken to be at the linear gain maximum.

This can mean that modes adjacent to a lasing mode suffer a locally-reduced gain, inhibiting mode hopping. If a mode hop does occur, the gain suppression region re-centres on the new lasing mode, making it unlikely that the mode will hop back (**Figure 6-11**). In this way the hysteresis is introduced. The useful width of the gain suppression region is reported to be approximately 3nm and it is necessary for adjacent modes to lie in this region, as well as for the mirror selectivity to be small across it.

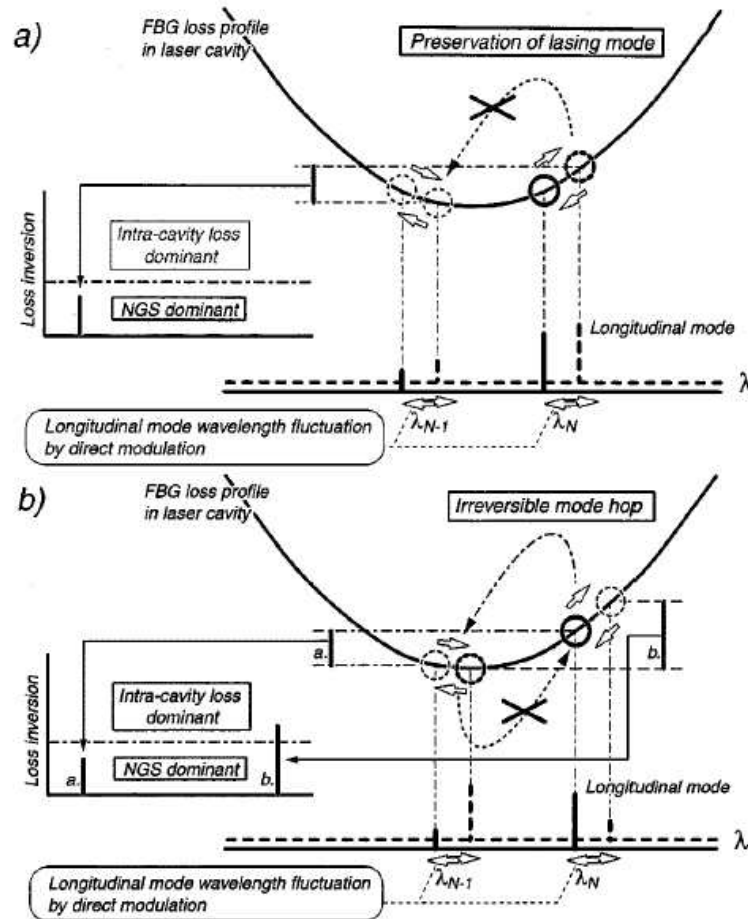


Figure 6-11 Schematic diagram of (a) lasing mode preservation and (b) mode-hop mechanism (from Sato et al [1])

External modulation is a second option, as it eliminates chirp due to dynamic refractive index variations in the laser diode. Mode hopping under modulation is then impossible, but intensity noise can still arise at certain temperatures.

In summary, the offset-grating method is promising but the associated mode hopping reduces its credibility.

- [1] Sato, T., Yamamoto, F., Tsuji, K., Takesue, H. and Horiguchi, T.: 'An Uncooled External Cavity Diode Laser for Coarse-WDM Access Network Systems', *IEEE Photonics Technology Letters*, 2002, **14**, (7), pp.1001-1003
- [2] Willatzen, M., Uskov, A., Mork, J., Olesen, H., Tromborg, B., Jauho, A.-P.: 'Nonlinear gain suppression in semiconductor lasers due to carrier heating', *IEEE Photonics Technology Letters*, **3**, (7), pp.606-609

Chapter 7

Design and Experimental Assessment of Deeply-Etched Edge-Emitting DBRs

Athermalisation without mode hopping must address cavity length, which ultimately determines resonant wavelengths. Measured in phase, the length of the cavity in general includes a contribution from the reflection phase of the DBR gratings, which are complex reflectors. It is proposed to use this to stabilise the cavity effective length over temperature. Short cavities in edge-emitting configurations are found theoretically practicable, but practically difficult.

7.1 Thermal Compensation using Mirror Phase

7.1.1 Cavity Stabilisation Requirement

Chapter 3 looked at the possibility of achieving wavelength athermalisation by means of modification of the reflection gratings. Chapter 6 offset grating pairs to improve wavelength selectivity, and introduced the cavity, in the context of mode hops, as another factor in mode drift. The length of the cavity defines the resonant modes and it was recognised that achieving mode athermalisation is only possible by stabilising the cavity length over temperature. Consider the optical cavity length of the cavity L_{opt} :

$$L_{opt} = nL_{phys} \tag{E7-1}$$

where L_{phys} is the physical length of the cavity and n is its refractive index. Differentiate with respect to temperature T to obtain

$$\frac{dL_{opt}}{dT} = n \frac{dL_{phys}}{dT} + \frac{dn}{dT} L_{phys} \tag{E7-2}$$

We would like dL_{opt}/dT to be zero, so putting this and rearranging to group the variables on either side we arrive at a mode-athermalisation condition

$$\frac{1}{L_{phys}} \frac{dL_{phys}}{dT} = - \frac{1}{n} \frac{dn}{dT} \tag{E7-3}$$

Of the four variables, L_{phys} is the only one over which it is obvious the designer exercises control. A number of alternative approaches to designing to this condition using length and the

other variables were discussed in the Chapter 1, but **Figure 6-6** suggests that reflection gratings may after all have a role to play.

7.1.2 Reflection Phase as Effective Length

We have already considered grating reflection phase as contributing to the phase-length of the cavity. It is a small step to consider this in length terms, as an *effective length* adding to the physical length of the cavity.

$$\phi_{reflector} = 2kL_{eff} \quad (\text{E7-4})$$

where k is the propagation constant. The factor of 2 appears because, being at the end of the cavity, it is necessary that $\phi_{reflector}$ be the phase increment due to a round-trip of L_{eff} .

As an example, a phase contribution of π can be considered as an effective length of one quarter wavelength – the length a round-trip of which would give an equivalent phase contribution. To convert this length in wavelengths to an effective physical length of cavity it is necessary only to divide by the refractive index of the cavity.

Rearranging (E7-4) and putting $k=2\pi n/\lambda$ puts this in mathematical form.

$$L_{eff} = \frac{\lambda}{4\pi n} \phi_{reflector} \quad (\text{E7-5})$$

If we leave the cavity refractive index n out of this equation, it gives the ‘effective optical length’ L_{eff_opt} . The importance of this is discussed in the next section.

7.1.3 Cavity Expansion Compensation

It is proposed to cancel cavity expansion using the grating effective length contribution, i.e. to set

$$\frac{dL_{eff_opt}}{dT} = - \frac{dL_{opt}}{dT}. \quad (\text{E7-6})$$

Figure 7-1 illustrates how this would work, cavity phase length combining with DBR reflection phase to athermalise total resonant length at some wavelength, ideally a resonant one. As temperature increases the optical length of the gratings’ periods tends to increase because of the large and increasing optical density of the semiconductor elements. The Bragg wavelength drifts to longer wavelengths, and because the reflection phase increases with wavelength across the Bragg peak the reflection phase at any given wavelength falls. At the same time the optical length of the cavity is increasing at all wavelengths. With careful design it should be possible to cause the two effects to cancel, giving a constant cavity length across temperature.

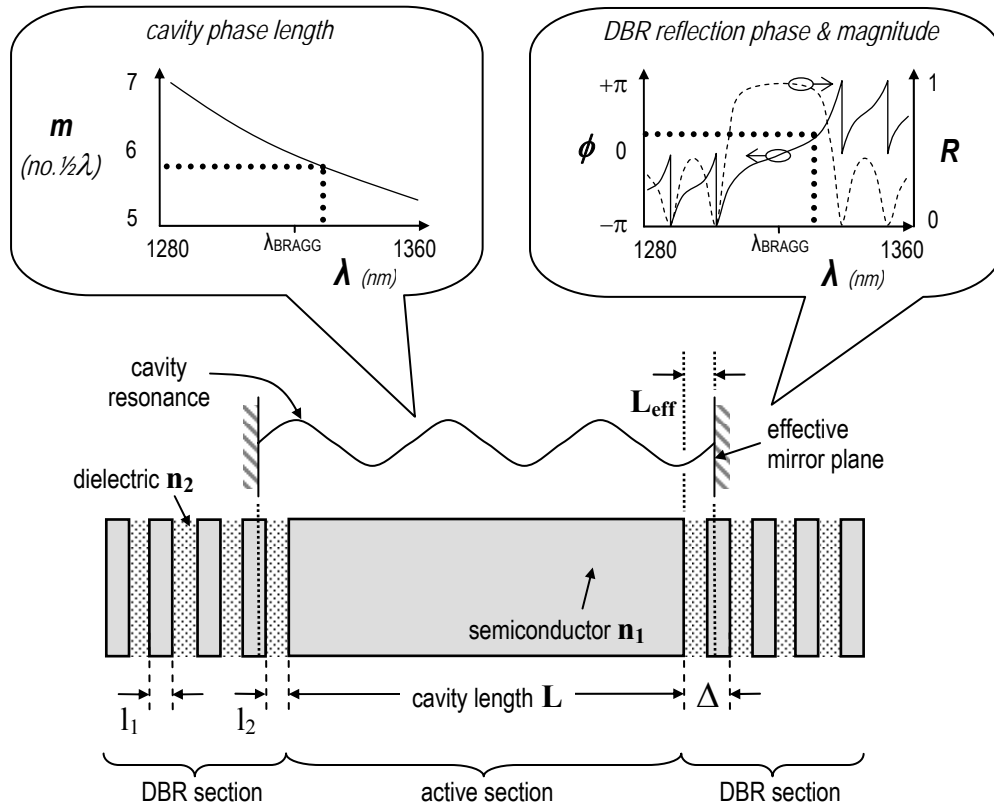


Figure 7-1 Schematic of cavity athermalisation mechanism exploiting mirror phase

As the optical length of the cavity increases with temperature, precisely-engineered mirror drift can be used to maintain a constant total optical length at the design wavelength.

Although the width of the grating peak changes as the grating contrast changes, this is a small effect and it is reasonably safe to assume that the shape of the grating response remains the same as it drifts. Considering only the relatively linear rate of change of reflection phase across the middle of the reflection peak, the rate of change of phase contribution at a particular wavelength can be obtained by multiplying the drift rate of the stop-band by the phase slope:

$$\left. \frac{d\phi_{\text{reflection}}}{dT} \right|_{\lambda} = - \frac{d\lambda_{\text{Bragg}}}{dT} \frac{d\phi_{\text{reflection}}}{d\lambda} \quad (\text{E7-7})$$

Since it is the drift-rate of the phase characteristic which is important, it is better to take $d\lambda_{\phi=0}/dT$ as the drift rate, but $d\lambda_{\text{Bragg}}/dT$ has the advantage of being relatively easy to measure.

Note that grating drift is now specifically required *not* to be athermal, and in fact must be carefully engineered in combination with the phase slope. Both depend on the grating design and are not fully independent of each other, making this a difficult task. One bonus is that positive grating drift – a much easier thing to arrange than negative drift – is now desirable. Acting with the positive phase slope it gives rise to a reduction in grating phase contribution with temperature, counteracting the increasing phase length of the cavity.

Another consequence of this approach is that the designer must now consider carefully *which* mode to athermalise. It is no use athermalising total resonant length at a particular wavelength if that wavelength does not correspond to a mode. Adjusting the mode positions through the cavity length, however, simultaneously changes the rate of change of cavity length with temperature, creating a difficult catch-22 situation. A given grating may be capable of athermalising a cavity of a particular length at some wavelength, but for that cavity length this wavelength may not correspond to a mode and adjusting the cavity length to bring a mode in to the correct position could destroy the athermalisation.

7.2 Cavity Length vs. Mode Drift Study

Given that it is not possible to design gratings with dL_{eff}/dT to order, an approach is adopted of using the previously-developed computational models to survey mode drift for a range of cavity lengths, using a given grating. The idea is to locate fortuitous combinations.

7.2.1 Cavity Length Survey with Athermal Grating

An athermal InP-BCB grating of 16th-order, very similar to that discussed in Chapter 3, was defined, with $L_{polymer} = 3731\text{nm}$, $L_{semiconductor} = 1478\text{nm}$, and using the same material parameters. In an arrangement modelled on a very short edge-emitting device with deeply-etched air-gap reflectors reported by Raffaele *et al* [1], 7 periods of this grating were specified on one side of the cavity with 3 on the other for preferential light extraction. The cavity itself was specified as InP ($n=3.2$, $TOC=0.000202/^\circ\text{C}$, $CTE=5.6\times 10^{-6}/^\circ\text{C}$).

The survey used a wavelength window of 1272nm to 1333nm with 0.1nm steps, bracketing the reflection peak. Temperatures from 19.5°C to 20.5°C in 0.1°C steps were used. This was a compromise between the improved reliability of drift measurement and hop-detection afforded by a denser temperature grid and the consequent increase in modelling time. Mode location precision was $5\times 10^{-3}\text{nm}$, and mode drifts were logged for a range of cavity lengths from 1 to 20µm in 10nm increments.

Figure 7-2 plots the survey results, which show a remarkable double population of drift rates – a high-drift group beginning at $\sim 5\mu\text{m}$ cavity length and apparently extending to infinity, and a low-drift group extending from the shortest cavity lengths to $\sim 13\mu\text{m}$. Large-scale ‘loops’ are apparent to the eye but are merely sampling artefacts. A fine 205nm periodicity is observed in both populations.

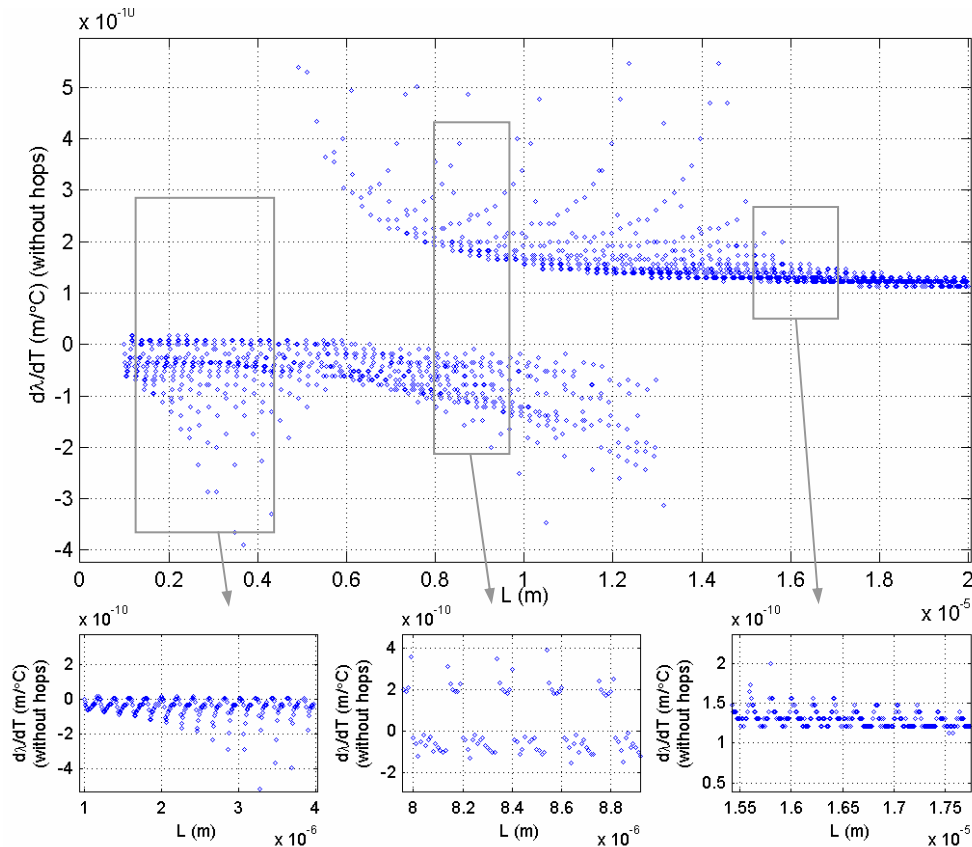


Figure 7-2 Mode-drift rate vs. cavity length survey

Cavity with two athermal gratings as specified in **Table 3-2** but with 3 and 7 periods, respectively. Each point represents the drift-rate recorded for one cavity length. Two ‘populations’ of points are apparent. Insets are three zoomed-in views: left – periodicity of low-drift population, middle – antiphase periodicity of low and high-drift populations, right – periodicity and quantisation in high-drift population

The two populations can be understood as follows. The low-drift population corresponds to the grating contribution (positive phase slope) dominating the total phase length, with the high-drift population corresponding to domination by the cavity contribution (negative phase slope). **Figure 6-6** illustrated these two cases. For cavities shorter than $\sim 5\mu\text{m}$ (in this case) the grating reflection phase dominates completely and total phase slope is positive at all points across the reflectivity peak. For longer cavities, total phase slope is only positive near the edges of the reflectivity peak where the slope of the reflection phase is greatest, accounting for the overlap of the low-drift with the high-drift population. As the cavity grows longer, modes near the edge of the reflection peak are more rarely ‘least-loss’ and disappear altogether by $13\mu\text{m}$ cavity length. There is no value in these long-cavity low-drift modes - being close to the edge of the reflectivity peak they suffer from high mirror losses and may at other temperatures even fall entirely outside it.

The fine periodicity originates in the grating stop band. Because 204.7nm in a refractive index of 3.2 represents exactly one half-wavelength of 1310nm light, changing the cavity length

by this much shifts the phase line upwards by $1m$ where m (in italics) is the number of half-wavelengths in the resonant length. As the cavity length is increased, the position of the resonant mode shifts across the $\pm 2m$ combined modulation placed on the cavity-phase line by the gratings, and at some point will hop to the next mode $1m$ away, explaining the $1m$ periodicity. Because the phase slope varies across the reflection peak, mode drift depends on the position of the resonance in the peak.

Modes located in the edges of the reflection peak, where reflection phase slope is steepest, are least sensitive to changes in the total cavity phase. Their drift approaches that of the grating, and does not change rapidly with changes in cavity length. They are represented in the peaks of the low-drift population.

The troughs of the high-drift population, however, represent modes in the middle of the reflection peak, which is why they trend with longer cavities to the cavity drift rate of $\sim 0.09\text{nm}/^\circ\text{C}$, as grating contribution becomes insignificant.

Some quantisation levels are apparent in the measured drift rates, of a scale that is comparable to the smallest features of the plot. Increased mode-location precision would avoid this.

A significant number of drifts were found to have been calculated from modes occurring in sidelobes of the main peak. This was particularly the case amongst the low-drift population, owing to the steep phase slopes present in the narrower side lobes. The survey parameters for subsequent surveys were tightened to exclude the sidelobes, beginning and ending the wavelength window at the nulls of the reflectivity peak.

The region of **Figure 7-2** useful in terms of laser design is therefore that concerning cavities less than $5\mu\text{m}$. It is notable that zero-drift is available at the peaks of the fine structure in the low-drift population, which being some 150nm wide are a much easier target to hit in terms of device fabrication.

7.2.2 Cavity Length Phenomenology Survey

A complex interplay between the mirrors and the cavity clearly exists in the determination of mode drift. A third survey was undertaken with the intention of unpacking some of the influences and discovering the characteristics of ‘good’ reflector designs – those capable of optimising the low-drift population or reducing the long-cavity trend drift. Non-athermal air-gap gratings were specified, both to investigate the effect of grating drift and to facilitate fabrication should any good designs be located.

Three mirror drifts were specified, a median case with air gaps of equal length to the semiconductor intervals, a high-drift version with proportionately shorter air gaps, and a

reduced-drift version with longer air gaps. Each ratio was implemented in 3rd, 6th, 9th and 14th – order gratings, to give 12 mirror specifications in all. Prior to the cavity-length surveys the reflection spectrum of each mirror design was checked using the TMM model. In three cases it was necessary to adjust grating order, in two cases fractionally, to centralise the Bragg peak on the desired wavelength more closely, and in one case by one whole grating order to select a neighbouring peak where the intended one was unusually weak.

The grating and material parameters were as follows.

Table 7-1 *Material and grating parameters at 20 °C*

n_{InP} :	3.487
n_{air} :	1.0003
$dn_{\text{semiconductor}}/dT$ (/°C):	2.98×10^{-04}
dn_{air}/dT (/°C):	-7.87×10^{-07}
number of periods N :	3
designed Bragg peak location (nm):	1315
HIGH Bragg-peak drift (nm/°C):	0.1080
MEDIAN Bragg-peak drift (nm/°C):	0.0871
LOW Bragg-peak drift (nm/°C):	0.0662

The refractive index and TOC used for the InP semiconductor waveguide are group effective index values measured from a sample of FP devices which were available for modification. These measurements are discussed later (§7.5.1.3) in this chapter.

Table 7-2 sets out the dimensions of the twelve gratings and data describing their reflection peaks. The peak bounds quoted are the null positions, not the 3dB points.

Table 7-2 Dimensions and reflection-peak data for twelve reflector designs (3 drifts by 4 grating orders)

Grating design number	Grating order <i>m</i>	Mirror Strategy	L2 (nm)	L1 (nm)	Reflection peak characteristics at 20° c				
					λ (nm)	short- λ bound (nm)	long- λ bound (nm)	width (nm)	drift rate (10-30°C) (nm/°C)
1	1	low drift (large airgap)	268	112	1300	904	2544	1640	0.067
	3		803	335	1298	1179	1513	335	0.065
	6		1606	671	1314	1220	1431	212	0.060
	9		2409	1006	1318	1251	1379	128	0.060
4	14	3747	1565	1317	1275	1353	79	0.060	
5	1	50:50, median drift	147	147	1338	999	2368	1368	0.100
	3		440	440	1305	1132	1502	370	0.085
	6		879	879	1320	1237	1431	194	0.090
	10		1465	1465	1318	1275	1377	102	0.090
8	15	2198	2198	1317	1283	1359	77	0.090	
9	1	high drift (short airgap)	25	181	1307	1014	2044	1029	0.120
	2.95		75	535	1320	1185	1508	322	0.110
	5.9		150	1070	1312	1233	1407	174	0.110
	10		254	1813	1321	1269	1380	111	0.110
12	14	355	2538	1313	1275	1354	79	0.110	

A mode-drift vs. cavity-length survey was carried out for each reflector design and certain characteristics recorded from each survey plot (Figure 7-3). The surveys used a wavelength window from null to null of each grating’s reflectivity peak, as measured at 20°C. For speed, 2nm steps were specified, this still being considerably smaller than the mode spacing. Also for speed, only three temperatures were surveyed – 10°C, 20°C and 30°C – the minimum necessary to measure drift and detect mode hops. Mode location precision was tightened up to 1×10^{-3} nm to reduce quantisation of the drift measurements. The range of cavity lengths was $0.01 \mu\text{m}$ to $5 \mu\text{m}$, in 5nm increments. The cavity itself was specified with the same material parameters as the grating ($n=3.487$, $\text{TOC}=0.000298/^\circ\text{C}$, $\text{CTE}=5.6 \times 10^{-6}/^\circ\text{C}$), with gratings at both ends.

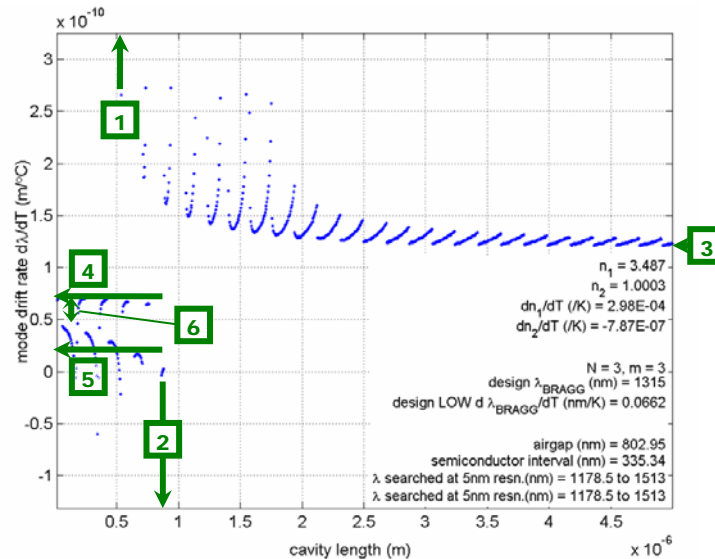


Figure 7-3 Example drift vs. cavity-length plot with key parameters indicated.

1. shortest cavity length of high-drift population
2. longest cavity length of low-drift population
3. long-cavity mode drift (converges to FP case)
4. maximum drift of low-drift population
5. drift of lowest-drift peak in low-drift population
6. size of drift discontinuity in highest-drift peak of low-drift population

Figure 7-4 is a composite of the twelve lasing mode drift vs. cavity length plots.

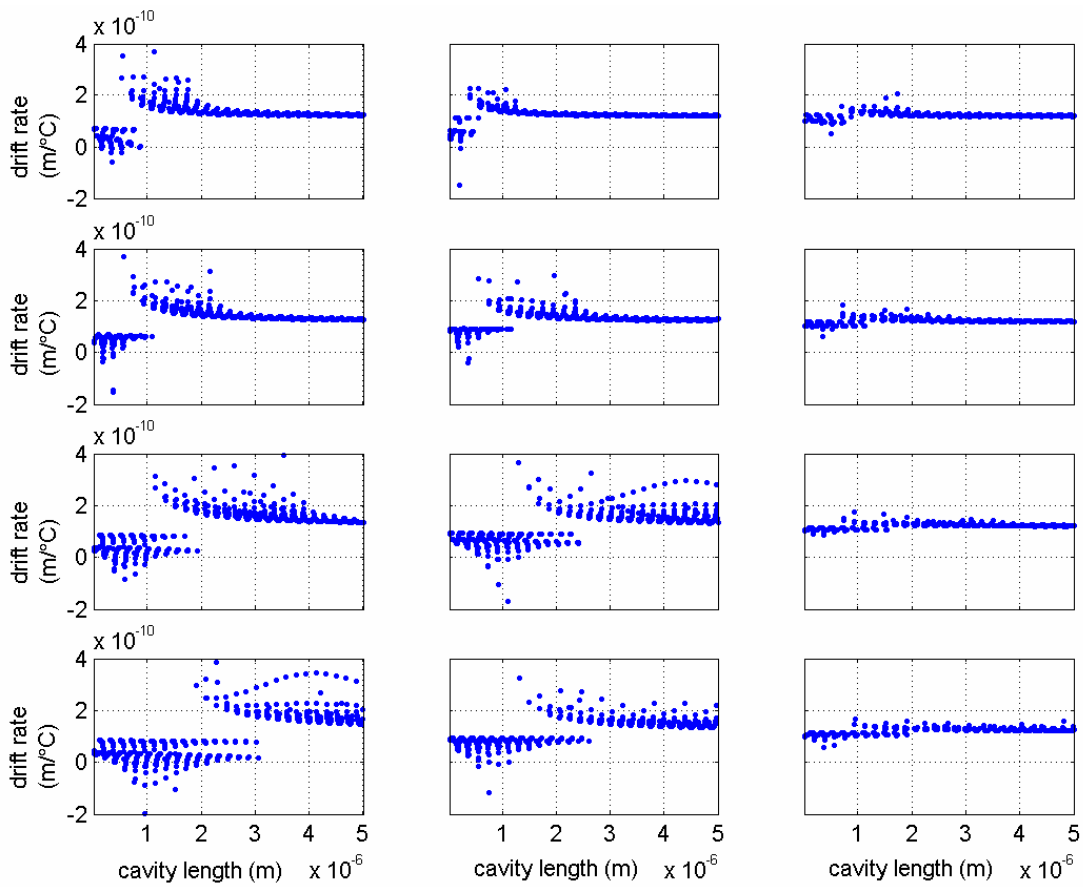


Figure 7-4 Mode drift vs. cavity length for all twelve mirror designs.

Left column is **low** drift, middle is **medium** drift, and right is **high** drift. From top to bottom the rows correspond to grating order $m \sim 3, 6, 9, 14$.

Table 7-3 sets out the key characteristics measured from the cavity-length survey plot for each reflector design.

Table 7-3 Parameters measured from cavity-length survey plots

Grating design number	Grating order m	Mirror Strategy	min. cavity length of high-drift population (μm)	max. cavity length of low-drift population (μm)	min. drift of high-drift population ($\text{nm}/^\circ\text{C}$)	peak drift of low-drift population ($\text{nm}/^\circ\text{C}$)	min. drift amongst peaks of low-drift population ($\text{nm}/^\circ\text{C}$)	discontinuity in drift in peak of low-drift population ($\text{nm}/^\circ\text{C}$)
1	3	low drift (large airgap)	0.535	0.880	0.1211	0.0723	0.0029	0.0283
2	6		0.560	1.095	0.1250	0.0693	0.0625	0.0254
3	9		0.960	1.935	0.1338	0.0859	0.0273	0.0420
4	14		1.715	3.070	0.1465	0.0850	0.0215	0.0410
5	3	50:50, median drift	0.385	0.550	0.1191	0.1143	0.0586	0.0703
6	6		0.550	1.150	0.1221	0.0928	0.0879	0.0488
7	10		1.295	2.405	0.1318	0.0938	0.0576	0.0498
8	15		1.305	2.600	0.1338	0.0947	0.0811	0.0508
9	2.95	high drift (short airgap)	0.700	0.875	0.1182	0.1260	0.0957	0.0820
10	5.9		0.715	1.130	0.1182	0.1191	0.1016	0.0752
11	10		0.745	1.535	0.1201	0.1162	0.1162	0.0723
12	14		0.945	1.915	0.1211	0.1143	0.1045	0.0703

Figure 7-5 and Figure 7-6 plot the drift and cavity-length parameters for the twelve designs for comparison.

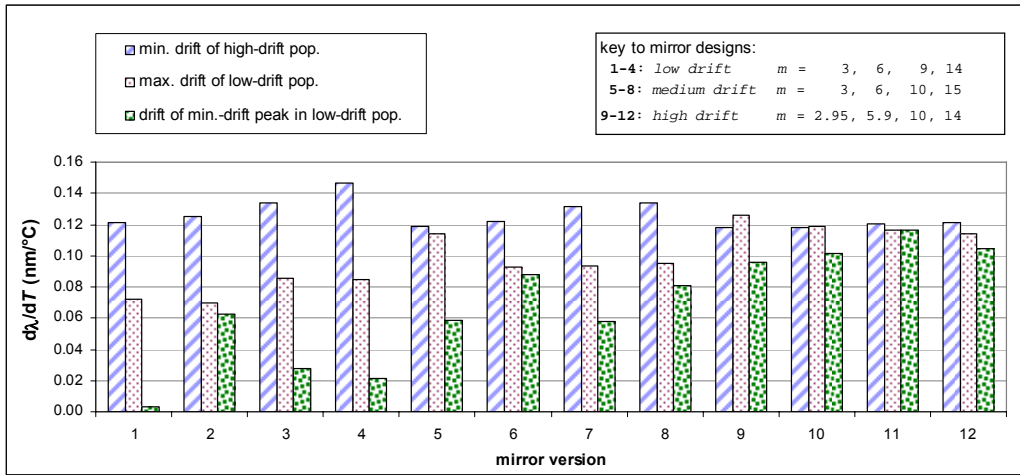


Figure 7-5 Key drift parameters from each reflector design's drift vs. cavity-length survey

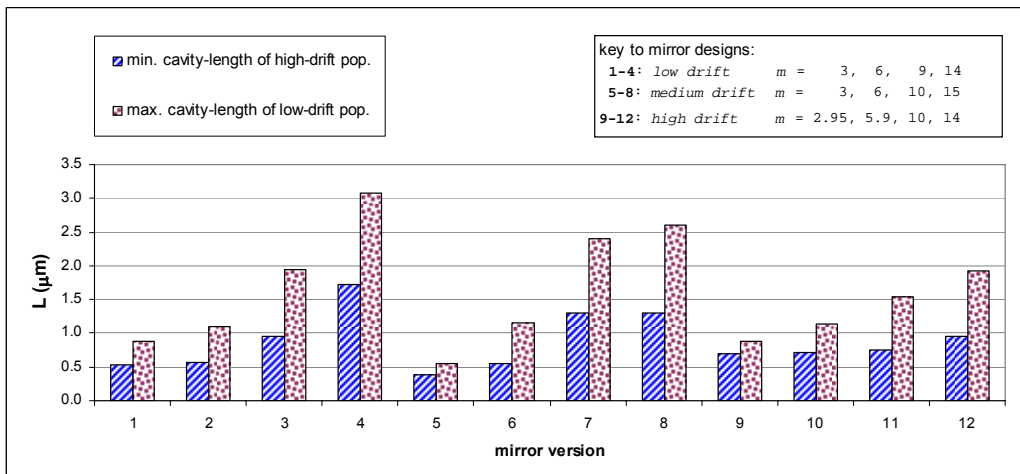


Figure 7-6 Key cavity-length parameters from each reflector design's drift vs. cavity-length survey

As grating **drift** increases the following trends are apparent:

1. drifts in the low-drift population increase quickly
2. the minimum drift of the high-drift population *decreases* slowly
3. difference between maximum & minimum drift peaks in bottom population falls
4. at high orders, the minimum cavity length of the high-drift population and the maximum cavity length of the low-drift population both decrease.

As grating **order** increases the following trends are apparent:

1. minimum drift of low-drift population rises slowly
2. sensitivity of minimum drift of high-drift population to mirror drift increases
3. minimum cavity length of the high-drift population and the maximum cavity length of the low-drift population both increase (less so at high mirror drift)

It is desirable to obtain low mode drift at the peaks of the low-drift population, requiring low grating drift. It is also desirable to maximize the cavity length for which the low-drift population exists, requiring high grating order. This suggests a low-drift high-order grating. However, it must be noted that this will entail large air gaps with concomitant diffraction losses. Including diffractive losses in the grating model would be useful here.

7.3 Designing Reflection and Phase Spectra

Any designer has a finite ‘design space’ in which to work, consisting of a number of independent or partially-correlated variables, some or all of which can be freely adjusted to meet necessary design specifications, and all of which vary only over certain ranges. The variables a DBR grating designer has to work with in shaping reflectivity and phase spectra include number of periods, grating order, period length, period composition and material systems. In section 6.3.2 it was shown how varying grating order was equivalent to changing the grating period (i.e. Bragg wavelength) and so represented the same degree of freedom. Grating order was not considered in terms of phase, however, which is of interest for purposes of stabilising the length of short cavities, where mirror phase plays a significant role in mode selection and drift. In this section this part of the design space is investigated further, along with the subtler influences both of period composition and number of periods on reflectivity and phase. A qualitative approach is taken, being more general.

7.3.1 Effect of Number of Periods

The number of periods N has a significant effect on the reflection spectrum and phase slope. Adding periods increases overall reflectivity and changes the overall phase relation of waves reflected from interfaces and arriving back at the start of the grating. Investigated below is the character of this contribution. The gratings investigated are all athermal InP:BCB designs for 1300nm Bragg peak.

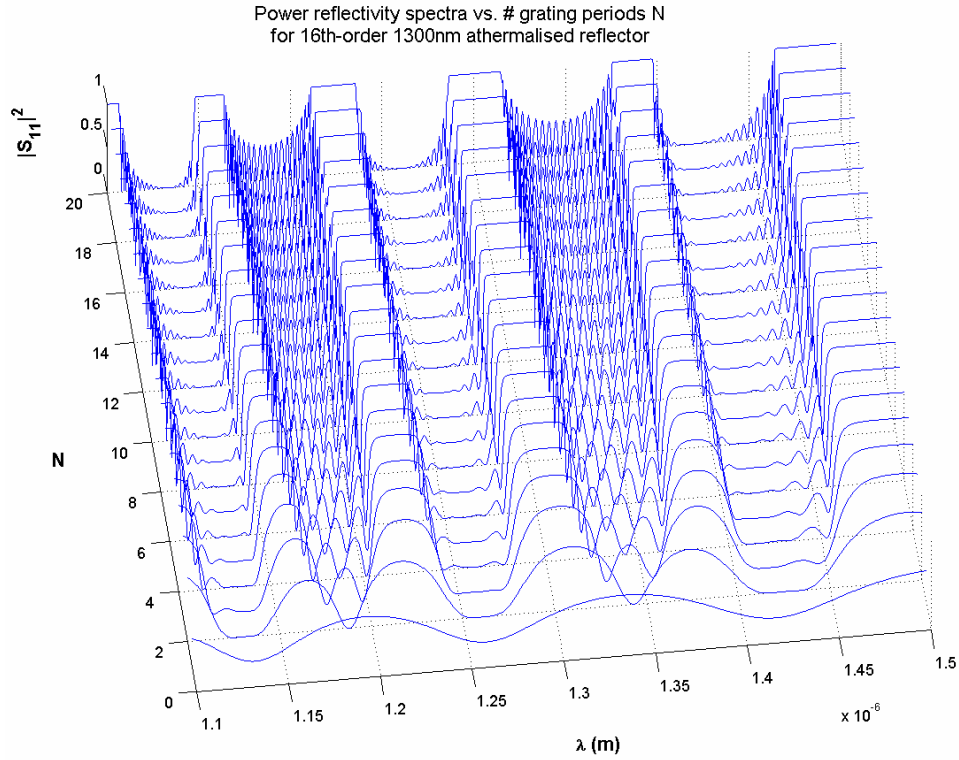


Figure 7-7 Power reflectivity spectrum for N -period grating, $N = 1$ to 20

16th-order athermal InP:BCB grating with 1300nm Bragg peak. $L_{\text{BCB}} = 3731.2\text{nm}$ and $L_{\text{InP}} = 1477.8\text{nm}$.

Figure 7-7 shows how increasing N sharpens the edges of the reflection peaks, so they become more top-hat shaped. More subsidiary peaks also appear between the main harmonics. For this high-contrast grating, peak power reflectivity is 99.9% from only $N = 6$. Stop-band width reduces with increasing N but it tends towards a limit and after $N = 5$ changes very slowly. This limit is set by the contrast between the refractive indices of the grating materials – the smaller the contrast the more periods the light sees and the narrower the reflection peak becomes.

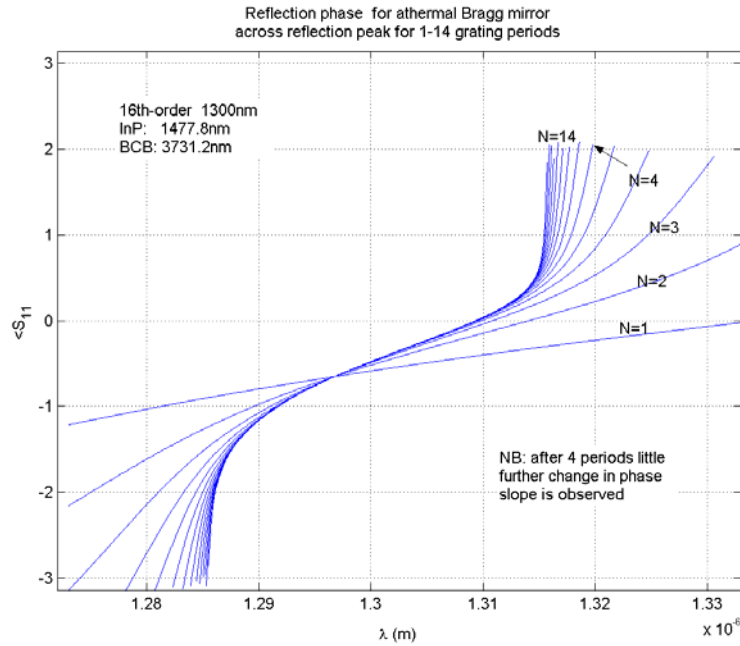


Figure 7-8 Associated Bragg-peak phase slopes across Bragg peak of N -period grating, $N = 1$ to 20

16th-order athermal InP:BCB grating with 1300nm Bragg peak. $L_{\text{BCB}} = 3731.2\text{nm}$ and $L_{\text{InP}} = 1477.8\text{nm}$.

Figure 7-8 shows that the slope of the central section of the phase curve is almost constant after $N = 4$, although the terminal slopes continue increasing until about $N = 12$ as the edges of the reflection peak become steeper.

Because in general at least three periods are necessary to achieve adequate reflection, it is clear that changing the number of periods offers the designer very little control over the central part of the phase slope. If the reflection peak width could be adjusted by changing the grating contrast much greater control would be possible – the narrower the peak the steeper the phase slope.

Using the steep terminal slopes has the disadvantage that these correspond to low reflectivity at the edges of the peak, but there are major advantages in that a mode selected in this region would be quite insensitive to cavity phase and could have its drift readily controlled by engineering the grating drift. Positioning a mode so precisely (within $< 10\text{nm}$) would be technically demanding and second-order effects could disrupt it. Care would also be needed to avoid having the mode drift into the reflectivity null due to cavity phase shift.

7.3.2 Material Proportions

The grating design procedure used so far has been to first set the Bragg wavelength by choosing an appropriate period, then to obtain the required drift by adjusting the material proportions within the period (see equations (E3-6) and (E3-7)), then to model the resulting

reflectivity spectrum and over a number of iterations adjust grating order fractionally to fine-tune the position of the reflectivity peak. The assumption has been that, to first order, the grating period sets the position of the reflection peak. This assumption is frequently not exact.

To investigate the role of period composition in this, a 1326nm InP:BCB grating was specified and the reflectivity at 1326nm recorded as the (optical) proportions of the two materials varied. The total optical length of the period was kept the same, as was the number of periods. This was repeated across a range of grating orders. **Figure 7-9** plots the results.

It is intuitive that gratings consisting entirely of one or the other material (ratios 0 or 1 in the figure) are not gratings at all and have zero reflectivity. Between these extremes are a number of evenly-spaced peaks equal in each case to the order of the grating. Thus, by symmetry, odd orders give high reflectivity at 50:50 material compositions, as is well known. Less well known is that high reflectivity can be obtained using *any* combination of layers odd numbers of quarter-wavelengths thick. This is a more nuanced version of the Bragg condition.

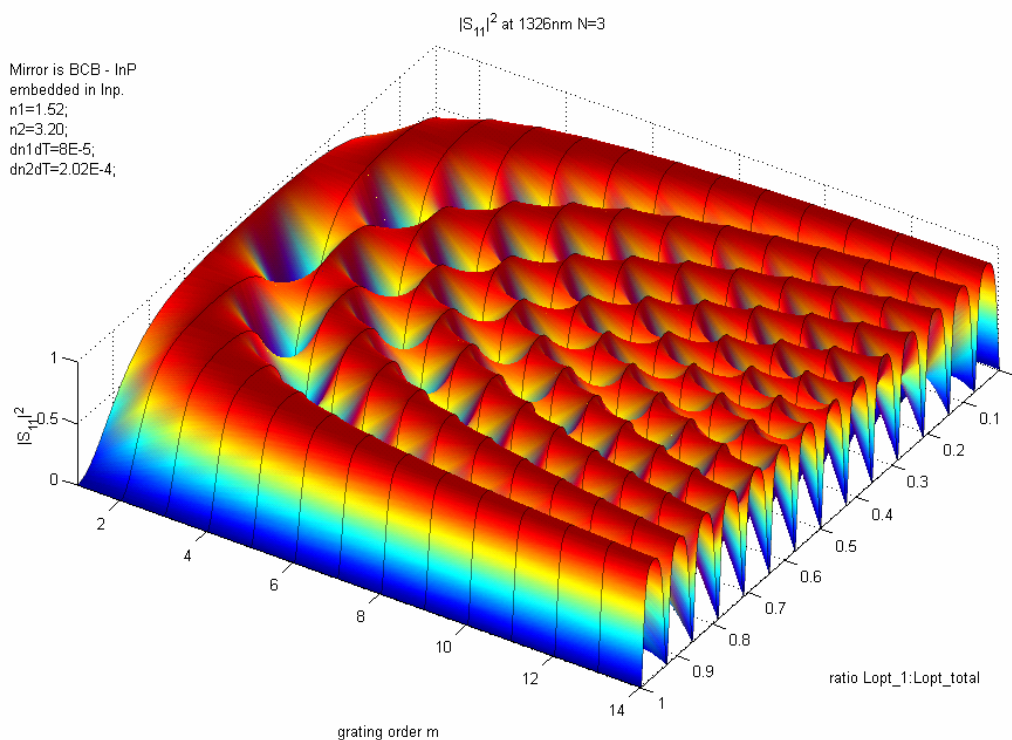


Figure 7-9 Reflectivity of 3-period InP:BCB grating at 1326nm, vs. grating order and ratio of optical lengths of InP and BCB

Just as in Bragg gratings reflected waves all add up in phase at the Bragg wavelength, at other wavelengths they add up in antiphase and cancel. Grating with periods formed from layers each an odd number of quarter-wavelengths thick automatically meet the first condition.

If two layers make up each period, which must be an integral number of half-wavelengths thick in total, for maximum reflectivity those layers must each be an odd number of quarter-wavelengths thick. In a first-order stack the layers are necessarily both one quarter-wave thick,

but in higher-order DBRs reflectivity peaks may be obtained using layers of different optical thicknesses, because the second condition allows for a selection of combinations satisfying the first (Figure 7-10). Indeed, for even-order stacks it is necessary.

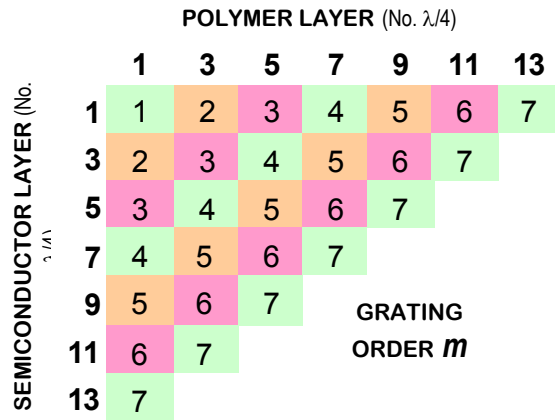


Figure 7-10 Combinations of layer-thicknesses satisfying the Bragg condition

Any combination of layers with optical thickness $n\lambda/4$ where $n = 1, 3, 5$ etc. gives a reflectivity maximum. Set out here are the grating orders corresponding to some combinations of smaller n . Note that grating order is the length of a period in half-wavelengths.

The question arises of whether the material proportions affect the mirror phase slope. To test this, a 3rd-order InP:BCB grating was specified and its reflection phase across the Bragg peak plotted (Figure 7-11) for the three possible configurations (see Figure 7-10).

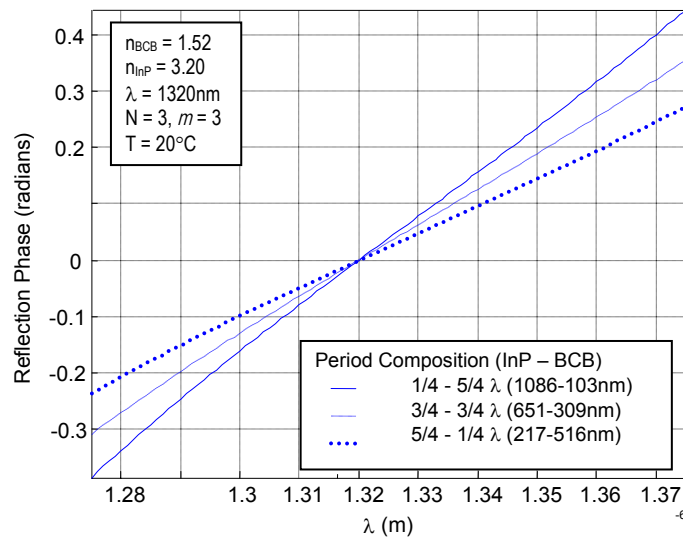


Figure 7-11 Reflection phase across Bragg peak for three alternative configurations of 3rd-order InP:BCB grating

Note that in each case the reflection phase is zero at the Bragg peak.

Material proportions clearly do affect phase slope, which increases as the thickness of polymer increases, or as that of the semiconductor decreases. The mechanism is unclear - the width of the reflection peak is not much changed, so the slope is changing intrinsically.

7.3.3 Effect of Grating Order

Grating order m has a significant effect on the reflection spectrum and phase slope. The character of this contribution was investigated using the high-contrast form of the Bragg condition to define the test grating, so that the reflection peak was always centred on the design wavelength. **Figure 7-12** clearly shows how phase slope increases with increasing grating order due to the narrowing reflection peak. It is also apparent that the shape of the phase slope across the reflection peak (the degree of double curvature) remains the same for all m . This is in fact set by the grating contrast, with lower contrast gratings giving more linear phase slopes.

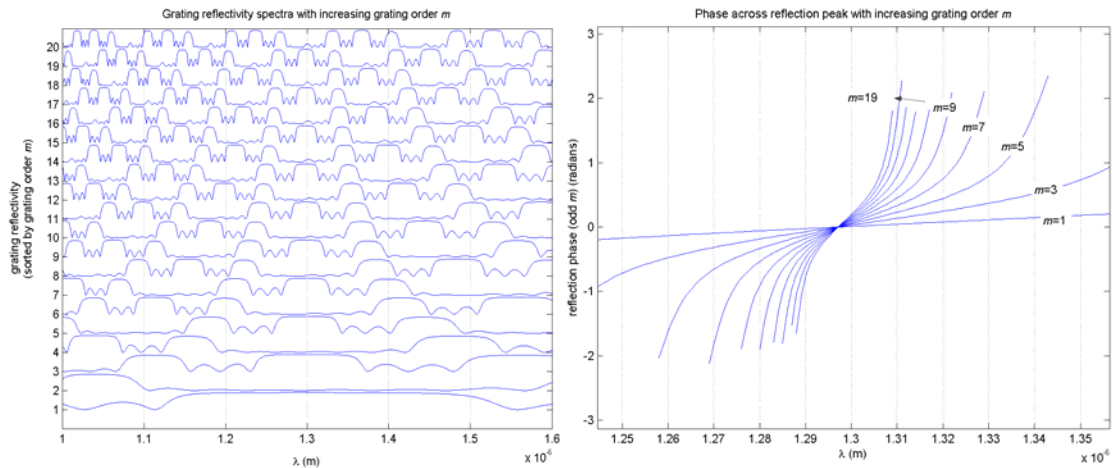


Figure 7-12 Power reflectivity spectra for m th-order grating, $m = 1$ to 20 (left) and associated Bragg-peak phase slopes (odd orders only) (right)

4 period athermal InP:BCB grating with 1300nm Bragg peak. $L_{BCB} = m\lambda/4n_{BCB} = m \times 216\text{nm}$ and $L_{InP} = 3m\lambda/4n_{InP} = m \times 305\text{nm}$.

It can be seen that as grating order increases the central wavelength is shifted to longer wavelengths, ‘stretching out’ the shorter-wavelength spectrum behind it (see also **Figure 6-3**). The trend of the peaks growing narrower and closer together with increasing m comes about because the harmonics of the central peak become more closely spaced the further from it one gets, appearing at $\lambda_{Bragg}/2, /3, /4$ etc.

7.3.4 Conclusions

Control of the reflection phase slope across the reflectivity peak is possible through appropriate selection of grating order. Higher orders select higher, narrower harmonics of the fundamental Bragg peak. Very low grating orders can have extremely wide reflection peaks, especially using high-contrast gratings. High orders are attractive for their superior selectivity and steep phase slope, but the designer should beware losses in the grating, especially if unguided sections are present.

Increasing the number of periods narrows the reflection peak and increases the phase slope until such point that negligible light penetrates to the next period. Few periods are sufficient to reach this point with high-contrast gratings such as described. Towards the edges of the peak reflectivity is less and light penetrates further, and this part of the peak continues to narrow with extra periods.

The grating contrast is an important factor but cannot be freely chosen given the small range of suitable material systems.

Whereas the half-wavelength Bragg condition is suitable for low-contrast gratings such as DFBs the version elucidated here is required for deep gratings and dielectric stacks. The previous, iterative method of grating design is not falsified in any way and has the advantage of allowing a continuum of grating drifts. The fixed proportions of **Figure 7-10** mean that only discrete drift rates are available for a given set of materials. However, using the full Bragg condition does mean that the Bragg peak is always where expected and has zero reflection phase, both of which make designing for cavity athermalisation easier.

Increasing the proportion of the less-dense material appears to give steeper phase slope, but again this risks increasing losses in the grating.

A designer, given a device format, range of short cavity lengths, materials and wavelength, can use these qualitative rules of thumb to arrive iteratively at a grating design combining grating drift and reflection phase slope to counter the cavity expansion.

7.4 Determination of Refractive Index

Before applying these design rules to real devices it is necessary to know the refractive index at the emission wavelength, and its rate of change with temperature. Recalling (E5-10), one method of determining this is to measure mode spacing of the unmodified FP device across some temperature range.

$$n_g = \frac{\lambda^2}{2\Delta\lambda L} \quad (\text{E7-8})$$

The relevant refractive index for mode spacing is the group effective index n_g .

Spectra were taken for a device (designated 20-2) taken from a set of Agilent Technologies 1300nm indium-phosphide based FP devices with five quantum wells (5QW). The set of devices were cleaved from the same bar of the same wafer and were therefore expected to possess the same characteristics. The instrument used was an HP86140A optical spectrum analyser (OSA), operated at -75dBm sensitivity and maximum 0.07nm wavelength resolution

across a range 1280-1320nm, deliberately oversampled with 10001 measurement points. The oversampling defines the convolution of the instrument resolution with the laser modes cleanly, assisting automation of mode location in Matlab. The spectra were taken at $I_{th}+15mA$ in an attempt to maintain the same carrier density across measurements. The devices were mounted on a copper heat sink, itself mounted on a Peltier-effect temperature stage with a feedback thermistor. Spectra were taken at 10, 30 and 50°C (**Figure 7-13**). The length of the device was measured with a travelling microscope as 369.3 μm .

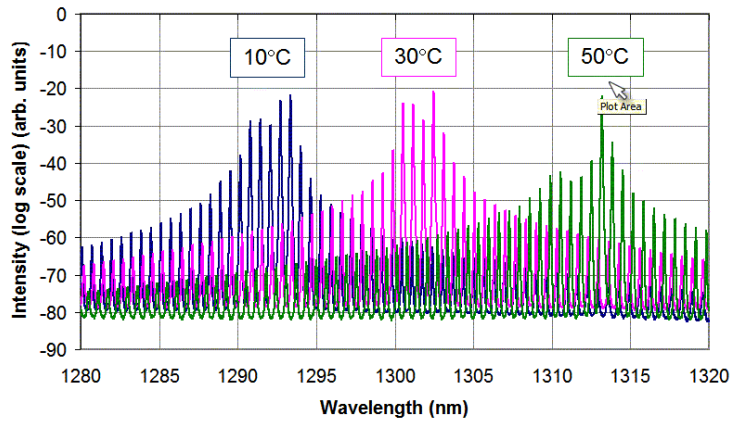


Figure 7-13 $I_{th}+15mA$ spectra for device 20-2

Figure 7-14 shows the group effective indices calculated from the mode spacings. Substantial noise is present due to the resolution of the instrument being comparable to the mode spacing of $\sim 0.7m$.

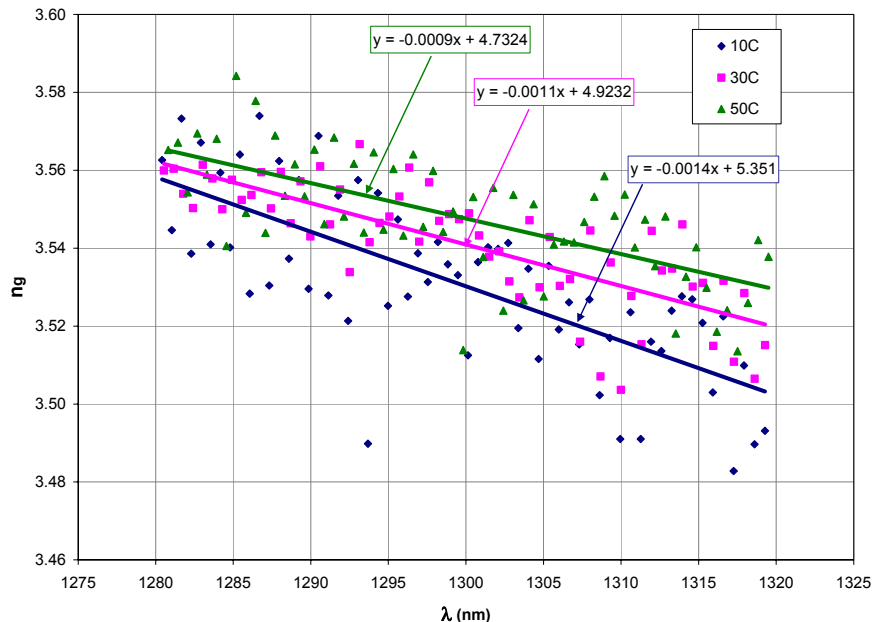


Figure 7-14 Group effective refractive index vs. wavelength at 10, 30 and 50°C

Calculated from mode spacings. Indicated are lines of best fit for each temperature: 50°C at top, 30°C middle, 10°C bottom. Dispersions are $-0.9 \times 10^{-3}/nm$, $-1.1 \times 10^{-3}/nm$ and $-1.4 \times 10^{-3}/nm$, respectively.

It is notable that the difference between the 50°C and 30°C trend lines is less than between the 30°C and 10°C trend lines. This was attributed to the poor temperature stability of the Peltier stage, although it could suggest that the rate of change of refractive index is not constant or that a temperature differential existed between the feedback thermistor and the device itself.

Being a quantum well device, the effective index is determined largely by the bulk semiconductor rather than active material and so no effect on index is observed across the emission peak. The same argument is applied below to otherwise-similar devices with different numbers of quantum wells.

Using the data in the graph an empirical formula for group index as a function of wavelength λ (nm) and temperature T (°C) in these ranges was obtained:

$$n_g \approx (0.122 \times 10^{-4} T - 14.914 \times 10^{-4}) \lambda + (5.4662 - 0.0155 T) \quad (\text{E7-9})$$

7.5 Single and Double-Grating Devices

A series of FP devices were modified with deep air-gap gratings etched using FIBE. The aims were to validate the models and demonstrate an observable effect on mode drift. The designs were developed using the iterative method and used the refractive index parameters obtained from analysis of the mode spacings.

7.5.1 Devices 20-1 and 20-2

7.5.1.1 Design and Observations

These designs were intended to show drift modification of resonances in a short cavity. Using $n = 3.54$ and $dn/dT = 4.325 \times 10^{-4}/^\circ\text{C}$ a 1308nm positive-drift (0.157nm/°C) air-gap grating of order 10.92 and 3 periods was designed. In 20-1 it was etched 5 μm from the laser facet and the other facet was etched at an angle to prevent resonances in the long section of the 370 μm waveguide. To eliminate alignment errors due to ion beam drift between imaging and etching, the front facet was also etched.

The devices used were Agilent Technologies 1300nm ridge waveguide FP lasers with 5 quantum wells.

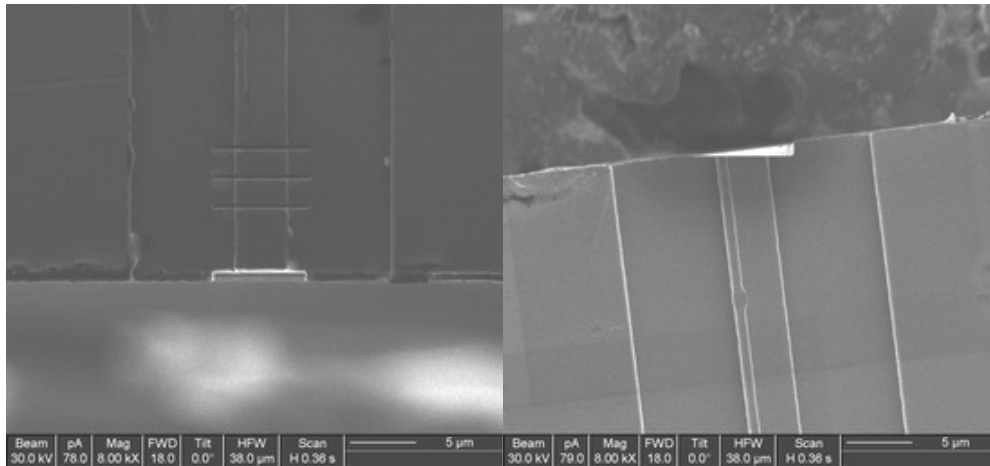


Figure 7-15 Device 20-1 cavity and grating (left) and angled facet (right).

The specified dimensions were 224nm air gaps, 1957nm semiconductor teeth, 5000nm cavity. FIB images at higher magnification show etched dimensions to be 240nm, 1974nm and 5020nm.

Constant drive current measurements on 20-1 showed an amplified spontaneous emission (ASE) spectrum following the material gain profile, with a number of evenly spaced ripples which were interpreted as cavity resonances. In an attempt to achieve lasing, pulsed drives up to 330mA were tried without success. Because the device is sub-threshold approximately the same carrier density was obtained at several temperatures by adjusting the drive current to obtain the same total output power each time, given optimal coupling of the output to a lensed fibre.

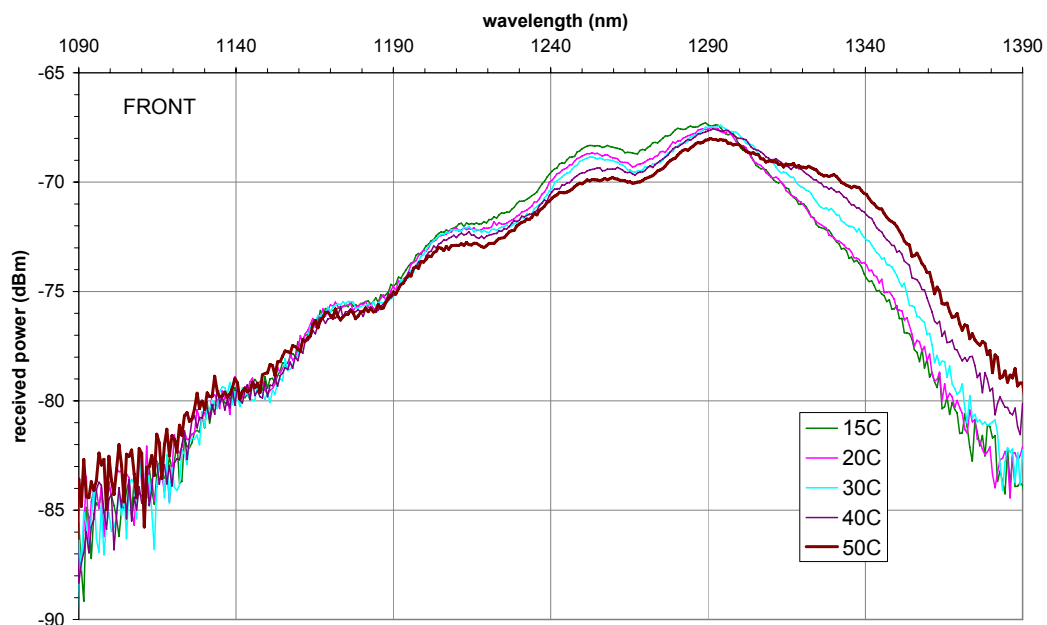


Figure 7-16 Post-etch ASE spectra from 20-1 from the front facet.

The spectrum follows the material gain spectrum apart from the ‘ripples’. A similar spectrum was obtained from the angled back facet, at higher power and without any ripples. The traces order themselves in sequence of temperatures.

20-2 was exactly similar to 20-1 but with a 20 μm cavity and etched using a lower beam dosage. The intention was to increase gain in the cavity and promote lasing but no ASE ripples were observed. Imaging showed that the grating was not deep enough. Analysis suggested that more time needed to be allowed for etching through the gold top contact.

7.5.1.2 20-1 Data Analysis Using DFT

Being superimposed on the gain spectrum and having such low signal power there is some difficulty in locating the resonance peaks to sufficient accuracy to show a trend with temperature. Smoothing out noise helps but the underlying ASE trend offsets the ripple peaks and must be subtracted. Subtracting the back-facet trace from the front was partially effective but exaggerated the divergence between the two spectra due to the proximity of the instrument noise floor in the front-facet measurement.

The method ultimately employed was to DFFT the spectra, filter them into low, medium and high spatial frequencies corresponding to the gain envelope, the ripples and noise, then IDFFT the ripple frequencies to obtain a smoothed signal which could be differentiated to locate the points of inflexion. **Figure 7-17** shows the three frequency ranges used in this case, IDFFT'd back into power-wavelength axes. The reason that the noise signal disappears over the ripples is that the ASE spectrum was measured in log units, rendering noise insignificant except at very low power levels.

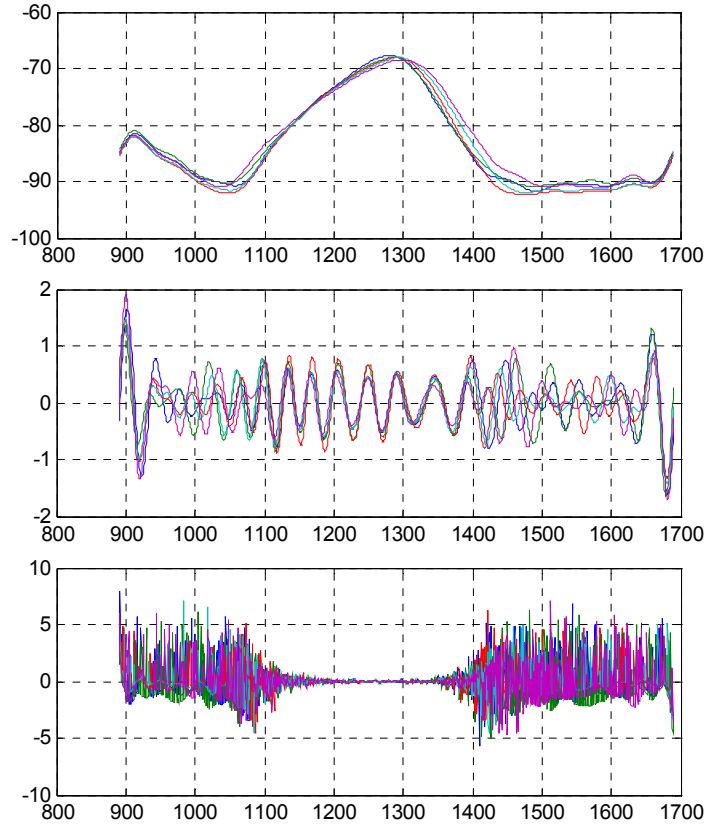


Figure 7-17 *DFFT-filtered Device 20-1 ASE spectra (Figure 7-16) (signal power in dBm vs. wavelength in nm)*

Top – large corresponding to the gain envelope (>29nm wide).
Middle – smoothed ripples.
Bottom – noise (features <15nm wide).

Seven ASE ripples are observable. If each is normalised about its mean wavelength over temperature and they are plotted together an interesting trend emerges:

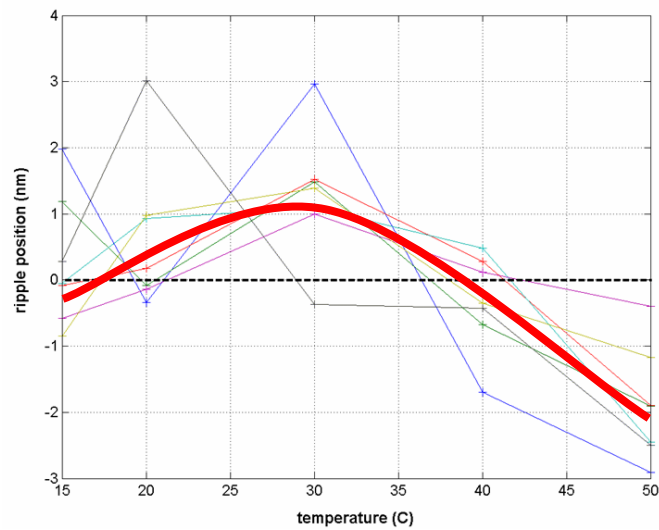


Figure 7-18 *Device 20-2 ASE ripple positions normalised about their mean positions over temperature.*

The two outlying traces represent the outlying ripples (the first and seventh). The thick line indicates the trend.

The rollover is unexpected and not predicted by modelling. Whether or not it is a real effect is questionable, it could be some effect of carrier density or, despite the care taken, an artefact of the peak-location process.

7.5.1.3 Determination of Refractive Index from 20-1

Using the ripple positions at 20°C obtained from the DFT analysis the root-mean-square (RMS) difference between modelled and observed mode positions was calculated for a range of possible cavity effective refractive indexes. An effective phase index of 3.487 gave the best fit.

Rather than use the cavity model, the mode positions were calculated using the resonance condition and the RMS difference recorded whenever the wavelength window contained six modes, to match the six ripples (**Figure 7-19**). This means no account was taken of the grating, but feeding the refractive index thus obtained into the cavity model gives reasonable agreement (**Figure 7-20**).

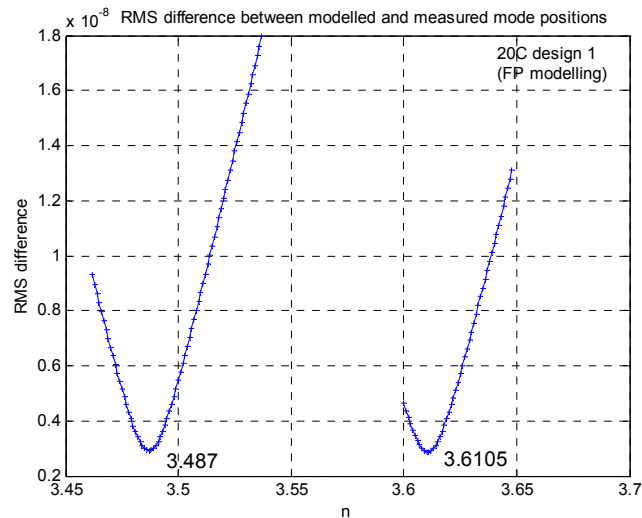


Figure 7-19 RMS difference between modelled and measured mode positions for a range of effective phase indices for a 5.15 μm FP cavity (device 20-1).

Minima occur for $n=3.487$ and $n=3.612$.

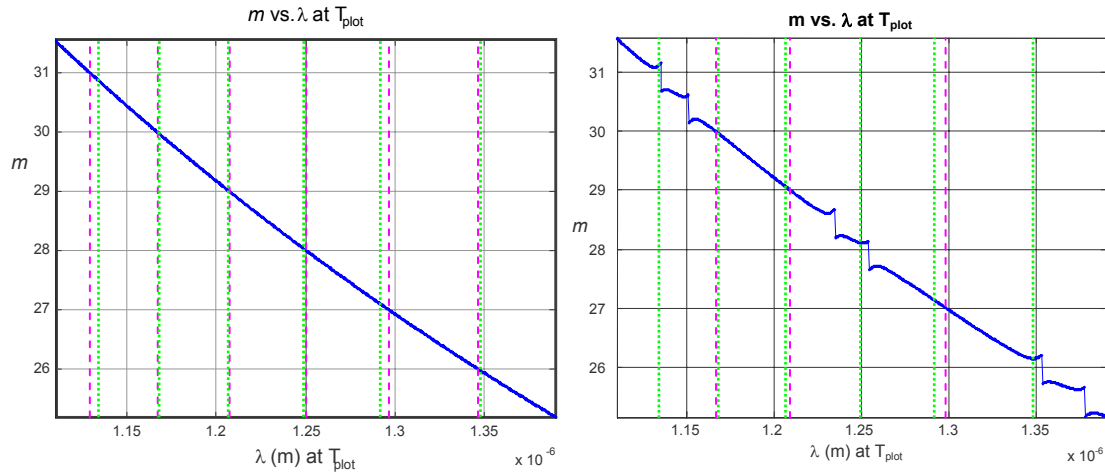


Figure 7-20 Modelled cavity phase slope and mode positions derived from it for $n=3.487$, with (right) and without (left) grating.

Modelled as cleave-cleave InP cavity at 20°C , $n_{\text{InP}}=3.487$. Wavelengths marked with dotted lines are measured mode positions, dark dashed lines are modelled mode positions.

7.5.2 Devices 36-3 and 35-4

In an attempt to obtain lasing by reducing mirror loss a similar design was produced, having gratings at both ends of the $5\mu\text{m}$ cavity and four periods of each instead of three. The same material parameters were used. Again the far facet was angled, and additionally the near facet was etched to provide exact grating tooth dimensions. This was performed in two stages – first a trench etch like the other grating trenches so that the same amount of redeposition on the sidewalls could be assumed, then a facet etch from that trench to the end of the laser.

Device 36-3 was a 5QW device similar to 20-1 and 20-2, but 35-4 was a 7QW device. This should have more gain and is $350\mu\text{m}$ long but is otherwise similar. All subsequent modifications were performed on similar 7QW devices.

No light could be detected at the front facet. Both devices emitted only unmodified ASE spectra from the back facet, because the short cavity did not lase and any resonances in emitted ASE were too weak to pass through the gratings, as previously observed in device 20-1, where no ASE ripples were observed at the back facet.

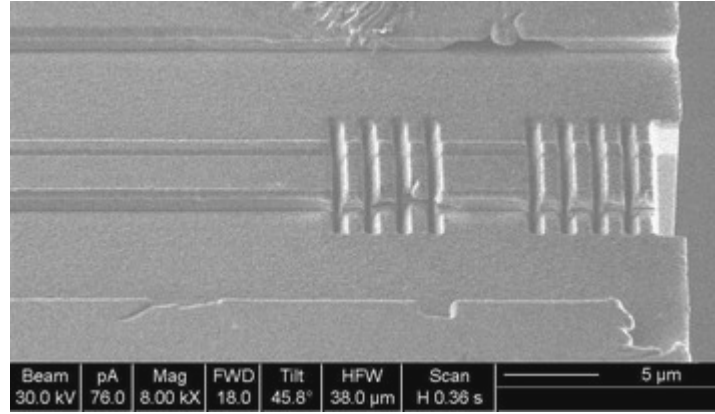


Figure 7-21 FIB close-up of device 35-4 grating and cavity.

Specified dimensions: 260nm air gap, 1390nm semiconductor teeth, 5000nm cavity. Note the high aspect ratio of the trenches, apparent in this perspective view.

Transmission and reflection experiments were attempted using fibre lenses to couple light from tunable sources in to the devices, but no clear results were obtained. In such experiments it is necessary to use emitted light to align the fibre lenses; having a deep grating at one end and an angled facet at the other made this impossible.

7.5.3 Device 55

Essentially the same design as device 35-4 but etched well away from either facet on a chip with previous, failed etches. Neither facet was angled. This configuration effectively placed an interrupted grating at one end of a long cavity. There was some doubt about the etch dimensions due to beam drift, the specifications were $L_{air}=252\text{nm}$, $L_{InP}=1348\text{nm}$, $L_{cavity}=4850\text{nm}$ and this was modelled as having a reflectivity peak at 1310nm with the first null on the long-wavelength side at 1327nm.

Using the mode-spacings technique an empirical formula for group index as a function of wavelength λ (nm) and temperature T ($^{\circ}\text{C}$) in the ranges 1260-1340nm and 10-50 $^{\circ}\text{C}$ was obtained:

$$n_g \approx (0.1259 \times 10^{-4} T - 18.20 \times 10^{-4}) \lambda + (5.889 - 0.01582 T) \quad (\text{E7-10})$$

This gives $n_g=3.5104$ at 20 $^{\circ}\text{C}$ and 1315nm with dn_g/dT of $7.36 \times 10^{-4}/^{\circ}\text{C}$ and $dn_g/d\lambda$ of $-1.57 \times 10^{-3}/\text{nm}$.

The long cavity to the right of the grating in **Figure 7-22** is 296 μm long and at first did not lase. After annealing at 220 $^{\circ}\text{C}$ for 40 minutes the device lased under constant drive with somewhat higher thresholds than before etching, although only minor improvements in VI characteristic were observed.

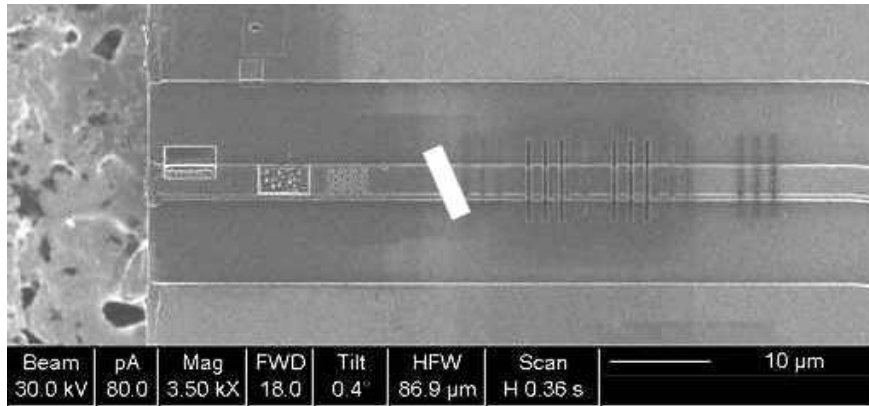


Figure 7-22 Device 55.

Failed 2D grating etches are visible at the left, the grating pair is on the right. An angled trench was subsequently etched at the position indicated to prevent coupled-cavity effects.

The emission spectrum (**Figure 7-23**) showed resonant modes in an envelope formed by the material gain profile and the mirror reflectivity spectrum. The reflectivity minimum is at 1315nm at 20°C, not 1327nm as modelled. It drifts at 0.10nm/°C.

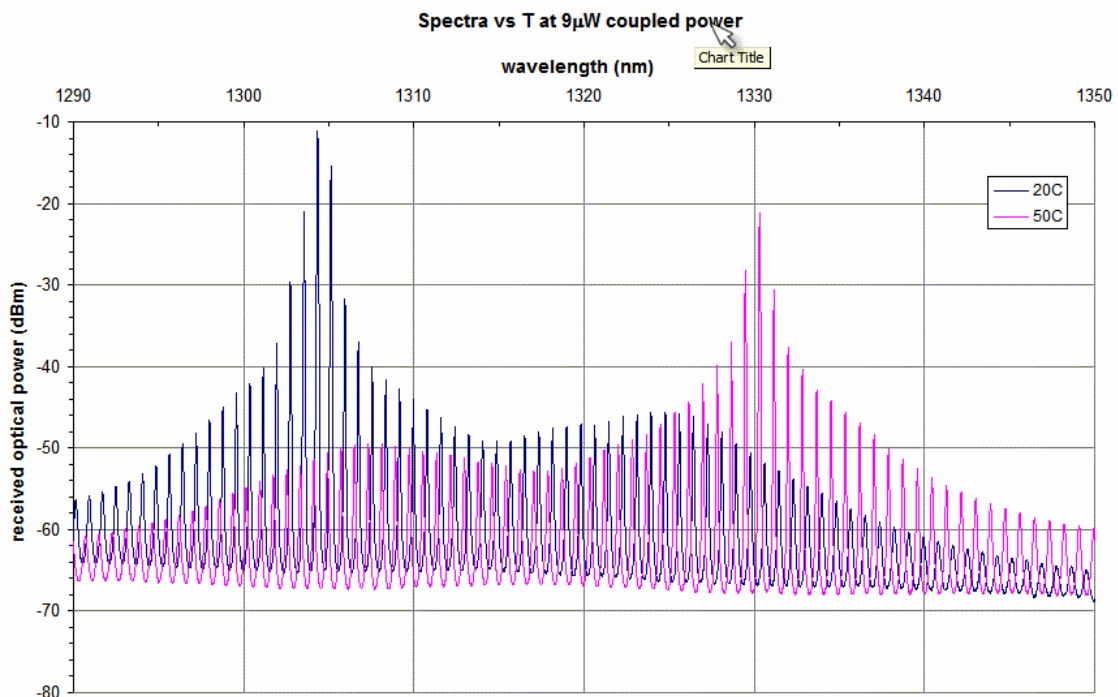


Figure 7-23 9μW emission spectra for device 55.

The spectral structure is attributable to the grating reflectivity spectrum, with the trough in output corresponding to a minimum in grating reflectivity. The trough lies at 1315nm at 20C.

The modes showed no peculiar drift characteristics (**Figure 7-24**), as expected - the cavity is approximately 1450 half-wavelengths long and its phase contribution dwarfs that of the grating. It was found that modelling the modes using n_g and dn_g/dT gave drift rates a factor of 2.49 too high. Given that n_g may be reasonably expected to be up to 10% different from n , whereas

dn_g/dT is a relative unknown, examination of (E5-22) suggested that dn_g/dT is approximately 2.49 times greater than dn/dT .

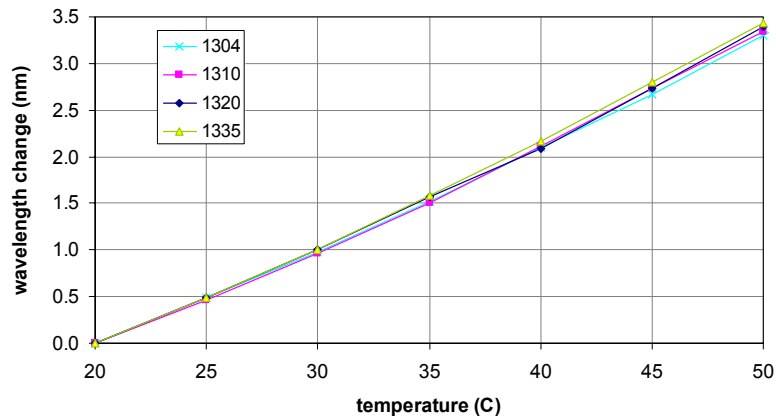


Figure 7-24 Relative drifts of four modes in device 55 emission spectrum, positioned at indicated wavelengths at 20 °C

The modes were tracked by eye on an OSA as device temperature was increased. They were chosen to be in areas of the spectrum corresponding to grating features. The drift rates, from short to long wavelengths, were 0.1102, 0.1121, 0.1127, 0.1150nm/°C

The anomalous position of the reflection minimum was attributable either to incorrect phase index in the model or to incorrectly-etched air gaps. A modelling space calculating the grating reflectivity for a range of combinations of air gap and cavity index was constructed (Figure 7-25).

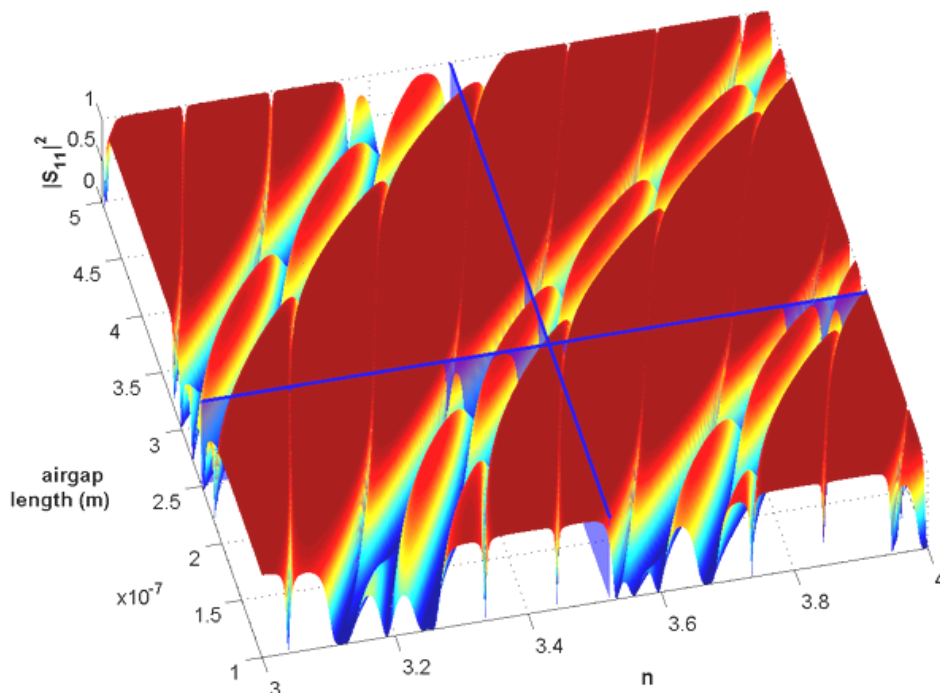


Figure 7-25 External reflectivity at 1315nm & 20C of device 55 grating for a range of air-gaps and phase indices.

The crossed lines indicate the design point.

If it is accepted that the air gaps are as designed, a reflectivity trough is obtained at 1315nm for a phase index of 3.487 (**Figure 7-26**). This result, independently arrived at, confirms that from the mode spacings of device 20-1.

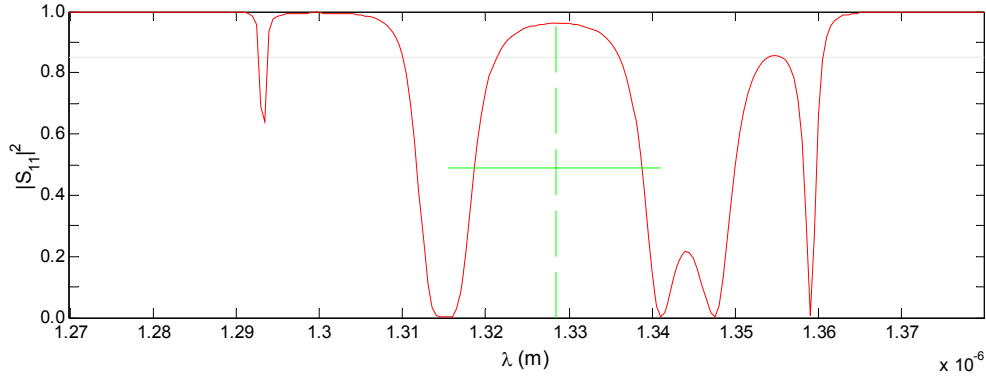


Figure 7-26 Modelled grating reflectivity spectrum at 20°C for device 55 using $n=3.487$

Looking from the waveguide, outside the grating. The trough at 1315nm is a good match to that observed in **Figure 7-23**.

The thermal dependence of the effective phase index may now be obtained. First recall the resonance condition:

$$m = \frac{2 n(\lambda, T) L(T)}{\lambda_{res}} \quad (\text{E7-11})$$

where m is the resonance order. Make λ_{res} the subject and differentiate with respect to temperature:

$$\frac{d\lambda_{res}}{dT} = \frac{2}{m} L_{def} \left[\left(1 + CTE(T - T_{def}) \right) \frac{dn|_{\lambda,T}}{dT} + n|_{\lambda,T} CTE \right] \quad (\text{E7-12})$$

Taking $CTE = 5.4 \times 10^{-6}/^\circ\text{C}$, neglect both terms containing it and rearrange to give

$$\frac{dn|_{\lambda,T}}{dT} = \frac{d\lambda_{res}}{dT} \frac{m}{2L_{def}} \quad (\text{E7-13})$$

Substitute (E7-11) back in for m to give

$$\frac{dn|_{\lambda,T}}{dT} = \frac{d\lambda_{res}}{dT} \frac{n|_{\lambda,T}}{\lambda_{res}} \quad (\text{E7-14})$$

At 1314.89nm and 20°C we find a mode with drift 0.1124nm/°C. We have already found that $n_{eff}=3.487$, so we obtain $dn/dT = 2.98 \times 10^{-4}/^\circ\text{C}$ for the effective cavity index. This is $^{1/2.47}$ of dn_g/dT , which is very close to the $^{1/2.49}$ predicted.

7.5.4 Conclusions

Although drift modification may have been observed in the resonances in the ASE spectrum of device 20-1, it is not certain that this was not an artefact of the measurement process. Since no resonances were observed in the other devices, the athermalisation concept can not be validated nor disproved.

The chief obstacle to achieving this objective is that the short-cavity devices do not lase. Analysis of spectra from devices 20-1 and 55 gave measurements of cavity effective index, and its rate of change with temperature. Observations of etched features show less than $\pm 20\text{nm}$ deviation from specification. Modelling based on these parameters accurately reproduces key spectral features, confirming the validity of the models and the parameters both. Grating reflectivity in all devices, excluding diffractive losses in the air gaps, is expected to be high, as designed. Mirror losses being low, the absence of lasing can only be explained by insufficient gain.

This is not entirely unexpected, as the shortest reported edge-emitting DFB is $12\mu\text{m}$ long [2]. With this in mind the feasibility of short cavities was investigated, with assistance from Dr. K. Williams of C.U.E.D. Based on the gain condition, an approximate calculation was made of minimum cavity lengths necessary for lasing given a selection of typical material gains and a range of facet reflectivities (**Figure 7-27**).

It was noted that threshold carrier densities become very high for low facet reflectivity. If a maximum possible carrier density of $3.7 \times 10^{18}/\text{cm}^3$ is assumed, it is apparent that a device with one cleaved facet can not lase at $< 80\mu\text{m}$ cavity length. Full DBRs with 70% reflectivity can not lase with $< 45\mu\text{m}$ cavity length. $5\mu\text{m}$ cavities (devices 20-1, 36-3, 35-4) are out of the question without extremely high-reflectivity mirrors.

Further considerations apply to these, as modified FP devices. First, the deep etches pass through the active layer and may introduce parallel current paths, reducing available gain. However, I-V characteristics do not support this, showing little change after etching. Second, the entire top surface is coated with gold, contacting the semiconductor along the ridge waveguide. Short cavities created by FIBE are optically, but not electrically, isolated – the non-resonant remainder of the device is driven along with the short cavity. This limits the drive-current densities which can be applied. Performing contact-separation FIB etches could ameliorate this.

Short cavities being necessary for this athermalisation scheme, means of increasing gain were investigated.

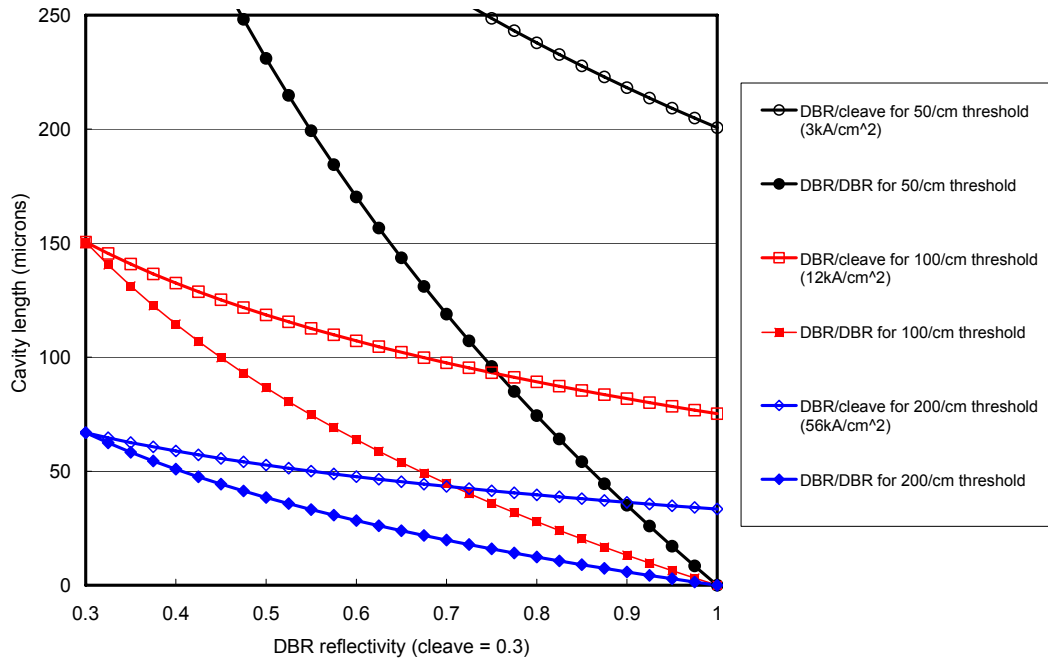


Figure 7-27 Required cavity length for DBR lasers, vs. mirror reflectivity, for material gain of 50/cm, 100/cm and 200/cm

$3.7 \times 10^{18}/\text{cm}^3$ carrier density (for 100/cm threshold gain) can be considered as high as possible using linear theory. Note that at this gain, a DBR of $50\mu\text{m}$ cavity length requires 67% reflectivity for both mirrors, $25\mu\text{m}$ requires 85% and $10\mu\text{m}$ requires 92%.

7.6 Serial Microcavities and Active Elements

Designs were investigated which aimed to increase total gain by placing athermalised cavities in series along the waveguide.

7.6.1 Device 69

This design used the material parameters obtained from device 55. It was conceived as an offset-grating short cavity (**Figure 7-28**), using different grating drifts to athermalise the resonant mode (**Figure 7-29**), cascaded together to reduce the gain requirement (**Figure 7-30**). The far facet was angled.

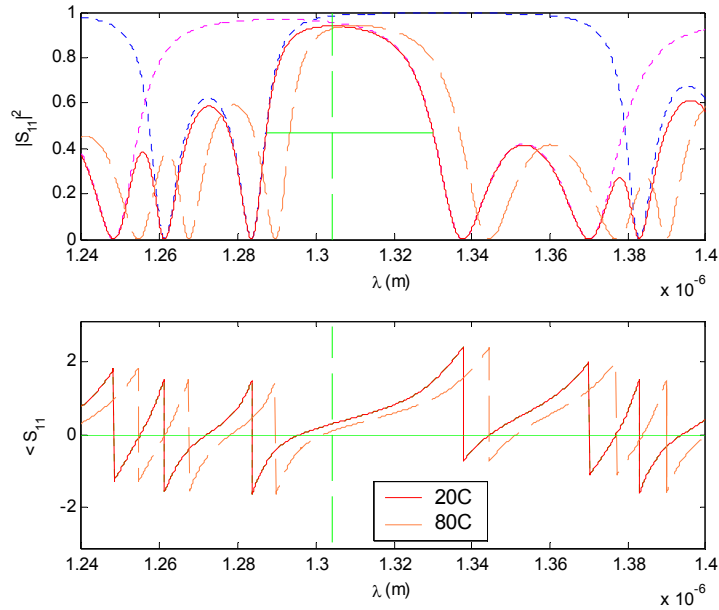


Figure 7-28 Device 69 offset grating, reflectivity (top) and phase (bottom).

Reflectivity peak drifts at 0.105nm/°C.

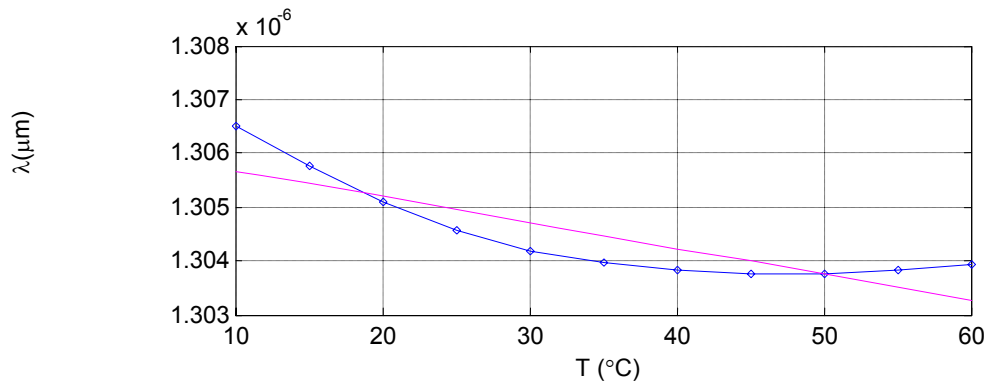


Figure 7-29 Modelled least-loss cavity mode position vs. temperature, device 69.

The mirror's different drift rates cause the mode to change drift direction. The average drift rate is -0.0048nm/°C.

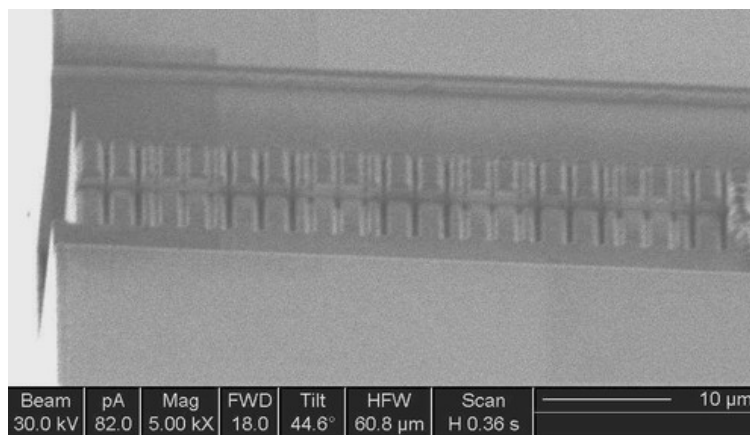


Figure 7-30 FIB image of part of device 69 cascaded short athermal cavity design, total length 51 μm.

The etched facet is clearly visible. Grating 1 dimensions: 1985nm teeth & 447nm air gaps. Grating 2: 1984nm & 120nm, respectively. 1113nm cavity.

Although the whole grating is active only the intended cavities have a resonant mode in the Bragg peak. However lasing was not obtained and the expected spectral features were not observed. Modelling indicates that the light in the spectra (**Figure 7-31**) originates in only the top two or three ‘teeth’ of the grating. This suggests there is very little coupling of light from one cavity to the next and each must still reach threshold as though individually.

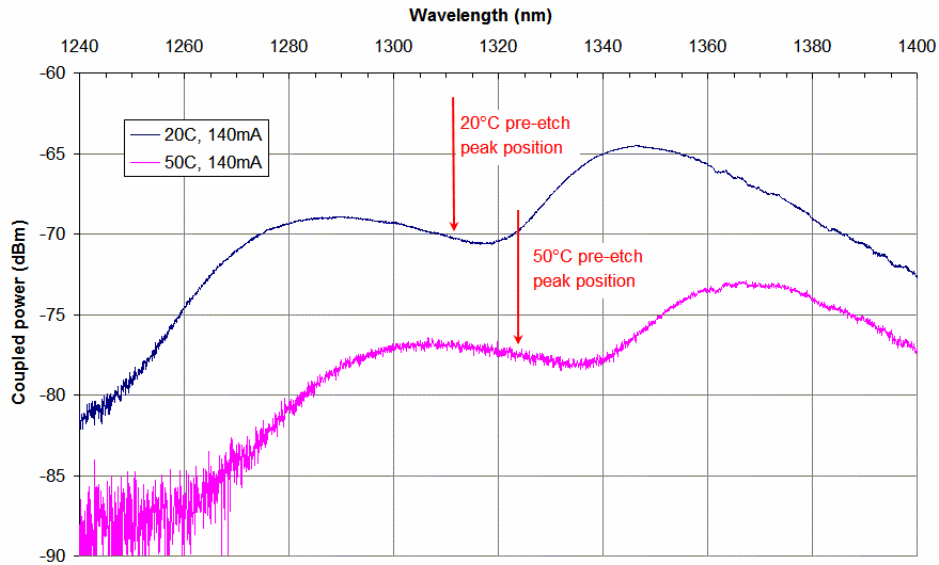


Figure 7-31 Post-etch post-anneal ASE spectra for device 69, at 140mA, 20°C and 50°C.

Drift rates: trough 0.630nm/°C, peak 0.680nm/°C, pre-etch gain peak 0.467nm/°C

Annealing this device caused a significant deterioration in I-V characteristic. This was attributed to solder creep up the device sides due to softening at 220°C.

7.6.2 Active Grating Survey

Short cavities with high-order mirrors are necessary for athermalisation with air-gap designs. In this situation the gratings may be many times bigger than the cavity itself. Designs where the cavity length is the same as the length of the semiconductor part of the grating are therefore very appealing – the situation then is a cascaded series of athermalised laser cavities which pump one another, separated by dielectric gaps. This is an *active* grating, analogous to a DFB.

This section describes two methods of identifying candidate designs.

7.6.2.1 Changing material ratio within constant grating period

Semiconductor:air ratio can be varied while maintaining the same grating period. Doing so changes the drift rate of the Bragg peak. As seen in §7.3, varying the composition of the period also moves the reflection peak and hence its phase contribution. For a grating with a given Bragg wavelength and material pair some grating drifts therefore give a cavity mode in the

Bragg peak. A survey of mode drift against grating drift and grating order was made for an InP:air 1300nm grating (**Figure 7-32**).

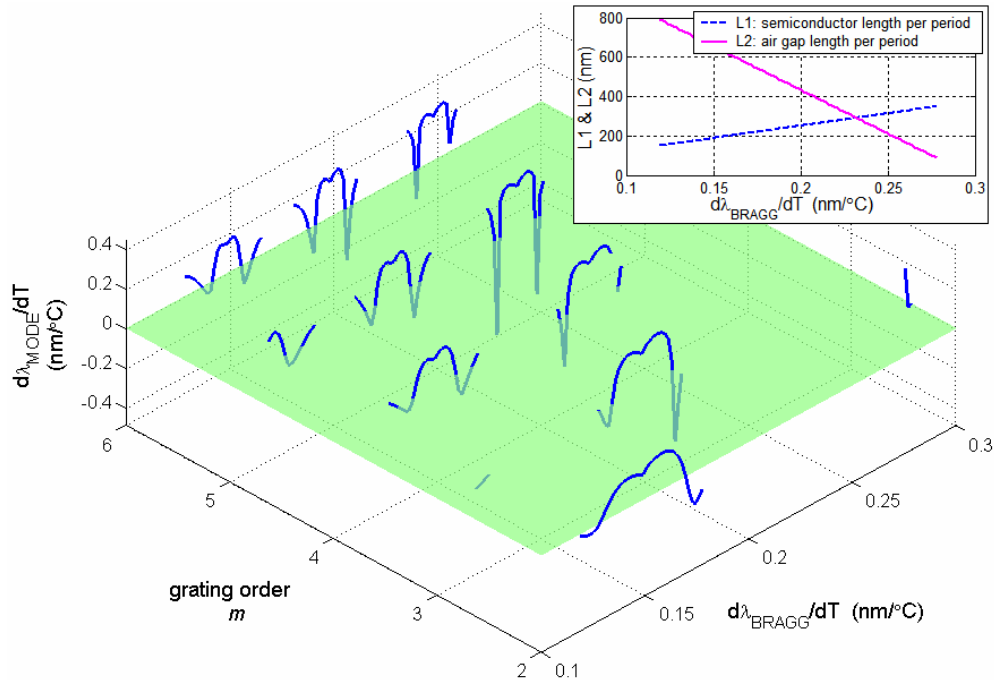


Figure 7-32 Drift rates available for 1300nm InP:air ‘deep DFB’

Cavity length is identical with the width of the semiconductor ‘teeth’, which is determined by the proportion of air to semiconductor (indicated here by drift rate – see inset for 1st-order dimensions) in the fixed optical length of the period.

The negative-drift troughs apparent in **Figure 7-32** require fabrication precision of better than 12nm.

7.6.2.2 Changing period of grating with constant material ratio

Choosing a suitable ratio to model this design space with is a trade-off between large air gaps with their associated diffraction losses and short air gaps with high grating drift. A one-to-one ratio of physical lengths was modelled.

Figure 7-33 (top) shows cavity modes moving across the Bragg peak as the grating period is increased. It is required that candidate designs emit near the gain peak of the device, 1320nm.

The survey located fortuitous combinations at which the phase contribution of the rest of the grating cancels out expansion of any individual ‘tooth’ (**Figure 7-33**, middle). This would be less effective in the periods near the ends of the device.

The mode-search window is the gain bandwidth of the Agilent ridge-waveguide devices obtained for modification, rather than the width of the Bragg peak. Some detected modes are likely to be in sidelobes of the Bragg peak therefore, with correspondingly higher required gains (**Figure 7-33** bottom).

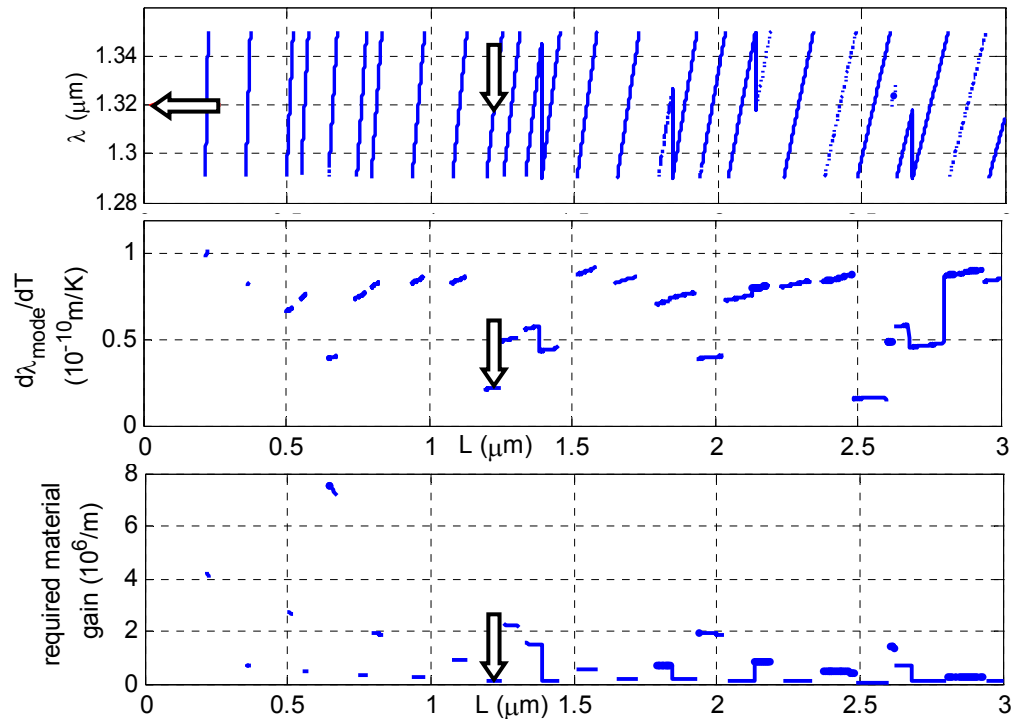


Figure 7-33 Modelled lasing modes of 1:1 air:semiconductor ‘deep DFB’ vs. cavity length L (half-period)

TOP – lasing wavelength

MIDDLE - lasing mode thermal drift rate

BOTTOM - material gain necessary for the least-loss mode to lase. The low-gain modes are in the Bragg peak, the higher-gain ones are not.

The arrows in the figures indicate an optimum design point at 1250nm cavity length combining low drift (0.02nm/°C) and low required-gain (1120/cm for a single 1.22μm tooth, which translates to 56/cm for 20 periods). The losses due to the relatively large air gap are not modelled and mean this estimate of required gain is too low.

7.6.3 Devices 88, 89 and 90

Three 1:1 semiconductor:air ratio designs were taken from the active grating survey. These designs were attractive for their potential to solve the gain problem and also for the relative insensitivity to fabrication errors apparent in the survey plots (**Figure 7-33**).

The three designs, etched in devices 88, 89 and 90, had 13, 14 and 20 periods and half-periods of 1430nm, 1465nm & 1225nm, respectively. 88 and 89 were given angled facets, 90 was not so that following a contact separation etch the long section could be driven independently to optically pump the active grating.

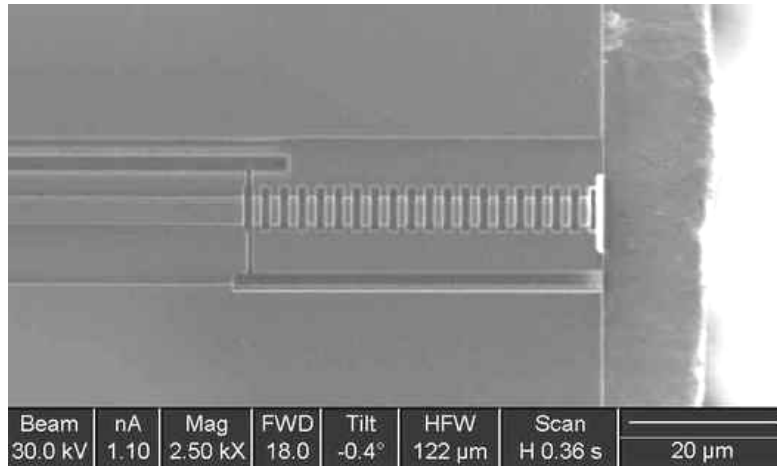


Figure 7-34 Device 90, with half-period of 1225nm, 20 periods.

Also visible is the electrical contact separation etch, isolating the rear section of the waveguide from the grating.

Neither 88 nor 89 lased following etching. Some deterioration in their diode characteristic was observed in I-V plots. Their spectra were similar to that of 69, showing no clear structure apart from a dip in the middle of the ASE, which drifts to longer wavelengths with increasing temperature at a rate different to that of the ASE peak, suggesting it originates in the grating characteristics.

The dip is difficult to explain using the grating model. Modelling two periods only gives a similar-looking trough but not at the right wavelength (inset, **Figure 7-35**). It is possible that pulsed operation would avoid cavity heating and give spectra which matched the model more closely.

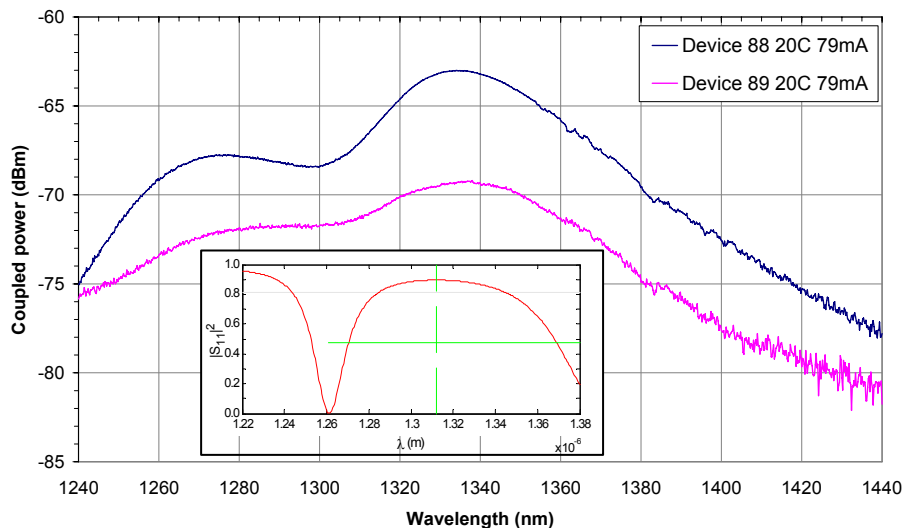


Figure 7-35 Device 88 post-etch ASE spectra various drive currents.

Inset: Modelled reflectivity spectrum at 20C for two periods of device 89.

To enable larger drive current densities a contact-separation etch was performed to electrically isolate the active grating of device 90 from the long waveguide section (**Figure**

7-34). A deep etch was made along the length of the device through the thinner gold in the ridge recess, and a second bond wire attached to drive the grating independently. Inter-contact resistance was 12Ω . However, no light was obtained from the grating section even under grating drive currents up to 20mA (equivalent to 280mA for the whole $350\mu\text{m}$ device). This was most likely due to damage caused to the facet during measurements, but investigation of the IV characteristics indicated that the grating section had also suffered catastrophic damage rendering it essentially ohmic (**Figure 7-36**).

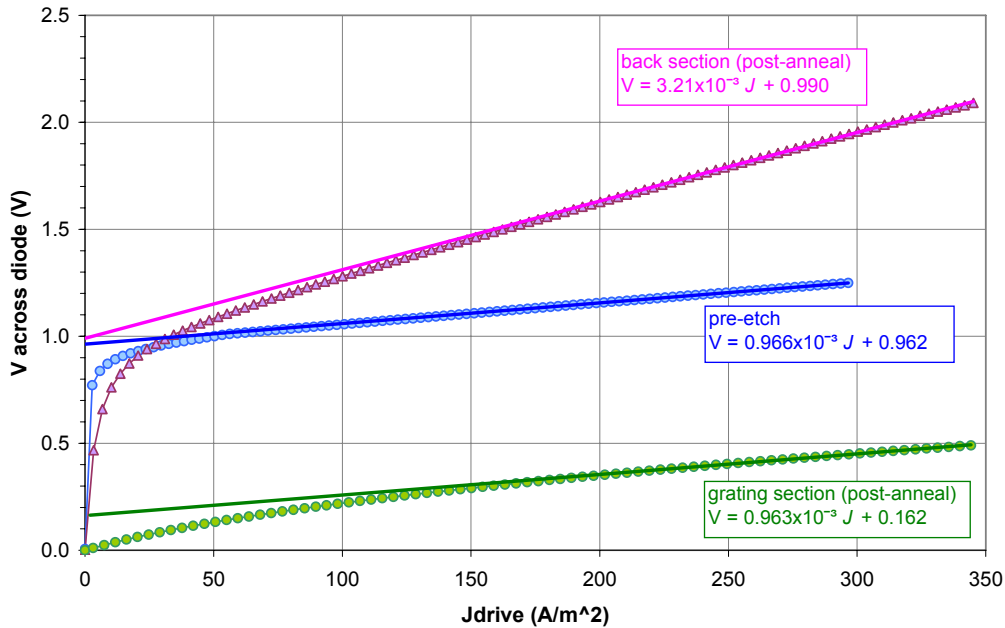


Figure 7-36 Current density J vs. voltage plots for device 90

Plots are given for before etching and for front and back sections afterwards. The linear sections beyond diode turn-on are extrapolated back to the voltage axis. In a diode, the intercept give the junction voltage. Gradients give resistance per unit area but include resistance of bond-wires used to contact the top of the device.

Evidently, parallel current paths have been introduced, attributable either to the facet damage or, significantly, to the etching process itself. In previously etched devices the IV characteristic has uniformly been observed to deteriorate after etching, but not to such a degree. This is the first measurement of an etched region in isolation. It is possible that the IV characteristic was only modified in the small etched region.

This latter possibility is supported by the fact that when the angled facet of device 88 was modified to a flat facet, lasing still proved impossible, although resonant ASE spectra were observed. These showed no unusual spectral features apart from a shifted peak wavelength – 1290nm at 20°C compared to 1326nm pre-etch. Modelling indicates spectral features should have been visible much as in device 55, the fact that none were observed suggests that optical losses due to the large air gaps diminish grating function.

Lasing was initially obtained from the back section of device 90, at higher threshold (35mA instead of 20mA) and with 15dB back-to-front power ratio. However it also was damaged, before spectra could be taken.

The fact that the back section of device 90 did lase, isolated from the grating etch, whereas that of device 88 did not, supports the idea that etching through the active layer significantly degrades current confinement. The problem would be worse in these devices compared to previous ones owing to the larger number of etches.

7.6.4 Electrical Characteristics of Etched Facets

A simple equivalent circuit model of a diode has an ideal diode, a series resistance due to the contacts and along the current path in the device, and a parallel resistance representing current paths circumventing the junction (**Figure 7-37**, left). It is hypothesised that FIB etching through the junction layer introduces such paths.

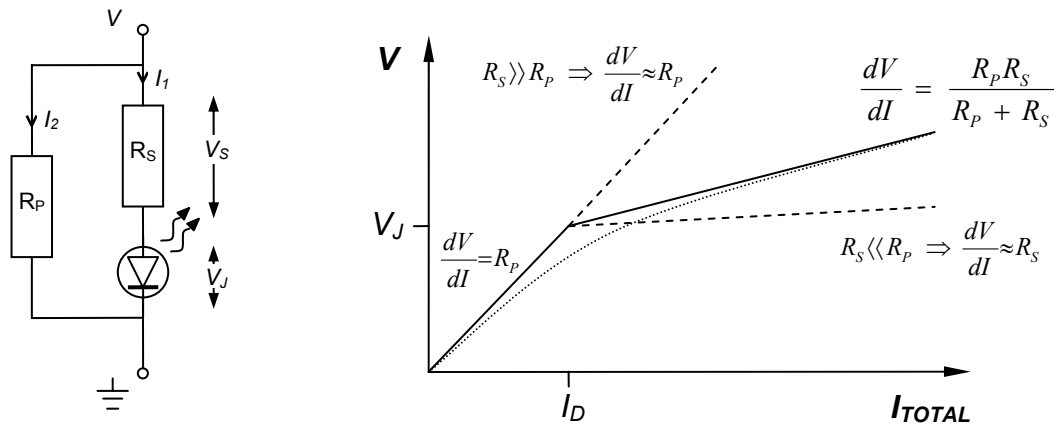


Figure 7-37 Laser diode equivalent circuit (left) and related effect on I-V characteristic (right)

A ‘realistic’ curve is also shown for comparison with the regimes of the equivalent circuit. In a real circuit some current does flow in the diode when the bias is less than the junction voltage.

A first-order analysis of the equivalent circuit has infinite diode resistance until the bias voltage V exceeds the junction voltage V_J , at which point the circuit becomes parallel and current flows in the diode. Total current then is given by:

$$I_{TOTAL} = I_1 + I_2 = \frac{V}{R_p} + \left[\frac{V - V_J}{R_s} \right]_{V > V_J} \tag{E7-15}$$

Rearranging to make V the subject the two cases $V > V_J$ and $V < V_J$ give

$$V = \left[\frac{I_{TOTAL}(R_p R_s) + V_J R_p}{R_p + R_s} \right]_{V > V_J} = [I_{TOTAL} R_p]_{V < V_J} \quad (\text{E7-16})$$

The differential resistance is then

$$\frac{dV}{dI_{TOTAL}} = \left[\frac{R_p R_s}{R_p + R_s} \right]_{V > V_J} = [R_p]_{V < V_J} \quad (\text{E7-17})$$

as shown in **Figure 7-37** (right). In the forward-bias regime this reduces to R_p when $R_s \gg R_p$, as is believed to be the case with the grating section of device 90, and to R_s when $R_s \ll R_p$.

Using (E7-17) estimates of R_p were obtained from the L-I data of the etched devices and plotted against the total length of etched sidewall (**Figure 7-38**).

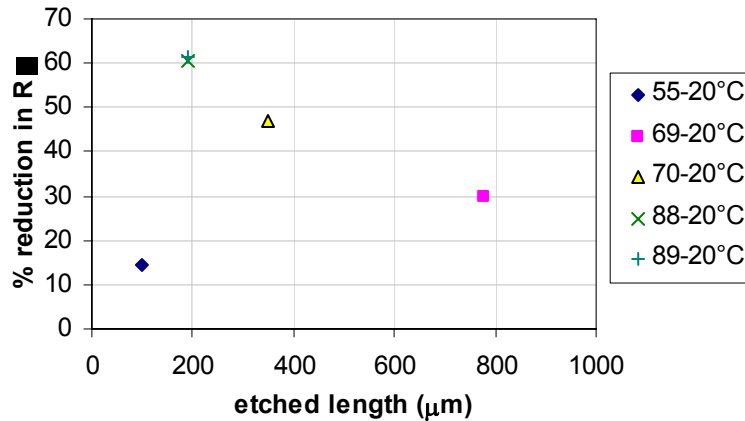


Figure 7-38 Parallel resistance vs. length of etched sidewall, measured from a selection of devices

R_p was calculated from the dV/dI at and above the origin. Frequently, the curvature on the V-I line was such that dV/dI is limited by the measurement resolution. The recorded R_p is then less than the true value, by an unknown factor.

It is clear that etching does decrease parallel resistance, but it is not possible to say it is proportional to the length of etched sidewall. If a trend exists, it may be obscured for two reasons. First, the R_p measurements are perforce not very consistent in terms of where on the IV curves they were taken. Second, the effect of the size of drive-current increments used in recording V-I data is significant. The V-I line is often not clearly divided in to two regimes and curves smoothly over. In such cases low resolution on the current axis (such as was the case for device 69, an outlier in **Figure 7-38**) limits the measurement of differential resistance at the origin.

7.7 Conclusions

It has been established through modelling that certain combinations of short cavity and grating reflector result in athermalisation of the total resonant length, without any necessity for negative grating drift. The fine structure of the drift vs. cavity length relationship suggests high fabrication precision is necessary to take advantage of this, of the order $\pm 5\text{nm}$.

The identification and development of athermal designs is an iterative process, based on rules of thumb relating grating design to reflection spectrum and phase. Grating designs based on narrowing the grating reflectivity peak and increasing the grating drift rate are trialled with a range of cavity lengths and candidate designs identified. A more systematic approach than this iteration would be beneficial in terms of design time and ease of use of the technique.

A step towards this is the adoption of the high-contrast grating version of the Bragg condition, enabling reliable placement of the reflection peak but reducing drift control via choice of material proportions from a continuum to a few discrete design points.

A number of edge-emitting designs were fabricated and although none of the short cavities lased, apparent modification of ASE resonance drift rate was observed in device 20-1 and device 55 provided definite measurements of device RI parameters and verification of the grating model.

Gain calculations showed the cavities were too short to be expected to lase without very high reflectivity (99%) mirrors. Air-gap gratings suffer from lack of guiding in the air gaps, resulting in beam expansion and significant scattering loss at interfaces back into guided sections. It is likely this degrades mirror reflectivity to well below the ideal 99% reported by the grating model, especially for longer air gaps. The 252nm trenches of device 55 evidently are not excessive, proper grating function being observed, but the larger (micron-scale) air gaps of subsequent multiple-microcavity devices are one possible reason for their disappointing performance.

These devices incorporated series of small cavities along the waveguide in order to increase the total gain length. More sophisticated versions incorporated the cavity into the grating structure to create a DFB-type arrangement. None lased and such ASE spectra as could be obtained suggested light only emerged from the top few periods. Electrical isolation of the etched region in device 90 allowed I-V measurements indicating the deep FIB etching process itself severely degrades current confinement in the region of the etch. Evidence from device 88 supported this interpretation.

In summary, while the athermalisation principle appears sound its implementation in edge-emitting devices is severely hindered by etch-induced damage and low mirror reflectivity.

The alternative, vertical format is therefore interesting. VCSELs routinely use short cavities and high-contrast, high reflectivity mirror stacks. They are investigated in the next chapter.

A list of test devices and their parameters are given in Appendix B.

-
- [1] Raffaele, L., De La Rue, R. M. and Krauss, T. F.: ‘Ultrashort in-plane semiconductor microlasers with high-reflectivity microstructured mirrors’, *Optical and Quantum Electronics*, 2002, **34**, (1/3), pp.101-111
 - [2] Rennon, S., Klopf, F., Reithmaier, J.P., Forchel, A.: ‘Quantum-dot microlasers as high-speed light-sources for monolithic integration’, *27th European Conference on Optical Components (ECOC 27) – Proceedings CD*, 2001, Mo.B.2.1

Chapter 8

Reflector Survey and Athermal VCSEL Design Methodology

Vertical Cavity Surface Emitting Lasers (VCSELs) are DBRs with high-contrast Bragg reflectors and very short cavities. Developments in long-wavelength (InP-based) VCSEL technology and in application-specific optical polymers are combined to introduce drift-engineered VCSEL DBRs. A survey of the reflector design space thus opened up forms the basis of a straightforward athermal design approach.

8.1 VCSEL Design Notes

8.1.1 Advantages of VCSEL Technology

VCSEL technology was originally developed in response to downward price pressure on short-wavelength laser diode components. Edge emitting devices can only be tested individually or in bars, after cleaving from the wafer. The manipulation required, even when roboticised, is time consuming and costly. The price advantage of VCSELs stems from elimination of this problem. Being vertically-orientated, VCSELs can be tested *in situ* on the wafer before cleaving, removing the need for precision handling of individual devices.

The slowness of epitaxial growth and the practical difficulty of implementing vertical active structures requires the use of short gain regions. Lasing is made possible by extremely high-reflectivity (>99.5%) Bragg reflectors. These are grown epitaxially so high reflectivity is achieved not by having many periods but by using high-contrast materials, with low grating orders. Structural robustness favours mirror stacks which are not significantly higher than they are wide. Drive current in most short-wavelength (600-900nm) designs is delivered through the mirror stack, effectively confining gain to the region of the active layer where vertical modes see high mirror reflectivity. Total output power increases with the area of the mirror stack. In the original, low-cost short wavelength market for VCSELs this broad area was an advantage, favouring coupling to multimode fibre.

Long-wavelength VCSELs have been a subject of considerable research as 1300nm laser diodes have also experienced commoditisation. Optimising the emission pattern for coupling to single-mode fibre while increasing total power output has begun to be an issue, but the greatest obstacle has been the lack of a high-contrast material pair epitaxially compatible with the established 1300nm material system; indium phosphide.

On the plus side, VCSELs offer two technical advantages over long-wavelength edge emitters. First, the small active volume permits direct modulation to very high rates. Second, as DBRs with short cavities, VCSELs are attractive targets for athermalisation by grating contribution. This is facilitated by the high precision possible in epitaxial growth.

8.1.2 Material Systems

Only recently has significant progress in long-wavelength VCSELs been made [1,2,3]. The problem has been finding a suitable combination of material system and epitaxial reflector technology.

At short wavelengths GaAs and AlAs serve admirably as reflector stack materials. They have high refractive index contrast, have similar lattice constants, and, doped, permit current injection through the mirrors. AlAs can also be selectively steam oxidised to create amorphous aluminium oxide ('AlOx') which is an insulator with low refractive index, facilitating fabrication of current and optical confinement structures.

No equivalent material pair exists for the long-wavelength InP material system. GaAs and AlAs can not be grown on indium phosphide substrate, which has a larger lattice constant (GaAs lattice constant = 5.65Å, InP lattice constant = 5.87Å). Although steam oxidation of AlIn, which can be lattice-matched to InP, is possible it is either extremely slow or requires very high temperatures (>500°C), degrading the device. InP and InGaAsP are the best native options but suffer from low refractive index contrast, requiring up to 60 periods to achieve sufficient reflectivity.

Much work has been done on alternative materials for both the active region, such as indium gallium arsenide nitride (InGaAsN) quantum dots [4], and for the DBRs [5,6,7]. Considerable effort has also been expended on combining GaAs reflectors with InP active layers by amorphous deposition, growth on patterned substrates, novel growth methods or wafer fusion [8,9,10,11]. One of the most successful approaches has been to use dielectric reflector stacks with intracavity electrical contacts [12,13,14,15]. Some groups have succeeded in making InP-native reflector stacks using a novel material: air [16,17]. As with deeply-etched air-gap edge gratings these devices could be infilled with optical polymer (**Figure 8-1**).

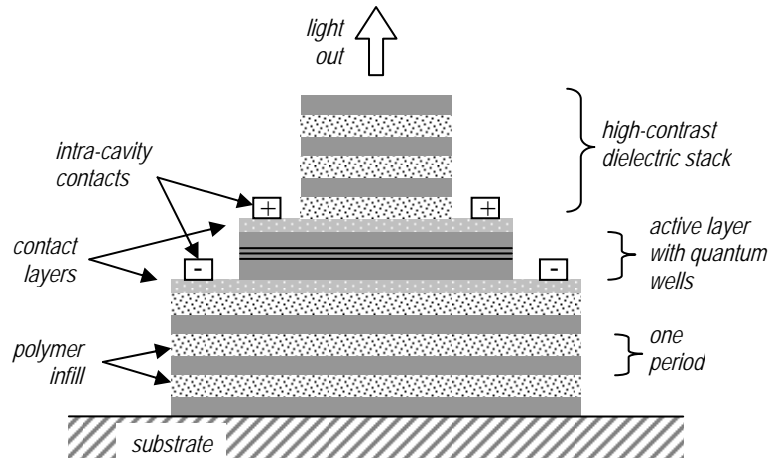


Figure 8-1 Schematic of long-wavelength VCSEL with intracavity contacts and dielectric reflector stacks

High-contrast dielectric reflector stacks mean only a few periods are necessary to achieve the 99.8% reflectivity typically required by VCSELs. They are also compatible with an InP-based active layer. It is necessary during fabrication to incorporate a support structure for the crystal layers, but the cost advantage of on-wafer testing capability is preserved.

8.2 Hybrid VCSEL Designs

8.2.1 Why Hybrid?

Hybrid VCSEL designs use different material systems for the top and bottom reflectors. Often this is so as to have a bottom mirror compatible with the active region material system; such structures offer at least one direct current injection path, simpler fabrication, robustness and good thermal conductivity. Top mirrors are also usually more accessible for etching and oxidation purposes, and are required to be less reflective. In terms of athermalisation, combining mirror systems offers a greater range of design options, which are limited by the range of material systems available.

Reported air-gap designs are often hybrids owing to the thermal problems experienced by cavities with air-gaps both above and below. Investigations were carried out to investigate the properties of such mirror pairs and identify athermalised cavity lengths.

8.2.2 Influence of Reflector Drift

An investigation was conducted into the influence of grating drift rate on mode drift in hybrid and double air-gap VCSELs. A range of air-gap reflector designs were prepared.

8.2.2.1 Reduced-drift VCSEL mirror designs

The low-contrast Bragg condition was used in designing InP:air top mirrors in order to allow control of grating drift, although the low-drift version was close to being a standard $\lambda/4$ stack.

8.0 Reflector Survey and Athermal VCSEL Design Methodology

Reflectivities >99.5% were nevertheless obtained for most orders of the two higher-drift designs. Owing to the low TOC of air all the top-mirror designs exhibited lower drift than that of the bottom mirror. Three grating orders modeled for each of the top-mirror designs in order to give a range of phase slopes, giving nine designs in total (**Table 8-1**). The bottom mirror was a standard InP:InGaAsP quarter-wave stack.

Table 8-1 1320nm Reflector design parameters

design	L InP (nm)	L air (nm)	drift (nm/°C)	3dB BW (nm)	order m	periods
1	100	339	0.040	1454	1	3
2	301	1017		396	3	
3	502	1694		232	5	
4	137	222	0.055	1342	1	
5	274	443		522	2	
6	685	1108		204	5	
7	174	104	0.070	1006	1	
8	521	313		370	3	
9	868	521		170	5	
10	109	103*	0.087	61	1	70

* Design 10 is an InP:InGaAsP bottom-mirror for hybrid designs. All designs had >99.5% reflectivity except design 7 (96.0%)

Reflectivity spectra and corresponding reflection phases of the nine air-gap mirrors are plotted in **Figure 8-2**.

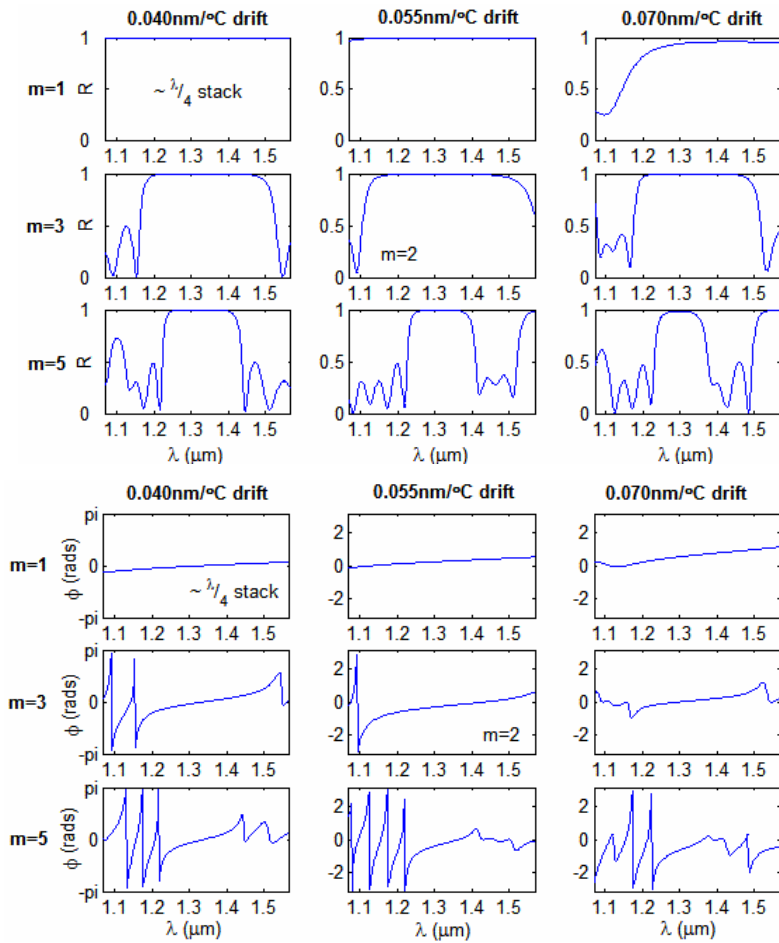


Figure 8-2 Reflectivity spectra (top) and corresponding reflection phases (bottom) of the nine air-gap mirror designs.

Note that the bottom mirror stack (**Figure 8-3**) has significantly narrower Bragg peak and so steeper mirror phase slope than the air-gap mirrors, which are broad due to their high refractive index contrast.

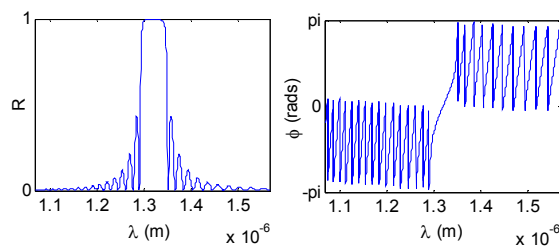


Figure 8-3 Reflectivity spectrum (left) and corresponding reflection phase (right) of 70-period quarter-wave InP-InGaAsP bottom DBR

Modeled mode drift rates were surveyed against cavity length for each top-mirror design, in hybrid and symmetric formats. It was expected that higher orders (narrower Bragg peak, steeper reflection phase slope) and higher grating drifts (faster change in effective-length contribution) would athermalise longer cavities.

8.2.2.2 Hybrid (air-gap and InP-InGaAsP reflectors) results

The drift of the least-loss mode in the InP gain window (~1275-1375nm) was determined for a range of cavity lengths for the nine air-gap top-mirror designs with the InP-InGaAsP bottom mirror, measured over 10-30°C and 1-3000nm (just over 7λ at 1320nm) in 1nm increments. These drifts are plotted in **Figure 8-4**.

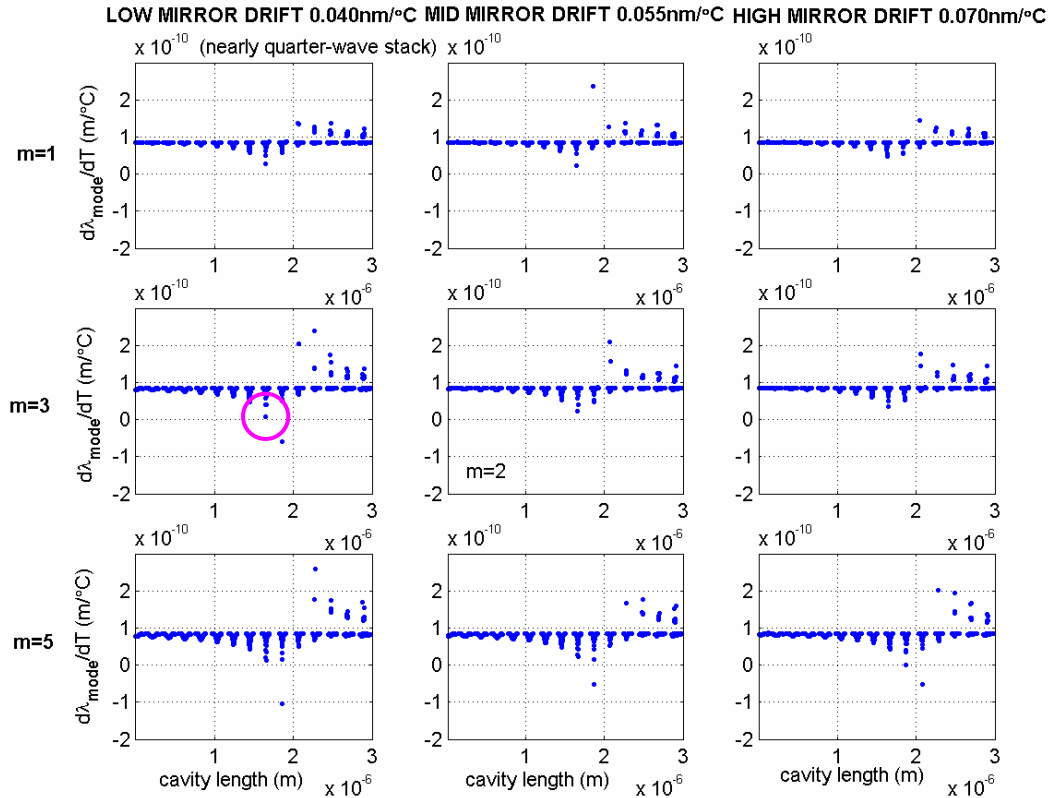


Figure 8-4 Mode drift rate vs. cavity length for a quarter-wave InP-InGaAsP bottom DBR with nine different air-gap top reflectors (see Figure 8-2)

Note that the bottom grating spectrum is completely within the 1275-1375nm search window and so the steep phase slopes at its edges contribute many features of these plots.

There is little difference between the plots for the 9 different top mirrors, indicating that the bottom mirror dominates the behaviour. This is as expected – its narrow Bragg peak gives it a steep reflection-phase slope compared to the air-gap reflector and the cavity phase slope. It dominates the cavity phase completely up to cavity lengths of approximately 2μm. However, this dominance means the cavity length contributions are still unbalanced and are determined by the mirror drift except in very particular circumstances. The majority of mode drift rates below 2μm are indeed observed to be around 0.087nm/°C, the mirror drift rate (**Table 8-1**).

Selecting the circled design in **Figure 8-4** - a three-quarter wave top stack with 1652nm cavity - **Figure 8-5** plots the total phase length of the cavity vs. wavelength at 10°C intervals from 10 to 80°C.

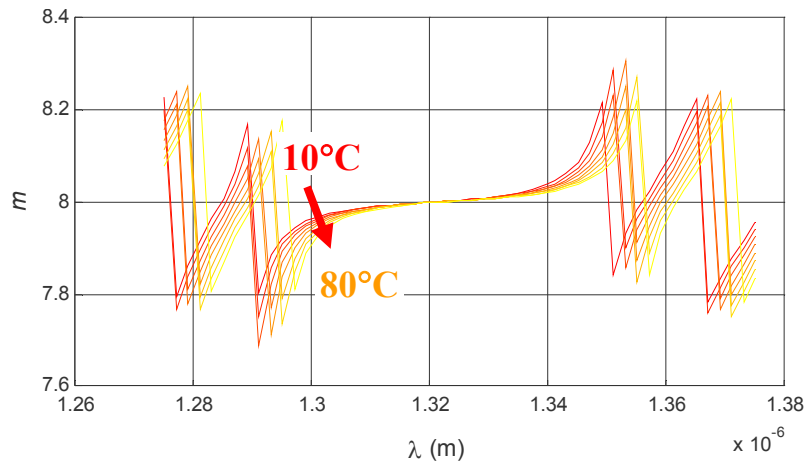


Figure 8-5 Total phase-length in half-wavelengths m vs. wavelength for 1652nm cavity with InP-InGaAsP quarter-wave bottom DBR and design 2 top DBR.

Note that the phase line crosses $m=8$ at $\sim 1320\text{nm}$ for all temperatures. The Bragg peak of the bottom mirror is responsible for most of the structure - that of the top mirror is wider than this wavelength window.

The low drift arises as the different movements in phase contribution cancel out at 1320nm.

Figure 8-6 plots the drift of the $m=8$ mode:

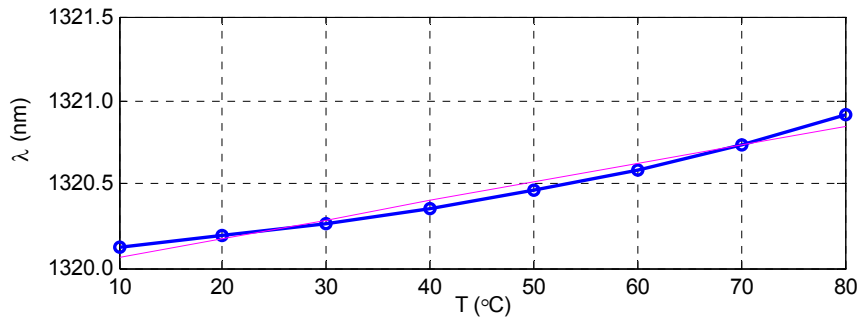


Figure 8-6 Wavelength of least mirror-loss mode of 1652nm cavity with InP-InGaAsP quarter-wave bottom DBR and design 2 top DBR vs. temperature.

An average drift rate of $0.011\text{nm}/^\circ\text{C}$ is evident.

A drift of $0.01\text{nm}/^\circ\text{C}$ is realised, 12% of normal drift. The cavity length precision required to obtain this reliably is $\pm 1\text{nm}$, with $\pm 2.5\text{nm}$ to achieve a reliable halving of drift. To investigate what the yield of low-drift devices might be given a 2% standard error on layer thickness, the same design was modelled 3000 times with random errors on the thickness of each layer (**Figure 8-7**). Very few specimens showed low drift and it must be concluded that given this level of fabrication error more error-tolerant designs are necessary.

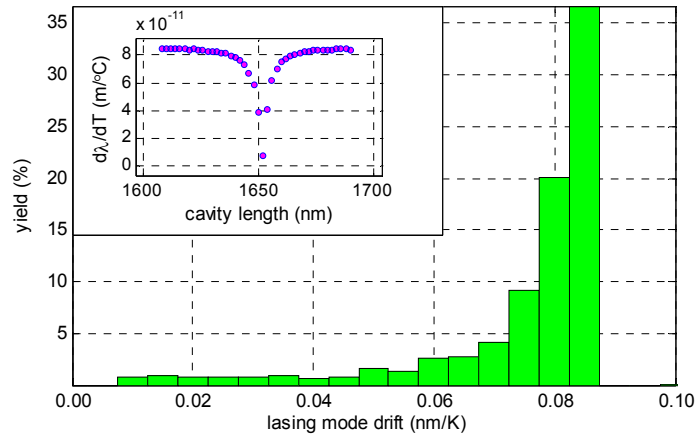


Figure 8-7 Drift-rate yields from 3000 simulations of the design used in Figure 8-6 with 2% standard error on cavity and stack thicknesses.

Inset: enlargement of appropriate part of the 3rd-order low-drift-mirror cavity-length survey of Figure 8-4.

8.2.2.3 Symmetric (double air-gap reflectors) results

A similar set of cavity-length surveys was made with the air-gap gratings placed on both sides of the cavity (Figure 8-8).

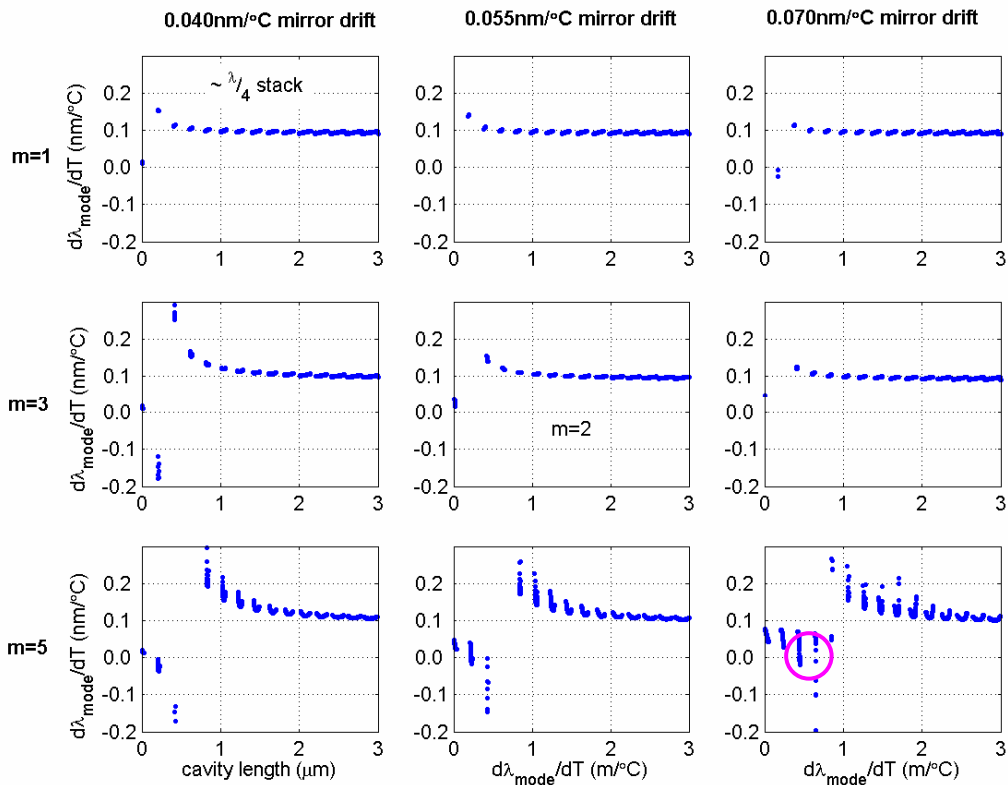


Figure 8-8 Modal drift rate vs. cavity length plots, for cavities with the nine grating designs of Figure 8-2 used above and below.

As expected the steepest mirror phase slope (i.e. highest mirror order) combined with the strongest mirror drift permits athermalisation of the longest cavities (design 9, bottom right panel of Figure 8-8).

Figure 8-9 is an enlargement of part of design 9's drift vs. cavity-length plot.

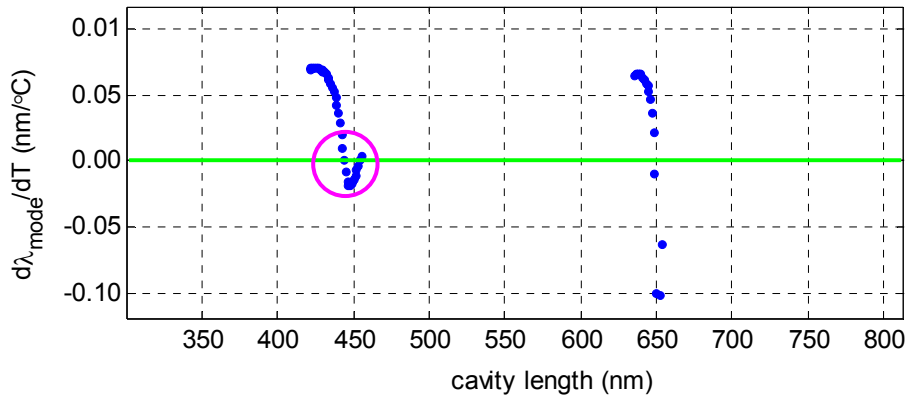


Figure 8-9 Enlargement of part of the 5th-order high-drift-mirror cavity-length survey of Figure 8-8 (circled there).

Circled is the design point used in Figure 8-10.

The minimum in the drift vs. cavity-length characteristic at 448nm is attractive because it offers superior tolerance of fabrication errors, giving low drifts for a greater range of cavity lengths. Selecting a 444nm cavity for its low drift and proximity to the minimum, we obtain the $m=2$ mode centrally positioned in the gain spectrum (Figure 8-10).

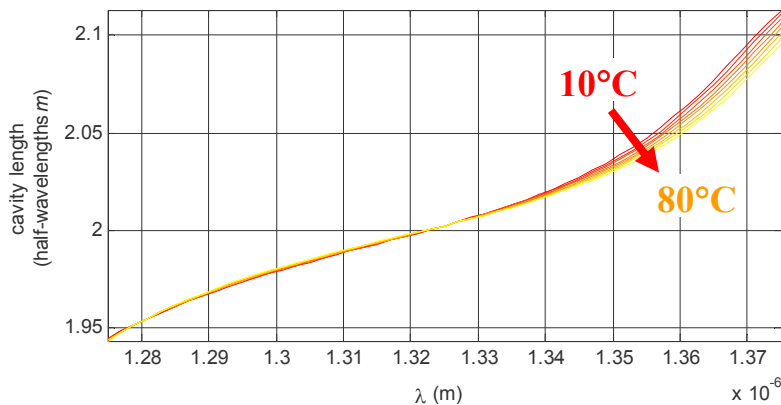


Figure 8-10 Total phase-length in half-wavelengths m vs. wavelength for 444nm cavity between design 9 air-gap reflectors.

The wavelength range used is narrower than the reflectors' Bragg peak.

The $m=2$ intercept barely changes as temperature increases, giving drift only 5% of that usually expected (Figure 8-11). Observing that the m -line 'slides' along its own gradient across a wide window 1280-1330nm, it is apparent that low drift is available for any wavelength in this range. By altering cavity length slightly the cavity-phase contribution can be increased or decreased to position the $m=2$ intercept at a particular wavelength without necessarily greatly unbalancing the athermalisation. This is also apparent in Figure 8-9 (circled region), which suggests that for drift rates <20% of the unmodified level, tolerance of cavity-length error could be ± 10 nm, an order of magnitude larger than for the hybrid configuration.

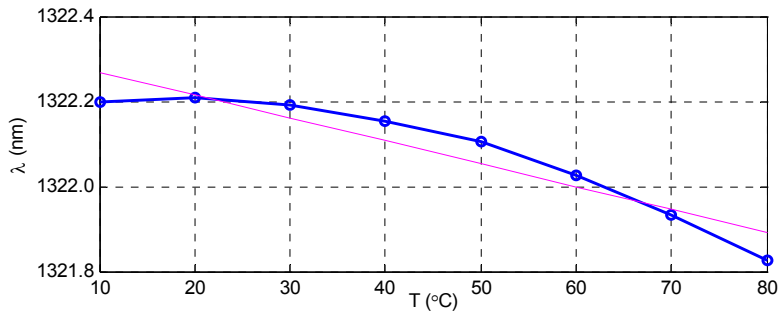


Figure 8-11 Wavelength vs. temperature plot for least mirror-loss mode of 444nm cavity between design 9 reflectors.

Average drift rate is $-0.0044\text{nm}/^\circ\text{C}$.

8.2.2.4 Conclusions

Although they have disadvantageous thermal properties it is apparent that the reduced-drift air-gap reflectors confer an advantage in fabrication tolerance which is eliminated by the presence of a standard bottom reflector.

Although both the hybrid and double-air-gap mirror designs have a positive total phase slope $dm/d\lambda$, and both have positive Bragg-peak drifts, they show very different behaviour in the mode-drift vs. cavity length plots. The main difference lies in the steepness of their reflection-phase slopes – a steep slope means less Bragg drift is required to compensate a given change in cavity phase contribution.

The distinct low-drift populations arise from positive slope of total phase-length (grating dominates resonant length) and the high-drift populations from negative slope of total phase-length (cavity dominates resonant length), as described in the previous chapter. All current edge-emitting DBR designs operate in the latter regime and it can be seen that as cavity length increases the mode drifts all converge to a typical $0.09\text{nm}/^\circ\text{C}$. Interestingly, DFBs operate in the low-drift regime, but their modal drifts are determined by the grating drift, much as in the hybrid designs of **Figure 8-4**. The ceilings of the low-drift populations of **Figure 8-8** also are determined by the grating drifts, a fact which is more apparent in this figure than in the edge-emitting cavity-length survey of **Figure 7-4**. Athermal gratings would therefore be expected to give plots similar to those of **Figure 8-4** but with drift-ceilings of zero. Recalling **Figure 7-2** we see that this is indeed the case.

8.3 Agilent Air-Gap VCSEL

In a post-deadline CLEO 2002 paper Mike Tan *et al* reported continuous-drive lasing at 1326nm over 10-80°C in an electrically-driven InP-based VCSEL with symmetrical air-gap DBRs [18], created in a single growth step.

The work presented in this dissertation was partly funded by Agilent Technologies. Lacking VCSEL fabrication facilities internally, a study was made of the possibility of modifying Mike Tan’s air-gap VCSEL design to show drift modification.

8.3.1 The Agilent Design

The Agilent device had a thick cavity (7λ including 5 InGaAsP quantum wells) and 3 periods above and below of 3rd-order airgap-InP DBR. A thick cavity (7λ rather than 3λ) and heat-spreading layers were found necessary to lower the thermal resistance enough for operation throughout this temperature range. The DBRs used $5\lambda/4$ InP layers and $\lambda/4$ air layers, the thicker layers of InP being motivated by considerations of structural stability. Electrically, the device used intracavity contacts and minimised free-carrier losses using a tunnel junction.

Taking 1326nm as the wavelength and 3.2 as the refractive index of InP at 20°C the device dimensions work out as follows: $L_{\text{cavity}} = 2900.6\text{nm}$, $L_{\text{air}} = 331.5\text{nm}$, $L_{\text{InP}} = 518.1\text{nm}$.

8.3.2 Mirror Modification Options

Taking the 7λ cavity with 3-period air-gap DBRs, a survey was made of mode drift rate against a range of alternative grating semiconductor and air-gap dimensions (**Figure 8-12**).

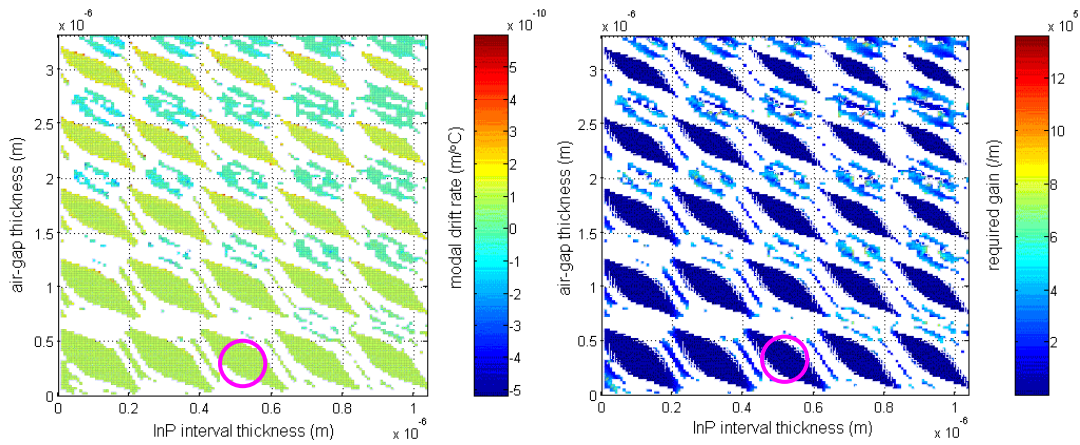


Figure 8-12 Thermal drift rate of lasing modes of InP-airgap VCSEL (left) and corresponding required material gain (right).

Drift measured in a window 1260-1380nm over 49.4-50.6°C, not including hops. Both axes go up to 5th order, that is, $10\lambda/4n$ where $\lambda=1326\text{nm}$ and n is refractive index. Circled is the location on these axes of the Agilent device.

Zones of low drift occur centred on points where air and InP layer thicknesses are both an odd number of quarter wavelengths thick. At higher orders drift decreases slightly and these zones become smaller. Modes apparent between these zones fall outside the Bragg peak and exist in side-lobes with correspondingly higher gain requirements. Neither athermalisation nor significant drift reduction is available using air-gaps.

A second survey was conducted supposing the air gaps filled with BCB (**Figure 8-13**).

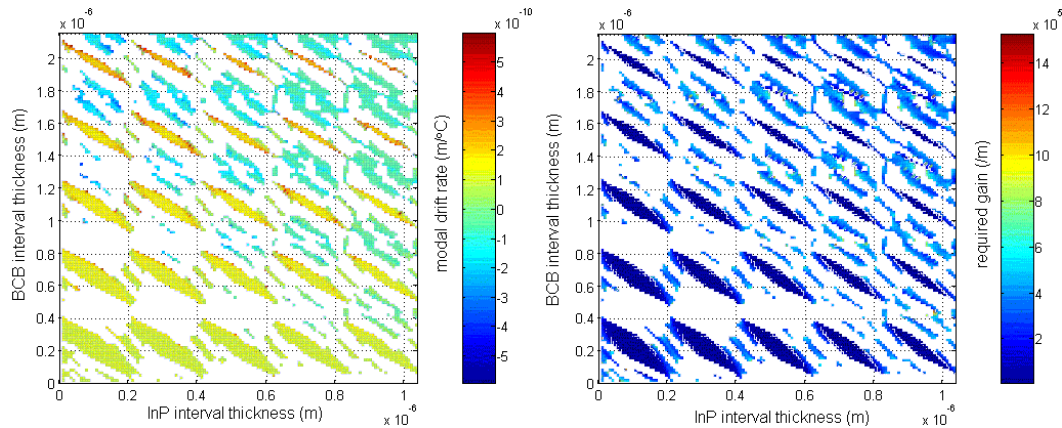


Figure 8-13 Thermal drift rate of lasing mode of InP-BCB VCSEL (left) and corresponding required material gain (right).

Drift measured in window 1260-1380nm over 49.4-50.6°C, not including hops. Both axes go up to 5th order, that is, $10\lambda/4n$ where $\lambda=1326\text{nm}$ and n is refractive index.

The greater optical density of BCB decreases grating contrast and narrows the Bragg peak and so the low-drift zones. However, these are of higher drift than those corresponding in the air-gap survey and, moreover, drift increases at higher orders. Again, neither athermalisation nor significant drift reduction is possible with reasonable gain requirements.

8.3.3 Polymer Infill Options

The possibility of obtaining improved wavelength stability using some other optical polymer than BCB to fill the air gaps was investigated.

Optical polymers with designable characteristics are becoming available commercially and usually consist of two or more copolymerisable molecular species whose proportions can be varied before polymerisation to obtain a range of refractive index and thermal tuning rates. They have the additional advantage of tending to be highly crosslinked, increasing lifetime. In the whole range of polymers, there are available n from 1.3 to 1.7 and dn/dT from -1×10^{-4} to $-4 \times 10^{-4}/^\circ\text{C}$ [19].

The Agilent double-air-gap structure was modelled to locate the least-loss cavity mode in the wavelength range 1280nm-1360nm for a range of temperatures. The rate of drift of this wavelength was recorded and the measurement repeated for the range of possible polymer refractive indices and TOCs, not all of which produced resonant modes in this wavelength window.

Modelling of the Agilent double-air-gap design indicates that suitable polymer infill (with $n=1.38-1.39$) may be able to increase the drift (**Figure 8-14** left) without much reducing

reflectivity (**Figure 8-14** right). It is not possible to obtain significantly reduced drift rates using any polymer infill.

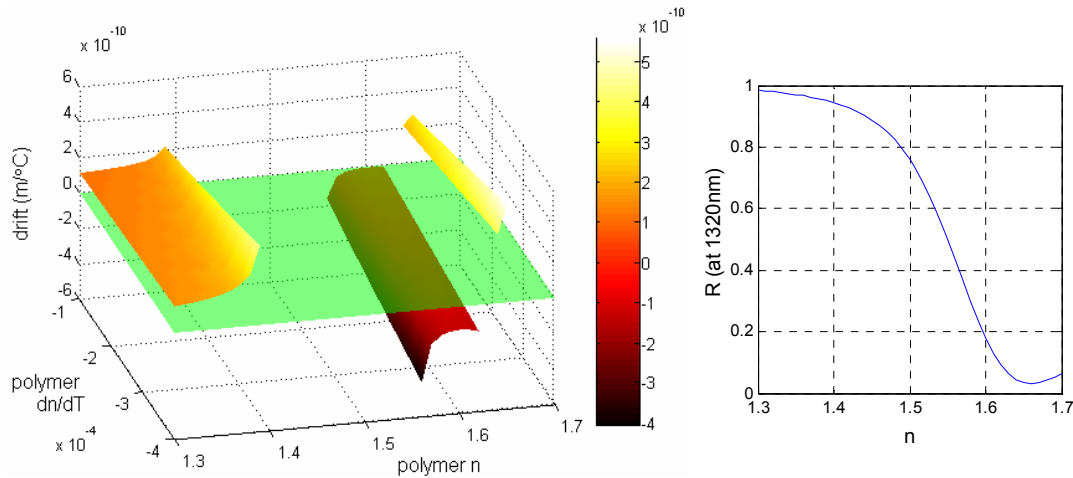


Figure 8-14 Effects of range of polymer infills on characteristics of Agilent double-air-gap VCSEL design

Left – thermal non-hop drift of least-loss mode, vs. n and dn/dT of infill polymer

Right – reflectivity at 20°C and 1320nm of one DBR, vs. n of infill polymer

8.3.4 Conclusions

It is not possible to show drift reduction by any simple modifications to the Agilent double-air-gap design, due to the thickness of the cavity. It is necessary to design athermal designs from scratch. A systematic method of doing so would be advantageous.

8.4 Infilling with Optical Polymers

The design options offered by ‘tailored’ optical polymer infills were investigated further.

8.4.1 Air-Gap VCSEL with Tailored-Polymer Infill

Returning to the Agilent design as representative and infilling with notional polymer of refractive index 1.52 at 20°C and 1326nm, the drift of the least-loss mode was modelled for a range of polymer dn/dT to give a linear relation (**Figure 8-15**).

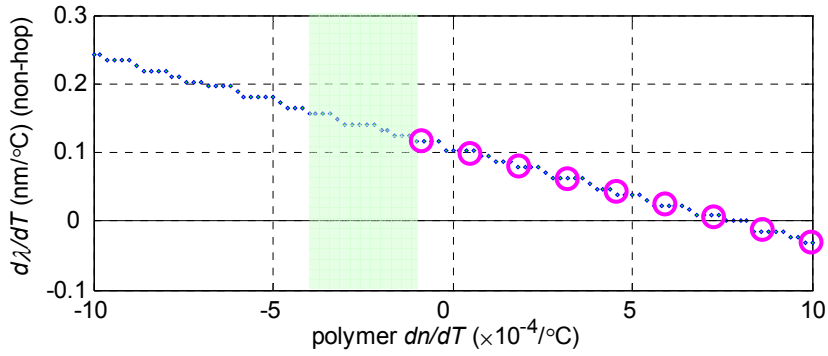


Figure 8-15 Modelled non-hop modal drift Agilent design double air-gap VCSEL infilled with hypothetical polymer of $n=1.52$ and variable dn/dT .

Zero mode-drift is obtained for polymer dn/dT of $7.7 \times 10^{-4}/^\circ\text{C}$. Circled are nine polymer dn/dT 's distributed between $-1 \times 10^{-4}/^\circ\text{C}$ and $10 \times 10^{-4}/^\circ\text{C}$. Shaded is the actual reported range of polymer dn/dT 's.

The large positive dn/dT found to give zero mode drift is unobtainable in polymers, whose refractive index change with temperature is due mostly to thermal expansion and therefore negative. A steeper mirror phase slope and a shorter cavity are necessary to athermalise with a realistic polymer dn/dT .

Keeping the same reflector structure, cavity-length surveys were made for each of the nine polymer dn/dT 's marked in **Figure 8-15** (**Figure 8-16**).

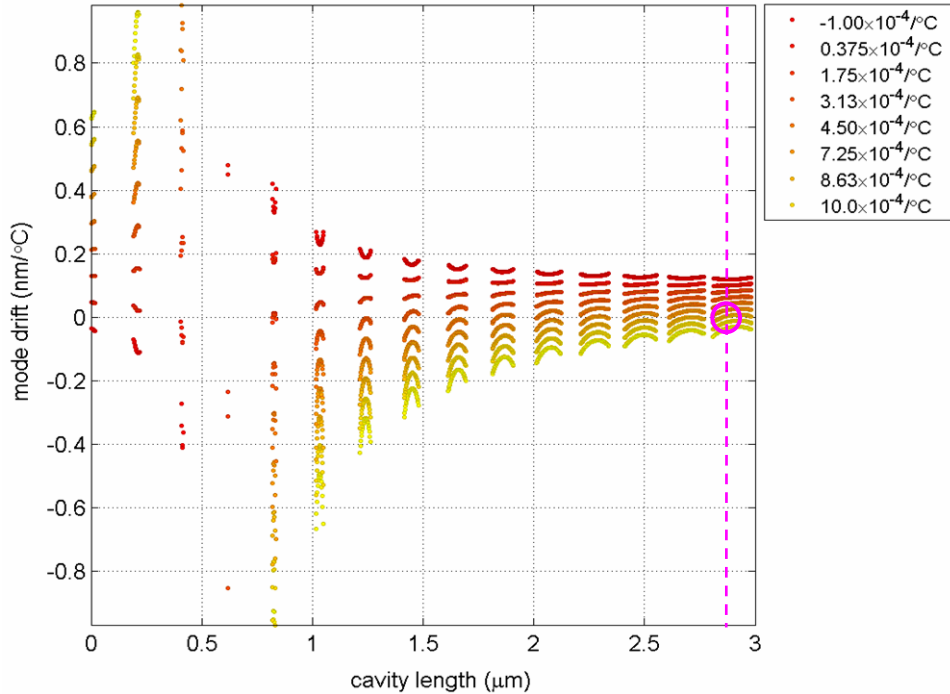


Figure 8-16 Non-hop mode drift vs. cavity length cavities bounded by 3-period air-gap reflectors of the Agilent design but infilled with notional polymer of $n=1.52$ and a range of dn/dT 's corresponding to those circled in **Figure 8-15**.

All converge to the same drift at long cavity lengths. Dashed line indicates the cavity length of the Agilent device, circled is the design point corresponding to athermalisation in **Figure 8-15**.

These plots do not lead to practical designs but illustrate some important points.

First, their structure along the cavity-length axis is determined by the mirror reflectivity spectrum – all the plot features appear at the same wavelengths despite having different drifts.

Second, it is possible for the ‘low-drift’ and ‘high-drift’ populations to invert if a sufficiently high-drift grating is used. This is the result of a reversal in another pair of competing effects – the rate of descent of the grating phase contribution down the cavity phase line as the grating drifts to longer wavelengths and the simultaneous increase of the cavity phase at all wavelengths. So far, the increase in cavity phase has been the dominant effect but here the grating drift can be seen ‘winning’ the competition. **Figure 8-17** summarises this and other key features of cavity-length surveys.

Note that, because of the great width of the reflection peak, its drift over normal temperature ranges does not greatly affect its reflectivity at the operating wavelength.

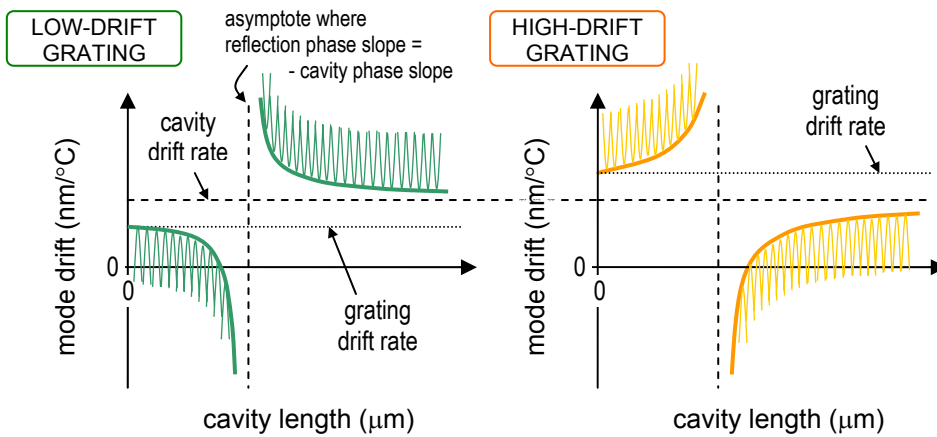


Figure 8-17 Main features of mode-drift vs. cavity-length plots

The fine structure is indicated. When grating drift-rate exceeds the long-cavity trend drift-rate the drift populations invert. In surveys searching outside the central region of the reflection peak and including a highly-selective reflector, the short-cavity drift population appears dominated by the steep phase slope at the edges of the peak (e.g. **Figure 8-4**)

Lastly, longer cavities give shallower drift-rate variation with cavity length. This is advantageous in that it increases tolerance of fabrication errors, but large, positive grating drifts are necessary to invert the drift populations and give low drift at such long cavity lengths.

Taking the athermal 2901nm design of **Figure 8-16** and **Figure 8-15** and iteratively modifying it to 4 grating periods, $L_{\text{cavity}}=2870\text{nm}$, $L_{\text{polymer}}=651\text{nm}$ and $L_{\text{InP}}=309\text{nm}$ this tolerance of error manifests in the large wavelength range over which there is no change in resonant length (**Figure 8-18**, left).

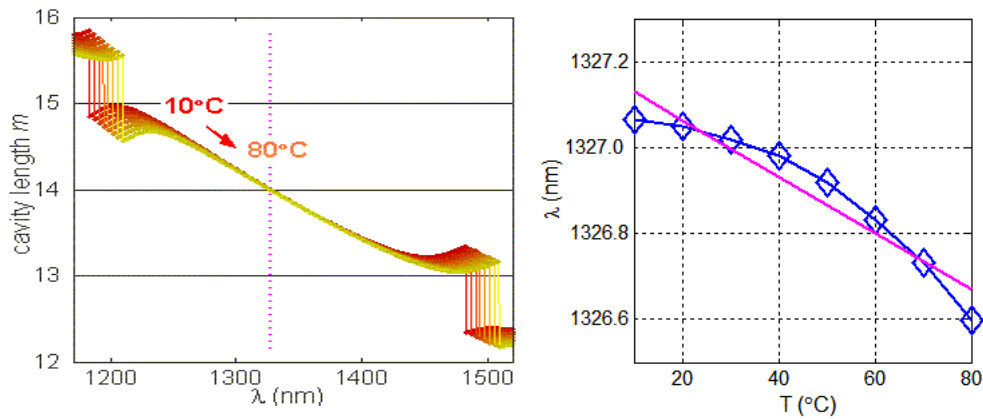


Figure 8-18 Resonant length of athermal design vs. wavelength for temperatures 10-80°C (left) and corresponding plot of emission wavelength ($m=14$ resonance) vs. temperature

Mirror drift is high, $0.396\text{nm}/^\circ\text{C}$. Average mode drift is $-4.5\text{pm}/^\circ\text{C}$. Note this design is entirely unlike the Agilent design apart from having double dielectric-gap reflectors.

To test the yield benefits of this regime, 3000 such devices were modeled including 2% error on each layer thickness. Yield was much greater than for the device of **Figure 8-7** (**Figure 8-19**).

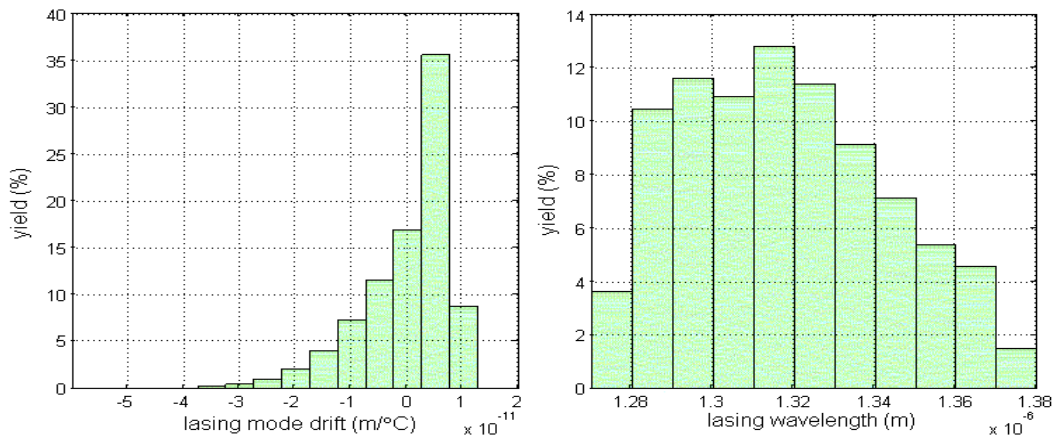


Figure 8-19 Drift (left) and wavelength (right) distributions of athermal device of **Figure 8-18**, modelled 3000 times with 2% standard error on each layer

All are low-drift but wavelengths are widely distributed.

Essentially, tolerance of fabrication errors increases with longer cavities and faster rates of change of grating phase-length contribution – the magnitude of the errors is fixed and diminishes proportionally when the errors affect bigger numbers. If high-drift gratings are available, this is an incentive to maximise grating drift, grating phase slope and cavity length in subsequent designs, subject to mode-drift requirements.

8.4.2 Hybrid VCSEL Tailored-Polymer Infill

Hybrid designs have no need of a thick cavity because there is a good thermal path through the semiconductor stack. A half-wave cavity was modeled with an InP-InGaAsP bottom DBR and a $\frac{3}{4}\lambda$ polymer-infilled top DBR, for a range of polymer dn/dT (**Figure 8-20**).

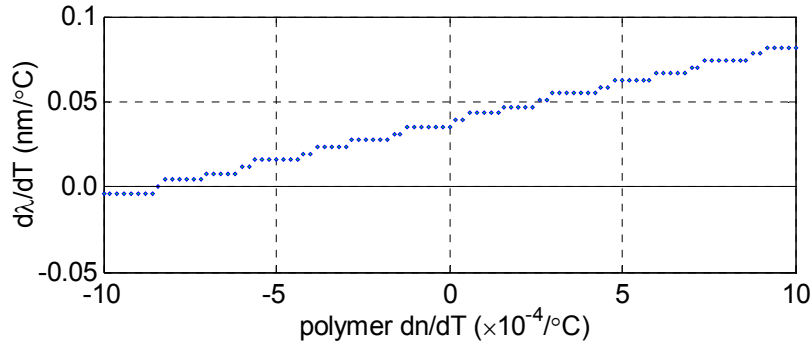


Figure 8-20 Modelled mode drift of $\frac{1}{2}\lambda$ InP cavity with 3-period $\frac{3}{4}\lambda$ InP-polymer top DBR and 70-period $\frac{1}{4}\lambda$ InP-nGaAsP bottom DBR.

The polymer has $n=1.52$ and a range of dn/dT 's. Zero mode drift is achieved for $-8 \times 10^{-4}/^\circ\text{C}$ polymer dn/dT .

More positive polymer TOCs give larger mode drifts, the opposite of the previous situation. In this case, the shorter cavity of the hybrid device, combined with the narrow Bragg peak of the bottom grating, gives a positive slope to the phase length plot (**Figure 8-21**).

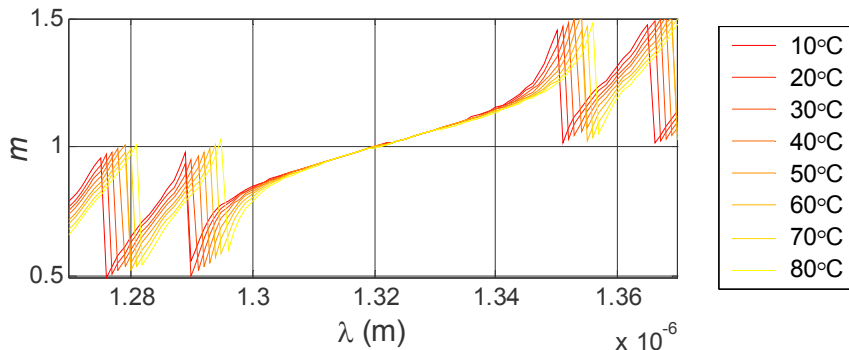


Figure 8-21 Total resonant phase-length of $\frac{1}{2}\lambda$ InP cavity with hybrid reflectors.

The polymer infill has $n=1.52$ and $dn/dT = -8 \times 10^{-4}/^\circ\text{C}$, athermalising the resonant length over 10-80°C.

Thus, the faster the Bragg peak drifts the faster the local decrease in cavity phase length in m and the faster the mode drifts to longer wavelengths. **Figure 8-22** compares this situation with the double-air-gap device in §8.4.1.

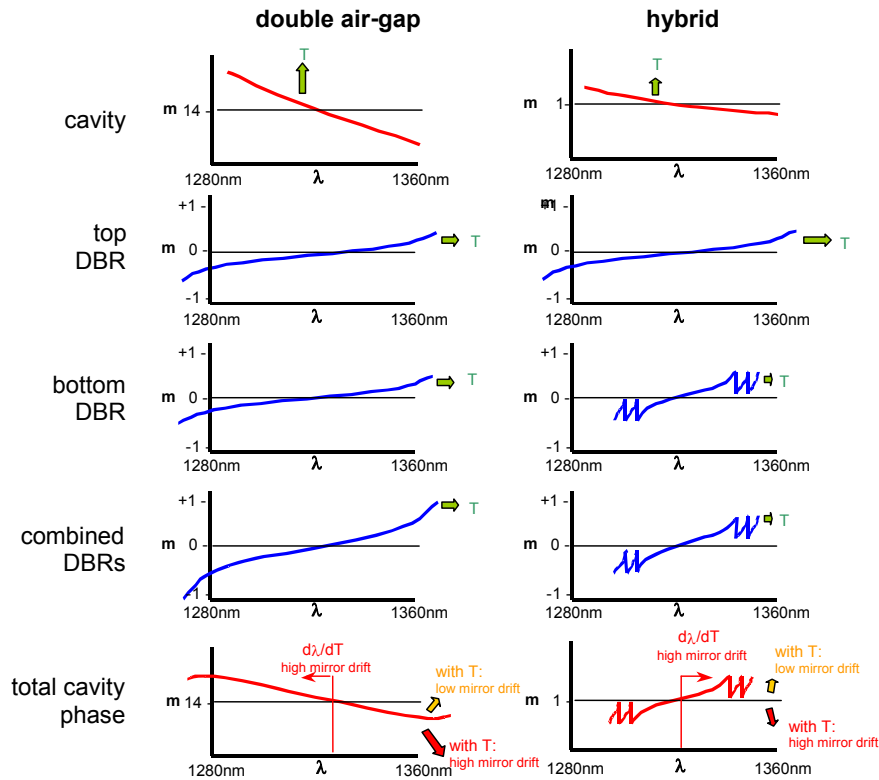


Figure 8-22 Explanation of impact of mirror drift on mode drift in the long-cavity double air-gap (left) and short-cavity hybrid (right) cases.

That there are two different mirrors in the hybrid device complicates interpretation somewhat. It is helpful to consider it in terms of the narrow and steep phase slope of the Bragg peak of the bottom stack drifting to longer wavelengths at a fixed rate, while sitting on top of a much wider and less steep phase contribution from the high-contrast top mirror, which drifts at a rate dependent of the polymer infill. As the mirrors drift to longer wavelengths the total phase contribution at a given wavelength will tend to fall. However there will be at the same time an increase in the contribution of the cavity to total phase. When these cancel there is athermalisation.

In terms of manufacturability, it is helpful to have shallow mirror phase contributions because the exact drift rate is then less critical.

Most simulations have shown a poor tolerance of fabrication variability in these designs, due to the very fine balance of the two contributions to optical cavity length. High phase-slope curvatures lead to athermalisation only in very local regimes and additionally make the lasing wavelength very sensitive to cavity length. Using only the linear part of the reflection phase slope, near the middle of the reflectivity maximum can ameliorate this. Reduced curvatures mean that emission wavelength and so the balance of phase contributions is less sensitive to fabrication errors.

8.5 Reflector Survey & Athermal Design Method

8.5.1 Athermalisation by Phase-Length Stabilisation

In the previous chapter the idea of a DBR resonant length consisting of cavity and grating contributions was introduced as a simple summation in half-wavelengths m , evaluated at a particular wavelength λ

$$m_{total} = m_{top} + m_{bottom} + m_{cavity} \quad (\text{E8-1})$$

where m_{total} is resonant length in half wavelengths, m_{top} and m_{bottom} the contributions of the top and bottom reflectors and m_{cavity} that of the cavity. Each contribution is a function of temperature and the rate of change of m_{total} is obtained by differentiating:

$$\left. \frac{dm_{total}}{dT} \right|_{\lambda} = \left. \frac{dm_{top}}{dT} \right|_{\lambda} + \left. \frac{dm_{bottom}}{dT} \right|_{\lambda} + \left. \frac{dm_{cavity}}{dT} \right|_{\lambda} \quad (\text{E8-2})$$

The two mirror terms may be expanded into the product of their reflection-phase slopes and Bragg-peak drift rates, the cavity term may be expanded and simplified in terms of the material's coefficient of thermal expansion (CTE) and its thermo-optic coefficient (TOC) at this wavelength and temperature:

$$\left. \frac{dm}{dT} \right|_{\lambda} = \left(\left. \frac{dm_{top}}{dT} \right|_{\lambda} \cdot \frac{d\lambda_{Bragg-top}}{dT} \right) + \left(\left. \frac{dm_{bottom}}{dT} \right|_{\lambda} \cdot \frac{d\lambda_{Bragg-bottom}}{dT} \right) + \frac{2}{\lambda} L_{def} \left(\left. \frac{dn}{dT} \right|_{\lambda} + CTE \cdot n_{def} \right) \quad (\text{E8-3})$$

L_{def} and n_{def} are the physical length of the cavity and its effective refractive index at a reference temperature T_{def} . All the terms except the phase slopes are controlled by the designer or analytically predictable. For InP ($n=3.2$ at 20°C 1320nm , $\text{TOC}=2.02 \times 10^{-4}/^{\circ}\text{C}$, $\text{CTE}=5.4 \times 10^{-6}$) at 1320nm the contribution to rate of change of phase length works out at $3.322 \times 10^{-4} m/^{\circ}\text{C}$ per micron of cavity length, or $10.24 \text{ rads}/^{\circ}\text{C}$ per micron.

Phase slopes are controlled by grating order, number of periods, index contrast and the proportions of materials in each period. Bragg-peak drifts are controllable by material TOCs and materials' proportions in each period.

8.5.2 Developing an Athermal Design Procedure

The design method so far has revolved around finding suitable cavity lengths for a given mirror design, with attendant focus on designing reflectors with advantageous properties. This approach has been necessary due to the unpredictable nature of grating reflection phase slope.

Chapter 4 explained the necessity of using the transfer-matrix method (TMM) incorporating TOC and CTE to permit rapid modelling of the whole reflection spectrum for arbitrary structures. Investigations using this tool have shown improved device manufacturability associated with using the linear phase slope at the centre of the reflection peak.

The Bragg condition for high-contrast gratings, introduced in Chapter 7, permits accurate and reliable positioning of the reflection peak, with zero reflection phase at the design temperature and wavelength. The advent of long-wavelength air-gap VCSELs and tailorable optical polymers allows a degree of drift control of the DBRs even while conforming to the high-contrast Bragg condition.

This improved understanding of the design space makes practicable the idea of designing mirrors to suit cavities, rather than the other way around. More accurately, since it is not possible to predict reflector phase slope away from the design point, it is practicable to make a survey of the whole range of grating designs and select appropriate designs from it.

To configure an athermal design it is necessary to calculate the rate of change of phase length with temperature of the desired resonant cavity using equation (E5-22), then choose reflector designs from the survey which between them give similar but opposite rates of change of phase contribution.

8.5.3 Mirror Design Survey

8.5.3.1 Survey design

Assuming an InP-based device, the design space available for 1320nm polymer-infilled VCSEL reflectors comprises five variables: thickness of polymer layers l_p , thickness of semiconductor layers l_s , polymer refractive index n_p , polymer thermo-optic coefficient TOC_p and number of periods N . The layer thicknesses are best confined to odd numbers of quarter-wavelengths in conformance with the Bragg condition. The TMM model was used to obtain reflection spectra for designs at survey points through the full ranges of these values. l_p and l_s were constrained to give a maximum grating order of 14, because large orders result in increased attenuation and large structures. The 28 possible combinations remaining (see figure **Figure 7-10**) multiply with the sample points in the other degrees of freedom (**Table 8-2**) to give 8820 reflector designs. For each design a number of characteristics were recorded including the rate of change of phase-length contribution with temperature.

Table 8-2 Mirror survey parameters

Parameter	Units	Range & step size	No. survey points
l_p	$\lambda/4$	1:2:13	7
l_s	$\lambda/4$	1:2:13	7
n_p		1.3:0.05:1.7	9
n_s		3.2	1
TOC_p	$^{\circ}C^{-1}$	$(-1:-0.5:-4) \times 10^{-4}$	7
TOC_s	$^{\circ}C^{-1}$	2.02×10^{-4}	1
N		2:1:6	5

Rate of change of reflection phase with temperature $d\phi/dT$ was measured only at the desired emission wavelength, 1320nm in this case. At the design temperature the cavity is exactly resonant at this wavelength and the reflector phase is zero. This means the survey does not capture resonances made up of fractional cavity and grating effective lengths, but it simplifies design in that reflectivity is at a maximum, the required cavity length is simply a number of half wavelengths at the design wavelength and temperature, and the phase slope across the Bragg peak is most linear. The Bragg peak was designed to be at 1320nm at 40°C, the mid point of the hypothetical 0-80°C operating range. Designing for this temperature minimises the maximum deviation of operating wavelength from specification at the extremes of the temperature range.

The design specifications and measurements were stored in a single large Matlab data array and a function written to find and return all designs falling within specified ranges of any parameter.

This is only an example survey – a designer looking to create a wavelength-stabilised device would have to begin by conducting a similar survey using parameters appropriate to the materials and design requirements at hand, perhaps including only n_p and TOC_p ranges of specific polymer systems.

8.5.3.2 Survey results

The most negative dm_{mirror}/dT found was $-3.26 \times 10^{-4} /^{\circ}C$ (-10.2×10^{-4} rads/ $^{\circ}C$), capable of compensating the expansion of approximately 1 μ m of InP cavity. The distribution of dm_{mirror}/dT over the 8820 modelled designs shows that 29% of designs produce negative dm_{mirror}/dT (Figure 8-23).

This indicates a substantial design space in which to find suitable mirrors with dm_{mirror}/dT appropriate to reducing or eliminating thermal dependence. Since dm_{mirror}/dT is measured at the design wavelength 1320nm in the middle of the Bragg peak there is zero phase contribution

from the mirror at the design temperature 20°C. This means reflector designs with suitable dm_{mirror}/dT can be taken directly from this survey for use with a cavity resonant at 1320nm at 20C, with no concerns about simultaneously obtaining athermalisation and resonance.

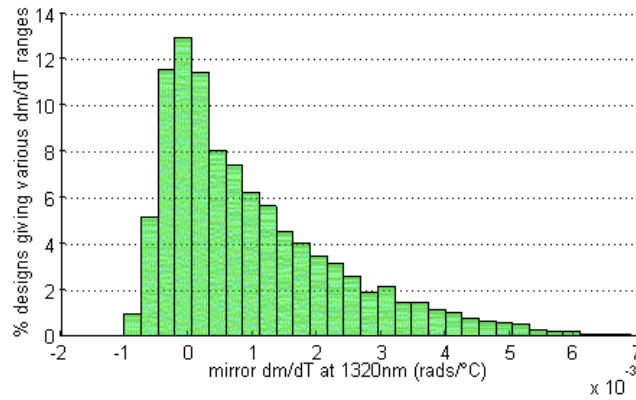


Figure 8-23 Distribution of dm_{mirror}/dT in 30 bins across range found in modeling 8820 polymer-infilled air-gap DBR designs across all design parameters.

Most negative rate of change of mirror contribution = -0.00102415 rads/°C
 Most positive rate of change of mirror contribution = 0.00690407 rads/°C

Other observations from the survey:

- Increasing n_p reduces the amount of polymer in a layer, so Bragg drift becomes more positive. It also increases the phase slope, so overall dm_{mirror}/dT is increased in the opposite sign to the Bragg drift, which may be positive or negative.
- Higher-order stacks have narrower Bragg peaks and greater phase slopes, so high orders also magnify dm_{mirror}/dT , making it more negative if Bragg drift is positive and vice versa.
- Positive Bragg drift is essential to obtaining negative dm_{mirror}/dT . High order and high n_p then make it more negative.
- Low ratio of polymer to semiconductor helps obtain positive Bragg drift. It also reduces the phase slope but effect on Bragg drift is more important.

To take an example from the survey, it is possible using a $1/4\lambda$ - $5/4\lambda$ mirror design similar to that reported at CLEO 2002 but with infill polymer of median n_{poly} and dn_{poly}/dT to obtain dm_{total}/dT of $-1.9 \times 10^{-4}/^\circ\text{C}$. This is enough to fully athermalise an InP cavity 570nm long, or largely athermalise a 619nm cavity, which is $3/4\lambda$ resonant at 1320nm.

The design procedure can start from cavity length and desired amount of athermalisation and proceed to selecting and interpolating amongst mirror designs, or it can start by selecting an advantageous mirror design and go on to design an athermalising cavity. Opposite rates of change of phase contribution matched to within 15% of each other rate are sufficient to achieve

an order of magnitude reduction in wavelength drift and many survey points yield useful designs. Furthermore a continuum of designs exists around each survey point, increasing the chances that for a given infill polymer designs to exploit it exist.

For a given cavity, survey results often show groups of athermalising reflector designs, similar in all respects except that the n_p required increases as TOC_p decreases. This can be explained as follows: if n_p is increased, index contrast falls, the Bragg peak narrows and the phase slope across it increases, so Bragg drift must decrease to obtain the same rate of change of phase contribution at the design wavelength, i.e. TOC_p must become more negative. Thus there is a continuum of athermalising designs, and there may be many such continua.

Because tailoring the optical properties of copolymer blends involves adjusting relative molecular abundances n_p is unlikely to vary independently of TOC_p . Varying the relative molecular abundance of copolymerising species in a copolymer mix therefore gives another line on the same axes. Where this copolymer mix line crosses a continuum of athermalising DBR designs a design can be realised (**Figure 8-24**).

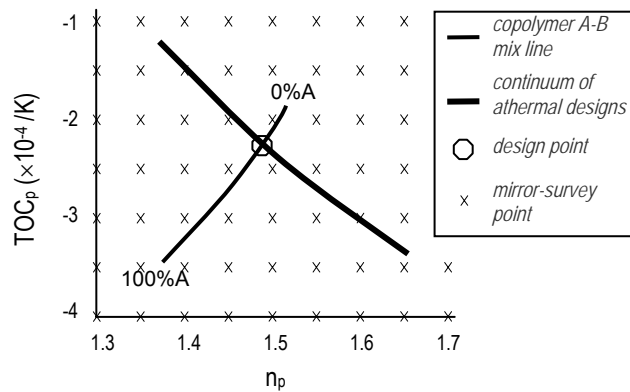


Figure 8-24 Matching surveyed reflector designs with available copolymer formulations (schematic)

A survey of the DFB design space is likely to locate a number of athermalising reflector configurations. Each is part of a continuum of athermalising designs in which polymer TOC decreases as refractive index increases. There may be several such continua. The intersection of such a continuum with the range of properties available by adjusting the relative abundance of monomer species ‘A’ and ‘B’ of a given copolymer represents a viable design point.

Athermalising mirror designs are likely to be available for most cavities, given a range of optical copolymers and suitable reflector configurations. The remarkable independent tailorability of refractive index and TOC of Dow-Corning’s polysiloxanes, achieved by varying monomer chemistry as well as the mix of monomers, further increases this likelihood. In **Figure 8-24** such a polymer system would be represented by a ‘window’ of reflector design viability.

8.5.3.3 Example Design Procedure

VCSEL active regions are typically epitaxially structured, with quantum wells, contact and confinement layers, but as a simple example we take a 1λ InP cavity. Taking the values in **Table 8-2** with equation (E5-19), the cavity is 412nm long at 40°C and its phase length (**Figure 8-25**) increases at a rate 4×10^{-4} rads/°C.

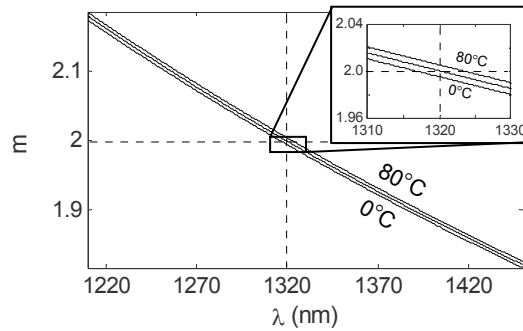


Figure 8-25 Phase length in half-wavelengths m of 412nm resonant cavity with refractive index $nS = 3.196, 3.204, \text{ and } 3.212$ at $0^\circ\text{C}, 40^\circ\text{C}$ and 80°C

As temperature increases, the optical length of the cavity increases at all wavelengths

To athermalise the resonant length with symmetrical reflectors each must make a phase contribution which decreases at half this rate, -2×10^{-4} rads/°C, being zero at 40°C. Searching the survey data finds 173 reflector designs with phase drift within $\pm 15\%$ of this, we choose one requiring $n_p=1.7$ and $TOC_p=-1.5 \times 10^{-4}$ for its low order and high reflectivity (**Figure 8-26** and **Figure 8-27**).

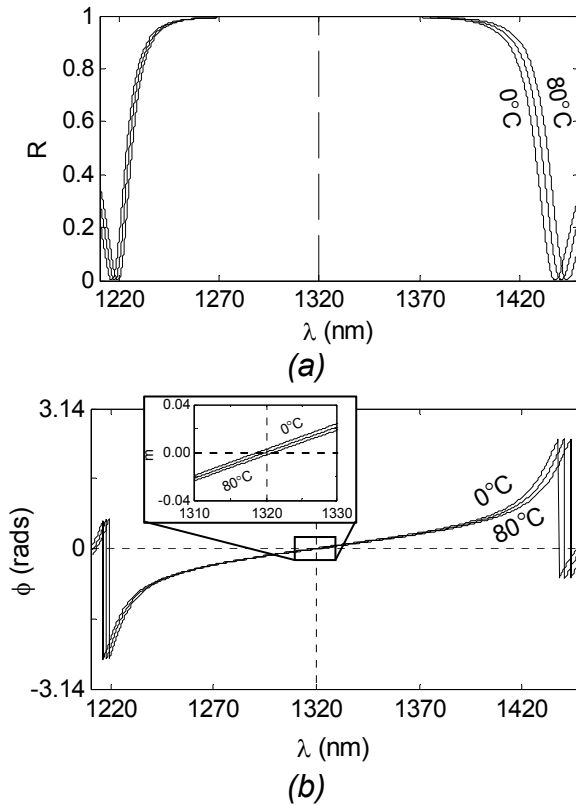


Figure 8-26 Complex reflection spectrum of 4-period 3rd-order polymer-infilled InP reflector stack with $IS = 515\text{nm}$, $LP = 194\text{nm}$, $nS = 3.2$ and $nP = 1.7$ at 20°C , $TOCS = 2.02 \times 10^{-4}/^\circ\text{C}$ and $TOCP = -1.50 \times 10^{-4}/^\circ\text{C}$

- (a) Power reflectivity spectrum
- (b) Reflection phase spectrum (at start of grating)

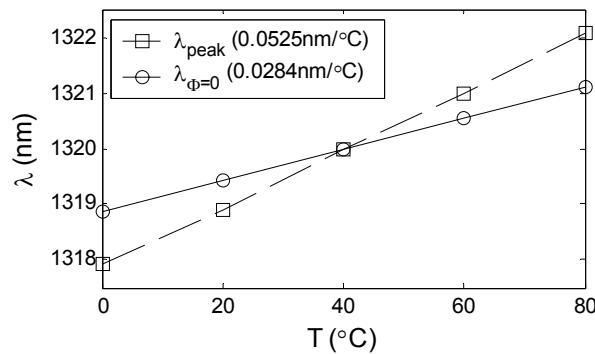


Figure 8-27 Temperature drift of wavelength of reflection peak λ_{peak} and zero reflection phase $\lambda_{\Phi=0}$

Away from the design temperature the semiconductor and polymer grating elements no longer meet the quarter-wave condition at the same wavelength and although there is a reflection peak it is not, strictly, a Bragg reflection peak. The wavelength of zero reflection phase and the reflection peak wavelength no longer coincide. The drift rate used in considering a reflector’s athermalising property is that of $\lambda_{\phi=0}$, the wavelength of zero reflection phase.

Placing one of these reflectors on each side of the resonant cavity gives us a cavity whose optical length is stabilised to within 0.23nm of 1320nm in the temperature range 0-80°C (Figure 8-28).

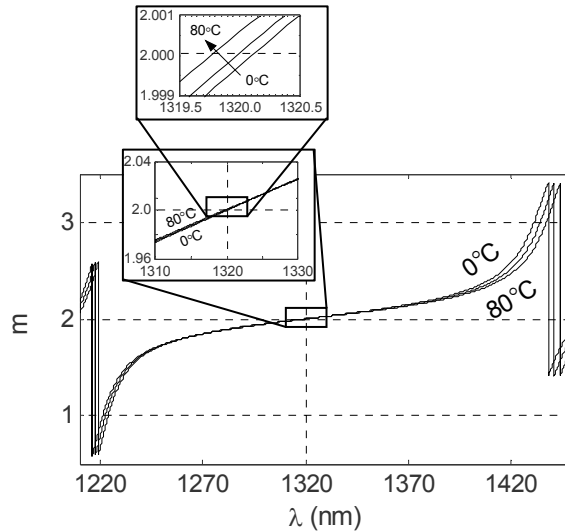


Figure 8-28 Total phase length of cavity (Fig. 4) plus athermalising Bragg reflectors on either side (Fig. 5b) for 0, 40 and 80 °C

The wavelength of the $m = 2$ resonance remains nearly constant over temperature

Athermalisation of the cavity length ensures the emission wavelength is 1320nm at 40°C and drifts at $-4.3\text{pm}/^\circ\text{C}$ (Figure 8-29).

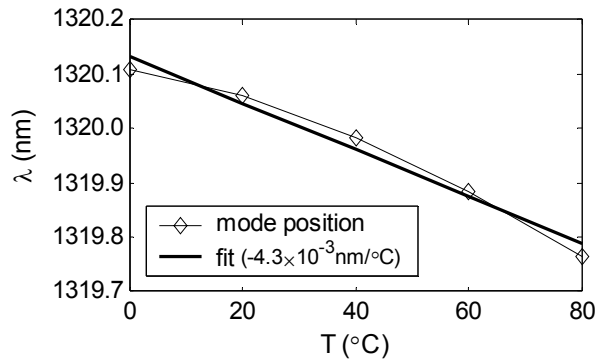


Figure 8-29 Wavelength of athermalised cavity resonance 0-80 °C

A linear fit to mode position over temperature gives drift of only $-4.3\text{nm}/^\circ\text{C}$. The maximum deviation from the 1320nm specification is 0.23nm

8.5.4 Air-Gaps Survey

A smaller survey examining only air-gap gratings, without infill, was made. Layer thicknesses were varied consistent with the high-contrast Bragg condition for 1320nm along with the number of periods. The Bragg drift (Figure 8-31), phase slope and rate of change of phase-length contribution (Figure 8-30) were measured at each design point.

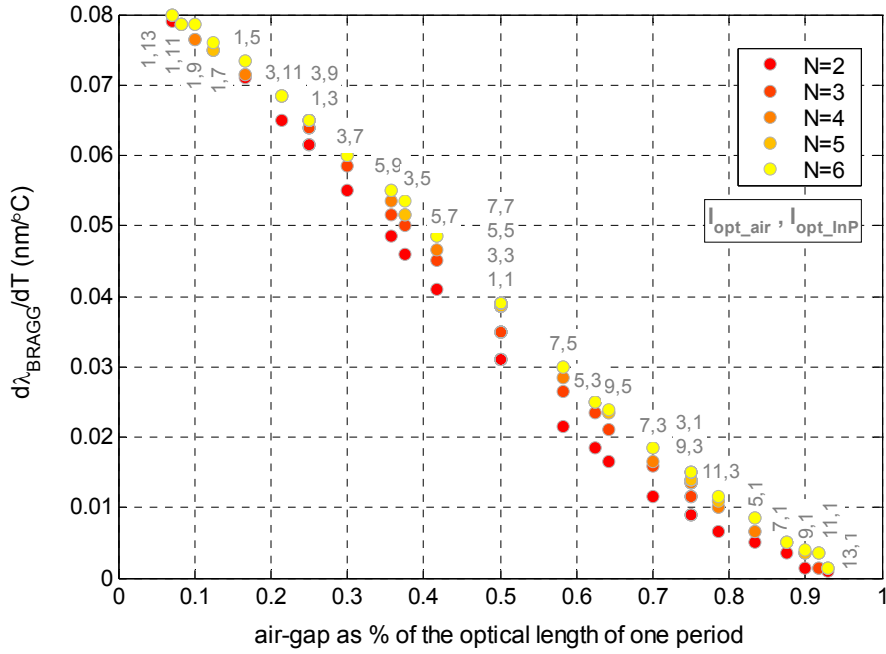


Figure 8-30 Drift rate of reflection peak of range of air-gap gratings

Lowest Bragg drift is obtained with the highest proportion of air, 13:1 in this plot.

Each Bragg-condition design point has points representing gratings with different numbers of periods. Interestingly, longer gratings drift faster.

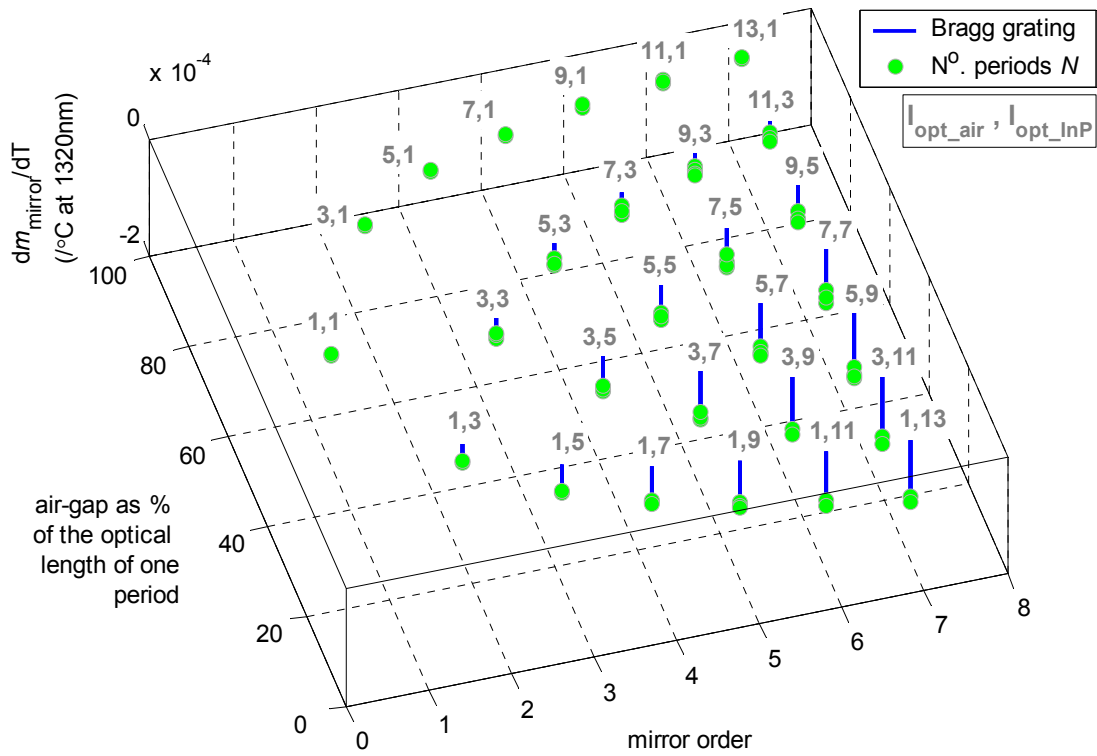


Figure 8-31 dm_{mirror}/dT for range of air-gap Bragg gratings

The stems extend downwards from the zero-plane, where their intercepts correspond to InP and air-gap layers both being an odd number of quarter-wavelengths thick.

The most negative rate of change of grating contribution, $-1.8 \times 10^{-4}/^{\circ}\text{C}$, is obtained for the smallest air-gaps as a fraction of the period length, i.e. the maximum grating drift. It would athermalise an InP cavity 533nm thick, but is impracticably thick itself for a VCSEL as the whole structure would be $>7\mu\text{m}$ high.

8.5.5 Conclusions

Athermalisation of the optical length of semiconductor laser resonant cavities using DBRs carefully designed to contribute an optical length which varies with temperature at exactly the opposite rate is a concept which requires very short cavities but has the potential to be realised in VCSELs. It is made possible by the recent advent of two new technologies; air-gap VCSELs and highly stable optical copolymers with tailorable properties.

The design procedure developed requires the use of a simple TMM model to survey the DBR design space. Knowledge of the epitaxial structure of the VCSEL cavity, the refractive indices and thermo-optic coefficients of the materials used is also necessary. The results of a survey conducted using representative parameters for InP indicate a broad range of alternative designs are typically available for athermalising any given VCSEL cavity.

In practice the designer will necessarily have to work around the available materials, in particular the available polymer systems, but given the robustness of this technique and the advent of tailorable polymers it is likely that suitable designs can be developed for a given infill medium. The design space is opened up further by the fact that the reflectors do not have to be symmetrical – if a hybrid design featuring an epitaxial stack bottom mirror were required it would be possible to find top-reflector designs to athermalise the combined resonant length.

-
- [1] Karim, A., Björilin, S., Piprek, J., and Bowers, J.E.: 'Long Wavelength Vertical-Cavity Lasers and Amplifiers', *IEEE Journal on Selected Topics in Quantum Electronics*, 2000, **6**, (6), pp.1244-1253
 - [2] Iga, K.: 'Vertical-cavity surface-emitting laser - Progress and prospects', *IEICE Transaction on Electronics*, 2002, **E85-C**, (1), pp.10-20
 - [3] Tan, M.R.T.: 'Progress in Long Wavelength VCSELs', IEEE-LEOS 2002 Annual Meeting, Glasgow, UK, 10-14 Nov. 2002, 1, pp.269-270
 - [4] Tan, K.T.: 'Enhanced performance 1.3 μm quantum dot laser for fibre optic communication', 2004, PhD Thesis, available from University of Cambridge Engineering Department Library
 - [5] Blum, O., Hafich, M.J., Klem, J.F., and Lear, K.L.: 'Electrical and optical characteristics of AlAsSb/GaAsSb distributed Bragg reflectors for surface emitting lasers', *Applied Physics Letters*, 1995, **67**, (22), pp.3233-3235
 - [6] Otsubo, K., Shoji, H., Fujii, T., Matsuda, M., Ishikawa, H.: 'High-Reflectivity In_{0.29}Ga_{0.71}As/In_{0.28}Al_{0.72}As Ternary Mirrors for 1.3 μm Vertical-Cavity Surface-

- Emitting Lasers Grown on GaAs', *Japanese Journal of Applied Physics Part 2 - Letters*, 1995, **34**, (2B), pp.227-229
- [7] Nakagawa, S., Hall, E., Almuneau, G., Kim, J.K., Buell, D.A., Kroemer, H., and Coldren, L.A.: '1.55 μm InP-lattice-matched VCSELs with AlGaAsSb-AlAsSb DBRs', *IEEE Journal on Selected Topics in Quantum Electronics*, 2001, **7**, (2), pp.224-230
- [8] Dudley, J.J., Babi, D.I., Mirin, R., Yang, L., Miller, B.I., Ram, R.J., Reynolds, T., Hu, E.L., and Bowers, J.E.: 'Low threshold, wafer fused long wavelength vertical cavity lasers', *Applied Physics Letters*, 1994, **64**, (12), pp.1463-1465
- [9] Boucart, J., Starck, C., Gaborit, F., Plais, A., Bouche, N., Derouin, E., Remy, J.C., Bonnet-Gamard, J., Goldstein, L., Fortin, C., Carpentier, D., Salet, P., Brillouet, F., and Jacquet, J.: 'Metamorphic DBR and tunnel-junction injection - A CW RT monolithic long-wavelength VCSEL', *IEEE Journal on Selected Topics in Quantum Electronics*, 1999, **5**, (3), pp.520-529
- [10] Gebretsadik, H., Qasaimeh, O., Jiang, H.T., Bhattacharya, P., Caneau, C., and Bhat, R.: 'Design and realization of a 1.55 μm patterned vertical cavity surface emitting laser with lattice-mismatched mirror layers', *IEEE Journal of Lightwave Technology*, 1999, **17**, (12), pp.2595-2604
- [11] Lin, H.C., and Cheng, K.Y.: 'Fabrication of Substrate-Independent Hybrid Distributed Bragg Reflectors Using Metallic Wafer Bonding', *IEEE Photonics Technology Letters*, 2004, **16**, (3), pp.837-839
- [12] Rapp, S., Piprek, J., Streubel, K., Andre, J., and Wallin, J.: 'Temperature sensitivity of 1.54 μm vertical-cavity lasers with an InP-based Bragg reflector', *IEEE Journal of Quantum Electronics*, 1997, **33**, (10), pp.1839-845
- [13] Huffaker, D.L., and Deppe, D.G.: 'Intracavity contacts for low-threshold oxide-confined vertical-cavity surface-emitting lasers', *IEEE Photonics Technology Letters*, 1999, **11**, (8), pp.934-936
- [14] Maleev, N.A., Kovsh, A.P., Zhukov, A.E., Vasil'ev, A.E., Mikhlin, S.S., Kuz'menkov, A.G., Bedarev, D.A., Zadiranov, Y.M., Kulagina, M.M., Shernyakov, Y.M., Shulenkov, A.S., Bykovski V.A., Solov'ev, Y.M., Möller, C., Ledentsov, N.N., and Ustinov, V.M.: 'Design and Technology of Vertical-Cavity Surface-Emitting Lasers with Nonconducting Epitaxial Mirrors', *Semiconductors (Fizika i Tekhnika Poluprovodnicov)*, 2003, **37**, (10), 1234-1238
- [15] Symonds, C., Dion, J., Sagnes, I., Dainese, M., Strassner, M., Leroy, L., and Oudar, J.-L.: 'High performance 1.55 μm vertical external cavity surface emitting laser with broadband integrated dielectric-metal mirror', *Electronics Letters*, 2004, **40**, (12), pp.734-735
- [16] Streubel, K., Rapp, S., Andre, J., and Chitica, N.: '1.26 μm vertical cavity laser with two InP/air-gap reflectors', *Electronics Letters*, 1996, **32**, (15), pp.1369-1370
- [17] Lin, C.K., Bour, D., Zhu, J., Perez, W.H., Leary, M.H., Tandon, A., Corzine, S.W., and Tan, M.R.T.: 'High temperature continuous-wave operation of 1.3 and 1.55 μm VCSELs with InP/air-gap DBRs', *IEEE Journal on Selected Topics in Quantum Electronics*, 2003, **9**, (5), pp.1415-1421
- [18] Lin, C.K., Bour, D., Zhu, J., Perez, W., Leary, M., Tandon, A., Corzine, S., Tan, M.: 'Electrically pumped 1.3 μm VCSELs with InP/air gap DBRs', *CLEO 2002*, 2002, post-deadline paper CPDB10-1
- [19] Eldada, L.: 'Advances in telecom and datacom optical components', *Optical Engineering*, 2001, **40**, (7), pp.1165-1178

Chapter 9

Polymers

Optical polymer technology has advanced under a series of motivations, most recently as a platform for optical integration. A review of material systems identifies the most suitable for athermalisation applications.

9.1 Introduction

Two forces have recently driven increasing commercial acceptance of polymer technologies: low costs and unique capabilities.

These unique capabilities are owed in large part to the great variety of structures and active groups that can be synthesised. It is possible to tailor polymeric materials to meet strict requirements for optical devices, although exploiting this demands comprehensive understanding of both the specific device applications and various polymer systems.

One key feature of polymeric materials is their high negative thermo-optical coefficients. This large TOC (about 25 times larger in most polymers than in glass) can be exploited to produce low-power and low-cost thermo-optically active optical components. Even merely reducing temperature sensitivity reduces costs by allowing less precise temperature control. Commercialised or demonstrated devices based on these properties include thermo-optical switches (TOSs) [1,2,3], variable optical attenuators (VOAs) [4,5], tunable waveguide devices [6,7,8] such as arrayed waveguide gratings (AWGs), and athermal AWGs [9,10].

Polymers' cost advantages derive from their low material cost and ease of processing. They are synthesised in liquid monomer or solution; a cheap bulk process requiring none of the delicate mechanical steps or high temperatures associated with inorganic crystalline materials. Depending on their properties they can be processed into optical components as molten polymer or polymerised *in situ*, as required. Many are compatible with established optical component manufacturing techniques such as etching and lithography; others offer the possibility of radically lower-cost techniques such as hot-embossing or direct deposition using technology borrowed from inkjet printers.

9.2 Structure and Chemistry

The term 'polymer' covers a diverse group of molecules whose common characteristic is that they are formed of many repeated elements, termed monomers. The monomers in a given

polymer need not be identical, but they must share a common polymerisation mechanism so that they can *copolymerise*. These linkages and monomers ultimately determine to a significant degree the characteristics of the resulting polymer including melt or solution processibility, surface energy, hardness, toughness, water uptake, stability and aging, birefringence, refractive index and thermo-optic coefficient.

Although most typically organic (based on carbon chains), there are also many ‘inorganic’ polymers based on silicon chains.

The attractive forces between polymer chains play a large part in determining a polymer's properties. *Crosslinked* polymers are of particular interest, possessing inter-chain covalent bonds which create a three-dimensional network. Such materials are tough, have high thermal stability and reduced hygroscopy.

In many modern optical polymers some fraction of the hydrogen atoms are replaced by halogens, typically fluorine. This is done primarily to reduce infra-red absorption but also leads to increased chemical stability, reduced crystallinity and decreased water absorption. However, the adhesion of fluorinated polymers to many substrates is often an engineering issue due to their inert nature and low surface energies.

9.3 Refractive Index

The refractive index of a material is related to the free volume (packing density), polarisability, and absorptions of the material. Usually, dense packing or high polarisability results in increased refractive index.

All amorphous polymers have a large free volume, responsible for a large temperature coefficient of volume expansion and in turn for a large negative rate of change of refractive index, typically of the order $10^{-4}/^{\circ}\text{C}$, an order of magnitude larger than for glass, silica and most semiconductor materials.

Polarisability has three constituents; electronic, atomic and dipole, in order of increasing time constant. At optical frequencies only electronic polarisation is significant. Inclusion in polymers of certain functional groups, aromatic groups (benzene rings) in particular, can be used to modify polarisability and hence refractive index.

In the whole range of polymers, there are available refractive indices from 1.3 to 1.7 and thermo-optic coefficients from -1×10^{-4} to $-4 \times 10^{-4} /^{\circ}\text{C}$ [11]. The properties of a particular polymer depend on the chemical elements and moieties in the polymeric chain structure.

Polymers constructed with no double bonds and fluorinated groups have lower refractive indices, due to lesser polarisability and increased free volume respectively. Aromatic groups and chlorine increase optical density due to better packing and electronic polarisability. The refractive indices of polymers can be easily and precisely tuned by copolymerization of two or more monomers bearing the same polymerizable groups.

The latest generation of optical polymers are copolymeric so that optical density and TOC can be adjusted by changing the proportions of the species in the monomer mix. Co-polymers in different ratios can produce a continuously-adjustable range of refractive indices. However, refractive index and TOC are usually highly correlated, being dependent on the proportion of a particular functional group in the mix.

9.4 Modern Optical Polymers

The first wave of optical polymers broke in the 1970's. In the last two decades several new families of optical polymers have been developed, many available commercially [12]. Here we examine those systems reported as having tailorable properties. BCB and sol-gels are also mentioned.

9.4.1 Halogenated Polyacrylates

A great number of intermiscible halogenated and nonhalogenated acrylic monomers have been studied. The variety of structural variables makes properties of the copolymerised materials widely adjustable.

AlliedSignal reported refractive index adjustability from 1.3 to 1.6 with reproducibility better than 0.0001 [13]. The value of dn/dT for different classes of halogenated and nonhalogenated cross-linked acrylate polymers varies between approximately -2 and $-3 \times 10^{-4} / ^\circ\text{C}$.

Because of the high photosensitivity of the acrylic double bond, exposure to actinic radiation (UV or e-beam) causes acrylic monomer systems to form highly crosslinked networks. The ability to be photochemically processed directly from undiluted monomer gives them low internal stress and dimension shrinkage, making them particularly suitable for integration in devices based on inorganic materials where delamination can be a problem.

These crosslinked acrylates have very low glass transition temperature ($T_g < -50^\circ\text{C}$) but show no degradation after prolonged deployment in operational temperature ranges (generally 25 to 75°C). Humidity sensitivity is also low, AlliedSignal reported Δn of -4.5×10^{-3} over 20-80% relative humidity (RH), and an order of magnitude less for 80% halogenated systems [13].

Although AlliedSignal has since merged with Honeywell and thence been sold to Corning, which prefers to keep AlliedSignal's materials for use in proprietary components, many other firms are working with polyacrylates. Demonstrated applications based on acrylic polymers include optical interconnects [14], waveguides with 45° micromirrors [15], AWGs [16,17], athermal ring resonators [18], athermal AWGs [10], thermally tunable Bragg-grating-based optical add/drop multiplexers (OADMs) [6,13], and TOSs [19,20].

9.4.2 Fluorinated poly(arylene ethers)

First developed by Dow Chemical in the early 1990s, poly-(aryl ether) polymers based on perfluorocyclobutyl (PFCB) repeating units are synthesised without catalysts, initiators or condensation products. With low moisture absorption, high temperature stability, high thermo-optic coefficient and low absorption at telecoms wavelengths these have properties well suited to optical applications [21,22,23].

Many other fluoropolymers based on polyimide condensation or chain addition polymerisation have low (<50% by weight) solubility in common solvents, which makes shrinkage a problem. PFCB-based polymers have no such problems and can be processed by standard techniques in the melt or in solution.

Their disadvantage is their small range of refractive index controllability (1.449-1.508 at 1550nm) [22,24] and the fact that they have not been made commercially available, although they have been sampled to some research groups [25].

9.4.3 Polysiloxanes (Silicone Resins)

Polysiloxanes, otherwise known as silicones, are unusual in having inorganic backbones consisting of alternating silicon and oxygen atoms (...-Si-O-Si-O-Si-O-...) with side groups attached to the silicon atoms. Various organic side groups can be used to link silicone backbones together or to provide specific optical properties.

They are impervious to moisture, oxidation resistant and stable against high temperature and optical power. Infra-red absorption is similar to other polymers but this is not a problem in thermal applications which typically require only short path lengths but do need polysiloxanes' very high thermo-optic coefficients of up to $4 \times 10^{-4}/^{\circ}\text{C}$.

Polymerisation involves the elimination of water as a condensation product, so the process must be conducted with care to avoid water retention which would thereafter cause a gradual change in properties. Spin coating can be performed, for some formulations, without solvent or elevated temperatures [26]. The material can then be reactive-ion etched or lithographically patterned.

Many waveguide elements have been made using silicones including directional couplers [27], TOSs [2,28], thermally tunable AWGs [8], thermally stabilised silica-based AWGs [9], reconfigurable OADMs [29] and (commercially-available) VOAs [30].

Dow Corning, a partnership between Dow Chemical and Corning specialising in silicones, has developed low T_g (below -70°C) optical silicones with wide, *independently* tailorable refractive index and thermo-optic coefficient. Altering the ratio of methyl to phenyl groups on the silicon atom varies the material's refractive index between 1.35 and 1.6 (over 1300-1600nm) with better than 0.5% precision. Thermo-optic coefficient meanwhile is controlled by the ratio of organic groups to oxygen linkages and by the cross-link density, which is influenced by the cure chemistry [30]. The materials are low in viscosity and are thermally cured, making them ideal for cavity-infilling. The company offers a materials prototyping service which makes these polymers particularly accessible.

9.4.4 Benzocyclobutene (BCB)

A widely-tested material [31,32,33,34,35,36] developed by Dow Chemical as a low-k spin-on dielectric and marketed as *Cyclotene*. Many optical device designs have been realised in BCB although it is not suitable for applications with long path lengths because of its high loss of approximately 1.5dB/cm, which arises largely from the high density of C-H bonds.

9.4.5 Sol-Gels

Not polymers as such, sol-gels are mentioned here as polymers' most serious competitors. The sol-gel process may be considered as a method for producing glass and ceramic materials from metallorganic precursors by low temperature polymerization reactions. The process represents a powerful tool for making almost all kinds of transparent materials with interesting optical or photonics properties [37,38]. It is still an emerging technology despite attracting considerable attention from a variety of research fields since its appearance as a popular technique some decades ago. Its use in the fabrication of optical glasses such as bulk structure and films has been subject to particularly extensive study.

9.5 Technical Considerations

9.5.1 Reliability & Environmental Stability

The stability of polymers' optical and mechanical characteristics against temperature and humidity is typically insufficient for operation in deployed communication environments. A number of the newest polymers have addressed this problem through cross-linking and fluorination and have been shown to exhibit excellent environmental stability in a variety of demanding applications.

The refractive index of many polymers is strongly humidity-dependent (10^{-5} per % relative humidity) and arises from moisture absorption and swelling due to the existence of hydrophilic groups. Cross-linking inhibits this by reducing the amount of room available for interstitial water. Fluorinated polymers are actively hydrophobic.

Glassy polymers that have been taken above their glass transition temperature return to their semicrystalline low-energy state only very slowly. Their fractional free volume is not constant but slowly reduces over time due to thermal relaxation, leading to problems with refractive index drift. *In situ* polymerisation or cross-linking avoids this problem as the resulting material does not contain residual stresses.

Crosslinked polymers are especially advantageous in that they do not flow and are mechanically stable even above T_g , so material with very low T_g can be used deliberately to avoid strain-related effects such as polarisation dependency or delamination. High T_g used to be considered desirable, as a guarantee that the material would not soften in deployed conditions, but crosslinked polymers mean that very low T_g is now preferred.

9.5.2 Processing & Fabrication

Crystallinity is generally avoided in polymers, but defects can still be a problem. Inclusions such as particles, voids, cracks and bubbles scatter largely independently of wavelength when larger than $\sim 1\mu\text{m}$. They may arise from unfiltered particles, condensation by-products, dust, unreacted monomer or dissolved gas. Rigorous clean-room conditions and careful curing are necessary, but these are already familiar requirements in plants fabricating semiconductor components.

Manufacturability concerns include particularly layer thickness tolerances, and, potentially, deviation of polymer TOC from specification in confined spaces, since polymer TOC arises in part from physical expansion. A general drawback of polymeric materials is batch-to-batch variability of refractive index and this must be carefully monitored.

Inserting polymer in to air gaps as required in the athermalisation scheme discussed in Chapter 7 and Chapter 8 is a potential problem, but is not expected to be a serious one given the variety of processing methods available and the previous success of BCB deposition in small cavities in edge emitters [31,34,35,39,40]. Performing a similar task in VCSELS likely to be straightforward, involving spin-coating of liquid monomer or polymer melt, followed by *in situ* polymerisation and crosslinking. Excess material can then be etched back. Spinning-on in solution is less attractive due to the unknown character of shrinkage of the material in the cavities during drying.

9.6 Conclusion

Reliability problems having been overcome, polymer technology's inherent low cost, ease of processing and ease of integration are driving acceptance in the optical communications industry.

The specific requirements of the athermalisation application discussed in Chapter 8 are precise tailorability of RI and TOC, the ability to penetrate and polymerise in small spaces, preferably thermal initiation of polymerization, longevity at elevated temperature, and chemical etchability for easy removal of excess. The thicknesses involved are sufficiently small that loss and birefringence properties are of secondary concern. It would be particularly useful during design to be able to vary TOC while retaining fixed RI; to date this property has only been reported in polysiloxanes.

Of the polymer materials reviewed, polysiloxanes and polyacrylates appear to fulfil these requirements well. Customised polyacrylates are promising but are not commercially available, the most promising having been taken in-house for use in proprietary devices by Corning. However, low-viscosity, tailored polysiloxanes are readily available from Dow-Corning, making them the practical choice.

-
- [1] Kobayashi, J., Matsuura, T., Hida, Y., Sasaki, S. and Maruno, T.: 'Fluorinated polyimide waveguides with low polarization-dependent loss and their applications to thermo-optic switches', *Journal of Lightwave Technology*, 1998, **16**, (6), pp.1024-1029
 - [2] Toyoda, S., Ooba, N., Katoh, Y., Kurihara, T. and Maruno, T.: 'Low crosstalk and low loss 2x2 thermo-optic digital optical switch using silicone resin waveguides', *Electronics Letters*, 2000, **36**, (21), pp.1803-1804
 - [3] Cross, G.: 'Optical Materials: For polymer switches, tailored synthesis meets the reliability challenge', *Laser Focus World*, 2003, **39**, (5), pp.150-152
 - [4] Lee, S.-S., Jin, Y.-S. and Son, Y.-S.: 'Variable optical attenuator based on a cutoff modulator with tapered waveguides in polymers', *Journal of Lightwave Technology*, 1999, **17**, (12), pp.2556-2561

-
- [5] Lee, S.-S., Bu, J.-U., Lee, S.-Y., Song, K.-C., Park, C.-G. and Kim, T.-S.: 'Low-power consumption polymeric attenuator using a micromachined membrane-type waveguide', *IEEE Photonics Technology Letters*, 2000, **12**, (4), pp.407-409
- [6] Kobayashi, J., Inoue, Y., Matsuura, T. and Maruno, T.: 'Tunable and Polarization-Insensitive Arrayed-Waveguide Grating Multiplexer Fabricated from Fluorinated Polyimides', *Denshi Joho Tsushin Gakkai Ronbunshi, C:Erekutoronikusu* (in Japanese) [Trans. IEICE, C], 1998, **E81-C**, (7), pp.1020-1026
- [7] Eldada, L., Blomquist, R., Maxfield, M., Pant, D., Boudoughian, G., Poga, C. and Norwood, R.A.: 'Thermooptic planar polymer Bragg grating OADMs with broad tuning range', *IEEE Photonics Technology Letters*, 1999, **11**, (4), pp.448-450
- [8] Toyoda, S., Kaneko, A., Ooba, N., Hikita, M., Tsukada, M., Kurihara, T. and Maruno, T.: 'Polymer tunable wavelength filter for WDM systems', *IEICE Transactions on Electronics*, part E, 2000, **E83-C**, (7), pp.1119-1124
- [9] Kaneko, A., Kamei, S., Inoue, Y., Takahashi, H. and Sugita, A.: 'Athermal silica-based arrayed-waveguide grating (AWG) multi/demultiplexers with new low loss groove design', *Electronics Letters*, 2000, **36**, (4), pp.318-319
- [10] Keil, N., Yao, H.H., Zawadzki, C.C., Bauer, J., Bauer, M., Dreyer, C. and Schneider, J.: 'Athermal all-polymer arrayed-waveguide grating multiplexer', *Electronics Letters*, 2001, **37**, (9), pp.579-580
- [11] Eldada, L.: 'Advances in telecom and datacom optical components', *Optical Engineering*, 2001, **40**, (7), pp.1165-1178
- [12] Eldada, L.: 'Key Properties of Optical Polymers Developed Globally', *WDM Solutions*, 2002, **26**
- [13] Eldada, L., Blomquist, R., Shacklette, L.W. and McFarland, M.J.: 'High-performance polymeric componentry for telecom and datacom applications', *Optical Engineering*, 2000, **39**, (3), pp.596-609
- [14] Booth, B.L., Marchegiano, J.E., Chang, C.T., Furmanak, R.J., Graham, D.M. and Wagner, R.G.: 'Polyguide polymeric technology for optical interconnect circuits and components', *Proceedings of SPIE - the International Society of Optical Engineering*, 1997, **3005**, pp.238-251
- [15] Cook, J.P.D., Este, G.O., Shepherd, F.R., Westwood, W.D., Arrington, J., Moyer, W., Nurse, J. and Powell, S.: 'Stable low-loss optical waveguides and micromirrors fabricated in acrylate polymers', *Applied Optics*, 1998, **37**, (7), pp.1220-1226
- [16] Viens, J.-F., Callender, C.L., Noad, J.P., Eldada, L. and Norwood, R.A.: 'Polymer-based waveguide devices for WDM applications', *Proceedings of SPIE - the International Society of Optical Engineering*, 1999, **3799**, pp.202-213
- [17] Viens, J.-F., Callender, C.L., Noad, J.P. and Eldada, L.: 'Compact wide-band polymer wavelength-division multiplexers', *IEEE Photonics Technology Letters*, 2000, **12**, (8), pp.1010-1012
- [18] Kokubun, Y., Yoneda, S. and Matsuura, S.: 'Athermal narrow-band optical filter at 155 nm wavelength by silica-based athermal waveguide', *IEICE Transactions on Electronics*, part E, 1998, **E81-C**, (8), pp.1187-1194
- [19] Hida, Y., Ooba, N., Yoshimura, R., Watanabe, T., Hikita, M. and Kurihara, T.: 'Influence of humidity on transmission in a Y-branch thermo-optic switch composed of deuterated fluoromethacrylate polymer waveguide', *Electronics Letters*, 1997, **33**, (7), pp.626-627
- [20] Keil, N., Yao, H.H., Zawadzki, C., Lüscher, K., Satzke, K., Wischmann, W., van Wirth, J., Schneider, J., Bauer, J. and Bauer, M.: 'Hybrid polymer/silica vertical coupler switch with 232 dB polarization-independent crosstalk', *Electronics Letters*, 2001, **37**, (2), pp.89-90
- [21] Fischbeck, G., Moosburger, R., Kostrzewa, C., Achen, A. and Petermann, K.: 'Singlemode optical waveguides using a high temperature stable polymer with low losses in the 1.55 μm range', *Electronics Letters*, 1997, **33**, (6), pp.518-519
- [22] Smith, D.W. Jr., Kumar, S.M., Chen, S.R., Ballato, J.M., Nelson, E.J., Jin, J.J. and Foulger, S.H.: 'Property tailored perfluorocyclobutyl (PFCB) copolymers for optical devices', *Design, Manufacturing, and Testing of Planar Optical Waveguide Devices* (Ed: Norwood RA), 2001, **4439**, pp.51-62
-

-
- [23] Choi, W.S. and Harris, F.W.: 'Synthesis and polymerization of trifluorovinylether-terminated imide oligomers', *Polymer*, 2000, **41**, (16), pp.6213-6221
- [24] Ma, H., Jen, A.K.-Y. and Dalton, L.R.: 'Polymer-Based Optical Waveguides: Materials, Processing, and Devices', *Advanced Materials*, 2002, **14**, (19), pp.1339-1365
- [25] Kim, J.-P., Lee, W.-Y., Kang, J.-W., Kwon, S.-K., Kim, J.-J. and Lee, J.-S.: 'Fluorinated poly(arylene ether sulfide) for polymeric optical waveguide devices', *Macromolecules*, 2001, **34**, (22), pp.7817-7821
- [26] Dow-Corning photonics web site: <http://www.dowcorning.com/content/photonic/>, accessed 17/12/04
- [27] Usui, M., Hikita, M., Watanabe, T., Amano, M., Sugawara, S., Hayashida, S. and Imamura, S.: 'Low-loss passive polymer optical waveguides with high environmental stability', *Journal of Lightwave Technology*, 1996, **14**, pp.2338-2343
- [28] Watanabe, T. and Ooba, N., Hayashida, S., Kurihara, T., Imamura, S.: 'Polymeric optical waveguide circuits formed using silicone resin', *Journal of Lightwave Technology*, 1998, **16**, (6), pp.1049-1055
- [29] Saida, T., Kaneko, A., Goh, T., Okuno, M., Himeno, A., Takiguchi, K. and Okamoto, K.: 'Athermal silica-based optical add/drop multiplexer consisting of arrayed waveguide gratings and double gate thermo-optical switches', *Electronics Letters*, 2000, **36**, (6), pp.528-529
- [30] Freeman, T.: 'Tough polymers eye optical comms', *FibreSystems Europe in association with LIGHTWAVE Europe*, 2004, pp.25
- [31] Strååt, A. and Nikolajeff, F.: 'Study of Benzocyclobutene as an Optical Material at Elevated Temperatures', *Applied Optics*, 2001, **40**, (29), pp.5147-5152
- [32] Kane, C.F. and Krchnavek, R.R.: 'Benzocyclobutene optical waveguides', *IEEE Photonics Technology Letters*, 1995, **7**, (5), pp.535-537
- [33] Raj, M.M., Wiedmann, J., Saka, Y., Ebihara, K. and Arai, S.: 'Highly uniform 1.5 μm wavelength deeply etched semiconductor/benzocyclobutene distributed Bragg reflector lasers', *Japanese Journal of Applied Physics Part 2 - Letters*, 2000, **39**, (12B), pp.L1297-9
- [34] Raj, M.M., Wiedmann, J., Toyoshima, S., Saka, Y., Ebihara, K. and Arai, S.: 'High-reflectivity semiconductor/benzocyclobutene Bragg reflector mirrors for GaInAsP/InP lasers', *Japanese Journal of Applied Physics Part 1-Regular Papers Short Notes & Review Papers*, 2001, **40**, (4A), pp.2269-77
- [35] Raj, M.M., Toyoshima, S. and Arai, S.: 'Multiple micro-cavity laser with benzocyclobutene/semiconductor high reflective mirrors fabricated by CH₄/H₂-reactive ion etching', *Japanese Journal of Applied Physics Part 2 - Letters*, 1999, **38**, (7B), pp.L811-L814
- [36] Ushigome, R., Fujita, M., Sakai, A., Baba, T. and Kokubun, Y.: 'GaInAsP Microdisk Injection Laser with Benzocyclobutene Polymer Cladding and Its Athermal Effect', *Japanese Journal of Applied Physics Part 1 - Regular Papers Short Notes & Review Papers*, 2002, **41**, (11A), pp.6364-6369
- [37] Schmidt, H.K.: 'Chances and limitations of sol-gel-derived metal oxide and chalcogenide nanocomposites for optic and photonic application', *Sol-Gel and Polymer Devices* (Eds: Andrews MP, Najafi SI), 1997, **CR 68**, pp.192-206
- [38] Kang, E.-S., Kim, W.-S., Kim, D.-J. and Bae, B.-S.: 'Reducing the Thermal Dependence of Silica-Based Arrayed-Waveguide Grating Using Inorganic-Organic Hybrid Materials', *IEEE Photonics Technology Letters*, 2004, **16**, (12), pp.2625-2627
- [39] Wiedmann, J., Raj, M.M., Ebihara, K., Matsui, K., Tamura, S. and Arai, S.: 'Deeply etched semiconductor/benzocyclobutene distributed Bragg reflector laser combined with multiple cavities for 1.5- μm -wavelength single-mode operation', *Japanese Journal of Applied Physics Part 1-Regular Papers Short Notes & Review Papers*, 2001, **40**, (6A), pp.4031-7
- [40] Raj, M.M., Saka, Y., Wiedmann, J., Yasumoto, H. and Arai, S.: 'Continuous wave operation of 1.55 μm GaInAsP/InP laser with semiconductor / benzocyclobutene distributed Bragg reflector.', *Japanese Journal of Applied Physics Part 2 - Letters*, 1999, **38**, (11A), pp.L1240-2
-

Chapter 10

Conclusion

A review is made of the work described in this thesis and of the conclusions drawn from it. These are placed in context in the current optical communications environment. Finally, possibilities are discussed for developing the work further.

10.1 Review

From the taking-off point of athermal grating design this work has proceeded via conception of a new method of passive wavelength stabilisation and exploration of its design space to, ultimately, a design procedure for athermal long-wavelength VCSELs (Chapter 8).

Preceding work on athermal gratings was discussed and generalised to engineered-drift gratings in Chapter 3. The necessity of deeply-etched gratings and the role of infill materials such as BCB were introduced. A test device showed only a 10% reduction in modal drift despite having an athermal grating. A computational model to predict mode drifts over temperature was created using the resonance and gain conditions for lasing (Chapter 5), with a separate TMM model for calculating the reflection characteristics of the reflection gratings (Chapter 4).

Simulations showed that the reflection peaks of these high-contrast gratings were tens to hundreds of nanometres wide, offering very little wavelength selectivity. The reflection spectra of pairs of athermal DBR gratings were offset so as to obtain a narrow high-reflectivity peak, further simulations indicating that wavelength confinement within bands of less than 1nm is possible, provided mode hops are tolerable in the application (Chapter 6).

In many applications, including high data-rate CWDM channels, mode hopping in the source is not tolerable. Since resonant modes are controlled by the length of the resonating cavity, reducing mode drift requires stabilisation of the cavity length. An approach premised on controlling the phase of the gratings' complex reflections to counteract the temperature-dependent phase length of the cavity itself was introduced in Chapter 7.

The non-analytic nature of grating reflectivity spectra making it impossible to design reflectors with specific rates of change of phase contribution, the problem was inverted to one of finding those cavity lengths athermalised by a given grating. However, investigations did identify rules of thumb for desirable grating characteristics.

A number of 1310nm MQW ridge-waveguide devices were modified to short cavities with deep trench gratings, using FIB etching. Device 20-1 showed a possible drift modification, and also enabled a measurement of the effective group index in the waveguide which was subsequently independently confirmed using device 55. The output spectra of these devices also helped confirm the validity of the numerical models.

Lasing was not obtained in these short cavities and this was attributed to the very high mirror reflectivities required not being achieved. Reference to published work on deep gratings indicated that diffractive loss in the unguided sections had likely degraded reflectivity significantly. Subsequent ‘deep DBR’ designs intended to increase the total active length and reduce the material gain requirement did not lase either. Analysis of electrical characteristics of the etched region indicated significant degradation of its diode characteristic.

VCSELs were considered as an alternative short-cavity configuration, eliminating diffractive losses and etching damage, and highly complementary to the low-cost market positioning of CWDM systems (Chapter 8). Conventional VCSELs are fabricated from a limited palette of materials and necessarily have quarter-wave reflector stacks, or an odd order thereof. This would severely limit opportunities for drift engineering were it not for the recent emergence of two technologies – air-gap reflectors for long-wavelength InP-based VCSELs and durable, customisable optical polymer materials. These were combined to produce a drift-engineered VCSEL configuration. The requirement for quarter-wave reflector stacks also emerged as an advantage, enabling confident prediction of the reflection peak maximum and associated zero reflection phase. With this uncertainty removed from the design process it became possible to survey the entire reflector design space, comprising the range of reflector configurations and possible polymer parameters, obtaining a data set spanning all possible reflector designs. Mirror designs can be selected from this according to criteria including rate of change of phase contribution and properties of the polymer.

Finally, current optical polymer materials were reviewed and candidates for use in this athermalisation technique identified, based on their optical and mechanical properties and also their availability.

10.2 Conclusions

Two techniques for engineering precise reflectivity-peak drift rates have been developed, neither of which, to the author’s knowledge, has been reported previously. Both involve the filling-in of empty intervals in the grating structure with material possessing high refractive index contrast and significantly different thermo-optic coefficient.

The first proceeds from a somewhat unconventional interpretation of the Bragg condition and depends on adjustment of the relative amounts of materials with different thermo-optic coefficients within the grating period, which remains an odd number of half wavelengths long, optically speaking. Although this technique makes the exact position of the reflection peak unpredictable it is easily obtained through numerical modelling, and fractional adjustment of the grating order can be used iteratively to centre the peak at the desired wavelength. Although not designed to demonstrate Bragg-peak drift modification, the observed drift rate of features in the reflectivity spectrum of device 55 matches that predicted by this method.

The second approach keeps to standard Bragg structures, which are highly predictable, maximise reflectivity and whose reflection peak wavelengths coincide with zero reflection phase. Continuous drift-rate tunability is obtained by use of customised optical polymeric materials. Such materials are now becoming commercially available and possess many other advantageous properties.

This latter technique has been applied to InP-based long-wavelength air-gap VCSEL DBRs to give the main result of this investigation; a low-cost method of athermalising short cavities such as to stabilise emission wavelength over deployed temperature ranges for CWDM systems. Based on use of the grating reflection phase to maintain a constant optical cavity length this approach has been developed in to a regularised design procedure with a clearly-delineated design space. It is possible to select athermalising reflectors to suit a given active structure, or *vice versa*. Designers can specify an optical polymer for their design, or proceed to a design utilising a given polymer.

A subsidiary conclusion, based on a review of the state of the art in optical polymers, is that Dow-Corning's tailored polysiloxanes are the best materials for this application by some margin. They have excellent mechanical, processing, environmental stability and optical properties, and are unique in having independently-customisable refractive index and thermo-optic coefficient.

Work on implementing this athermalisation method in edge emitters served to illuminate the design space but ultimately was not successful due to the limitations of the format and the fabrication technique. It was found that air gaps must be kept as short as possible, preferably to a minimum one quarter wavelength, in order to minimise losses in the unguided sections. It was also found that FIB etching seriously degrades the heterojunction characteristics. For these reasons the VCSEL format is preferred.

Although use of offset pairs of athermal Bragg reflectors was shown to be capable of confining emission wavelength within a range equivalent to the mode spacing, mode hopping made the method unappealing. The only way to effectively stabilise emission wavelength is

found to be to stabilise the length of the resonant cavity, and the reflection grating as well if it plays any role in wavelength selection. High contrast reflection gratings with their broad reflection peaks are found to relax this second requirement, leaving only the problem of stabilisation of cavity length, which has been achieved as described above.

10.3 Evaluation

It was established in the introductory Chapter 1 that passive athermalisation of emission wavelength is desirable; the question which must be asked now is whether this particular scheme is practicable.

VCSELs are complex structures and not so simple as has been assumed for the purposes of proof-of-principle. Current injection, spacer, quantum well and current confinement layers are all frequently found between VCSEL DBRs. Predicting the rate of change of optical length of this compound cavity will likely require more sophisticated simulation techniques. It is certainly possible, however.

Many of the athermal points located in the cavity-length surveys of Chapter 7 were extremely finely balanced and so vulnerable to small fabrication errors. This was because they utilised points towards the edges of the reflectivity peak where the slope of the reflection phase with wavelength was highly curved, so that a small movement away from the optimum position destroyed the athermalisation. In contrast, the athermal designs found using the reflector survey in Chapter 8 all use the central, linear-phase region of the Bragg peak and are thus should be much more tolerant of fabrication errors, allowing acceptable yields.

The use of dielectric stacks with InP-based active regions is only one possible solution to the problem of creating long-wavelength VCSELs. It is quite likely that an alternative solution based on GaInAs quantum dot or GaInNAs quantum well active material with the highly-effective and well established GaAs-AlAs reflector stack will prevail. If so, the risk associated with developing athermal air-gap-based VCSELs, for a market which can not exist before their advent, may be unappealing. However it is not possible to foresee all applications and there are often niches to be filled.

10.4 Future Work

Apart from device 21, the results from which are not in themselves sufficient, the evidence that this athermalisation method works is based on simulation results. There is some evidence of anomalous mode-drift in other VCSELs: Nishiyama *et al* [1] observed a drift rate of 0.043nm/°C in a 1200nm GaInAs VCSEL but did not investigate further. The models

independently show good agreement with observed results. Nevertheless it is necessary to show practical proof of concept.

The group has recently joined the CAPE collaboration; an industrially-sponsored University of Cambridge centre of excellence, and thus has good contacts with Dow-Corning who are one of the sponsors. Access to advanced optical polymers is therefore assured. Fabrication facilities for air-gap VCSELs are lacking however and it would be necessary to collaborate with another group on these.

The 'deep DFB' concept was promising and should be revisited using smaller air-gaps and an alternative etching technique such as reactive ion etching (RIE). Alternatively, the materials science FIB machine has recently been upgraded and now has the capability to deposit amorphous silica, deposition of which in the etched trenches before exposure to the atmosphere may prevent formation of current paths over the etched surfaces. Silica has low thermo-optic coefficient ($\sim 1 \times 10^{-5}/^{\circ}\text{C}$) and refractive index (~ 1.5) and so is an excellent material for this application. It may also be possible to monitor damage to the active region during etching in real time using a pump laser and taking the output via optical fibre to an OSA.

A number of groups have reported the ability to 'write' waveguides in a variety of materials by inducing local but permanent changes in refractive index using high-intensity ultraviolet light [2]. It may be possible to use this to write waveguides in the polymer sections of 'deep DFBs', reducing optical losses. It may even be possible to exploit this ability to create hybrid polymer-semiconductor cavities whose resonant length is constant over temperature, but there is a danger that attempting this would only create a compound cavity instead. An interesting possibility created by customisable polymers is the introduction of index-matching layers between the two cavities, but were this put in to practice scattering losses due to mismatch between transverse mode profiles would be very hard to avoid.

Theoretically, an investigation of interaction length, that is how far light penetrates in to gratings, could be illuminating. A long interaction length in a two-phase grating could be interpreted as altering the 'mean' material composition seen by the light.

The addition of gain and especially loss parameters to the models would be useful for locating modes and investigating diffractive losses in edge emitters.

Finally, shallow gratings in edge emitting lasers, dismissed on the basis of preceding work as impracticable for high material contrasts, may warrant further investigation. They avoid the considerable problems of etching through the active layer and waveguide and potentially offer another degree of freedom for refractive-index modification: by altering the degree of overlap with the transverse mode profile the designer can adjust the effective index. Furthermore, analysis of Gefan Huang's results indicates that the only possible explanation for the observed

reduction in mode drift is that the etch made did not penetrate the wave guide but stopped just short, and by cladding this section with BCB its optical length was partially stabilised.

Examination of the mode spacing before and after the etch shows no change, indicating that the etch did not go through the waveguide. The good output power obtained despite the very large air gaps supports this deduction. However there was undeniably some selection as the devices were single-moded at higher drive levels, indicating that the etch got very close to the waveguide. The reduction in mode drift is explicable only by the formation of a kind of hybrid cavity, in which drift was reduced by cladding part of the waveguide in negative-TOC material. This idea is not entirely novel, it has been reported in relation to BCB-clad microdisc lasers by Ushigome *et al* [3] and in relation to DFBs and DBRs formed by deep cladding grooves by Oku *et al* [4]. Despite being the genesis of this investigation, Gefan Huang's result was obtained by a different mechanism to that elucidated in this dissertation.

-
- [1] Nishiyama, N., Arai, M., Shinada, S., Azuchi, M., Matsutani, A., Miyamoto, T., Koyama, F. and Iga, K.: '1.12 μm Polarization Controlled Highly Strained GaInAs Vertical-Cavity Surface-Emitting Lasers on GaAs(311)B by Metal Organic Chemical Vapor Deposition', 2001, *Japanese Journal of Applied Physics Part 2-Letters*, **5A**, (40), L437-L439
 - [2] Koo, J., Smith, P.G.R., Williams, R.B., Riziotis, C. and Grossel, M.C.: 'UV written waveguides using crosslinkable PMMA-based copolymers', 2003, *Optical Materials*, **23**, pp.583-592
 - [3] Ushigome, R., Fujita, M., Sakai, A., Baba, T. and Kokubun, Y.: 'GaInAsP Microdisk Injection Laser with Benzocyclobutene Polymer Cladding and Its Athermal Effect', 2002, *Japanese Journal of Applied Physics Part 1- Regular Papers Short Notes & Review Papers*, **41**, (11A), pp.6364-6369
 - [4] Oku, S., Ishii, T., Iga, R. and Hirono, T.: 'Fabrication and performance of AlGaAs-GaAs distributed Bragg reflector lasers and distributed feedback lasers utilizing first-order diffraction gratings formed by a periodic groove structure', 2001, *IEEE Journal on Selected Topics in Quantum Electronics*, **5**, (3), pp.682-687

Appendix Device List

Device No.	Purpose of Device	Wafer	#CW	Date	Position	Structure	Purpose of Structure	Good etch?	Damage / Failure?	Status			In 20C before (mA)	In 20C after (mA)	Key Results	Further Work	Other Experiments		
										Characterised before? L/V, FL/MM	Characterised after? L/V, FL/MM	Effects of Annealing History							
20-1	Show modification of cavity resonances drift & position	?	5	19/03/2002	front facet	facet etch	accurately set cavity length	Y	N	lit only 10:10:50C (AP)	FL front 10:10:50C, pulsed drive. Also lited in 20C. OSA flat.	N	24	n/a	Spectrum is combination of resonance between facet and first trench, grating reflectivity from back section. Shows resonances which more to longer wavelength and more to shorter wavelength. Resonance positions most consistent with n=3.487 given 5um cavity (not exact match though).	Flat etch angled facet and use laser in long section to see reflectivity spectrum of grating. Use HP and back-to-back configuration.	Tried transmission measurement using tunable, FL launch & MM capture but observed structure seemed due to FL/MM coupling effects in the back-to-back configuration.	Designed using n=3.54 and dndT=4.325E-4 (obtained from the unetched device)	
6				*	3 thin air-gap trenches, beginning 5um from etched front facet	224nm trenches, 1957nm teeth	complex wavelength selective reflector	Y											
20-2	Ditto 21 with long cavity to facilitate lasing	?	5	2/10/2002	back facet	angled facet etch	prevent lasing in back section	Y	N	lit only 10:10:50C	FL front 10:10:50C, high-res	None	24	?	None - believe etch depth insufficient (PUB) but same dose and pattern as 20-1. (drift?)	Measure IV change due to etches?			
35-4	Similar to 21, (theoretically) more reflective mirrors at both ends of the cavity to facilitate lasing	DF1601-4	7	16/04/2002	front facet end, 4 periods of thin air-cavity gap grating, cavity then another 4 periods	260nm air gaps, 1390nm teeth, 5um high-reflectivity mirrors	high-Q cavity using high-reflectivity mirrors	Y	N	lit only 10:10:50C	FL front 10:10:50C, high-res	N	?	?	ASE observed but no ripples. Actually, some ripples were observed but seemed dependent on fibre position so ONLY the cavity walls in front of the grating. This might be expected from device 20-1, where no ASE ripples were observed at the back facet.	Try similar design with contact separation to drive (only 2 etched walls in front)	Tried transmission measurement using tunable, FL launch & MM capture but observed structure seemed due to FL/MM coupling effects in the control back-to-back configuration. Have transmission spectrum at 1.550/nm input.	Designed using n=3.487, dndT=4.325E-4	
36-3	Ditto 35-4.		5	*	back facet	angled facet etch	prevent lasing in back section	Y	N	lit only 10:10:50C	FL front 10:10:50C, high-res	N	?	?	Ditto 35-4		Tried transmission measurement using tunable, FL launch & MM capture but observed structure seemed due to FL/MM coupling effects in the control back-to-back configuration. Have transmission spectrum at 1.550/nm input.		
55	Etched as follows following failure of 2D etch on same device.	DF1601-4	7	06/06/2002	back facet	angled facet etch	prevent lasing in back section	Y	N	lit only 10:10:50C, FL & back 30mA at 10:20:30.5 OC	FL front 10:10:50C, 10mA & 9uW output after annealing stage	Y	19	38	Observed two peaks in the output envelope separated by 25nm (mode spacing 0.9nm). This is not consistent with a coupled cavity of 236 & 5um, which would impose an envelope peak spacing of 49nm & mode spacing 0.84nm. The structure is therefore due to grating selectivity. Working backwards from this and comparing with the etch we obtain n=3.487 and dndT=2.98E-4/K	Measure drift of mode at 1355nm to confirm normal			

Device No.	Purpose of Device	Water	#QW	Etch				Status				Ith 20C before (mA)	Ith 20C after (mA)	Key Results	Further Work	Other Experiments
				Date	Position	Structure	Purpose of Structure	Good etch?	Damage/Failure?	Characterised before? LIV FLMM Spectra	Characterised after? LIV FLMM Spectra					
69	Cascaded sequence of gratings and short cavities, with offset gratings for better selectivity; modelled as 0.06nm drift 10.60C	DF1601-4	7	24/07/2002	8 periods of grating, 1 - cavity etched from 2-stage-etched front facet	In nm, one period is 447 air, 1985nm tooth, 447 air, 1985nm tooth, 447 air, 1113 cavity, 120 air, 1984 tooth, 120 air, 1113 cavity	To increase prob. Of lasing by having the cavities pump each other in a series arrangement. To modify mode drift inside short cavities.	Y	N	IV 20.35.50C FL-front; LI 20C; back, 35C & 50C; FL-drift front	Ith-5mA & +10mA FL-front at 20C; after each anneal, also at 50C after final anneal	20min 220C; 20min 220C	18.5	Observed ASE spectrum with trough in middle. Difficult to explain well with model. Large drift with temperature, approx. 0.63nm/K - cf. pre-etch gain-peak drift 0.46nm/K		Designed using data from 55; $n_{eff}=3.487$; $d_{gr}/dT=2.98E-4/K$
70	Multiple-active-grating design in which each grating tooth is also a laser cavity. Intended to see if lasing could be achieved this way, with more gain and (arguably) less loss. Modelled as low-drift.	DF1601-4	7	23/07/2002	back facet	21 periods from 2-stage-etched front facet including 763nm air gap	prevent lasing in back section Grating laser.	Y	N	LIV 20.35.50C FL-front	Ith-5mA & +10mA FL-front at 20C; after each anneal, also at 50C after final anneal	20min 220C; 20min 220C	18.5	Observed ASE spectrum with trough in middle. Difficult to explain well with model. Similar shape to 69 but shifted about 10nm to longer wavelength.		
71	Ditto 69 with 9 periods and double etch time	DF1601-4	7	15/08/2002	back facet	back facet etch through region of thin gold	prevent lasing in back section contact separation	Y	N	LIV FL-front	Ith-5mA & +10mA FL-front at 20C; after each anneal, also at 50C after final anneal		18.5 (probable)	Seems to have been passed over. Location?		
77	Ditto 69 with 9 periods and double etch time	DF1601-4	7	15/08/2002	back facet	back facet etch through region of thin gold	prevent lasing in back section contact separation	Y	N	LIV FL-front	Ith-5mA & +10mA FL-front at 20C; after each anneal, also at 50C after final anneal		18.5 (probable)	Seems to have been passed over. Location?		
88	1:1 semiconductor multiple-active-grating design, modelled as having low drift.			15/08/2002	back facet	Equal 1430nm length air-gap & semiconductor tooth (= 1 period)	prevent lasing in back section Grating laser.	Y	N	LIV FL-front	Ith-5mA & +10mA FL-front at 20C; after each anneal, also at 50C after final anneal		18	Similar spectrum to 69 with a bit more power. Difficult to replicate in grating model - perhaps pulsed operation would avoid heating and bring the spectrum into agreement?		
				04/09/2002	back facet	flat facet etch	prevent lasing in back section allow lasing in back section so to observe spectral features due to grating reflectivity	Y	Y?	LIV FL-front	Ith-5mA & +10mA FL-front at 20C; after each anneal, also at 50C after final anneal			Measure back-section spectrum.		Some confusion over whether this is actually of device 69. I think it is really 68.

Device No.	Purpose of Device	Water	#DW	Etch				Status				Ith 20C before (mA)	Ith 20C after (mA)	Key Results	Further Work	Other Experiments	
				Date	Position	Structure	Purpose of Structure	Good etch?	Damage / Failure?	Characterised before? LIV FL/MM	Characterised after? LIV FL/MM Spectra						Annealing History
89	Ditto 88 with slight change in grating pitch.			15/08/2002	13 periods starting at front facet	Equal 1465nm length air-gap & semiconductor tooth (= 1 period)	Grating laser.	Y	N	LIV FL - Ith=5mA at 20.35:50C using FL-front	LIV FL - Ith=5mA & LIV FL-front at 20.35:50C (20C), 30.45:80mA (35C), 32.47:82 (50C)	N	18.5	Similar spectrum to 68 with a bit more power.			
90	Ditto 88 with slight change in grating pitch modelled as giving lower drift & less mirror loss. Electrical isolation so as to drive only the grating section & allow optical pumping by back section.			04/09/2002	19 periods starting at front facet	Equal 1225nm length air-gap & semiconductor tooth (= 1 period)	Grating laser.	Y	Y - gold lifted of front few periods of grating, some crystal damage on facet, back section no longer lases	LIV FL - Ith=5mA at 20.35:50C using FL-front	LIV FL - Ith=5mA & LIV FL-front at 20.35:50C (20C), 30.45:80mA (35C), 32.47:82 (50C)	2 anneals at 2000C of 20 min	19	Did not obtain lasing or even modified ASE from grating section. Back-section lased initially, with a 16mA increase in Ith due to 4655nm length reduction and leakage down a etched single sidewall.		PJB performed pulsed-drive investigation.	
				*	back facet	angled facet etch	prevent lasing in back section	Y	Post-damage: FL & MM - front obtained grating-drive back-drive & back-drive LIVs								
				*	length of RWG recess	etch through region of thin gold	contact separation	Y - 12 Ohm									